

The Chemistry of Heteroporphyrinium Cations

ヘテロポルフィリニウムカチオンの化学

TAKIGUCHI Asahi

瀧口 あさひ

**Department of Molecular and Macromolecular Chemistry,
Graduate School of Engineering, Nagoya University**

2022

Preface

The studies in this thesis were conducted under the guidance of Prof. Dr. Hiroshi Shinokubo at Graduate School of Engineering, Nagoya University during the period from April 2017 to March 2022.

This thesis mainly focuses on the synthesis and function of heteroatom-inserted porphyrin with cationic charge. To date, neutral heteroporphyrins accumulated rich chemistry, such as synthesis, physical properties, and applications. On the contrary, the examples of charged heteroporphyrins were limited even though they were expected to exhibit novel properties. The main aim of the study in this thesis is the development of the effective synthesis of various heteroporphyrinium cations and the investigation of the functionalities based on the cationic charge.

Table of Contents

List of Abbreviations	1
Chapter 1	3
General Introduction	
Chapter 2	19
Dual Emission of a Free-Base 5-Oxaporphyrinium Cation	
Chapter 3	33
5-Thiaporphyrinium Cation: Effect of Sulfur Incorporation into Porphyrin Skeleton	
Chapter 4	45
Synthesis and Tautomerization of 5-Azaporphyrinium Cations	
Chapter 5	55
Ion-Pairing Assembly of 5-Oxaporphyrinium Cation and Pentacyanocyclopentadienide	
Chapter 6	65
A Heme-Acquisition Protein Reconstructed with a Cobalt 5-Oxaporphyrinium Cation	
Chapter 7	78
Summary of This Thesis	
Appendix 1	81
Synthesis of Dihydropyrazine-Fused Porphyrin Dimers	
Appendix 2	89
Synthesis of Hydroxyisooxophlorins by Oxidative Degradation of <i>meso</i> -Hydroxyporphyrins	
Experimental Section	100
Cover Art Gallery	127
List of Publications	132
Acknowledgment	134

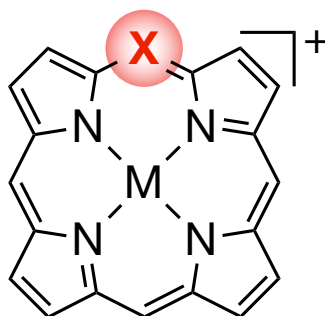
List of Abbreviations

Å	ångström unit	E_{es}	electrostatic interaction
Abs	absorbance		energy
Ac	acetyl	E_{ex}	exchange repulsion
acac	acetylacetone		interaction energy
ACID	anisotropy of the induced	equiv	equivalent(s)
	current density	ESA	excited-state absorption
APCI	atmospheric pressure	ESI	electrospray ionization
	chemical ionization	ESR	electron spin resonance
aq	aqueous solution	Et	ethyl
Ar	aryl	E_{tot}	total interaction energy
Ar ^F	3,5-	Fc	ferrocene
	bis(trifluoromethyl)phenyl	FMO	fragment molecular orbital
CV	cyclic voltammogram	fs-TA	femtosecond transient
δ	chemical shift		absorption
DDQ	2,3-dichloro-5,6-dicyano-	GSB	ground-state bleaching
	1,4-benzoquinone	h	hour(s)
DFT	density functional theory	His	histidine
DMSO	dimethyl sulfoxide	HOMO	highest occupied molecular
DPV	differential pulse		orbital
	voltammetry	HRMS	high resolution mass
EAS	evolution-associative species		spectrometry
E_{ct}	charge-transfer interaction	IC	internal conversion
	energy	IRF	instrument response function
EDA	energy decomposition	ISC	intersystem crossing
	analysis	J	coupling constant (NMR)
E_{disp}	dispersion interaction energy	LUMO	lowest unoccupied molecular
EDTA	ethylenediaminetetraacetic		orbital
	acid	M	molar

Me	methyl	T ₂	the second lowest triplet
Mes	mesityl		excited state
min	minute(s)	<i>t</i> -Bu	1,1-dimethyl-1-ethyl
MPD	mean plane deviation	TCSPC	time-correlated single photon
NICS	nucleus-independent		counting
	chemical shift	TD	time dependent
NIR	near infrared reflectance	Tf	trifluoromethanesulfonyl
NMR	nuclear magnetic resonance	TFA	trifluoroacetic acid
OEOP	octaethyloxaporphyrinium	THF	tetrahydrofuran
	cation	TLC	thin layer chromatography
OEP	octaethylporphyrin	TOF	time of flight
<i>P. aeruginosa</i>	<i>Pseudomonas aeruginosa</i>	TS	transition state
PCCp ⁻	pentacyanocyclopentadienide	Tyr	tyrosine
	anion	UV	ultraviolet
PCM	polarizable continuum model	Vis	visible
PDB	protein data bank		
Ph	phenyl		
PIFA	phenyliodine(III)		
	bis(trifluoroacetate)		
ppm	part per million		
py	pyridine		
R	an organic group		
rt	room temperature		
S ₀	singlet ground state		
S ₁	the lowest singlet excited		
	state		
sat	saturated solution		
T ₁	the lowest triplet excited		
	state		

Chapter 1

General Introduction



Contents

1-1.	Porphyrins and charged porphyrins.....	4
1-2.	Synthesis of heteroporphyrins with even-numbered <i>meso</i> -heteroatoms.....	6
1-3.	Synthesis of heteroporphyrins with odd-numbered <i>meso</i> -heteroatoms	8
1-4.	Overview of this thesis	12
1-5.	References	15

1-1. Porphyrins and charged porphyrins

Porphyrin is a square-planar macrocycle that consists of four pyrrole units and four inter-connecting methine carbon atoms (*meso*-carbons). Owing to its intriguing physicochemical and photophysical properties, porphyrin has been exploited as a key component for diverse practical applications such as photodynamic therapy,¹ organic photovoltaics,² artificial photosynthesis,³ and supramolecular chemistry.⁴ The creation of new porphyrin-based macrocyclic π -systems with appropriately tuned electronic structures represents an attractive research topic in modern organic chemistry.

The introduction of charges on the porphyrin skeleton is a promising approach to modify the electronic structure of porphyrin. Three strategies to obtain charged porphyrins have been developed:⁵ 1) introduction of charged substituents at the periphery of porphyrins,⁶ 2) complexation with valence-mismatched metal into dianionic cavity,⁷ and 3) insertion of heteroatoms into the porphyrin skeleton (Figure 1-1).⁸ Porphyrins with the charged substituents exhibit solubility in water, enabling the construction of various nano architectures.^{6a,d,f-i} For example, assembly of Sn(IV)(OH)₂ tetrakis(4-pyridyl)porphyrin tetracation and tetrakis(sulfonatophenyl)porphyrin tetraanion constructed *J*-aggregated nanotubes.^{6f} However, the charge is not directly introduced on the macrocyclic core. Valence-mismatched metalloporphyrins typically are not charged (e.g., M = Fe, Co, Mn, Al, Sn, Ga, Bi), because axial ligands on the metal neutralize the charge.^{7a,c,d,f} Without the axial ligand, such as lithium or bismuth porphyrins, they are often too reactive to handle under inert gas and without moisture.^{7e,h} To isolate charged metalloporphyrins, bulky peripheral substituents are required to protect the charged metal center kinetically. In this manner, an iron(III) porphyrinium cation with 2,6-bis(triisopropylsiloxy)phenyl groups on the *meso*-positions was isolated.^{7g} Consequently, the insertion of heteroatoms into the porphyrin skeleton should be appropriate to clarify the effect of the charge introduction into the porphyrin core because the charge is directly introduced into the porphyrinic main skeleton in which the charge is not be neutralized by axial coordinating ligand.

Heteroporphyrins have three positions in which a heteroatom is introduced: *meso*-position,^{8a} β -position,^{8a} and inner position.^{8b} In these three categories, *meso*-modified heteroporphyrins are expected to induce the dramatic electronic modulation because the heteroatom is directly embedded into the macrocyclic conjugation, whereas heteroatoms of β -modified or core-modified porphyrins partially participate in the conjugated circuit (Figure 1-2).

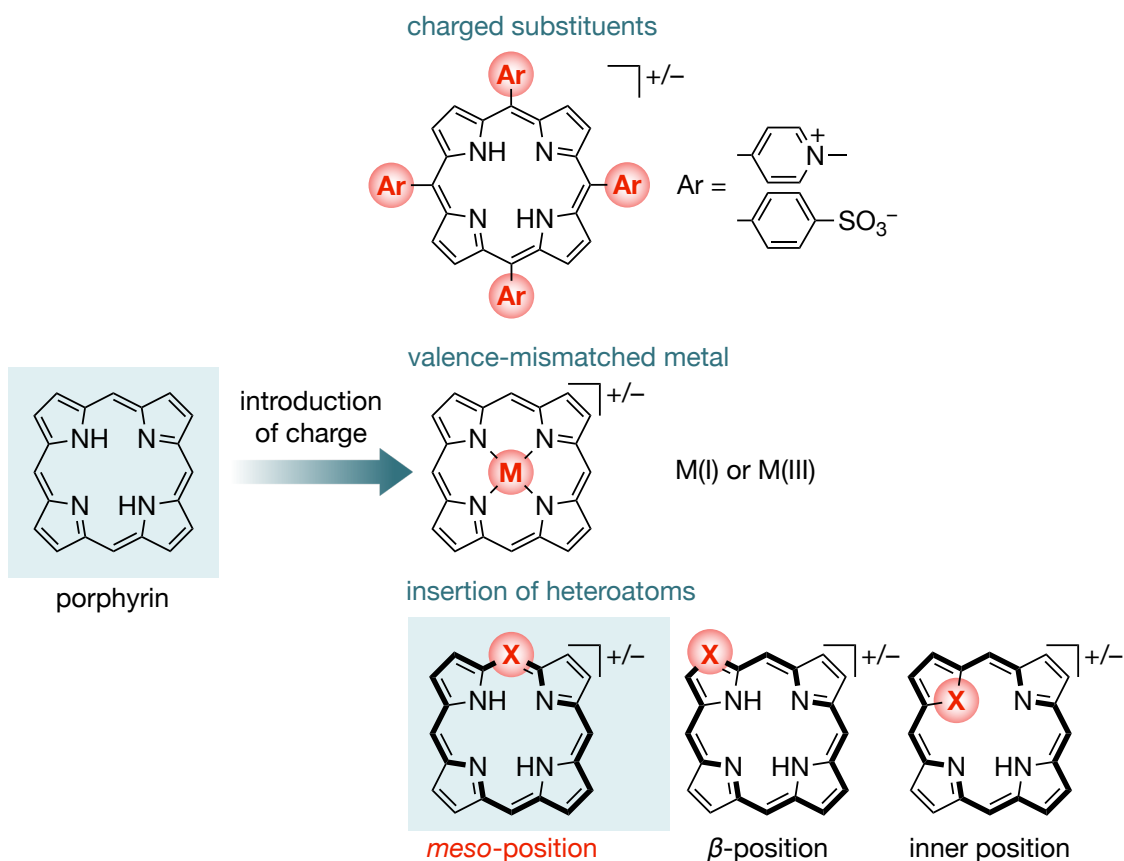


Figure 1-1. Porphyrin and charged porphyrins.

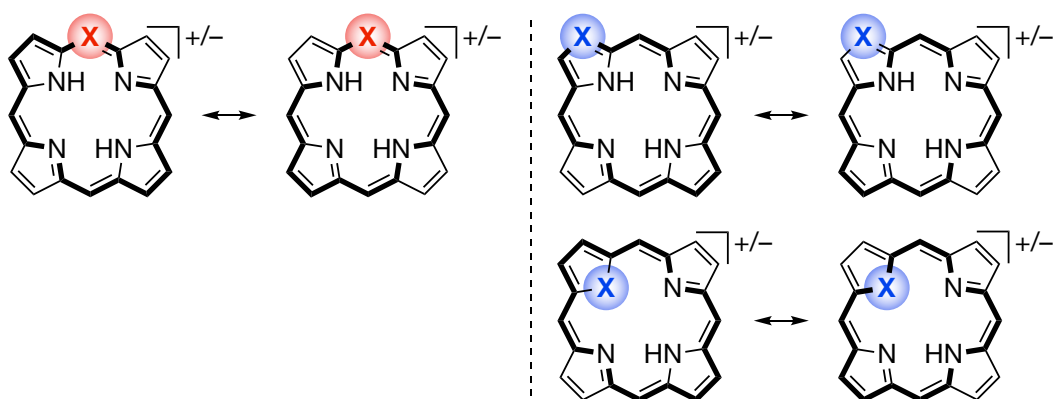
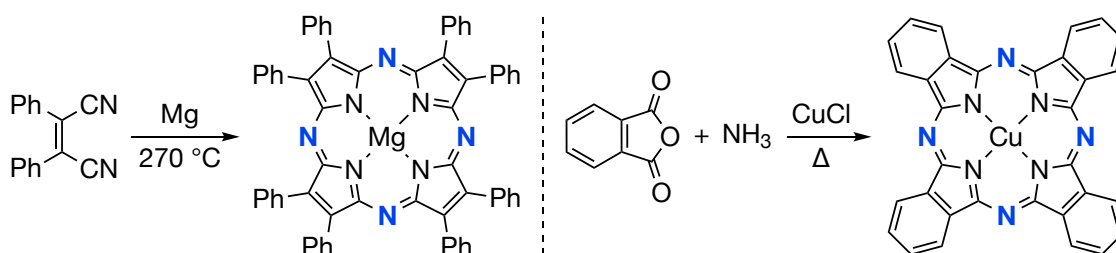


Figure 1-2. Conjugated circuit of heteroporphyrins.

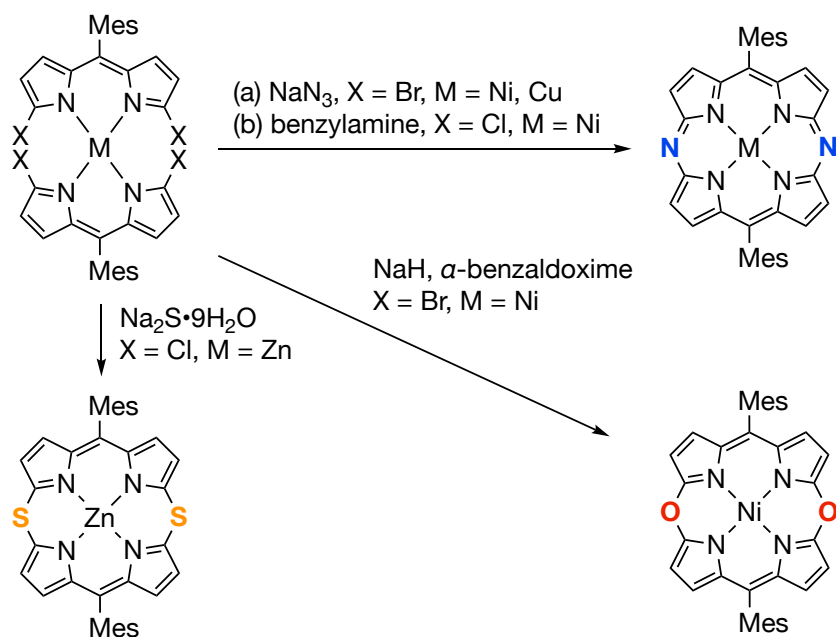
1-2. Synthesis of heteroporphyrins with even-numbered *meso*-heteroatoms

A variety of *meso*-heteroporphyrins have been previously synthesized. Among them, porphyrins with even-numbered heteroatoms were relatively easily synthesized by taking advantage of their high symmetry. Porphyrazines (tetraazaporphyrins)⁹ and phthalocyanines¹⁰ were produced through classical condensation methods (Scheme 1-1).

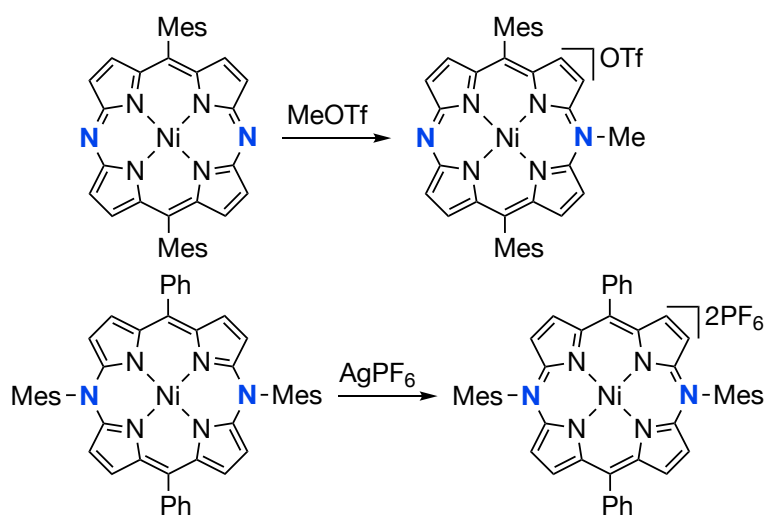


Scheme 1-1. Classical synthesis of porphyrazine (left) and phthalocyanine (right).

In 2012, Shinokubo group and Matano group independently developed the preparation of diazaporphyrins from the reaction of bis(α,α' -dibromodipyrin) metal complexes with nitrogen sources (Scheme 1-2).¹¹ Later, dithia-¹² and dioxaporphyrins¹³ were synthesized similarly by Shinokubo group and Shimizu group. In respect to charged species, however, the precedented examples have been limited to *N*-alkylated diazaporphyrin cations¹⁴ and *N,N'*-diarylated diazaporphyrin dications (Scheme 1-3).¹⁵



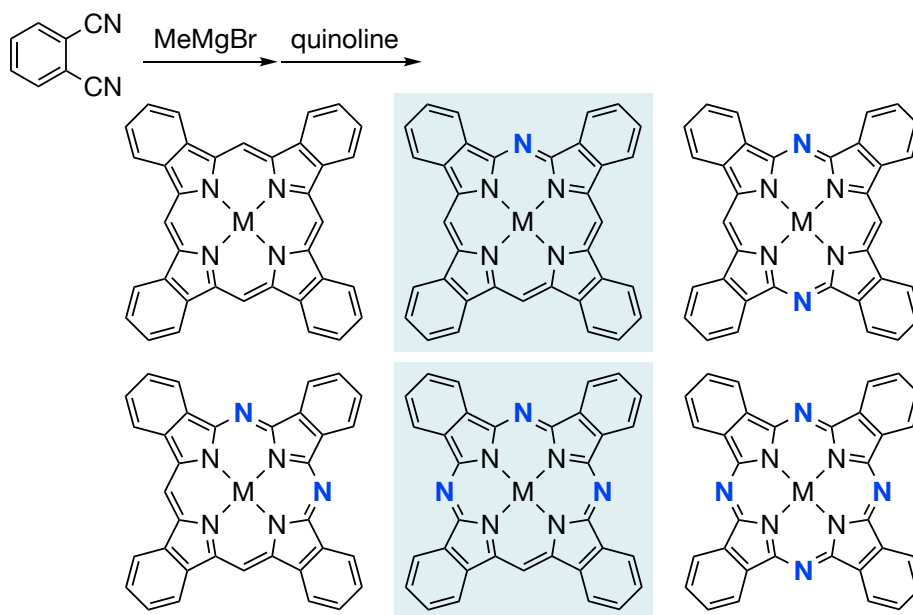
Scheme 1-2. Synthesis of various diheteroporphyrins via bis(α, α' -dibromodipyririn) metal complexes.



Scheme 1-3. *N*-Alkylated and *N,N'*-diarylated diazaporphyrins.

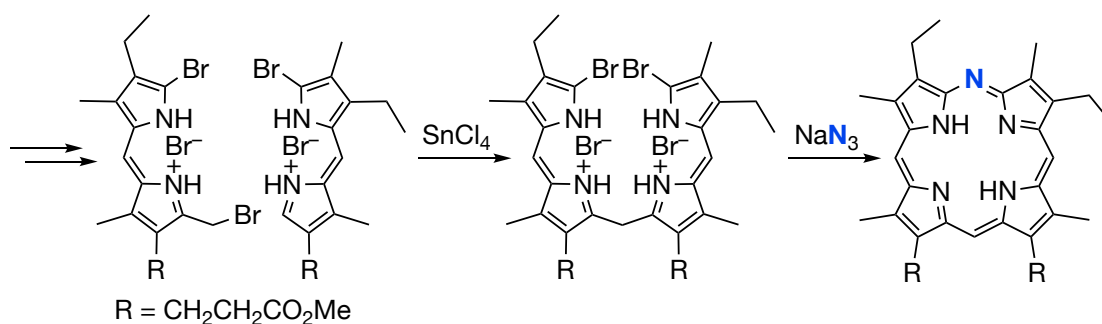
1-3. Synthesis of heteroporphyrins with odd-numbered *meso*-heteroatoms

The synthesis of *meso*-heteroporphyrins with odd-numbered heteroatoms is even more difficult due to their lower symmetry. For example, mono- and triazaporphyrins were synthesized through mixed condensation reactions (Scheme 1-4).¹⁶ However, this procedure afforded a mixture of all the possible tetrabenzozaporphyrin derivatives, among which the desired product was isolated in a low yield after troublesome separation.

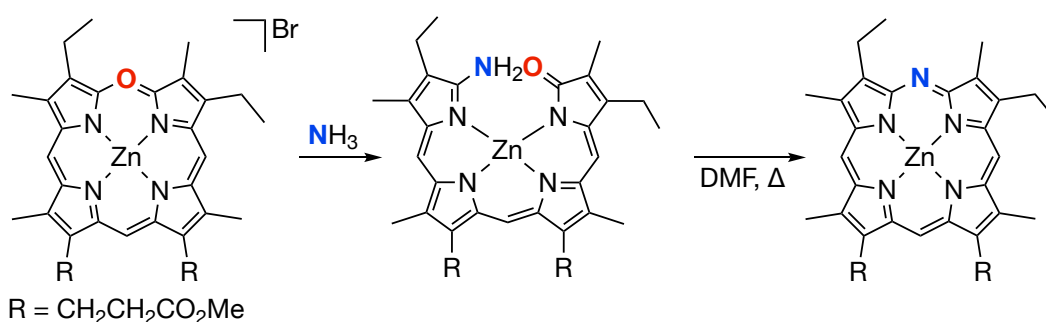


Scheme 1-4. Unselective synthesis of nitrogen incorporated porphyrin derivatives.

Selective synthesis of monoazaporphyrins is divided into two methodologies: one is the cyclization of tetrapyrroles with a nitrogen source. The other is the conversion of an oxaporphyrinium cation into a monoazaporphyrin. In 1966, Harris synthesized a monoazaporphyrin through cyclization of 1,19-dibromo-1,19-dideoxybiladiene-ac dihydrobromide with sodium azide (Scheme 1-5).¹⁷ Note that Dolphin and co-workers improved the cyclization reaction by adding dibenzo-18-crown-6 as a phase transfer agent.¹⁸ The method required multiple synthetic steps because of the use of unsymmetric building blocks. Fuhrhop and co-workers developed the synthesis of a monoazaporphyrin from an oxaporphyrinium cation in 1977 (Scheme 1-6).¹⁹ Although various methods for the synthesis of neutral monoazaporphyrins were developed, charged *meso*-monoazaporphyrins have not been investigated.

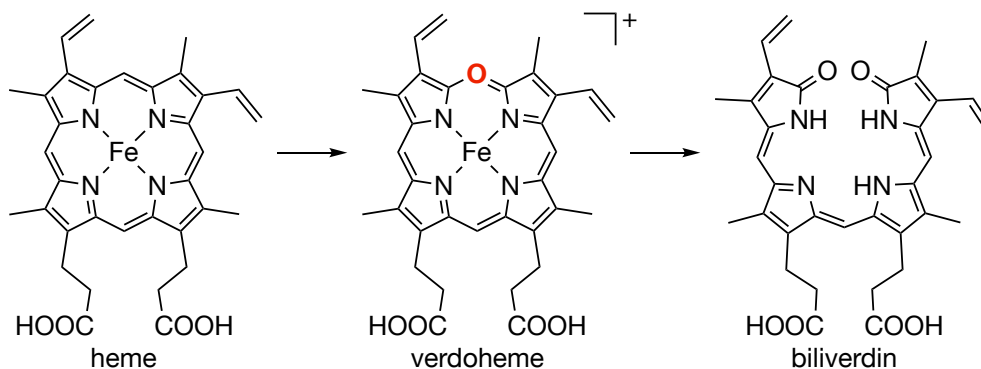


Scheme 1-5. Synthesis of monoazaporphyrin via cyclization of tetrapyrrole.

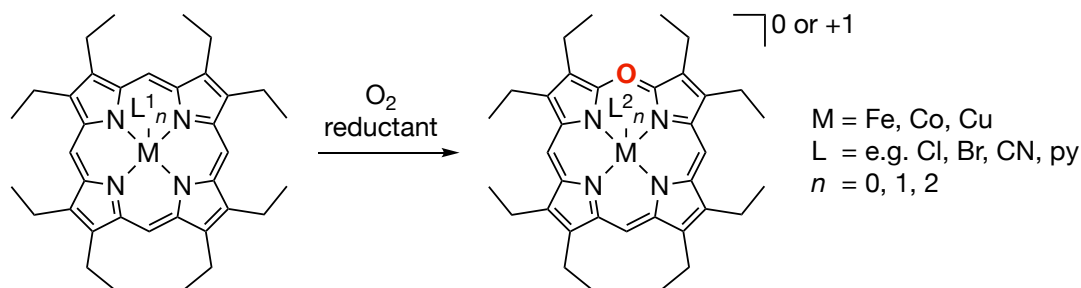


Scheme 1-6. Synthesis of monoazaporphyrin via oxaporphyrinium cation.

Oxaporphyrin has been actively explored because it is a key intermediate in the catabolic transformation of heme to biliverdin (Scheme 1-7).²⁰ In the 1990s, Balch and co-workers developed a coupled-oxidation method to prepare metal oxaporphyrins (Scheme 1-8),²¹ which was inspired by heme degradation. Oxidation of metal porphyrins by dioxygen in the presence of reductant such as ascorbic acid afforded neutral or cationic metal oxaporphyrins. The existence of the charge on the oxaporphyrins depended on the axial ligands.

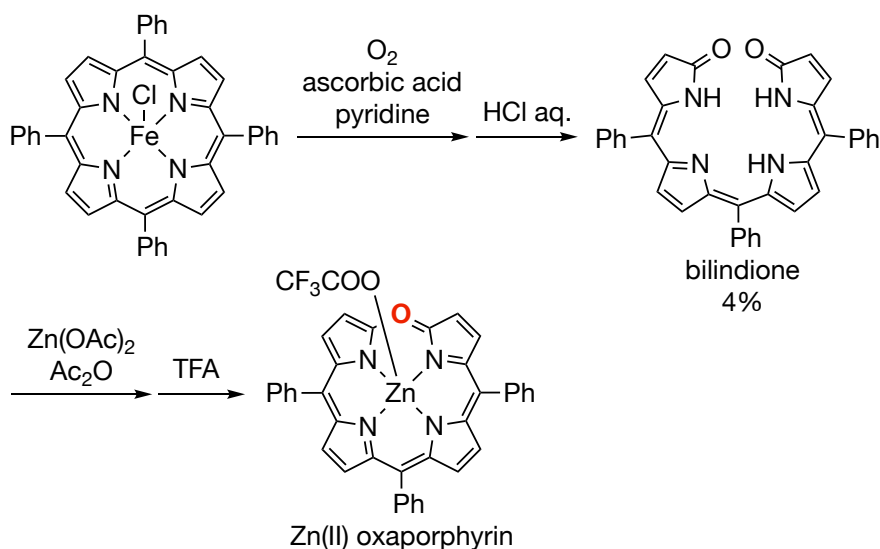


Scheme 1-7. Heme degradation catabolized by heme oxygenase.

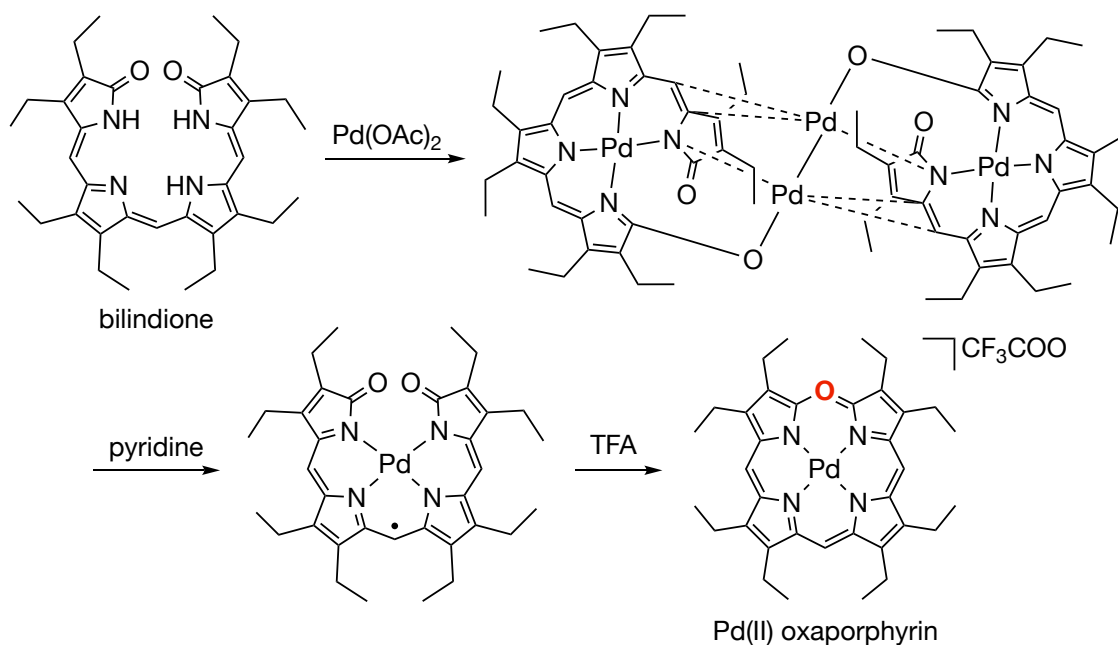


Scheme 1-8. Synthesis of metal oxaporphyrins through the coupled-oxidation method.

Mizutani and co-workers synthesized zinc oxaporphyrins through the complexation of bilindione with a Zn(II) ion followed by acid-catalyzed dehydration condensation (Scheme 1-9).²² Bilindione is a tetrapyrin analogue having carbonyl groups at the terminal α -positions. However, unfortunately, the yield of the precursory bilindione, which was synthesized by coupled oxidation and following hydrolysis, was low (4%).²³ Palladium complex of oxaporphyrin was synthesized via palladium complexation of bilindione by Balch and co-workers (Scheme 1-10).²⁴

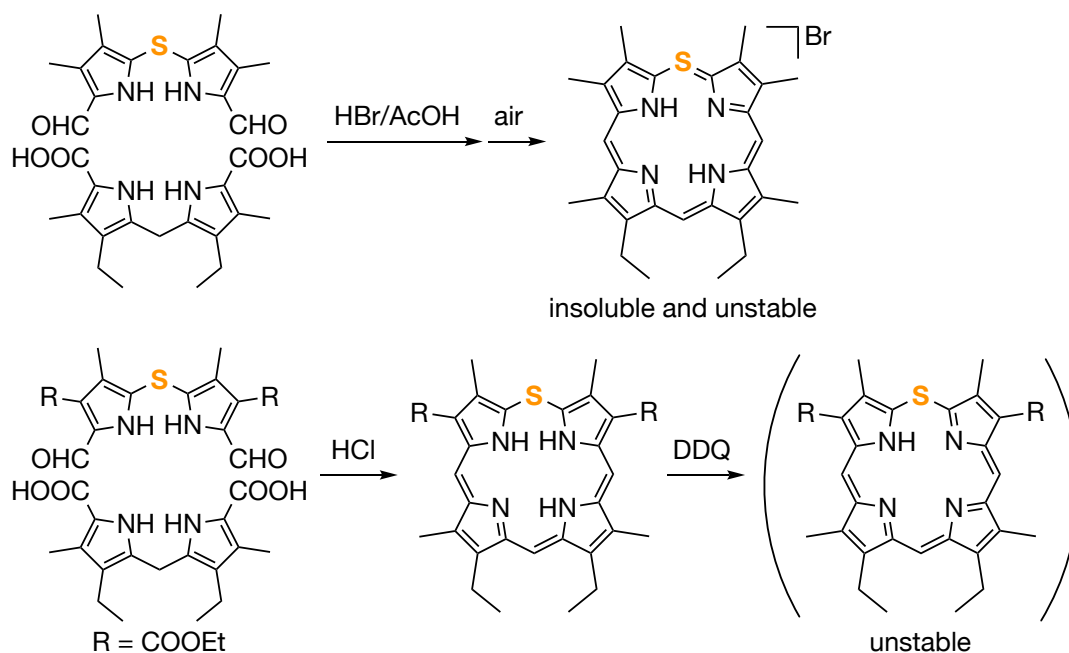


Scheme 1-9. Synthesis of Zn(II) oxaporphyrin from bilindione.



Scheme 1-10. Synthesis of Pd(II) oxaporphyrin from bilindione.

The synthesis of monothiaporphyrins was reported around 1970. Harris synthesized a cationic thiaporphyrin through condensation of dipyrrolyl monosulphidedialdehyde and dipyrromethane diacid. However, the insolubility and instability hampered the characterization of the thiaporphyrinium cation by ¹H NMR and mass spectra (Scheme 1-11 top).²⁵ Grigg group conducted a similar reaction and obtained neutral thiaporphyrin and its oxidation by DDQ (Scheme 1-11 bottom).²⁶ Unfortunately, the oxidized form was too unstable to isolate.



Scheme 1-11. Synthesis of monothiaporphyrins.

1-4. Overview of this thesis

As mentioned above, charged heteroporphyrins are expected to exhibit fascinating electronic properties. However, their difficult synthesis hampered further investigation. The author conceived the synthesis of mono-heteroporphyrinium cations to evaluate the effect of charge-insertion into the porphyrin core. For the synthesis of heteroporphyrinium cations, bilindione was adopted as a key precursor (Figure 1-3): Bilindione has two reactive carbonyl groups, which should be cyclized to heteroporphyrinium cations upon treatment of heteroatom nucleophiles.

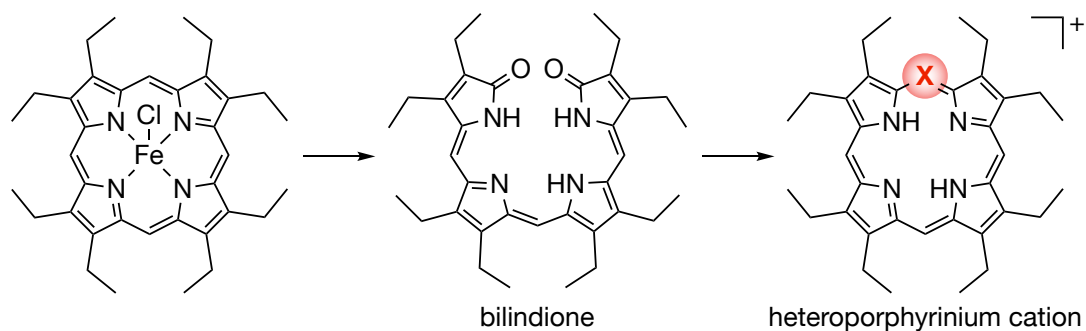


Figure 1-3. Strategy for the synthesis of heteroporphyrinium cations.

In this thesis, the author succeeded in synthesizing various heteroatom-containing porphyrinium cations via bilindione and its derivatives (Figure 1-4). Moreover, the functions of heteroporphyrinium cations exploiting the cationic charge were investigated (Figure 1-5). In Chapter 2, the facile and practical synthesis of bilindione and oxaporphyrinium cations was developed. Delocalization of the cationic charge stabilized *cis*-form of inner NH protons to exhibit dual-emission derived from *cis*- and *trans*-NH tautomers. In Chapter 3, the author succeeded in the synthesis of stable thiaporphyrinium cations. The compounds exhibited ultrafast quenching of the excited state compared to the corresponding oxaporphyrinium cations. Theoretical calculations clarified that the insertion of sulfur accelerated the rate of internal conversion, which resulted in the low fluorescence quantum yield. In Chapter 4, the author synthesized azaporphyrinium cations. The inner cavity of the azaporphyrinium cation was distorted into a rectangle owing to the steric repulsion between the peripheral substituents. The rectangular inner cavity affected the tautomerization behavior of inner-NH protons.

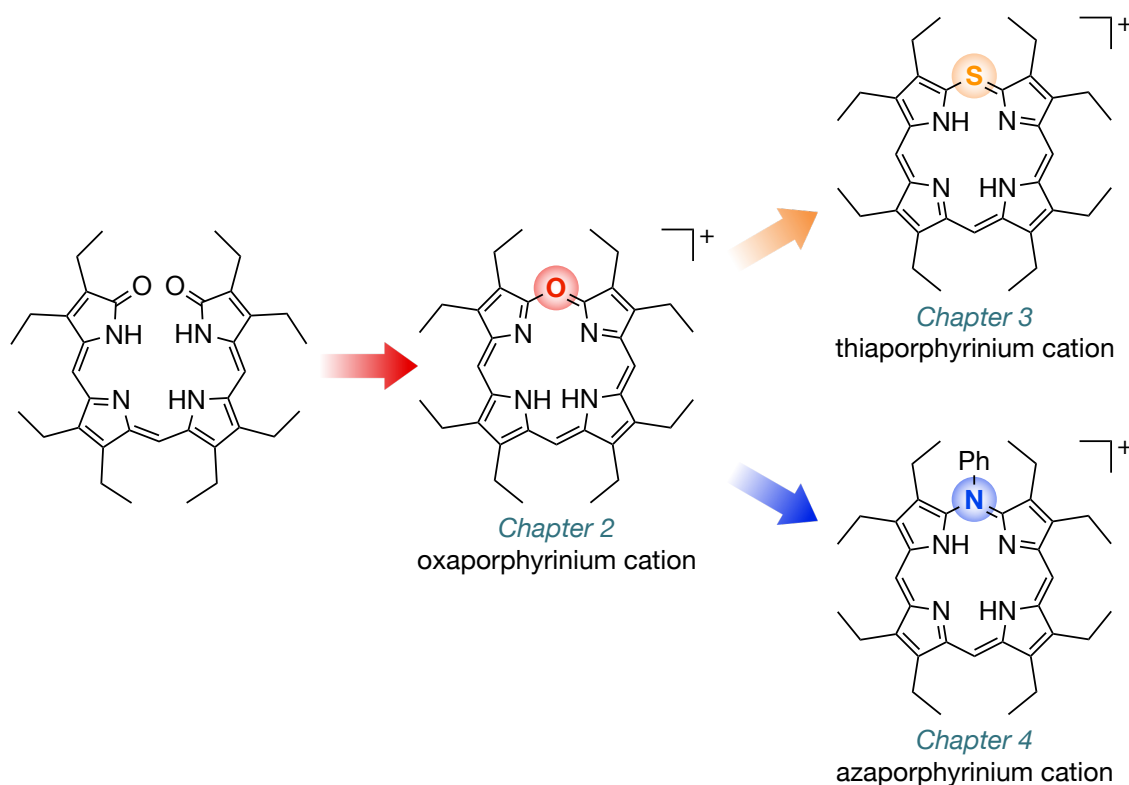


Figure 1-4. Synthesis of various heteroporphyrinium cations.

Various heteroporphyrinium cations were prepared in hand. Because the synthesis of thia- and azaporphyrinium cation was low yield and tedious purification was required for the thiaporphyrinium cation, the author focused on the oxaporphyrinium cation to examine the effect of charge introduction (Figure 1-5). The cationic charge into porphyrinic macrocycles causes effective charge delocalization and enhances electron accepting nature. In Chapter 5, the author investigated the assembling behavior of various metal oxaporphyrinium cations with planar π -anion pentacyanocyclopentadienide utilizing charge delocalization. They took different packing structure depending on the metal of oxaporphyrinium cations. In Chapter 6, the cobalt oxaporphyrinium cation was inserted into the heme-acquisition protein HasA of *Pseudomonas aeruginosa*. The reconstructed HasA exhibited strong growth-inhibition ability due to the cationic charge of the incorporated porphyrin. The reconstructed HasA also inhibited the growth of multidrug-resistant *P. aeruginosa*.

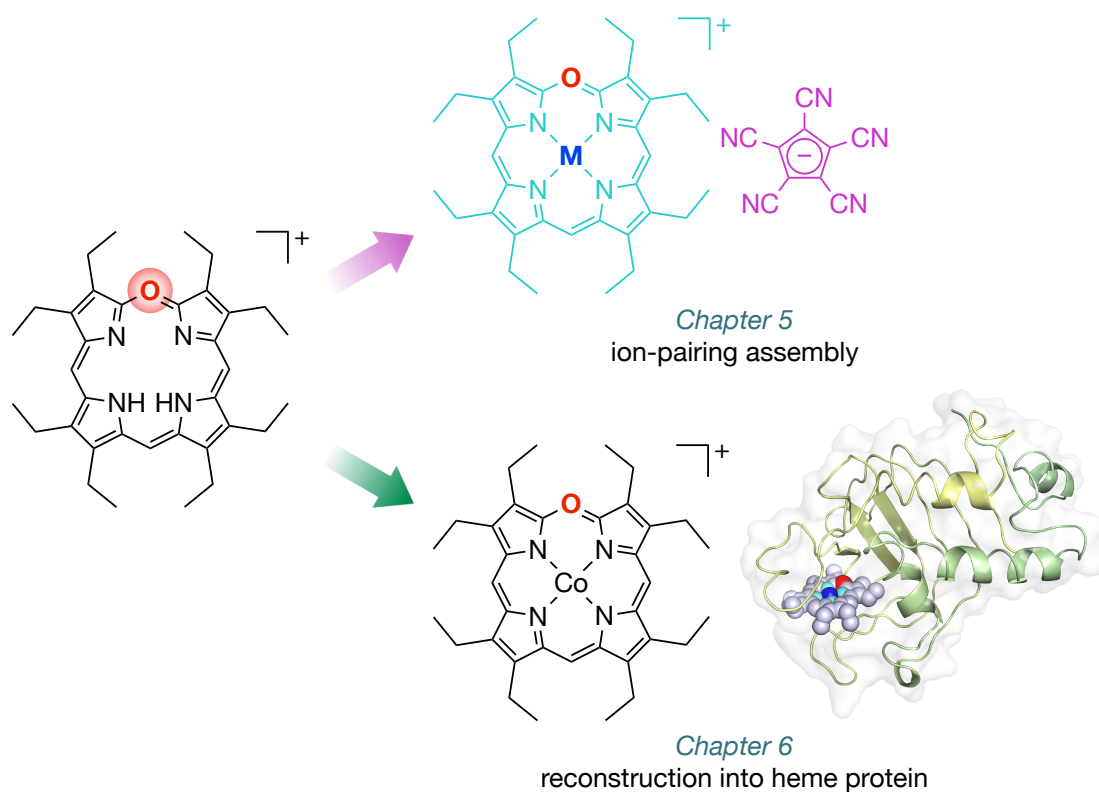


Figure 1-5. Functions of oxaporphyrinium cations.

1-5. References

1. (a) Pandey, R. K.; Zheng, G. In *The Porphyrin Handbook*; Kadish, K. M., Smith, K. M., Guillard, R., Eds.; Academic Press: San Diego, 2000; Vol. 6, pp 157–230. (b) Sternberg, E. D.; Dolphin, D.; Brückner, C. *Tetrahedron* **1998**, *54*, 4151–4202. (c) Ethirajan, M.; Chen, Y.; Joshi, P.; Pandey, R. K. *Chem. Soc. Rev.* **2011**, *40*, 340–362.
2. Kesters, J.; Verstappen, P.; Kelchtermans, M.; Lutsen, L.; Vanderzande, D.; Maes, W. *Adv. Energy Mater.* **2015**, *5*, 1500218.
3. (a) Wasielewski, M. R. *Chem. Rev.* **1992**, *92*, 435–461. (b) Gust, D.; Moore, T. A.; Moore, A. L. *Acc. Chem. Res.* **2000**, *34*, 40–48. (c) Fukuzumi, S.; Ohkubo, K.; Suenobu, T. *Acc. Chem. Res.* **2014**, *47*, 1455–1464.
4. (a) Chambron, J.-C.; Heitz, V.; Sauvage, J.-P. In *The Porphyrin Handbook*; Kadish, K. M., Smith, K. M., Guillard, R., Eds.; Academic Press: San Diego, 2000; Vol. 6, pp 1–42. (b) Ogoshi, H.; Mizutani, T.; Hayashi, T.; Kuroda, Y. In *The Porphyrin Handbook*; Kadish, K. M., Smith, K. M., Guillard, R., Eds.; Academic Press: San Diego, 2000; Vol. 6, pp 279–340.
5. Yamasumi, K.; Maeda, H. *Bull. Chem. Soc. Jpn.* **2021**, *94*, 2252–2262.
6. (a) Pasternack, R. F.; Huber, P. R.; Boyd, P.; Engasser, G.; Francesconi, L.; Gibbs, E.; Fasella, P.; Cerio Venturo, G.; Hinds, L. deC. *J. Am. Chem. Soc.* **1972**, *94*, 4511–4517. (b) Fuhrhop, J.-H. *Angew. Chem. Int. Ed. Engl.* **1976**, *15*, 648–659. (c) Ohno, O.; Kaizu, Y.; Kobayashi, H. *J. Chem. Phys.* **1993**, *99*, 4128–4139. (d) Endisch, C.; Fuhrhop, J.-H.; Buschmann, J.; Luger, P.; Siggel, U. *J. Am. Chem. Soc.* **1996**, *118*, 6671–6680. (e) Ruhlmann, L.; Nakamura, A.; Vos, J. G.; Fuhrhop, J.-H. *Inorg. Chem.* **1998**, *37*, 6052–6059. (f) Wang, Z.; Medforth, C. J.; Shelnutt, J. A. *J. Am. Chem. Soc.* **2004**, *126*, 15954–15955. (g) Wang, Z.; Medforth, C. J.; Shelnutt, J. A. *J. Am. Chem. Soc.* **2004**, *126*, 16720–16721. (h) Wang, Z.; Ho, K. J.; Medforth, C. J.; Shelnutt, J. A. *Adv. Mater.* **2006**, *18*, 2557–2560. (i) Martin, K. E.; Wang, Z.; Busani, T.; Garcia, R. M.; Chen, Z.; Jiang, Y.; Song, Y.; Jacobsen, J. L.; Vu, T. T.; Schore, N. E.; Swartzentruber, B. S.; Medforth, C. J.; Shelnutt, J. A. *J. Am. Chem. Soc.* **2010**, *132*, 8194–8201. (j) Sasano, Y.; Yasuda, N.; Maeda, H. *Dalton Trans.* **2017**, *46*, 8924–8928. (k) Sasano, Y.; Haketa, Y.; Tanaka, H.; Yasuda, N.; Hisaki, I.; Maeda, H. *Chem. Eur. J.* **2019**, *25*, 6712–6717.
7. (a) Treibs, A. *Justus Liebigs Ann. Chem.* **1969**, *728*, 115–143. (b) Fleischer, E. B.; Laszlo, A.

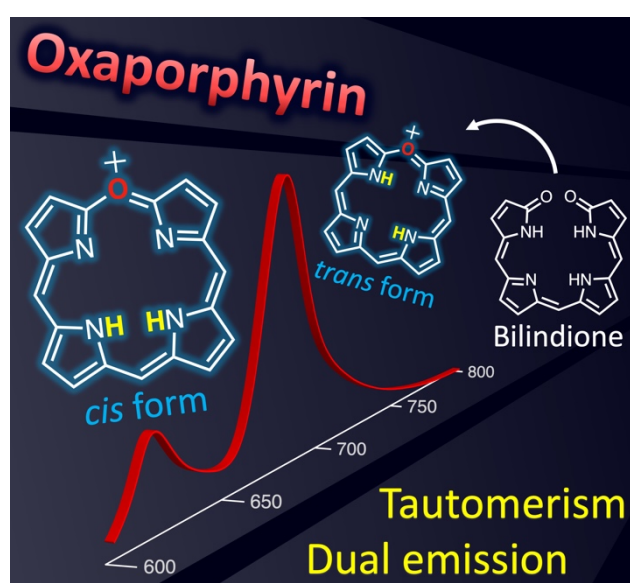
- Inorg. Nucl. Chem. Lett.* **1969**, *5*, 373–376. (c) Buchler, J. W.; Puppe, L.; Schneehage, H. H. *Justus Liebigs Ann. Chem.* **1971**, *749*, 134–145. (d) Cheng, R. J.; Latos-Grażyński, L.; Balch, A. L. *Inorg. Chem.* **1982**, *21*, 2412–2418. (e) Arnold, J. J. *Chem. Soc., Chem. Commun.* **1990**, 976–978. (f) Kane, K. M.; Lemke, F. R.; Petersen, J. L. *Inorg. Chem.* **1995**, *34*, 4085–4091. (g) Fang, M.; Wilson, S. R.; Suslick, K. S. *J. Am. Chem. Soc.* **2008**, *130*, 1134–1135. (h) Balasanthiran, V.; Chisholm, M. H.; Durr, C. B. *Angew. Chem. Int. Ed.* **2013**, *53*, 1594–1597. (i) Haketa, Y.; Bando, Y.; Sasano, Y.; Tanaka, H.; Yasuda, N.; Hisaki, I.; Maeda, H. *iScience* **2019**, *14*, 241–256.
8. (a) Matano, Y. *Chem. Rev.* **2017**, *117*, 3138–3191. (b) Chatterjee, T.; Shetti, V. S.; Sharma, R.; Ravikanth, M. *Chem. Rev.* **2017**, *117*, 3254–3328.
 9. Cook, A. H.; Linstead, R. P. *J. Chem. Soc.* **1937**, 929–933.
 10. (a) Nemykin, V. N.; Lukyanets, E. A. In *Handbook of Porphyrin Science*; Kadish, K. M., Smith, K. M., Guillard, R., Eds.; World Scientific Publishing: Singapore, 2010; Vol. 3, pp 1–323. (b) von Braun, A.; Tcherniak, J. *Ber. Dtsch. Chem. Ges.* **1907**, *40*, 2709–2714. (c) de Diesbach, H.; von der Weid, E. *Helv. Chim. Acta* **1927**, *10*, 886–888. (d) Dandridge, A. G.; Drescher, H. A.; Thomas, J.; *GB Patent*, 322169, **1928**.
 11. (a) Horie, M.; Hayashi, Y.; Yamaguchi, S.; Shinokubo, H. *Chem. Eur. J.* **2012**, *18*, 5919–5923. (b) Matano, Y.; Shibano, T.; Nakano, H.; Imahori, H. *Chem. Eur. J.* **2012**, *18*, 6208–6216. (c) Shimizu, S. *Heterocycles* **2020**, *100*, 1123.
 12. Kamiya, H.; Kondo, T.; Sakida, T.; Yamaguchi, S.; Shinokubo, H. *Chem. Eur. J.* **2012**, *18*, 16129–16135.
 13. Nishiyama, A.; Fukuda, M.; Mori, S.; Furukawa, K.; Fliegl, H.; Furuta, H.; Shimizu, S. *Angew. Chem. Int. Ed.* **2018**, *57*, 9728–9733.
 14. Chia, W. X.; Nishijo, M.; Kang, S.; Oh, J.; Nishimura, T.; Omori, H.; Longevial, J.-F.; Miyake, Y.; Kim, D.; Shinokubo, H. *Chem. Eur. J.* **2020**, *26*, 2754–2760.
 15. (a) Satoh, T.; Minoura, M.; Nakano, H.; Furukawa, K.; Matano, Y. *Angew. Chem. Int. Ed.* **2016**, *55*, 2235–2238. (b) Sudoh, K.; Satoh, T.; Amaya, T.; Furukawa, K.; Minoura, M.; Nakano, H.; Matano, Y. *Chem. Eur. J.* **2017**, *23*, 16364–16373. (c) Sudoh, K.; Hatakeyama, T.; Furukawa, K.; Nakano, H.; Matano, Y. *J. Porphyrins Phthalocyanines* **2018**, *22*, 542–551. (d) Sudoh, K.; Satoh, Y.; Furukawa, K.; Nakano, H.; Matano, Y. *J. Porphyrins*

- Phthalocyanines* **2020**, *24*, 286–297. (e) Ochiai, H.; Furukawa, K.; Nakano, H.; Matano, Y. *J. Org. Chem.* **2021**, *86*, 2283–2296. (f) Shimizu, Y.; Matano, Y. *J. Porphyrins Phthalocyanines* **2021**, *25*, 1004–1014. (g) Satoh, Y.; Fujita, Y.; Muramatsu, N.; Furukawa, K.; Ikoma, T.; Minoura, M.; Nakano, H.; Matano, Y. *ChemPlusChem* **2021**, *86*, 1476–1486.
16. (a) Barrett, P. A.; Linstead, R. P.; Tuey, G. A. P.; Robertson, J. M. *J. Chem. Soc.* **1939**, 1809–1810. (b) Barrett, P. A.; Linstead, R. P.; Leavitt, J. J.; Rowe, G. A. *J. Chem. Soc.* **1940**, 1076–1092. (c) van As, A.; Joubert, C. C.; Buitendach, B. E.; Erasmus, E.; Conradie, J.; Cammidge, A. N.; Chambrier, I.; Cook, M. J.; Swarts, J. C. *Inorg. Chem.* **2015**, *54*, 5329–5341. (d) Mack, J.; Sosa-Vargas, L.; Coles, S. J.; Tizzard, G. J.; Chambrier, I.; Cammidge, A. N.; Cook, M. J.; Kobayashi, N. *Inorg. Chem.* **2012**, *51*, 12820–12833. (e) Cammidge, A. N.; Chambrier, I.; Cook, M. J.; Hughes, D. L.; Rahman, M.; Sosa-Vargas, L. *Chem. Eur. J.* **2011**, *17*, 3136–3146. (f) Cammidge, A. N.; Chambrier, I.; Cook, M. J.; Langner, E. H. G.; Rahman, M.; Swarts, J. C. *J. Porphyrins Phthalocyanines* **2011**, *15*, 890–897. (g) Ivanova, Yu. B.; Churakhina, Yu. I.; Semeikin, A. S.; Mamardashvili, N. *Zh. Russ. J. Gen. Chem.* **2009**, *79*, 833–838. (h) Cammidge, A. N.; Cook, M. J.; Hughes, D. L.; Nekelson, F.; Rahman, M. *Chem. Commun.* **2005**, 930–932. (i) Leznoff, C. C.; McKeown, N. B. *J. Org. Chem.* **1990**, *55*, 2186–2190.
17. Harris, R. L. N. *Tetrahedron Lett.* **1969**, *10*, 3689–3692.
18. Singh, J. P.; Xie, L. Y.; Dolphin, D. *Tetrahedron Lett.* **1995**, *36*, 1567–1570.
19. (a) Fuhrhop, J.-H.; Krüger, P.; Sheldrick, W. S. *Justus Liebigs Ann. Chem.* **1977**, *1977*, 339–359. (b) Fuhrhop, J.-H.; Krüger, P. *Justus Liebigs Ann. Chem.* **1977**, *1977*, 360–370.
20. (a) Schmid, R.; McDonagh, A. F. In *The Porphyrins*; Dolphin, D., Eds.; Academic Press: New York, 1979; Vol. 6, pp 257–292. (b) Ortiz de Montellano, P. R. *Curr. Opin. Chem. Biol.* **2000**, *4*, 221–227. (c) Ortiz de Montellano, P. R. In *The Porphyrin Handbook*; Kadish, K. M., Smith, K. M., Guillard, R., Eds.; Academic Press: San Diego, 2003; Vol. 12, pp 183–210. (d) Matsui, T.; Unno, M.; Ikeda-Saito, M. *Acc. Chem. Res.* **2009**, *43*, 240–247.
21. (a) Balch, A. L.; Bowles, F. L. In *Handbook of Porphyrin Science*; Kadish, K. M., Smith, K. M., Guillard, R., Eds.; World Scientific Publishing: Singapore, 2010; Vol. 8, pp 293–342. (b) Balch, A. L.; Latos-Grażyński, L.; Noll, B. C.; Olmstead, M. M.; Szterenber, L.; Safari, N. *J. Am. Chem. Soc.* **1993**, *115*, 1422–1429. (c) Balch, A. L.; Noll, B. C.; Safari, N. *Inorg.*

- Chem.* **1993**, *32*, 2901–2905. (d) Balch, A. L.; Koerner, R.; Olmstead, M. M. *J. Chem. Soc., Chem. Commun.* **1995**, 873–874. (e) Balch, A. L.; Koerner, R.; Latos-Grażyński, L.; Lewis, J. E.; St. Claire, T. N.; Zovinka, E. P. *Inorg. Chem.* **1997**, *36*, 3892–3897. (f) Rath, S. P.; Olmstead, M. M.; Balch, A. L. *Inorg. Chem.* **2004**, *43*, 7648–7655. (g) Balch, A. L.; Mazzanti, M.; Olmstead, M. M. *J. Chem. Soc., Chem. Commun.* **1994**, 269–270. (h) Balch, A. L.; Mazzanti, M.; St. Claire, T. N.; Olmstead, M. M. *Inorg. Chem.* **1995**, *34*, 2194–2200. (i) Koerner, R.; Olmstead, M. M.; Ozarowski, A.; Phillips, S. L.; Van Calcar, P. M.; Winkler, K.; Balch, A. L. *J. Am. Chem. Soc.* **1998**, *120*, 1274–1284.
22. Kakeya, K.; Nakagawa, A.; Mizutani, T.; Hitomi, Y.; Kodera, M. *J. Org. Chem.* **2012**, *77*, 6510–6519.
23. Nakamura, R.; Kakeya, K.; Furuta, N.; Muta, E.; Nishisaka, H.; Mizutani, T. *J. Org. Chem.* **2011**, *76*, 6108–6115.
24. (a) Lord, P.; Olmstead, M. M.; Balch, A. L. *Angew. Chem. Int. Ed.* **1999**, *38*, 2761–2763. (b) Lord, P. A.; Noll, B. C.; Olmstead, M. M.; Balch, A. L. *J. Am. Chem. Soc.* **2001**, *123*, 10554–10559.
25. Harris, R. L. N. *Tetrahedron Lett.* **1969**, *10*, 3689–3692.
26. (a) Broadhurst, M. J.; Grigg, R.; Johnson, A. W. *J. Chem. Soc. D* **1970**, 807–809. (b) Broadhurst, M. J.; Grigg, R.; Johnson, A. W. *J. Chem. Soc., Perkin Trans. I* **1972**, 1124–1135.

Chapter 2

Dual Emission of a Free-Base 5-Oxaporphyrinium Cation



Contents

2-1.	Introduction	20
2-2.	Synthesis of bilindione and oxaporphyrinium cations	21
2-3.	Structure analysis	23
2-4.	Optical properties and excited states dynamics.....	26
2-5.	Summary of Chapter 2	29
2-6.	References	30

2-1. Introduction

As explained in Chapter 1, the 5-oxaporphyrin has been actively explored because it is the main skeleton of verdoheme, a key intermediate in the catabolic transformation of heme to biliverdin (Chapter 1, Scheme 1-7).¹ A variety of 5-oxaporphyrin metal complexes have been prepared by several research groups, and systematic investigations² into their photophysical, magnetic, and redox properties, as well as their reactivity toward nucleophiles³ have been carried out (Figure 2-1). Notably, the replacement of one *meso*-carbon of a typical porphyrin structure with an oxygen decreases the structural and electronic symmetry, resulting in increased Q-like absorption.^{2b}

In this chapter, the author described the synthesis and properties of a free-base 5-oxaporphyrinium cation (**2-5⁺**) (Figure 2-1 (b)), which was efficiently prepared by the treatment of bilindione, a linear tetrapyrrole with terminal carbonyl groups, with trifluoromethanesulfonic anhydride. Interestingly, **2-5⁺** exhibited unique NH tautomerization behavior that is markedly different from that of normal porphyrins: the two inner NH units in **2-5⁺** are predominantly arranged in a *cis* manner, while regular porphyrins usually prefer adopting a *trans* configuration.⁴ This anomalous NH tautomerism manifests in dual emission.⁵ Although *cis* tautomers have been recognized as key intermediates in the NH tautomerism of free-base porphyrins, examples of their isolation and characterization remain scarce.^{6,7} In this work, the author elucidated that the introduction of charged heteroatoms at the *meso*-positions effectively stabilizes the *cis* form of free-base porphyrinic macrocycles.

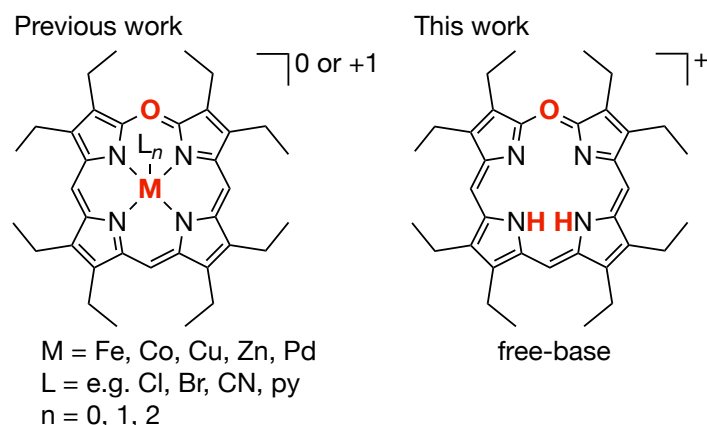
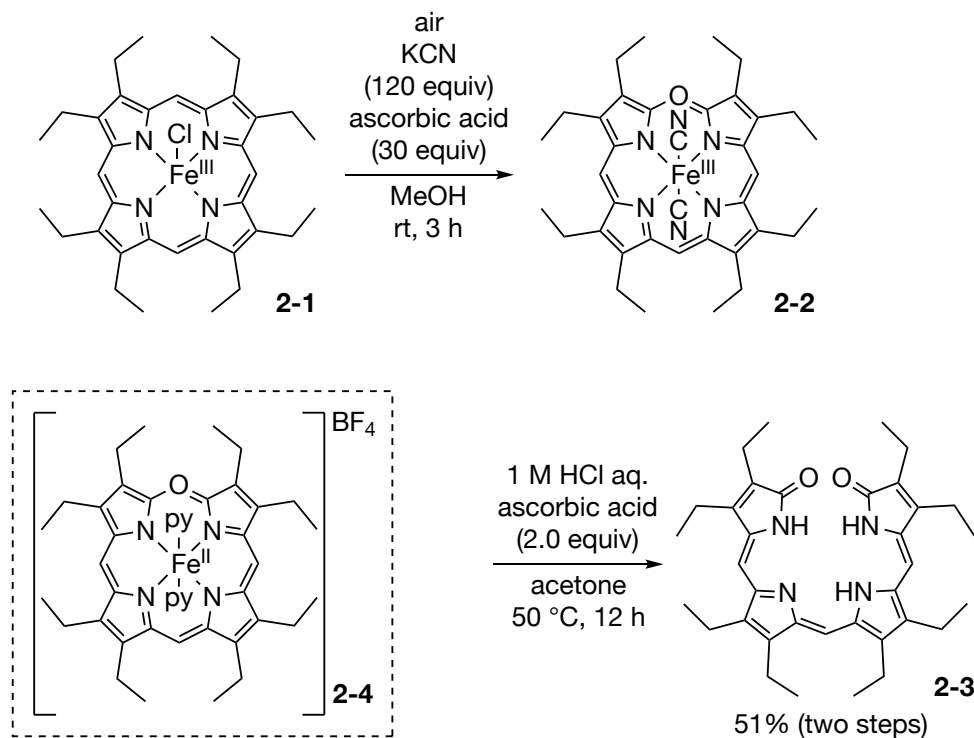


Figure 2-1. 5-Oxaporphyrin derivatives.

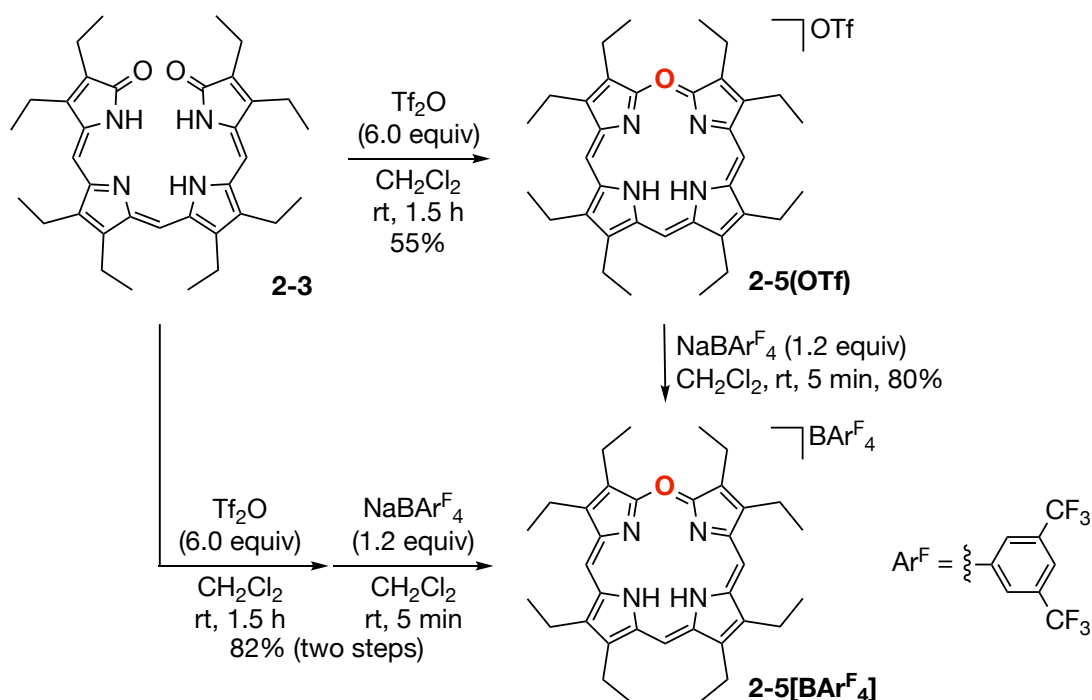
2-2. Synthesis of bilindione and oxaporphyrinium cations

For the preparation of bilindione **2-3**, a modified ‘coupled oxidation’ protocol was developed (Scheme 2-1). Saito and Itano have synthesized pyridine-coordinated iron(II) oxaporphyrin **2-4** by a ligand-exchange reaction of iron(III) octaethylporphyrin **2-1** with pyridine⁸ and subsequent coupled oxidation using molecular oxygen and ascorbic acid.⁹ Subsequent hydrolysis of **2-4** with 1 M HCl aq. provided bilindione **2-3**¹⁰ in 28% yield over three steps. However, the isolation of **2-4** required a multi-step work-up and careful handling under anaerobic conditions. The author thus focused on cyanoiron(III) oxaporphyrin **2-2** as a potential intermediate,¹¹ as **2-2** is air-stable. The initial attempt to remove the iron(III) ion from **2-2** by acidic hydrolysis afforded the desired bilindione **2-3** in a very low yield. However, the addition of ascorbic acid significantly enhanced the efficiency of the hydrolysis of **2-2**. After optimization, **2-3** was obtained in 51% yield over two steps through coupled oxidation of **2-1** in the presence of potassium cyanide and hydrolysis in the presence of ascorbic acid. **Caution:** As these procedures may generate hazardous hydrogen cyanide, all operations were conducted in a well-ventilated hood.



Scheme 2-1. Synthesis of **2-3** by coupled oxidation and hydrolysis.

Scheme 2-2 shows the syntheses of free-base 5-oxaporphyrinium cations **2-5(OTf)** and **2-5[BAr^F₄]**. Treatment of **2-3** with trifluoromethanesulfonic anhydride (Tf₂O) provided 5-oxaporphyrinium trifluoromethanesulfonate **2-5(OTf)** in 55% yield. The use of acetic anhydride (Ac₂O) instead of Tf₂O did not generate the ring-closing product. A subsequent ion-exchange reaction of **2-5(OTf)** with sodium tetrakis[3,5-bis(trifluoromethyl)phenyl]borate (NaBAr^F₄) afforded the corresponding borate salt **2-5[BAr^F₄]** in 80% yield. When these two steps were conducted consecutively, **2-5[BAr^F₄]** was isolated in 82% yield from **2-3**. While **2-5(OTf)** gradually underwent degradation on silica gel, **2-5[BAr^F₄]** was sufficiently stable in both solution and the solid state as well as on silica gel, enabling its purification via column chromatography. The author attempted protonation of the inner nitrogen atoms of **2-5[BAr^F₄]** with methanesulfonic acid. However, protonated product was not detected. Instead, hydrolysis proceeded to afford the ring-opening product.



Scheme 2-2. Synthesis of oxaporphyrins **2-5(OTf)** and **2-5[BAr^F₄]**.

2-3. Structure analysis

The structure of **2-5[BAr^F₄]** was unambiguously confirmed by single-crystal X-ray diffraction analysis (Figure 2-2). The oxaporphyrinium skeleton is substantially removed from the counter ion, suggesting negligible electronic interactions. The positions of the two inner NH protons were determined based on the C–N–C bond angles.¹² Importantly, these two NH units are arranged in a *cis* configuration, while typical porphyrins prefer to adopt a *trans* form due to the intramolecular steric repulsion.⁴ The predominant formation of the *cis* form was supported by theoretical calculations (*vide infra*). The four central nitrogen atoms are arranged in a rectangular geometry (long side: 2.97–3.02 Å; short side: 2.71 Å), while octaethylporphyrin (**OEP**) contains a square inner cavity (side length: 2.92 Å).¹³ The rectangular structure of **2-5[BAr^F₄]** could be due to the relaxation of the structural strain derived from the steric repulsion between the two NH units. Consequently, **2-5[BAr^F₄]** exhibits a highly planar structure with a mean plane deviation of 0.041 Å. The lengths of the C–O bonds (1.362(4) and 1.365(5) Å) lie between that of typical C–O single bonds (1.43 Å) and C–O double bonds (1.15–1.28 Å),¹⁴ suggesting that the oxygen atom contributes to the overall conjugation.

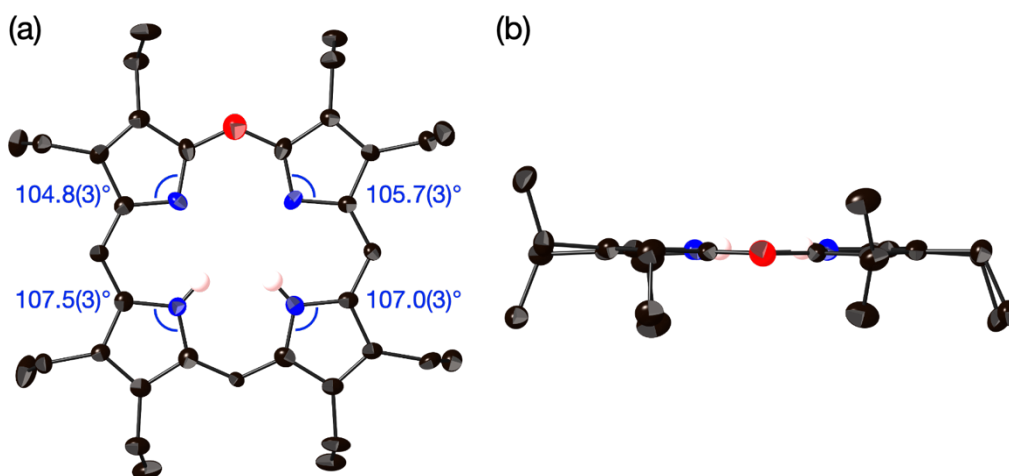


Figure 2-2. X-ray crystal structure of **2-5[BAr^F₄]** with ellipsoids set at 50 % probability; (a) top view and (b) side view. Tetraarylborate anion and all hydrogen atoms except for those on the inner nitrogen atoms are omitted for clarity.

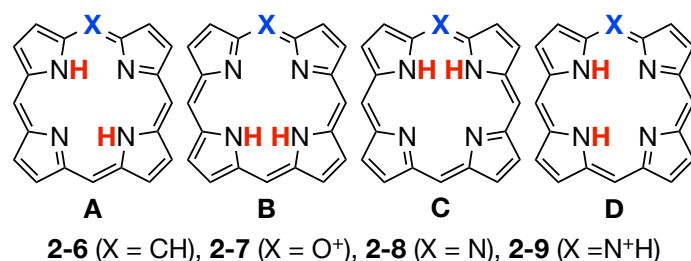
The ^1H NMR spectra of **2-5(OTf)** and **2-5[BAr^F₄]** exhibited signals for the *meso*-protons at 9.05–9.44 ppm, which are substantially downfield shifted relative to those of bilindione **2-3** (5.88 and 6.62 ppm).¹⁵ This result indicates the presence of a diatropic ring current in the macrocyclic conjugation. The aromatic nature of the **2-5⁺** was supported by NICS calculations, which afforded a NICS(1) value of $\delta = -5.96$ ppm at the center of the macrocycle. In addition, the ACID plot clearly indicated the existence of a clockwise current stream.

The electrochemical properties of **2-5[BAr^F₄]** and **OEP** were studied using cyclic voltammetry against the ferrocene/ferrocenium couple (Fc/Fc^+) as an external reference. Oxaporphyrin **2-5[BAr^F₄]** exhibited one reversible oxidation wave and one reversible reduction wave at 1.08 and -0.74 V, respectively. These redox potentials are positively shifted relative to those of **OEP** (0.38 and -1.91 V), highlighting its enhanced electron acceptability due to the positive charge. The electrochemical HOMO–LUMO gap of **2-5[BAr^F₄]** (1.82 V) is narrower than that of **OEP** (2.29 V).

To clarify the reason for the preferential formation of the *cis* form in **2-5⁺**, DFT calculations at the CAM-B3LYP/6-311+G(2d,p) level of theory were conducted (Table 2-1). The solvent effect was accounted for using the polarizable continuum model (PCM). In general, porphyrin adopts the *trans* form **2-6A** rather than the *cis* form **2-6B** to avoid steric congestion between the inner NH protons.⁴ Indeed, the DFT calculations confirmed that **2-6A** is by 6.9 kcal mol^{-1} energetically more stable than **2-6B**. In sharp contrast, the opposite trend was observed for the 5-oxaporphyrinium cation, i.e., the *cis* form **2-7B** is by 1.5 kcal mol^{-1} more favorable than the *trans* form **2-7A**. The other possible tautomers, i.e., **2-7C** and **2-7D** are energetically unfavorable, suggesting that their contribution is negligible. The charge distributions of the four tautomers **2-7A–D** are shown in Figure 2-3. Importantly, **2-7B** shows the greatest delocalization of the positive charge over the macrocycle among all tautomers. This observation can be rationalized by considering the resonance contributors (Figure 2-4). In **2-7B**, the positive charge can be delocalized on the side opposite the *meso*-oxygen atom due to the presence of two electron-donating amine-type nitrogen atoms. Furthermore, the relative stability of *cis*- and *trans*-tautomers was also evaluated for 5-azaporphyrin **2-8** and its protonated form **2-9**. Interestingly, cationic **2-9** exhibited a *cis–trans* energy gap that is by 6.6 kcal mol^{-1} smaller than that of neutral compound **2-8**. These results indicate the role of charge delocalization in the stabilization of the

cis form. The author examined the tautomerism of **2-5**[BAr^F₄] via variable-temperature ¹H NMR measurements. However, decreasing the temperature only resulted in broadening of the ¹H NMR signal, indicating a fast equilibrium among the NH tautomers. This notion was also supported by DFT calculations.

Table 2-1. Relative free energies of the tautomers **A–D** of porphyrin **2-6** and porphyrin analogues **2-7–2-9**, calculated at the CAM-B3LYP/6-311+G(2d,p) level of theory.^a



Compound	X	A ^b	B ^b	C ^b	D ^b
2-6	CH	0	+6.91	^c	^c
2-7	O ⁺	0	−1.49	+16.87	+5.81
2-8	N	0	+8.05	+8.70	+7.14
2-9	N ⁺ H	0	+1.45	+14.40	+6.02

^a To reduce calculation costs, ethyl substituents were replaced with hydrogen atoms in the model compounds. The solvent effect was accounted for using the PCM method. ^b All values in (kcal mol^{−1}).

^c Same as **2-6B**.

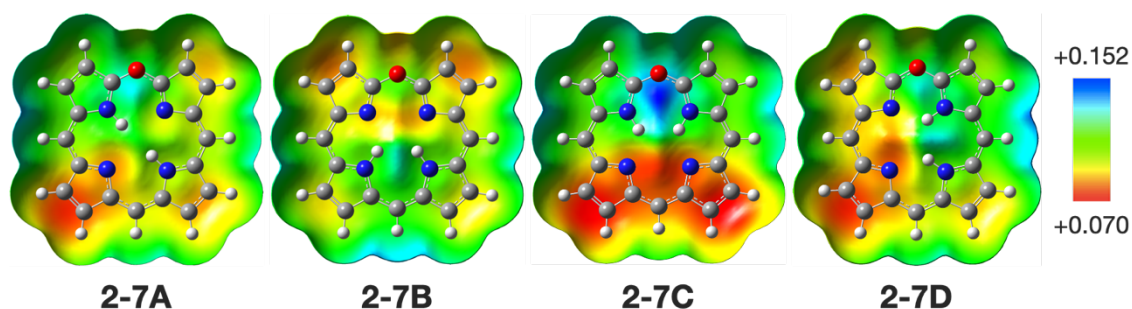


Figure 2-3. Electrostatic potential maps of **2-7A–D**.

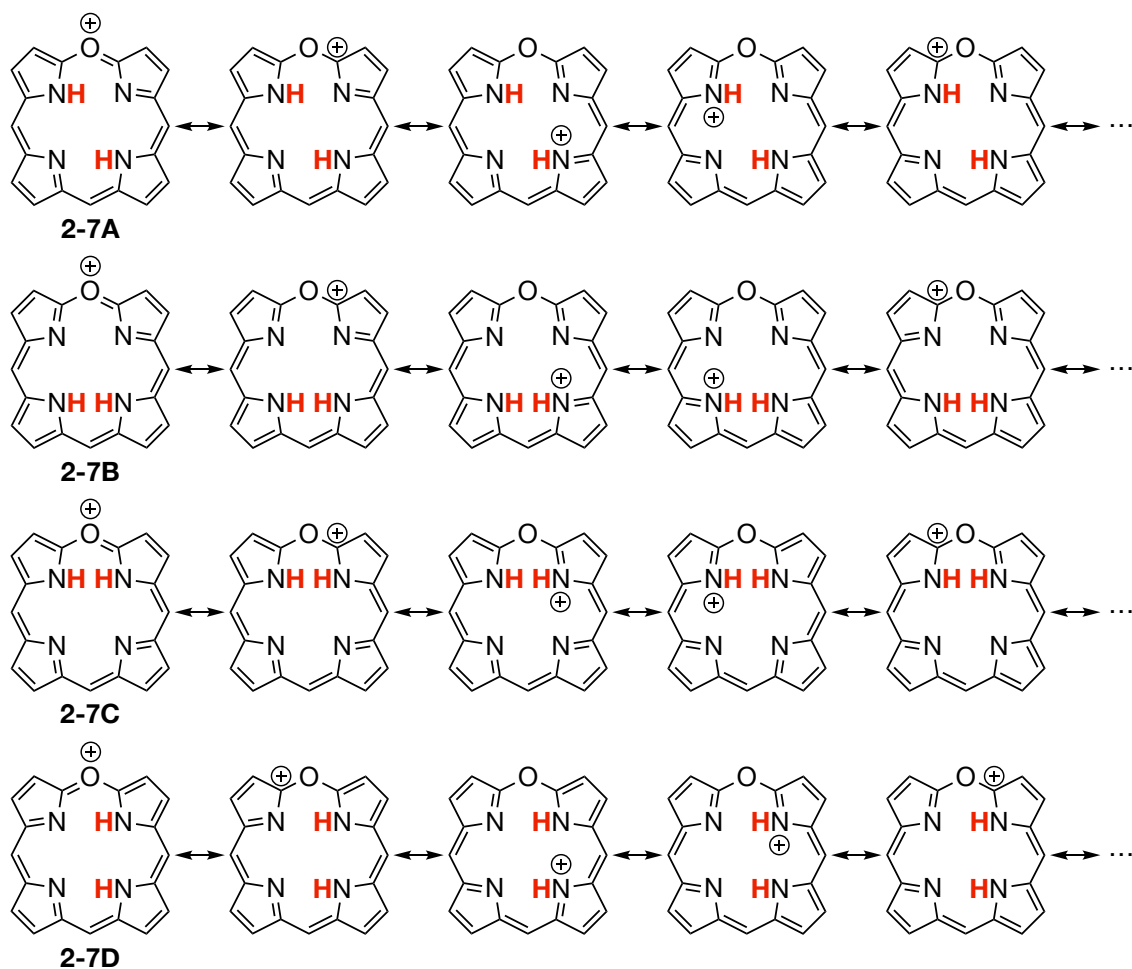


Figure 2-4. Resonance contributors of tautomers of **2-7**.

2-4. Optical properties and excited states dynamics

The UV/Vis absorption and fluorescence spectra of **2-5**[BAr^F₄] are shown in Figure 2-5 (a). The absorption spectrum consisted of a slightly broad Soret-like band at 367 nm and sharp Q-like bands at 565, 607, and 667 nm. The fluorescence spectra ($\lambda_{\text{ex}} = 550$ nm) exhibited two bands at 616 and 677 nm. Importantly, the excitation spectra of **2-5**(OTf) and **2-5**[BAr^F₄] revealed that the emission peaks at 616 and 677 nm originated from two different absorbing species (Figure 2-5 (b)). The effect of the counter ion on the electronic spectra of **2-5**(OTf) and **2-5**[BAr^F₄] was negligible. In addition, when the temperature of the solution of **2-5**[BAr^F₄] was lowered, the absorption peak at 607 nm intensified, while that at 667 nm decreased (Figure 2-5 (c)). These experimental results strongly suggest that oxaporphyrin **2-5**[BAr^F₄] contains two tautomeric

species in solution in the ground state: the *cis* form **2-7B** and the *trans* form **2-7A**.¹⁶ DFT and TD-DFT calculations indicated a blue-shift in the absorption maxima of **2-7B** relative to that of **2-7A** and thus support these results.

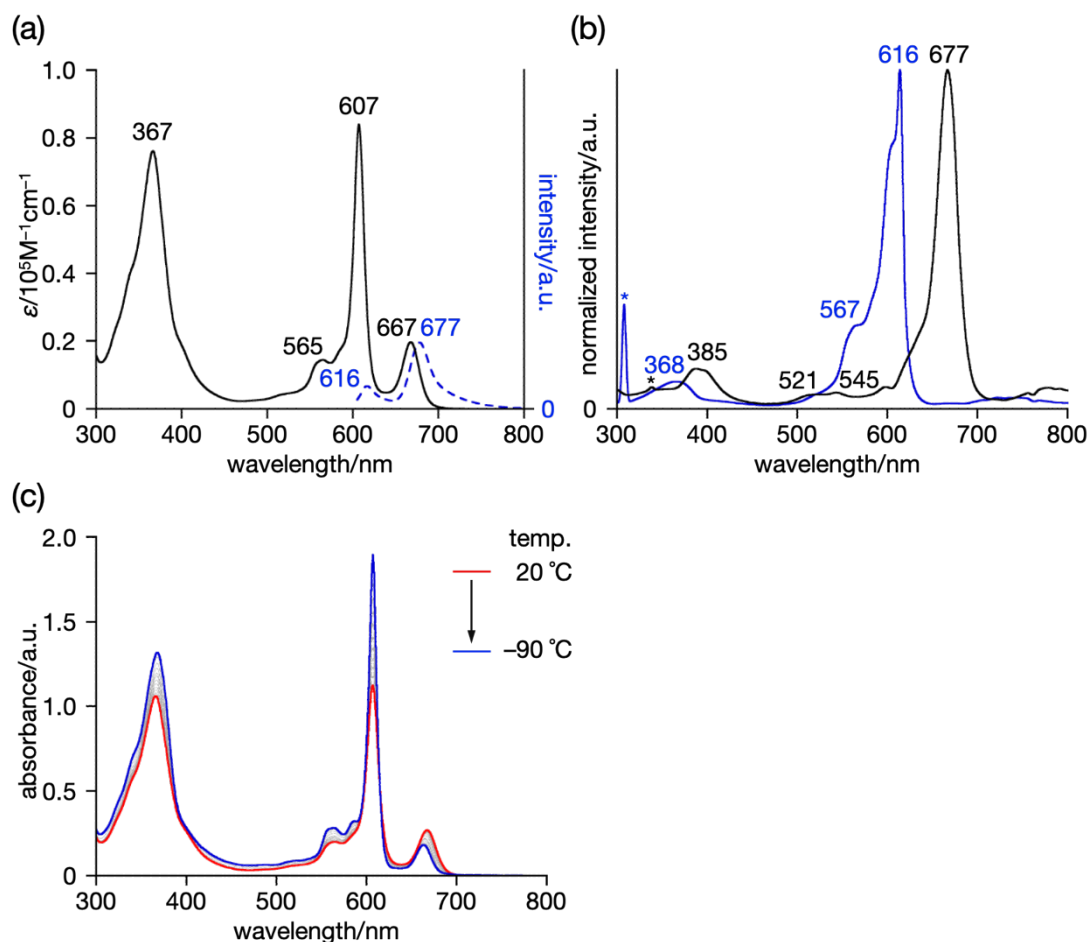


Figure 2-5. (a) UV/Vis absorption (black solid line) and fluorescence (blue dashed line; $\lambda_{\text{ex}} = 550$ nm) spectra of **2-5[BAr^F₄]** in dichloromethane. (b) Excitation spectra of **2-5[BAr^F₄]** detected at $\lambda_{\text{em}} = 616$ nm (blue line) and $\lambda_{\text{em}} = 677$ nm (black line) in dichloromethane. (c) Temperature-dependent UV/Vis absorption spectra of **2-5[BAr^F₄]** in dichloromethane.

To obtain detailed insight into the excited-state dynamics, femtosecond transient absorption (fs-TA) and time-correlated single photon counting (TCSPC) measurements of **2-5[BAr^F₄]** were conducted in dichloromethane.¹⁷ First, upon a selective excitation at 670 nm, fs-TA spectra corresponding to the excited state of **2-7A** (**2-7A***) were observed, from which two components were obtained in the global analysis (evolution-associative species: EAS). As shown in Figure 2-6, EAS₁ and EAS₂ can be assigned to the singlet-state lifetime (1000 ps) and the generation of the long-lived triplet states (infinite) in **2-7A***, respectively. Additionally, upon excitation at 600 nm, three EASs were obtained, corresponding to the singlet-state lifetime (EAS₁, 20 ps) and the long-lived triplet state (EAS₃, infinite) of the excited state of **2-7B** (**2-7B***) and the singlet-state lifetime (EAS₂, 1000 ps) of **2-7A***. These results are consistent with the temperature-dependent ¹H NMR analysis of **2-5[BAr^F₄]**, corroborating the equilibrium of the NH tautomers in the ground state. Moreover, the time-resolved fluorescence decay profiles of **2-5[BAr^F₄]**, probed at 615 and 680 nm, can be fitted by a single exponential function in two regions with time constants of <30 ps and 1000 ps, respectively. These time-resolved spectroscopic results demonstrate the absence of a **2-7B*** to **2-7A*** tautomerization process in the singlet excited state, because no spectral evolution is observed in the fs-TA under excitation at 600 nm and no rising fluorescence decay profiles are detected in the TCSPC upon probing at 680 nm. TD-DFT calculations at the CAM-B3LYP/6-311+G(2d,p) level of theory corroborated these spectroscopic observations (Figure 2-7), indicating that the **2-7B*** to **2-7A*** tautomerization is impeded by a high activation barrier (10.05 kcal mol⁻¹) in the excited state.

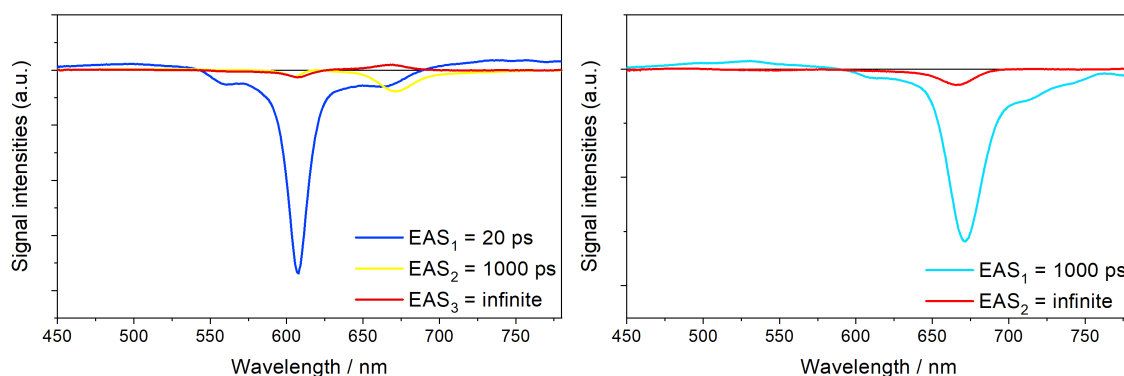


Figure 2-6. Evolution-associative spectra (EAS) of **2-5[BAr^F₄]** in dichloromethane. $\lambda_{\text{ex}} = 600$ nm (left) and 670 nm (right).

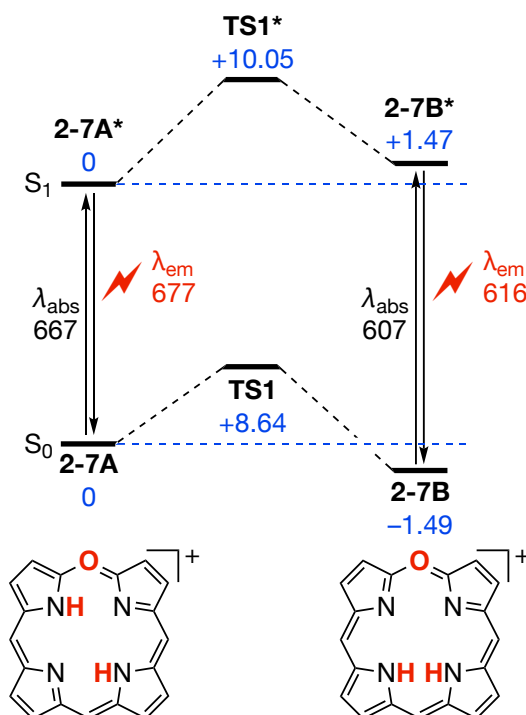


Figure 2-7. Energy diagram of tautomerization between **2-7A** and **2-7B** in the ground and excited states, calculated at the CAM-B3LYP/6-311+G(2d,p) level of theory (unit: kcal mol⁻¹). The solvent effect was accounted for using the PCM method. Absorption and emission wavelengths (unit: nm) are also shown.

2-5. Summary of Chapter 2

The author succeeded in the synthesis and properties of free-base 5-oxaporphyrinium cation **2-5**⁺ via bilindione **2-3**. Importantly, the two inner NH units of **2-5**⁺ were arranged in a *cis* configuration. The photophysical analysis of **2-5**⁺ revealed an equilibrium between two tautomers in the ground state, leading to characteristic dual emission. Furthermore, DFT calculations revealed that the driving force for the stabilization of the inherently unstable *cis* form is the effective delocalization of the positive charge over the low-symmetry π-conjugation system. The present research demonstrated the profound effect of heteroatoms at the *meso*-position of porphyrinoids on their photophysical property. These results provide a new concept for the design of dual-emissive porphyrinic chromophores through the manipulation of charge delocalization to control the NH tautomerism.

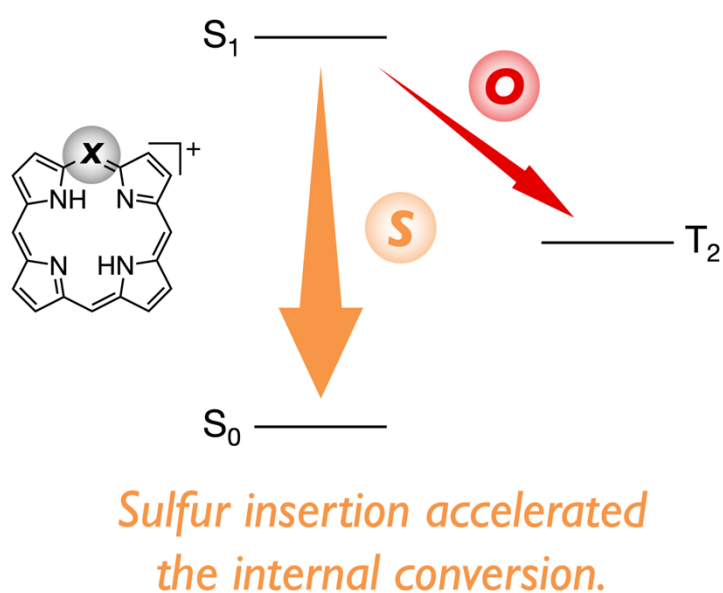
2-6. References

1. (a) Schmid, R.; McDonagh, A. F. In *The Porphyrins*; Dolphin, D., Eds.; Academic Press: New York, 1979; Vol. 6, pp 257–292. (b) Ortiz de Montellano, P. R. *Curr. Opin. Chem. Biol.* **2000**, 4, 221–227. (c) Ortiz de Montellano, P. R. In *The Porphyrin Handbook*; Kadish, K. M., Smith, K. M., Guillard, R., Eds.; Academic Press: San Diego, 2003; Vol. 12, pp 183–210. (d) Matsui, T.; Unno, M.; Ikeda-Saito, M. *Acc. Chem. Res.* **2009**, 43, 240–247.
2. (a) Balch, A.L.; Bowles, F. L. In *Handbook of Porphyrin Science*; Kadish, K. M., Smith, K. M., Guillard, R., Eds.; World Scientific Publishing: Singapore, **2010**; Vol. 8, pp 293–342. (b) Kakeya, K.; Nakagawa, A.; Mizutani, T.; Hitomi, Y.; Kodera, M. *J. Org. Chem.* **2012**, 77, 6510–6519.
3. (a) Latos-Grażyński, L.; Johnson, J.; Attar, S.; Olmstead, M. M.; Balch, A. L. *Inorg. Chem.* **1998**, 37, 4493–4499. (b) Koerner, R.; Latos-Grażyński, L.; Balch, A. L. *J. Am. Chem. Soc.* **1998**, 120, 9246–9255. (c) Johnson, J. A.; Olmstead, M. M.; Balch, A. L. *Inorg. Chem.* **1999**, 38, 5379–5383. (d) Latos-Grażyński, L.; Wojaczyński, J.; Koerner, R.; Johnson, J. J.; Balch, A. L. *Inorg. Chem.* **2001**, 40, 4971–4977. (e) Johnson, J. A.; Olmstead, M. M.; Stolzenberg, A. M.; Balch, A. L. *Inorg. Chem.* **2001**, 40, 5585–5595. (f) Nguyen, K. T.; Rath, S. P.; Latos-Grażyński, L.; Olmstead, M. M.; Balch, A. L. *J. Am. Chem. Soc.* **2004**, 126, 6210–6211. (g) Kakeya, K.; Aozasa, M.; Mizutani, T.; Hitomi, Y.; Kodera, M. *J. Org. Chem.* **2014**, 79, 2591–2600.
4. (a) Merz, K. M.; Reynolds, C. H. *J. Chem. Soc., Chem. Commun.* **1988**, 90–92. (b) Wu, Y.-D.; Chan, K. W. K.; Yip, C.-P.; Vogel, E.; Plattner, D. A.; Houk, K. N. *J. Org. Chem.* **1997**, 62, 9240–9250. (c) Schlabach, M.; Wehrle, B.; Rumpel, H.; Braun, J.; Scherer, G.; Limbach, H.-H. *Ber. Bunsenges. Phys. Chem.* **1992**, 96, 821–833. (d) Braun, J.; Koecher, M.; Schlabach, M.; Wehrle, B.; Limbach, H.-H.; Vogel, E. *J. Am. Chem. Soc.* **1994**, 116, 6593–6604. (e) Braun, J.; Limbach, H.-H.; Williams, P. G.; Morimoto, H.; Wemmer, D. E. *J. Am. Chem. Soc.* **1996**, 118, 7231–7232. (f) Waluk, J. *Chem. Rev.* **2017**, 117, 2447–2480. (g) Waluk, J. *Acc. Chem. Res.* **2006**, 39, 945–952.
5. Kruk, M.; Ngo, T. H.; Verstappen, P.; Starukhin, A.; Hofkens, J.; Dehaen, W.; Maes, W. *J. Phys. Chem. A* **2012**, 116, 10695–10703.
6. (a) Limbach, H.-H.; Hennig, J.; Gerritzen, D.; Rumpel, H. *Faraday Discuss. Chem. Soc.*

- 1982**, 74, 229–243. (b) Butenhoff, T. J.; Moore, C. B. *J. Am. Chem. Soc.* **1988**, 110, 8336–8341. (c) Butenhoff, T. J.; Chuck, R. S.; Limbach, H. Heinrich.; Moore, C. B. *J. Phys. Chem.* **1990**, 94, 7847–7851. (d) Ghosh, A.; Almlöf, J. *J. Phys. Chem.* **1995**, 99, 1073–1075. (e) Maity, D. K.; Bell, R. L.; Truong, T. N. *J. Am. Chem. Soc.* **2000**, 122, 897–906.
7. (a) Burkhalter, F. A.; Meister, E. C.; Wild, U. P. *J. Phys. Chem.* **1987**, 91, 3228–3233. (b) Thomas, K. E.; McCormick, L. J.; Vazquez-Lima, H.; Ghosh, A. *Angew. Chem. Int. Ed.* **2017**, 56, 10088–10092. (c) Thomassen, I. K.; McCormick, L. J.; Ghosh, A. *Cryst. Growth Des.* **2018**, 18, 4257–4259. (d) Thomas, K. E.; Slebodnick, C.; Ghosh, A. *ACS Omega*, **2020**, 5, 8893–8901.
8. Bonnett, R.; Dimsdale, M. *J. Chem. Soc. Perkin Trans. 1* **1972**, 2540–2548.
9. Lagarias, J. C. *Biochim. Biophys. Acta Gen. Subj.* **1982**, 717, 12–19.
10. Saito, S.; Itano, H. A. *J. Chem. Soc. Perkin Trans. 1* **1987**, 1183–1188.
11. (a) Balch, A. L.; Noll, B. C.; Safari, N. *Inorg. Chem.* **1993**, 32, 2901–2905. (b) Balch, A. L.; Koerner, R.; Latos-Grażyński, L.; Lewis, J. E.; St. Claire, T. N.; Zovinka, E. P. *Inorg. Chem.* **1997**, 36, 3892–3897.
12. Senge, M. O. In *The Porphyrin Handbook*; Kadish, K. M., Smith, K. M., Guillard, R., Eds.; Academic Press: San Diego, 2000; Vol. 10, pp 1–254.
13. Deposition Number 1225729 (for 2,3,7,8,12,13,17,18-octaethylporphyrin) for Cambridge Crystallographic Data Centre and Fachinformationszentrum Karlsruhe Access Structures service www.ccdc.cam.ac.uk/structures.
14. (a) Glockler, G. *J. Phys. Chem.* **1958**, 62, 1049–1054. (b) Harris, C.; Hardcastle, F. D. *J. Arkansas Acad. Sci.* **2015**, 69, 45–53.
15. Bonnett, R.; Buckley, D. G.; Hamzesh, D. *J. Chem. Soc. Perkin Trans. 1* **1981**, 322.
16. Acuña, A. U.; Amat-Guerri, F.; Catalan, J.; Gonzalez-Tablas, F. *J. Phys. Chem.* **1980**, 84, 629–631.
17. (a) Duran-Frigola, M.; Tejedor-Estrada, R.; Sánchez-García, D.; Nonell, S. *Phys. Chem. Chem. Phys.* **2011**, 13, 10326–10332. (b) Fita, P.; Pszona, M.; Orzanowska, G.; Sánchez-García, D.; Nonell, S.; Vauthey, E.; Waluk, J. *Chem. Eur. J.* **2012**, 18, 13160–13167.

Chapter 3

5-Thiaporphyrinium Cation: Effect of Sulfur Incorporation into Porphyrin Skeleton



Contents

3-1.	Introduction.....	34
3-2.	Synthesis of thiaporphyrinium cations.....	35
3-3.	Structure analysis	36
3-4.	Excited states dynamics and rate constant calculations.....	41
3-5.	Summary of Chapter 3	44
3-6.	References.....	44

3-1. Introduction

Sulfur-containing π -conjugated molecules have rich chemistry. Various applications have been explored to utilize attractive properties from the electronic structures of chalcogens.¹ Sulfur atoms are often embedded in aromatic π -systems in five-membered rings such as thiophene derivatives. Thiophene is a 6π aromatic system, which substitutes for a benzene ring structure without inducing charges. In contrast, introducing sulfur in a six-membered ring without disrupting the aromaticity generates a positive charge in a thiopyrylium cation structure. The incorporation of positive charges into heteroatom-containing π -conjugated molecules drastically changes the electronic structure. However, their inherent high reactivity often results in difficult isolation. Consequently, thionium ion-embedded π -conjugated molecules have been less explored than the thiophene embedded counterparts.

The sulfur substitution strategy is also valid for porphyrin derivatives. Various sulfur-embedded porphyrins have been synthesized² such as core-modified porphyrins, dithiaporphyrins, and thiacorroles (Figure 3-1). Those sulfur embedded porphyrins are electrically neutral.³ Thionium ion incorporated porphyrins, 5-thiaporphyrinium cations, were synthesized around 1970.⁴ Unfortunately, their instability hampered complete characterization and further investigation.

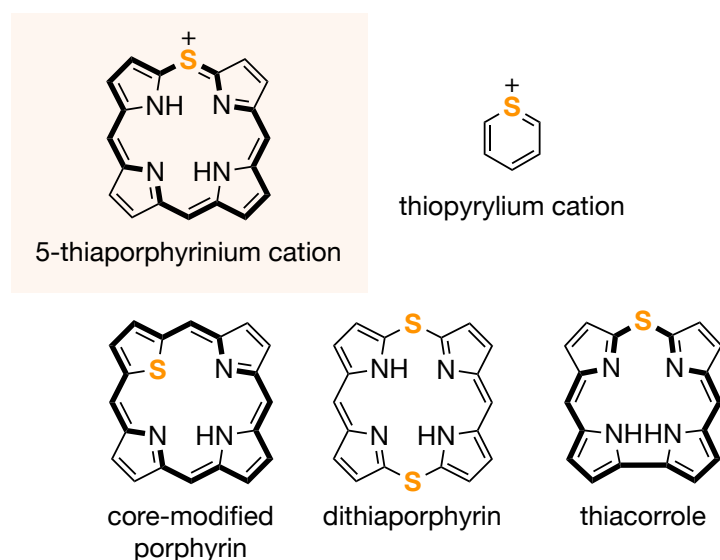


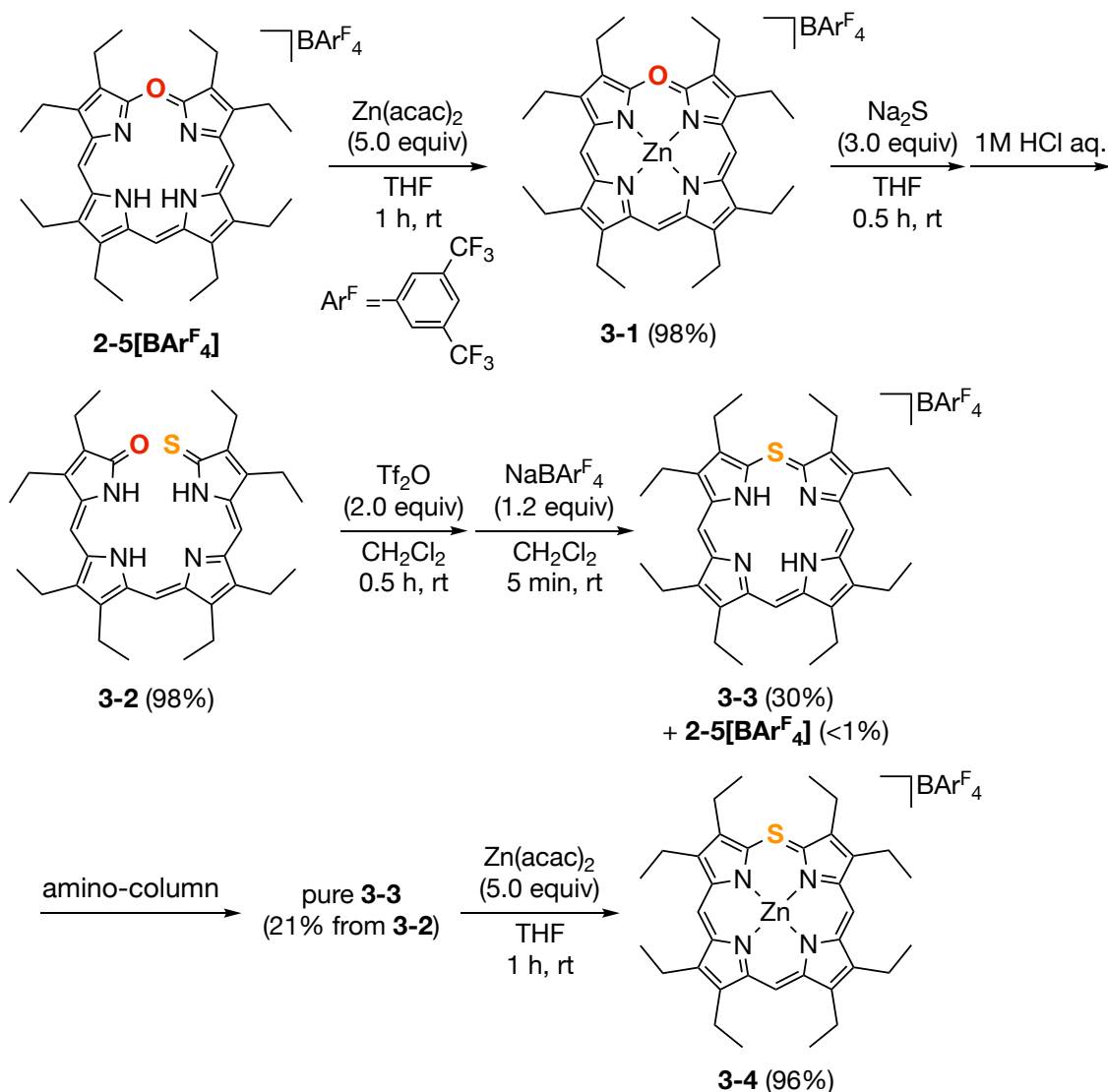
Figure 3-1. Sulfur-containing porphyrin derivatives.

Macrocyclic conjugation depends on the types of sulfur insertion. The sulfur atom in the core-modified porphyrins does not directly participate in the macrocyclic conjugation. Dithiaporphyrins and thiakorroles are porphyrinoids with sulfur at the *meso*-position. However, their conjugation patterns are different from regular porphyrins. 5-Thiaporphyrinium cations retain the porphyrin skeleton, in which the sulfur atom directly participates in the macrocyclic conjugation.

In this chapter, the author synthesized stable 5-thiaporphyrinium cations, which are regarded as π -expanded thiopyrylium cations. The author discloses the aromaticity and excited state dynamics of the 5-thiaporphyrinium cations to compare with those of the corresponding 5-oxaporphyrinium cations. The findings shed light on the effect of sulfur insertion into the porphyrin skeleton.

3-2. Synthesis of thiaporphyrinium cations

The synthetic route for thiaporphyrinium cations is shown in Scheme 3-1. Treatment of **2-5[BAr^F₄]** with zinc salt afforded the corresponding metal 5-octaethyloxaporphyrinium cation **3-1** in 98% yield. Nucleophilic addition of **3-1** by sodium sulfide and demetallation with aqueous hydrochloric acid provided 19-oxo-1-thioxo-bilin **3-2**. Among various metal complexes (zinc, nickel, cobalt, and silver), the use of zinc complex **3-1** afforded **3-2** in the highest yield (98%). Dehydration condensation of **3-2** with trifluoromethanesulfonic anhydride and the subsequent anion exchange afforded free-base 5-thiaporphyrinium cation **3-3** containing ca. 1% of free-base 5-oxaporphyrinium cation **2-5[BAr^F₄]**. This result indicates that the cyclization reaction proceeded through selective nucleophilic attack of the terminal sulfur atom on the carbonyl group. The trace amount of **2-5[BAr^F₄]** in the crude product was removed by column chromatography with amino-functionalized silica gel. Treatment of **3-3** with zinc acetylacetonate furnished zinc(II) 5-thiaporphyrinium cation **3-4**. Thiaporphyrinium cations **3-3** and **3-4** were stable in the solution and solid states under ambient conditions. On the contrary, free-base 5-thiaporphyrinium bromide salt was reported to be unstable and insoluble, hampering their complete characterization.^{4a} The stability of the present 5-thiaporphyrinium cations **3-3** and **3-4** is likely due to the bulky and soft tetraarylborate anion.



Scheme 3-1. Synthesis of thiaporphyrinium cations.

3-3. Structure analysis

Single crystal X-ray analysis revealed the structures of **3-2**, **3-3**, and **3-4** (Figure 3-2). The overall structure of **3-2** was helical to avoid steric hindrance between carbonyl and thiocarbonyl groups. The positions of three inner NH protons were assigned on the basis of C–N–C bond angles. Thiaporphyrinium cations **3-3** and **3-4** exhibited a planar structure, suggesting sulfur substantially contributed to the macrocycle conjugation. The position of sulfur was disordered at the four *meso*-positions.

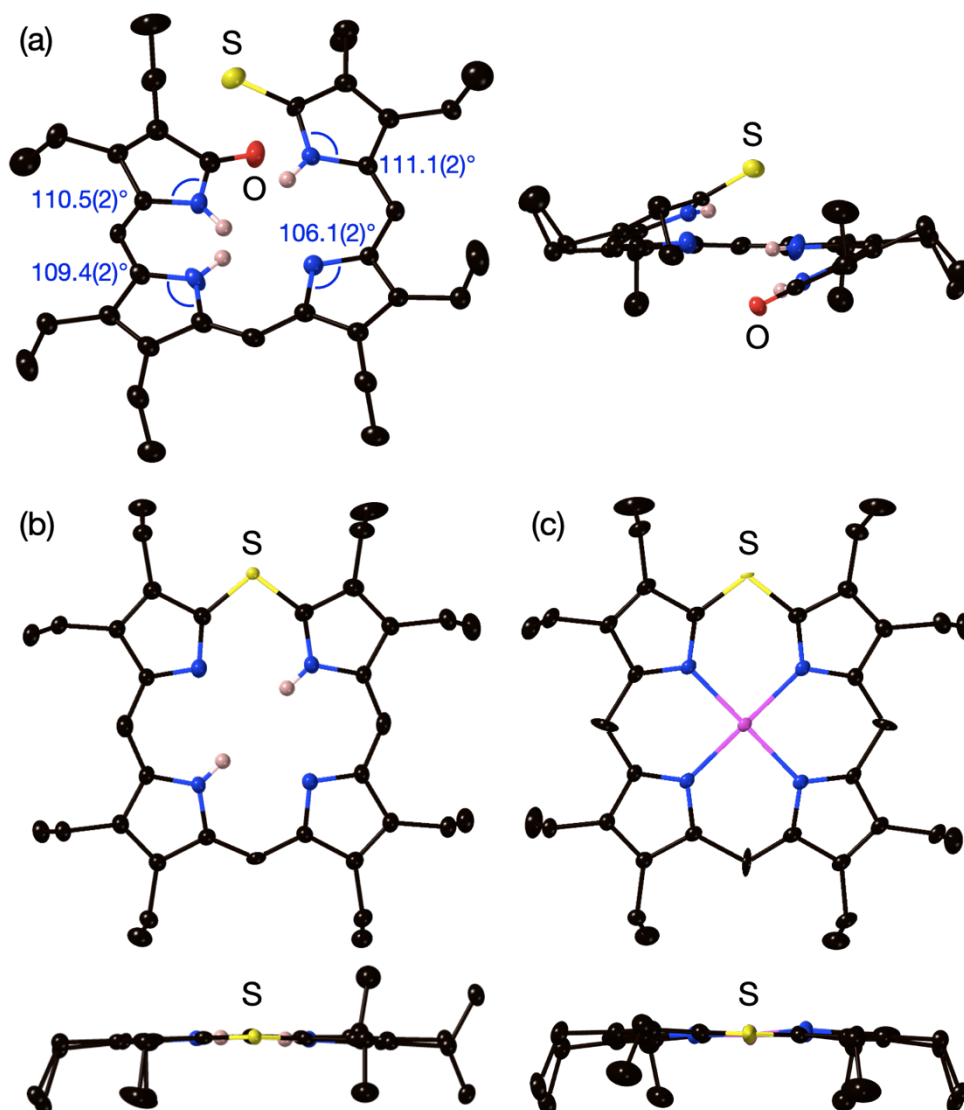


Figure 3-2. X-ray crystal structures with thermal ellipsoids drawn at 50% probability. Hydrogen atoms except those on the inner nitrogen atoms, and tetraarylborate anions are omitted for clarity. (a) Overall and side views of **3-2**, (b) top and side views of **3-3**, and (c) top and side views of **3-4**.

The *meso* protons in thiaporphyrinium cation **3-3** appear at 10.26 and 10.24 ppm, which are downfield-shifted compared with those of oxaporphyrinium cation **2-5**[BAr^F₄] (9.41 and 9.05 ppm). In contrast, the inner-NH protons of **3-3** (−1.05 ppm) were upfield shifted compared with those of **2-5**[BAr^F₄] (3.28 ppm). A similar trend was also observed between thiopyrylium cation and pyrylium cation.⁵ These shifts imply thiaporphyrinium cation **3-3** possesses a stronger ring current effect than oxaporphyrinium cation **2-5**[BAr^F₄]. The NICS values and ACID plot support the stronger diatropicity of **3-3**.

Electrochemical potentials of **3-2**, **3-3**, and **3-4** were measured using cyclic voltammograms. Free-base thiaporphyrinium cation **3-3** exhibited one reversible oxidation wave at 1.23 V and two reversible waves at −0.65 V and −1.21 V, which were positively shifted compared with those of free-base oxaporphyrinium cation **2-5**[BAr^F₄] (oxidation potential: 1.08 V, reduction potential: −0.74 V). The difference would be derived from the larger electron affinity of sulfur than oxygen. The oxidation and reduction potentials of zinc thiaporphyrinium cation **3-4** at 0.79 V and −0.98 V, respectively, were negatively shifted in comparison to free-base **3-3**.

The optical spectra of **3-2**, **3-3**, and **3-4** exhibited the effect of sulfur insertion. The UV/Vis/NIR absorption spectrum of **3-2** was red-shifted to ca. 860 nm as compared to that of **3-3** (Figure 3-3 (a)). Time-dependent density-functional theory (TD-DFT) calculations suggested that the bathochromic shift in **3-2** is derived from narrower π – π^* transition owing to stabilized LUMO and LUMO+1 by the sulfur atom. Whereas oxaporphyrinium cation **2-5**[BAr^F₄] showed complex Q-like bands due to the presence of *cis*- and *trans*-NH tautomers, the UV/Vis/NIR absorption spectrum of **3-3** exhibited a simple Q-band (671 nm) (Figure 3-3 (b)). DFT calculations supported that the *trans*-NH tautomer of **3-3** is dominant, unlike free-base oxaporphyrinium cation **2-5**[BAr^F₄], in which the *cis*-NH tautomer is more energetically stable. The spectral feature of **3-4** resembles **3-3**. TD-DFT calculations indicate that the excited state of **3-Zn** is derived from π – π^* transition without the contribution of orbitals on zinc. The situation is similar to **3-3** (Figure 3-4, Figure 3-5 and Table 3-1, Table 3-2).

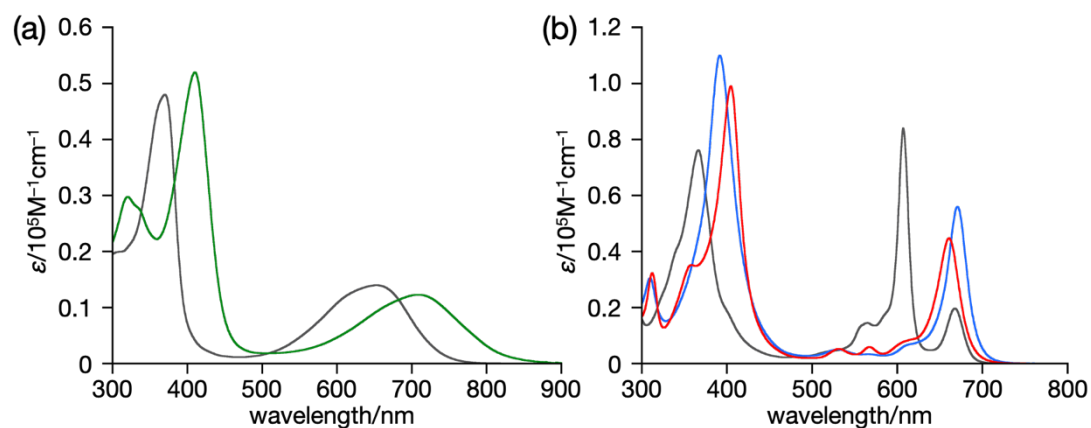


Figure 3-3. UV/Vis/NIR absorption spectra in dichloromethane. (a) **3-2** (green) and **2-3** (grey). (b) **3-3** (blue), **3-4** (red), and **2-5[BAr^F₄]** (grey).

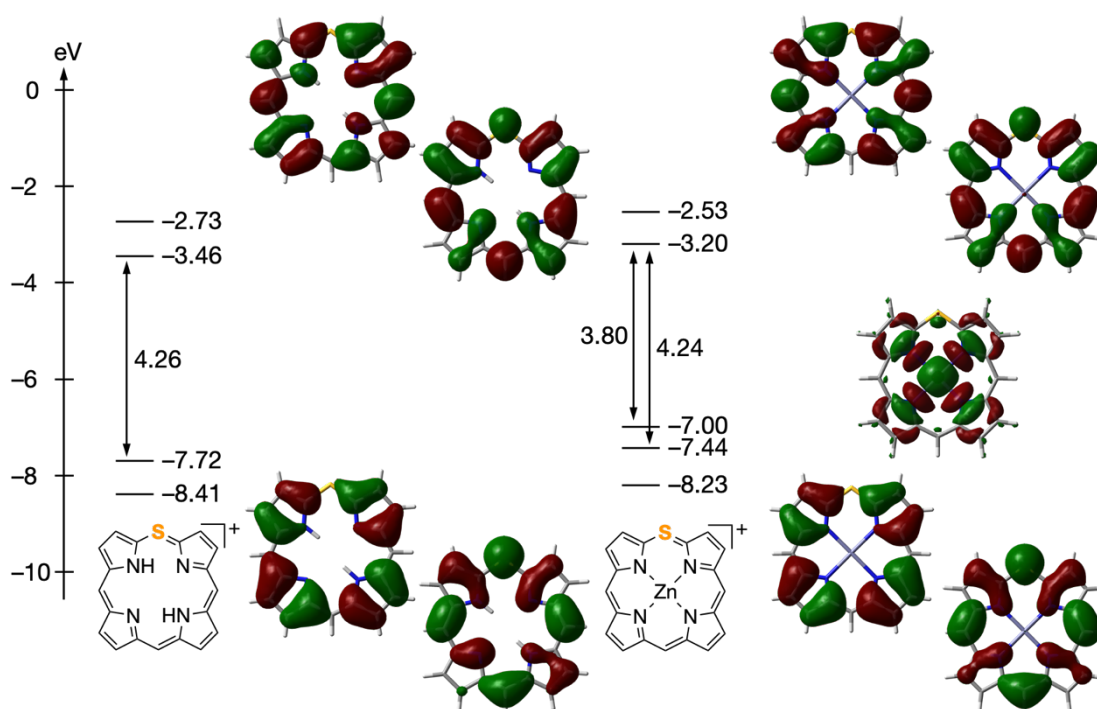


Figure 3-4. Kohn-Sham MOs and energy diagrams of **3-3** (left) and **3-4** (right).

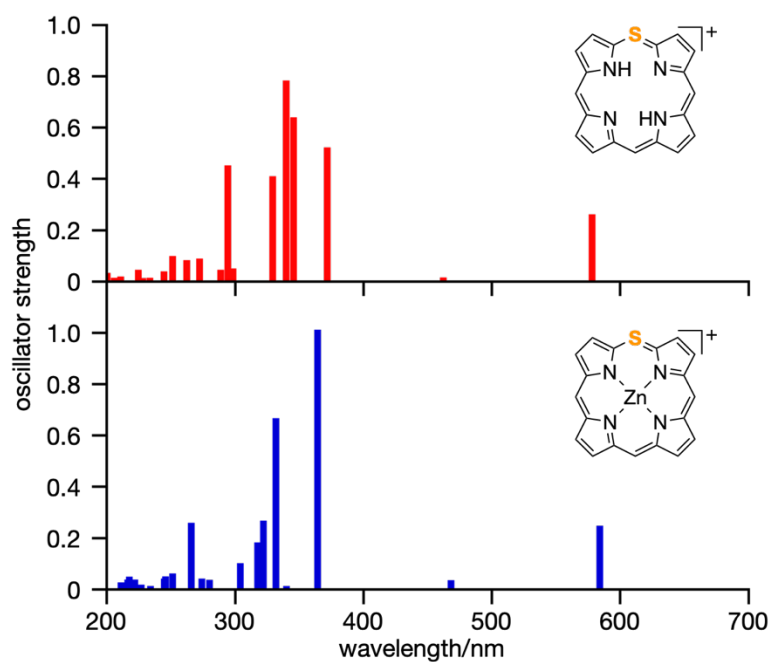


Figure 3-5. Simulated electronic absorption spectra of **3-3** (top) and **3-4** (bottom).

Table 3-1. Summary of simulated excited states of **3-3**.

wavelength/nm	oscillator strength	transition
577.94	0.2487	HOMO-1 \rightarrow LUMO+1 (12.5%) HOMO \rightarrow LUMO (87.5%)
462.00	0.0035	HOMO-1 \rightarrow LUMO (47.2%) HOMO \rightarrow LUMO+1 (52.8%)

Table 3-2. Summary of simulated excited states of **3-4**.

wavelength/nm	oscillator strength	transition
1175.82	0.0000	HOMO \rightarrow LUMO (100%)
731.96	0.0000	HOMO \rightarrow LUMO+1 (100%)
584.08	0.2357	HOMO-2 \rightarrow LUMO+1 (11.2%) HOMO-1 \rightarrow LUMO (88.8%)
467.98	0.0229	HOMO-2 \rightarrow LUMO (37.4%) HOMO-1 \rightarrow LUMO+1 (62.6%)

3-4. Excited states dynamics and rate constant calculations

Next, the author focused on the effect of sulfur on the excited states. Thiaporphyrinium cations **3-3** and **3-4** emitted very weak fluorescence. Both quantum yields were lower than 1%, whereas those of oxaporphyrinium cations **2-5**[BAr^F₄] and **3-1** were 1.7% and 27%, respectively. The fluorescence peaks of thiaporphyrinium cations exhibited almost no enhancement at 77 K without detection of phosphorescence, while those of oxaporphyrinium cations were significantly increased (Table 3-3). These results suggest that low quantum yields of thiaporphyrinium cations were not explained due to phosphorescence.

Table 3-3. Quantum yields of thiaporphyrinium cations and oxaporphyrinium cations.

	rt ^a	77 K ^{b,c}
3-3	<1%	n.d.
3-4	<1%	<5%
2-5 [BAr ^F ₄]	1.7%	40%
3-1	27%	56%

^a solvent: dichloromethane. ^b solvent: 2-methyltetrahydrofuran. ^c Absolute fluorescence quantum yields determined by a calibrated integrating sphere system within $\pm 3\%$ error.

The time-resolved fluorescence measurements using the time-correlated single photon counting (TCSPC) technique for **3-1**, **3-3**, and **3-4** in dichloromethane were conducted to investigate the effect of sulfur incorporation into porphyrin skeleton. An excitation pump at 400 nm was employed. **3-1** showed decay profiles with a fluorescence lifetime of a few nanoseconds, which is a relatively long-lived component to that of **2-5**[BAr^F₄] (see Chapter 2). On the other hand, **3-4** showed biexponential decay involving fast fluorescence quenching process with the lifetime of tens of picoseconds, which is followed by a long-lived fluorescence similar to that of **3-1**. In the case of **3-3**, the fluorescence lifetime is too short to observe within the IRF time (30 ps) window of the apparatus. These results imply that the structural rigidification due to zinc metalation in oxa- and thiaporphyrinium cations disrupts the nonradiative decay process.

To get deep insights into the excited-state population dynamics of these porphyrins, the femtosecond transient absorption (fs-TA) spectroscopy was used where the excitation pump at 660 nm is employed to probe the TA spectra in the visible region (Figure 3-6). In all compounds, the TA spectra showed similar ground-state bleaching (GSB) band near 660 nm, which corresponds to the steady-state absorption spectra. The excited-state absorption (ESA) bands were observed below 590 nm with relatively weak band intensities compared with GSB intensities. Compared with the singlet state lifetime of **2-5[Bar^F₄]** with the time constant of 1 ns (see Chapter 2), the TA decay profiles of **3-1** showed a longer singlet state lifetime over a few nanoseconds. This result is well-matched with the fluorescence lifetime obtained by the TCSPC measurements. However, the excited-state dynamics in thiaporphyrinium cations displayed much faster decay profiles than those of oxaporphyrinium cations. Double exponential decay components were obtained in both **3-3** and **3-4**, where initial decay components for **3-3** and **3-4** were fitted in the time constant of 12.6 ps and 37 ps, respectively, followed by the long-lived minor components.

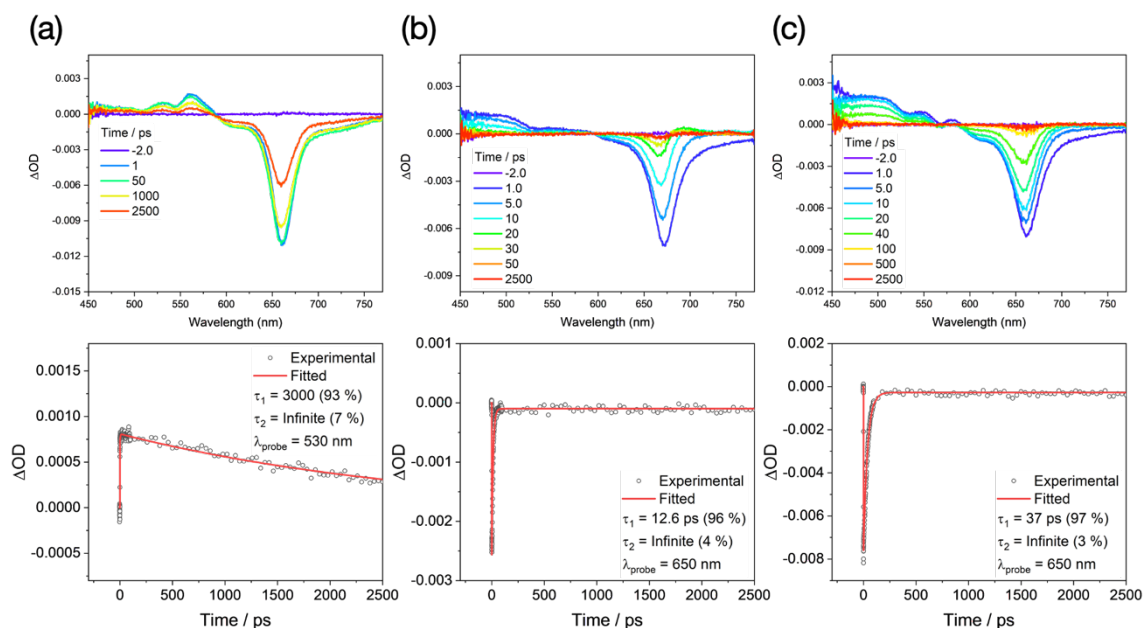


Figure 3-6. Femtosecond transient absorption spectra and decay profiles of (a) **3-1**, (b) **3-3**, and (c) **3-4** in dichloromethane probed at the visible region. The excitation wavelength of 660 nm is employed.

To gain another insight into much faster nonradiative decay in photoexcited thiaporphyrinium cations than oxaporphyrinium cations, theoretical analysis was performed on **3-4** and **3-1** to simulate their decay rate constants for the electronic- and spin-vibronic transitions from the photoexcited S_1 state (Table 3-4). The components of the predicted rates suggested that the major decay pathway of photoexcited **3-1** should be the intersystem crossing to the T_2 state with a rate constant of $4.7 \times 10^8 \text{ s}^{-1}$, which is consistent with the previous experimental observation (see Chapter 2). Meanwhile, the rate constant of the internal conversion to the S_0 state in **3-4** was predicted to be $2.1 \times 10^9 \text{ s}^{-1}$, suggesting that the photoexcited **3-4** mainly decays through the internal conversion. Further detailed analysis revealed that the remarkable enhancement of the internal conversion decay rate in **3-4** is mediated by the lowest-lying vibrational mode associated with the out-of-plane motion of the sulfur atom with a notably low frequency (22.4 cm^{-1}), which is not present in **3-1** (Figure 3-7). This largely-enhanced internal conversion should underlie the small lifetime of the photoexcited thiaporphyrinium cations.

Table 3-4. Summary of transition rate constants of **3-4** and **3-1**.

		3-4	3-1
	Radiative transition		
	$k_r (S_1 \rightarrow S_0)$	$9.26 \times 10^7 \text{ s}^{-1}$	$1.03 \times 10^8 \text{ s}^{-1}$
	Nonradiative transition		
	$k_{ISC} (S_1 \rightarrow T_1)$	$3.55 \times 10^3 \text{ s}^{-1}$	$4.51 \times 10^2 \text{ s}^{-1}$
	$k_{ISC} (S_1 \rightarrow T_2)$	$9.59 \times 10^8 \text{ s}^{-1}$	$4.68 \times 10^8 \text{ s}^{-1}$
	$k_{IC} (S_1 \rightarrow S_0)$	$2.06 \times 10^9 \text{ s}^{-1}$	$1.95 \times 10^3 \text{ s}^{-1}$

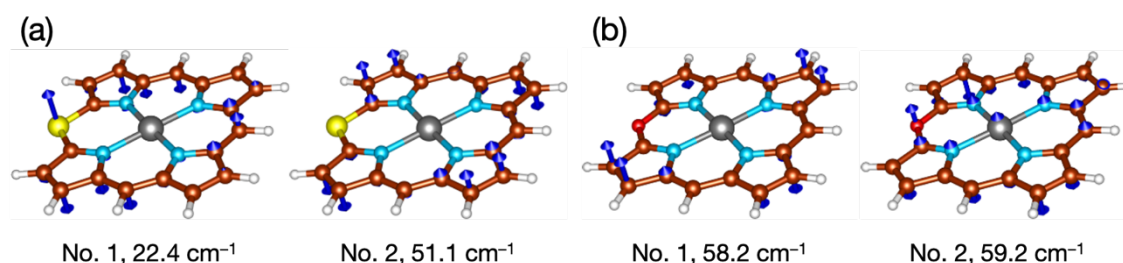


Figure 3-7. The displacement vectors of the two lowest-lying vibration modes in the S_1 state for (a) **3-4** and (b) **3-1**.

3-5. Summary of Chapter 3

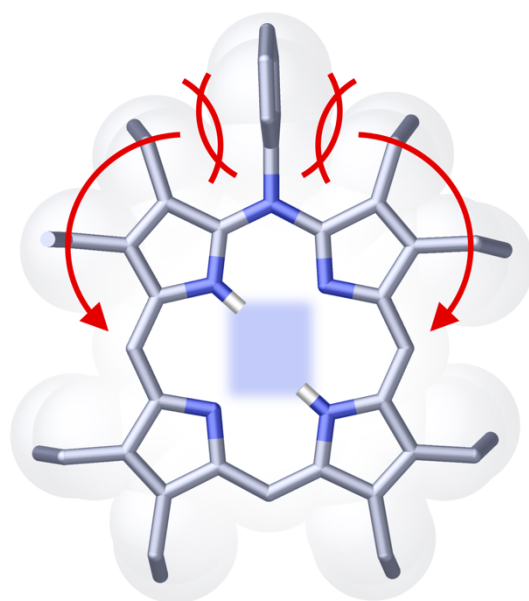
In summary, the author synthesized 19-oxo-1-thioxo-bilin **3-2** as a precursor of 5-thiaporphyrinium cation. The author also synthesized free-base 5-thiaporphyrinium cation **3-3**, which was stable under ambient conditions. Complexation of **3-3** with zinc acetylacetonate afforded zinc(II) 5-thiaporphyrinium cation **3-4**. These thiaporphyrinium cations exhibited distinct macrocyclic conjugation from NMR and UV/Vis/NIR spectra. Moreover, detailed optical measurements and theoretical calculations clarified that sulfur insertion into the porphyrinic skeleton accelerated the internal conversion, resulting in low fluorescence quantum yields. The findings would help design bio-active materials based on heteroporphyrins.

3-6. References

1. (a) Stępień, M.; Gońka, E.; Żyła, M.; Sprutta, N. *Chem. Rev.* **2017**, *117*, 3479–3716. (b) Mishra, A.; Ma, C.-Q.; Bäuerle, P. *Chem. Rev.* **2009**, *109*, 1141–1276. (c) Takimiya, K.; Shinamura, S.; Osaka, I.; Miyazaki, E. *Adv. Mater.* **2011**, *23*, 4347–4370. (d) Guo, X.; Baumgarten, M.; Müllen, K. *Prog. Polym. Sci.* **2013**, *38*, 1832–1908. (e) Cinar, M. E.; Ozturk, T. *Chem. Rev.* **2015**, *115*, 3036–3140. (f) Yao, H.; Ye, L.; Zhang, H.; Li, S.; Zhang, S.; Hou, J. *Chem. Rev.* **2016**, *116*, 7397–7457.
2. (a) Wu, D.; Pisula, W.; Haberecht, M. C.; Feng, X.; Müllen, K. *Org. Lett.* **2009**, *11*, 5686–5689. (b) Chow, C. H. E.; Phan, H.; Zhang, X.; Wu, J. *J. Org. Chem.* **2020**, *85*, 234–240.
3. (a) Chatterjee, T.; Shetti, V. S.; Sharma, R.; Ravikanth, M. *Chem. Rev.* **2017**, *117*, 3254–3328. (b) Matano, Y. *Chem. Rev.* **2017**, *117*, 3138–3191. (c) Shimizu, S. *Heterocycles* **2020**, *100*, 1123–1162. (d) Sakow, D.; Böker, B.; Brandhorst, K.; Burghaus, O.; Bröring, M. *Angew. Chem. Int. Ed.* **2013**, *52*, 4912–4915. (e) Kamiya, H.; Kondo, T.; Sakida, T.; Yamaguchi, S.; Shinokubo, H. *Chem. Eur. J.* **2012**, *18*, 16129–16135.
4. (a) Harris, R. L. N. *Tetrahedron Lett.* **1969**, *10*, 3689–3692. (b) Broadhurst, M. J.; Grigg, R.; Johnson, A. W. *J. Chem. Soc. D* **1970**, 807–809. (c) Broadhurst, M. J.; Grigg, R.; Johnson, A. W. *J. Chem. Soc., Perkin Trans. I* **1972**, 1124–1135.
5. Doddi, G.; Ercolani, G. *Adv. Heterocycl. Chem.* **1994**, *60*, 65–195.

Chapter 4

Synthesis and Tautomerization of 5-Azaporphyrinium Cations



rectangular inner cavity

Contents

4-1.	Introduction.....	46
4-2.	Synthesis of azaporphyrinium cations	46
4-3.	Structure analysis	47
4-4.	Rectangular inner-cavity	49
4-5.	Summary of Chapter 4	52
4-6.	References.....	52

4-1. Introduction

The replacement of *meso*-carbon with nitrogen is a versatile method to modulate the electronic property of porphyrins.¹ The insertion of sp^2 -hybridized nitrogen atoms into the porphyrin skeleton enhances the electron accepting nature and lowers the symmetry. The Matano group² and Shinokubo group³ independently developed further functionalization of 5,15-diazaporphyrins by introducing substituents on the *meso*-nitrogen atoms. On the other hand, *N*-substituted cationic monoazaporphyrins have not been explored due to the synthetic difficulty of monoazaporphyrins associated with the lower symmetry (see Chapter 1).^{4,5} In this chapter, the author synthesized 5-azaporphyrinium cations to reveal the effect of the substituent on the nitrogen atom (Figure 4-1).

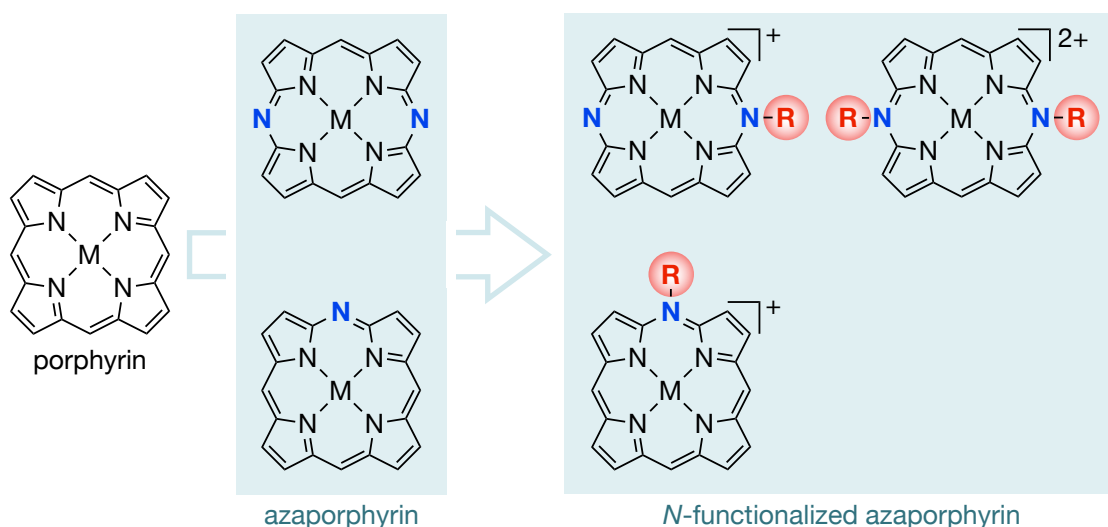
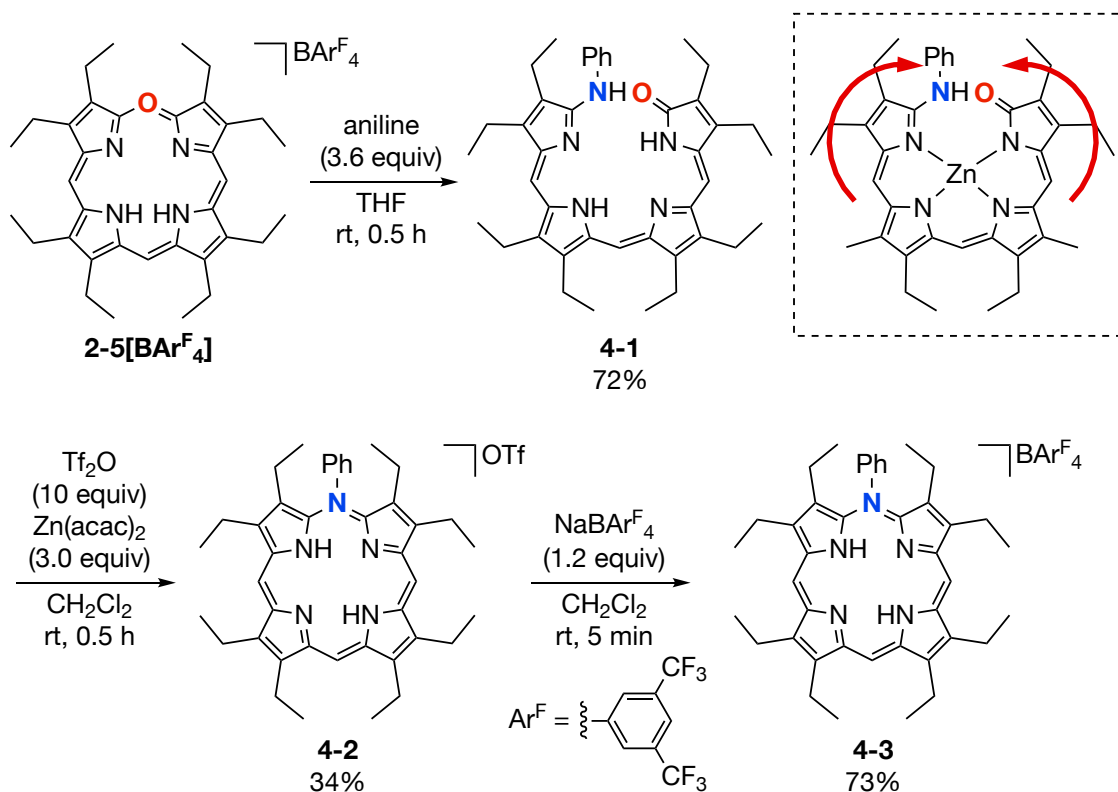


Figure 4-1. Functionalization of *meso*-nitrogen atoms embedded in the porphyrin skeleton.

4-2. Synthesis of azaporphyrinium cations

Ring-opening of oxaporphyrinium cation **2-5**[Bar^{F}_4] via nucleophilic addition with aniline afforded 1-oxo-19-(phenylamino)-bilin **4-1** in 72% yield (Scheme 4-1). Ring-closure with Tf_2O and $\text{Zn}(\text{acac})_2$ provided azaporphyrinium trifluoromethanesulfonate **4-2** in 34% yield. No ring-closure reaction proceeded in the absence of $\text{Zn}(\text{acac})_2$. Zinc chelation with four pyrrolic nitrogen atoms results in the close proximity of the amino and carbonyl groups to facilitate the ring-closure reaction. Trifluoromethanesulfonic acid, generated in the reaction mixture, demetalated the zinc. After ion-

exchange reaction with $\text{NaBAr}^{\text{F}}_4$, the corresponding tetraarylborate salt **4-3** was obtained. Both azaporphyrinium cations **4-2** and **4-3** were stable and isolable on the silica-gel column chromatography unlike the free-base oxaporphyrinium cation (**2-5(OTf)**). All products were characterized by NMR, HRMS, and UV/Vis/NIR absorption spectroscopy.



Scheme 4-1. Synthesis of 5-azaporphyrinium cations and the plausible intermediate in the dashed box.

4-3. Structure analysis

The structure of **4-1**, **4-2**, and **4-3** were unambiguously confirmed by X-ray crystallography. The structure of **4-1** was helical to avoid the steric hindrance between the phenyl group and pyrrolone (Figure 4-2). The position of two inner-NH protons in the cavity was assigned on the basis of C–N–C bond angles of pyrrole rings, while the other was located at the outer nitrogen. The ^1H NMR spectrum of **4-1** supported this assignment: Two protons were observed in the lower magnetic field region (13.8 and 10.5 ppm), while the other was observed in the higher magnetic field region (6.1 ppm). In the crystal, *M*- and *P*-forms of **4-1** were detected in a 1:1 ratio. The

NMR spectrum of **4-1** exhibited several minor peaks even after exhaustive purification. The minor peaks could be originated from the imine-form tautomer.⁶ As the solution of **4-1** was heated, the intensity of the minor peaks increased, while that of the major component decreased. Unfortunately, the low solubility of **4-1** in organic solvents except halogenated solvents hampered further investigation on the solvent dependent tautomerism.

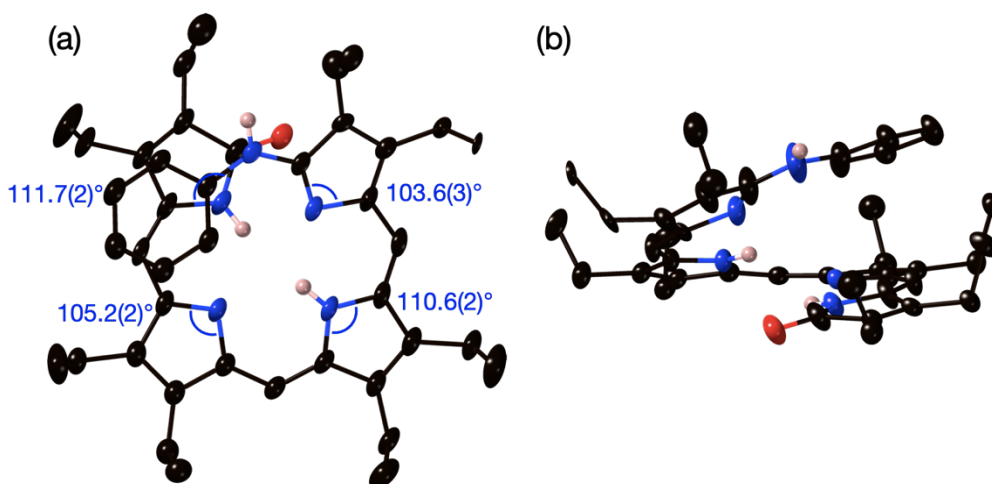


Figure 4-2. (a) Top view and (b) side view of the X-ray crystal structure of **4-1** with ellipsoids at 50%. Carbon-bonded hydrogens were omitted for clarity.

Two azaporphyrinium cations **4-2** and **4-3** exhibited different crystal structures (Figure 4-3). The phenyl group of **4-2** was tilted at 8.52° with respect to the porphyrin plane. Moreover, the azaporphyrinium skeleton of **4-2** was warped, while that of **4-3** is rather planar: The mean plane deviation of **4-2** and **4-3** were 0.113 \AA and 0.036 \AA , respectively. The structure optimization of the crystal structure geometries afforded planar conformation, revealing that the distortion was induced by the crystal packing force. Focusing on the packing mode, **4-2** exhibited a face-to-face dimeric packing. The distance between the two azaporphyrinium cations was 3.415 \AA . In contrast, azaporphyrinium cations of **4-3** were aligned in a columnar manner. The plane distances of 3.348 \AA and 4.929 \AA alternated, suggesting that **4-3** also formed a dimeric structure in crystal. The difference in the packing structure of **4-2** and **4-3** could be derived from the different sizes of the anions.⁷ Tetraarylborate, a larger anion than triflate, would extrude the azaporphyrinium cation to form the columnar alignment. The positions of the inner-NH protons in both azaporphyrinium cations were assigned to *trans*-form based on the bond angles of the pyrrolic C–N–C linkages.

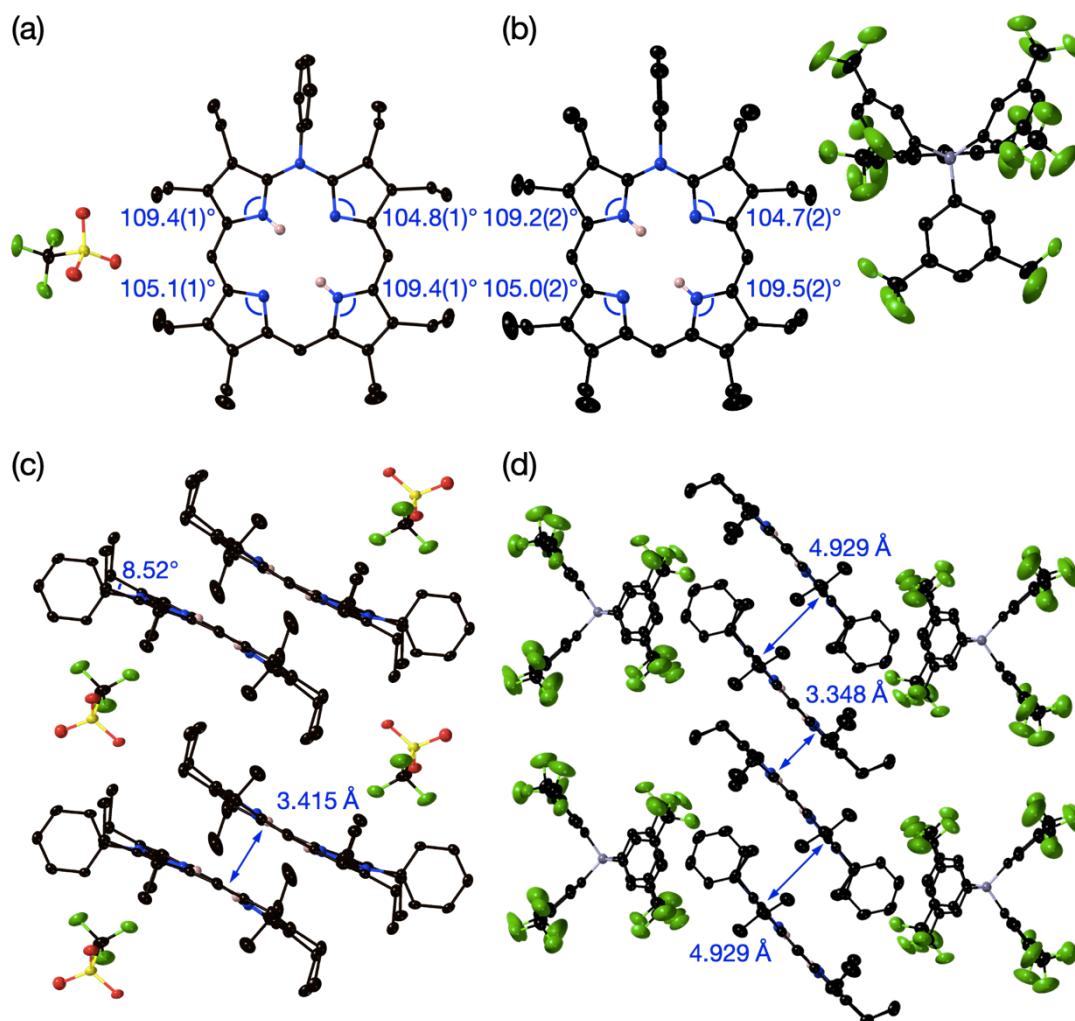


Figure 4-3. X-ray crystal structures of (a) **4-2** and (b) **4-3**. Packing structures of (c) **4-2** and (d) **4-3**. Solvent molecules (cyclohexane) were omitted in the packing structure of **4-3**. Thermal ellipsoids were drawn at 50% probability. All hydrogen atoms except for those on the inner nitrogen atoms are omitted for clarity.

4-4. Rectangular inner-cavity

The ^1H NMR peaks of inner-NH protons of azaporphyrinium cations **4-2** and **4-3** were broad and split. The variable temperature NMR analysis clarified that the two inner-NH proton signals coalesced at 45 °C (Figure 4-4). The activation energy of the inner proton exchange of **4-2** was determined to be 14.6 kcal mol $^{-1}$ from the Eyring equation.⁸ In contrast, the ^1H NMR peaks of the inner-NH protons of oxaporphyrinium cations (**2-5(OTf)** and **2-5[BAr $^{\text{F}}$ $_4$]) and**

thiaporphyrinium cation (**3-3**) were sharp at room temperature. Coalescence of the NH signals of **2-5**[**BAr^F₄**] was not observed upon decreasing the temperatures until $-90\text{ }^{\circ}\text{C}$.

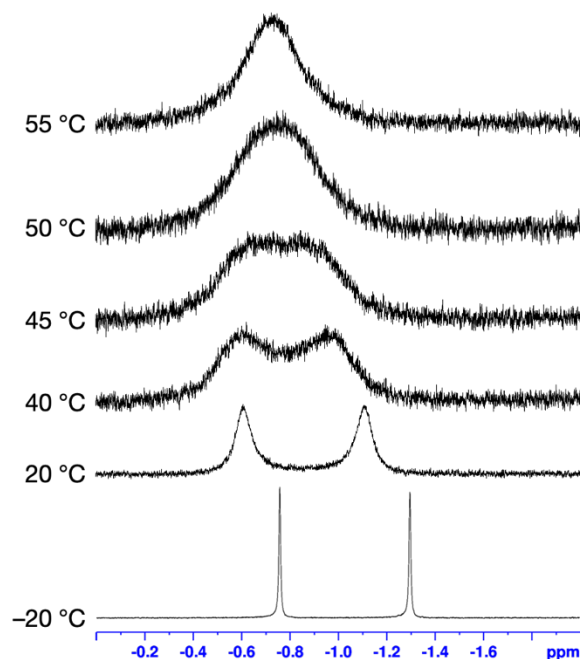


Figure 4-4. Variable temperature ^1H NMR spectra of **4-2** in CDCl_3 .

To clarify the origin of the coalescence of inner NH protons, theoretical calculations on the tautomerization behavior of **4-2** were conducted at the CAM-B3LYP/6-311+G(2d,p) level (Figure 4-5). DFT calculations clarify the effect of β -alkyl substituents on the tautomerization behavior (Figure 4-5 (a) and (b)). The structures of **TS3** and **TS4** are stabilized in the octamethyl-substituted azaporphyrinium cation compared to those in the azaporphyrinium cation without methyl groups. Comparison of the inner cavity sizes suggests that steric repulsion between the *N*-phenyl and β -ethyl substituents results in deformation of the inner-cavity to a rectangle (Figure 4-6). Accordingly, the distance of two nitrogen atoms in a horizontal direction is shortened by the distortion, which lowers the activation barriers of tautomerization via **TS3** and **TS4**. Owing to the small activation energies, coalescence or peak splitting due to the horizontal proton transfer cannot be observed. Consequently, the coalescence detected by the ^1H NMR analysis should be assigned as tautomerization via vertical protons transfer. The activation energy of **TS1** ($14.18\text{ kcal mol}^{-1}$; Figure 4-5 (b)) are in line with the experimental value. In comparison with a neutral regular porphyrin (Figure 4-5 (c)), **TS1** and *cisC* were stabilized in the case of azaporphyrinium cations owing to the cationic charge (see Chapter 2). Moreover, the signals of inner NH protons in the ^1H

NMR spectrum of neutral octaethylporphyrin are split at room temperature, highlighting the effect of the cationic charge to lower the activation NH barrier of proton migration.⁹

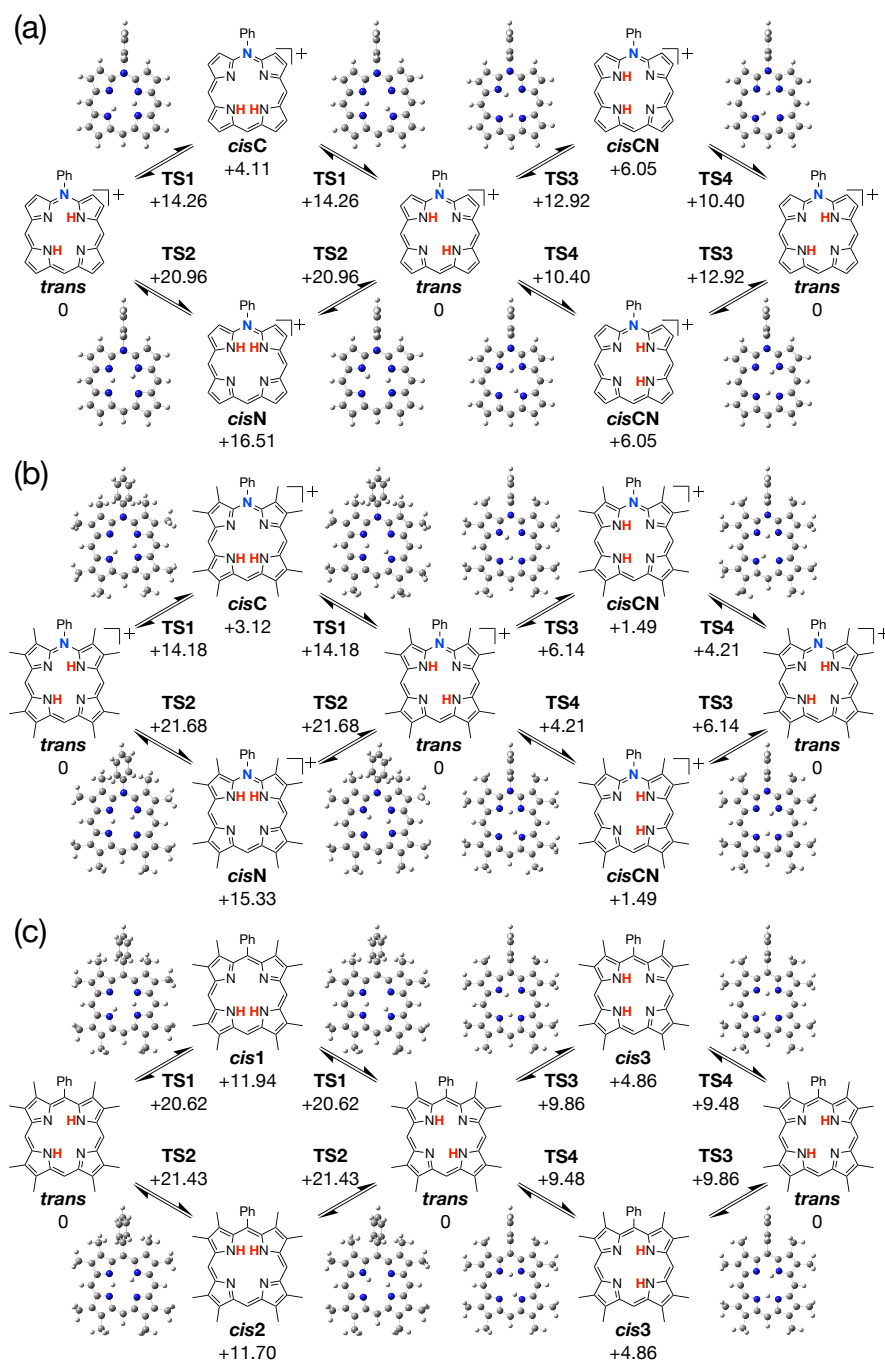


Figure 4-5. Energy diagram of the tautomerization process of (a) azaporphyrinium cation, (b) octamethylazaporphyrinium cation, and (c) octamethylporphyrin. Unit: kcal mol⁻¹. The calculations were conducted at the CAM-B3LYP/6-311+G(2d,p) level.

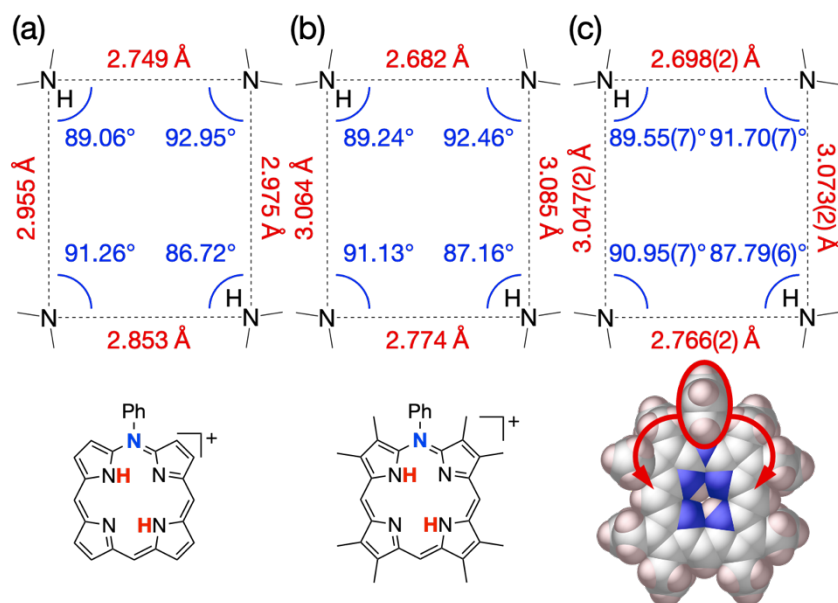


Figure 4-6. Bond length and angles of (a) azaporphyrinium cation, (b) octamethylazaporphyrinium cation, and (c) octaethylazaporphyrinium cation (crystal structure of **4-3**). The values of (a) and (b) are taken from the optimized structures at the CAM-B3LYP/6-311+G(2d,p) level.

4-5. Summary of Chapter 4

The author synthesized *N*-phenylazaporphyrinium cations. The inner cavity was distorted due to the steric hindrance between *N*-phenyl and β -ethyl groups. The distorted cavity affected the tautomerism of inner-NH protons.

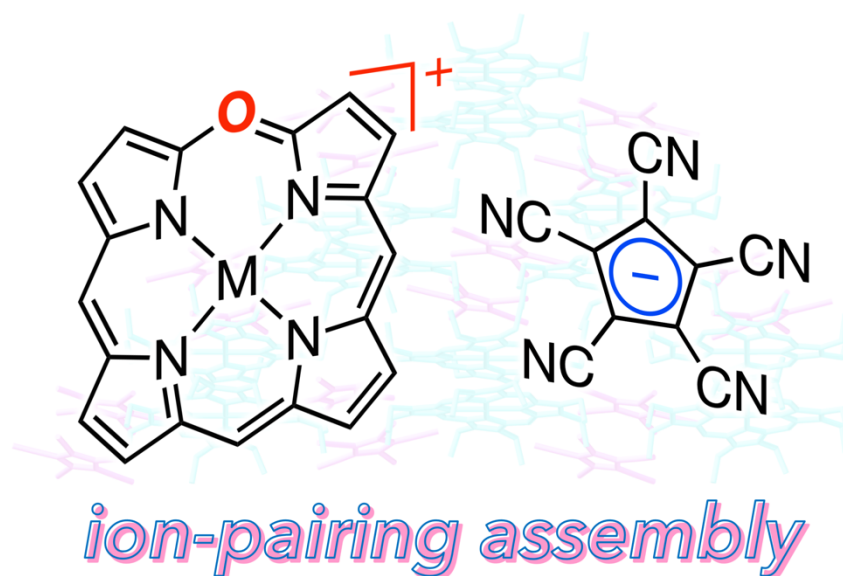
4-6. References

1. Matano, Y. *Chem. Rev.* **2017**, *117*, 3138–3191.
2. (a) Satoh, T.; Minoura, M.; Nakano, H.; Furukawa, K.; Matano, Y. *Angew. Chem. Int. Ed.* **2016**, *55*, 2235–2238. (b) Sudoh, K.; Satoh, T.; Amaya, T.; Furukawa, K.; Minoura, M.; Nakano, H.; Matano, Y. *Chem. Eur. J.* **2017**, *23*, 16364–16373. (c) Sudoh, K.; Hatakeyama, T.; Furukawa, K.; Nakano, H.; Matano, Y. *J. Porphyrins Phthalocyanines* **2018**, *22*, 542–551. (d) Sudoh, K.; Satoh, Y.; Furukawa, K.; Nakano, H.; Matano, Y. *J. Porphyrins Phthalocyanines* **2020**, *24*, 286–297. (e) Ochiai, H.; Furukawa, K.; Nakano, H.; Matano, Y.

- J. Org. Chem.* **2021**, *86*, 2283–2296. (f) Shimizu, Y.; Matano, Y. *J. Porphyrins Phthalocyanines* **2021**, *25*, 1004–1014. (g) Satoh, Y.; Fujita, Y.; Muramatsu, N.; Furukawa, K.; Ikoma, T.; Minoura, M.; Nakano, H.; Matano, Y. *ChemPlusChem* **2021**, *86*, 1476–1486.
3. Chia, W. X.; Nishijo, M.; Kang, S.; Oh, J.; Nishimura, T.; Omori, H.; Longevial, J.-F.; Miyake, Y.; Kim, D.; Shinokubo, H. *Chem. Eur. J.* **2020**, *26*, 2754–2760.
 4. Unselective synthesis of monoazaporphyrins. (a) Barrett, P. A.; Linstead, R. P.; Tuey, G. A. P.; Robertson, J. M. *J. Chem. Soc.* **1939**, 1809–1810. (b) Barrett, P. A.; Linstead, R. P.; Leavitt, J. J.; Rowe, G. A. *J. Chem. Soc.* **1940**, 1076–1092. (c) van As, A.; Joubert, C. C.; Buitendach, B. E.; Erasmus, E.; Conradie, J.; Cammidge, A. N.; Chambrier, I.; Cook, M. J.; Swarts, J. C. *Inorg. Chem.* **2015**, *54*, 5329–5341. (d) Mack, J.; Sosa-Vargas, L.; Coles, S. J.; Tizzard, G. J.; Chambrier, I.; Cammidge, A. N.; Cook, M. J.; Kobayashi, N. *Inorg. Chem.* **2012**, *51*, 12820–12833. (e) Cammidge, A. N.; Chambrier, I.; Cook, M. J.; Hughes, D. L.; Rahman, M.; Sosa-Vargas, L. *Chem. Eur. J.* **2011**, *17*, 3136–3146. (f) Cammidge, A. N.; Chambrier, I.; Cook, M. J.; Langner, E. H. G.; Rahman, M.; Swarts, J. C. *J. Porphyrins Phthalocyanines* **2011**, *15*, 890–897. (g) Ivanova, Yu. B.; Churakhina, Yu. I.; Semeikin, A. S.; Mamardashvili, N. Zh. *Russ. J. Gen. Chem.* **2009**, *79*, 833–838. (h) Cammidge, A. N.; Cook, M. J.; Hughes, D. L.; Nekelson, F.; Rahman, M. *Chem. Commun.* **2005**, 930–932. (i) Leznoff, C. C.; McKeown, N. B. *J. Org. Chem.* **1990**, *55*, 2186–2190.
 5. Selective synthesis of monoazaporphyrins. (a) Harris, R. L. N.; Johnson, A. W.; Kay, I. T. *J. Chem. Soc. C* **1966**, 22–29. (b) Engel, J.; Gossauer, A.; Johnson, A. W. *J. Chem. Soc., Perkin Trans. I* **1978**, 871–875. (c) Singh, J. P.; Xie, L. Y.; Dolphin, D. *Tetrahedron Lett.* **1995**, *36*, 1567–1570.
 6. Kakeya, K.; Aozasa, M.; Mizutani, T.; Hitomi, Y.; Kodera, M. *The J. Org. Chem.* **2014**, *79*, 2591–2600.
 7. Bando, Y.; Haketa, Y.; Sakurai, T.; Matsuda, W.; Seki, S.; Takaya, H.; Maeda, H. *Chem. Eur. J.* **2016**, *22*, 7843–7850.
 8. Sandström, J. In *Dynamic NMR Spectroscopy*; Academic Press: London, 1982; pp 96.
 9. Syrbu, S. A.; Lyubimova, T. V.; Semeikin, A. S. *Chem. Heterocycl. Compd.* **2004**, *40*, 1262–1270.

Chapter 5

Ion-Pairing Assembly of 5-Oxaporphyrinium Cation and Pentacyanocyclopentadienide



Contents

5-1.	Introduction	56
5-2.	Synthesis and characterization	56
5-3.	Crystal structure analysis	58
5-4.	Summary of Chapter 5	63
5-5.	References	64

5-1. Introduction

Crystal engineering is the discipline to understand the structure–property relationship between one specific molecule and its crystalline assembly.¹ The assembly mode of the molecular component is governed by noncovalent interactions such as hydrogen bonding, coordination bonding, and halogen bonding. In particular, ion-pairing assembly is an attractive target of crystal engineering because various charged components afford multiple cation–anion pairs, which provide diverse packing structures and physical properties.

Among various ion-pair assemblies, the Maeda group has focused on charged π -systems.² As well as neutral π -systems, a crystalline assembly constituted from charged π -systems is a fascinating target for optical and electronic materials. Recently, the group has proposed that the interplay of charged π -systems, which are named as $^i\pi$ – $^j\pi$ interaction, mainly is originated from dispersion force, not only electrostatic force (Figure 5-1).

In this chapter, the author discovered ion-pairing assemblies of oxaporphyrinium cations with pentacyanocyclopentadienide (PCCp[−]). The positive charge of an oxaporphyrinium cation is delocalized in the whole porphyrinic core (see Chapter 2). PCCp[−] is a stable π -anion with electron-withdrawing cyano groups.³ Metal oxaporphyrinium cations adopt various crystal packing structures in the solid state. Energy decomposition analysis (EDA) revealed the origin of the different packing structures, in which $^i\pi$ – $^j\pi$ interaction played an essential role.

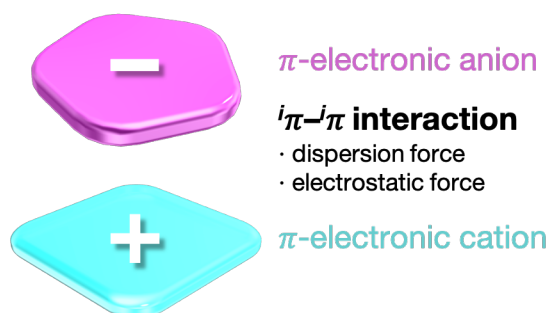
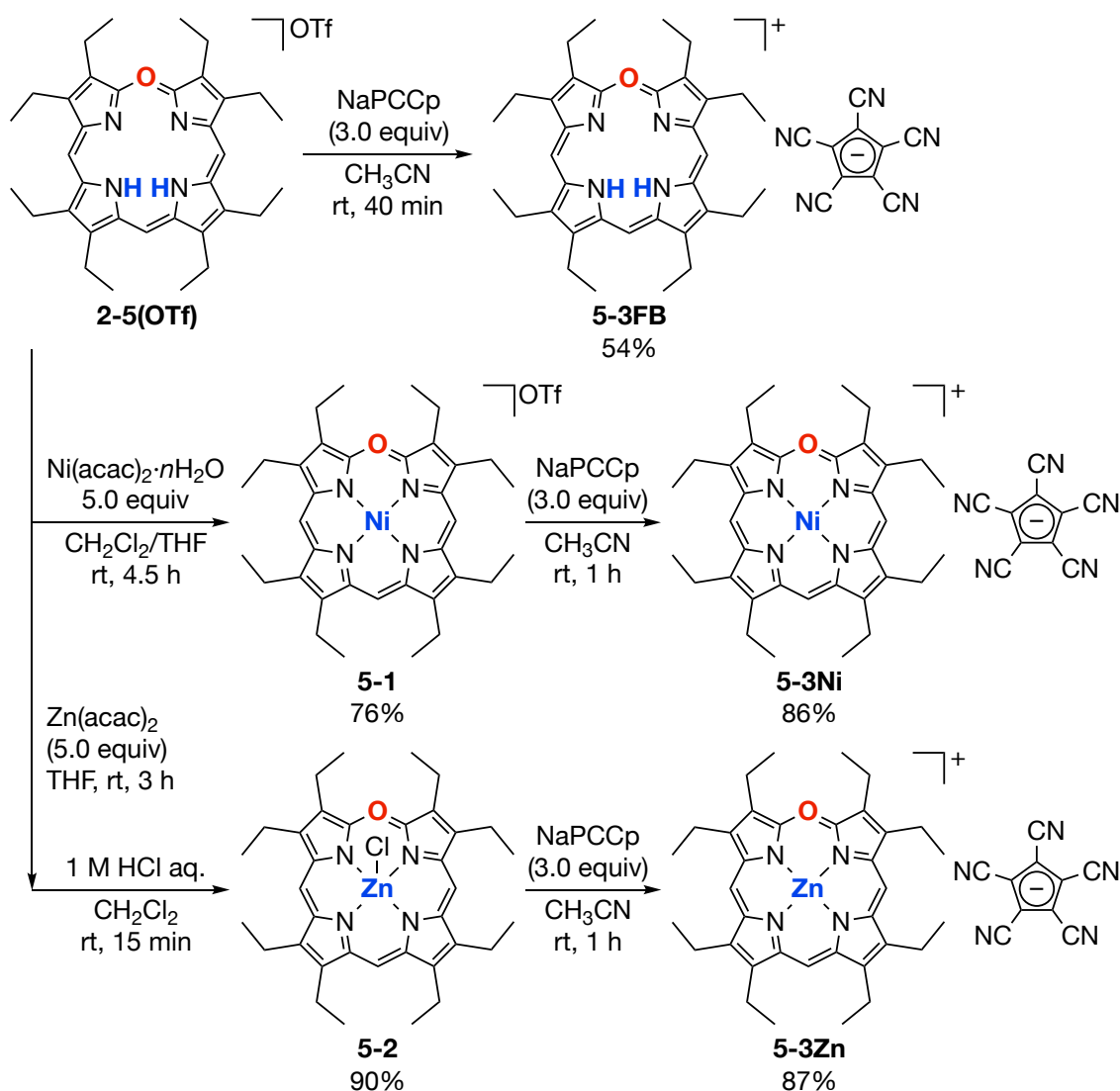


Figure 5-1. Ion-pairing assembly of charged π -systems.

5-2. Synthesis and characterization

The author attempted to prepare an ion pair with PCCp[−] and zinc oxaporphyrinium cation (**5-3Zn**) by treatment of zinc oxaporphyrinium tetrakis[3,5-bis(trifluoromethyl)phenyl]borate (**3-**

1) with sodium pentacyanocyclopentadienide (NaPCCp).⁴ Unfortunately, ion-metathesis reaction did not proceed, suggesting that harder counter anions are required for efficient ion exchange. The author then prepared oxaporphyrinium cations with triflate or chloride as the counter ion (Scheme 5-1). Treatment of **2-5(OTf)** with nickel acetylacetonate furnished corresponding nickel complex **5-1**. The reaction of **2-5(OTf)** with zinc acetylacetonate and work-up with 1 M HCl aq. afforded zinc oxaporphyrinium chloride **5-2**. Then, anion exchange of oxaporphyrinium cations with hard anions by NaPCCp was conducted in acetonitrile. After silica-gel column chromatography and recrystallization afforded corresponding metal oxaporphyrinium pentacyanocyclopentadienides **5-3Ms** (M = 2H, Ni, Zn). All products were characterized by NMR, HRMS, UV/Vis absorption spectroscopy, and X-ray analysis.



Scheme 5-1. Synthesis of **5-3Ms**.

In ^{13}C NMR spectra of **5-3Ms**, two additional peaks appeared at around 100–115 ppm in comparison to the precursors, indicating the presence of PCCp^- .^{3c,4} In addition, the inner-NH proton signal of **5-3FB** (2.78 ppm) was up-field shifted than those of **2-5(OTf)** (3.13 ppm) and **2-5[BAr^F₄]** (3.28 ppm). This implies the free-base oxaporphyrinium cation and the PCCp^- interact mutually in solution to shift the inner-NH proton signal due to the ring-current effect of the PCCp^- .

In UV/Vis absorption spectra of **5-3Ms** (Figure 5-2), peaks at 248 and 257 nm suggest the presence of PCCp^- .^{3c} The spectral shape of **5-3Ms** from 300 to 800 nm resembled those of their precursors, indicating that the absorption bands are originated from the oxaporphyrinium cations. **5-3FB** exhibited dual emission due to *cis*- and *trans*-tautomers of inner-NH protons, as is the case of **FB-BAr^F₄** (see Chapter 2).

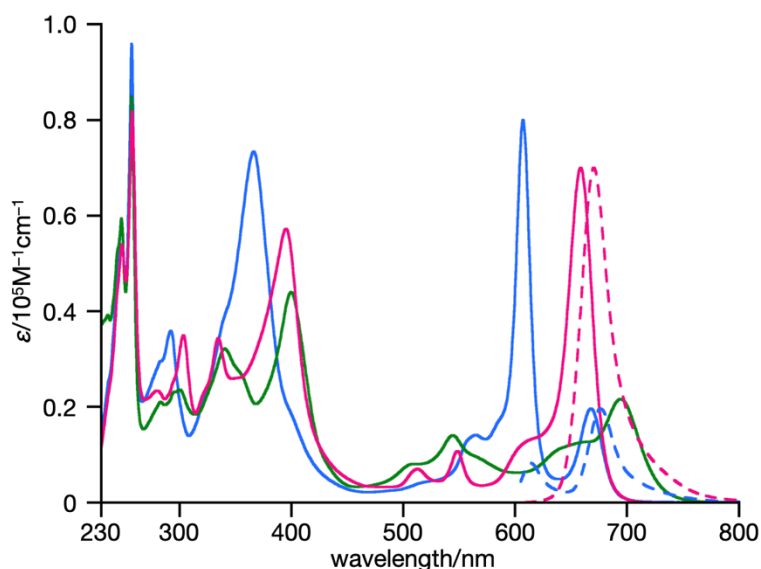


Figure 5-2. UV/Vis absorption (solid line) and fluorescence (dashed line, $\lambda_{\text{ex}} = 550$ nm) spectra of **5-3FB** (blue), **5-3Ni** (green), and **5-3Zn** (magenta) in dichloromethane.

5-3. Crystal structure analysis

Crystals for X-ray diffraction analysis were prepared by the slow vapor diffusion method. Structures of **5-3Ms** and precursors were unambiguously confirmed, in which **5-3FB**, **5-3Zn**, and **5-3Ni** exhibited different packing structures. All solid-state structures of **5-3Ms** included no solvent molecules in the crystals. The packing structure of **5-3FB** consisted of two independent

FB⁺s (FB-a and FB-b) and three independent PCCp[−]s (PCCp-a, PCCp-b, and PCCp-c). These ionic species were repeated in the order of PCCp-c, FB-a, PCCp-a, FB-a, PCCp-c, FB-b, PCCp-b, and FB-b (Figure 5-3). The PCCp[−] unit in **5-3FB** aligned in parallel to the oxaporphyrinium cation. The oxaporphyrinium cation and PCCp[−] were closely packed at distances of 3.34–3.54 Å. In contrast, the PCCp anion in **5-3Zn** was tilted and coordinated to the zinc center with the nitrogen atom (Figure 5-4). The distance between zinc and nitrogen atoms was 2.60 Å, which was shorter than the distance between the FB-a plane and the nitrogen atom of PCCp-c (2.88 Å). Interestingly, **5-3Ni** exhibited face-to-face dimeric stacking of positively charged oxaporphyrinium cations (Figure 5-5), while positively and negatively charged species were stacked together alternately in **5-3FB** and **5-3Zn**. The plane distance of oxaporphyrinium cations was 3.31 Å and that of PCCp[−] was 3.28 Å. The oxaporphyrinium unit in **5-3Ni** was distorted with a mean plane deviation (MPD) of 0.086 Å as compared with **5-1** (MPD = 0.026 Å), **5-3Zn** (MPD = 0.015 Å), and **5-3FB** (MPD = 0.028 and 0.049 Å). The distortion could be caused by the small ionic size of nickel(II), which is not matched with the inner cavity size.

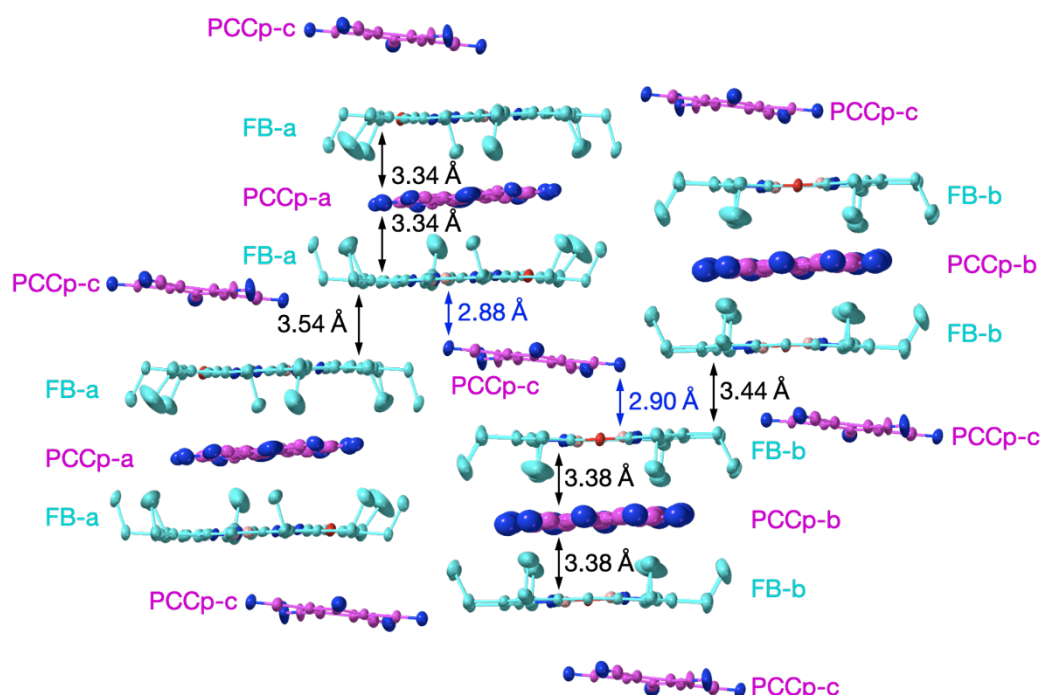


Figure 5-3. X-ray crystal structure of **5-3FB**. Carbons of oxaporphyrinium cations and PCCp[−] are colored in cyan and magenta, respectively. Black arrows and values mean the distances between planes. Blue arrows and values mean the distances between the nitrogen atom of PCCp[−] and oxaporphyrinium cation plane.

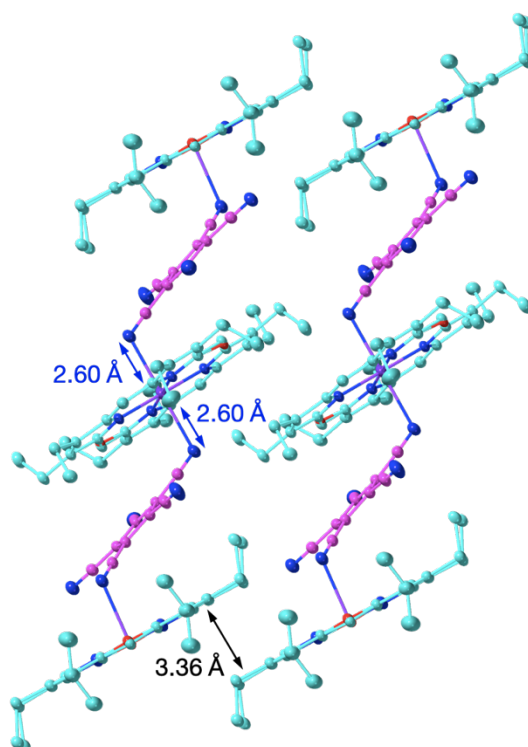


Figure 5-4. X-ray crystal structure of **5-3Zn**. Carbons of oxaporphyrinium cations and PCCp⁻ are colored in cyan and magenta, respectively. Black arrow and value mean the distance between planes. Blue arrows and values mean bond length of axial coordination.

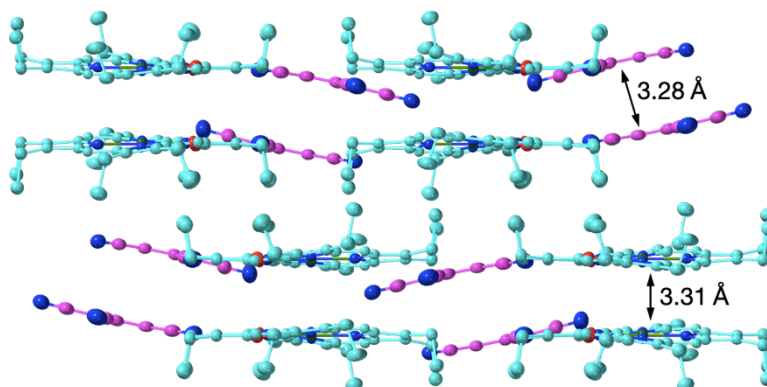


Figure 5-5. X-ray crystal structure of **5-3Ni**. Carbons of oxaporphyrinium cations and PCCp⁻ are colored in cyan and magenta, respectively. Black arrows and values mean the distances between planes.

To elucidate the origin of different packings of **5-3Ms**, the author conducted the energy decomposition analysis (EDA)⁵ based on the fragment molecular orbital (FMO) method FMO2-MP2 using the mixed basis sets including NOSeC-V-TZP with model core potential (MCP) for Ni and Zn and NOSeC-V-DZP with MCP for the other atoms.⁶⁻⁸ The EDA calculations using the FMO yielded the resulting outputs of electrostatic (E_{es}), dispersion (E_{disp}), charge transfer (E_{ct}), and exchange-repulsion (E_{ex}) interaction energies along with the total interaction energy (E_{tot}). The induction energy is taken into account as that by polarization effects. In FMO calculations, the wave functions of the fragment monomers are optimized in the presence of the classical electrostatic potentials of the other fragment monomers so that the converged fragment monomers are polarized. Consequently, the induction interaction energy is distributed in the energy values obtained using EDA. In **5-3FB**, the E_{tot} values of the stacking pairs (-152.92 and -130.24 kcal mol⁻¹ for c5-a2 and c5-a5, respectively) were larger than that of the lateral pair (-21.26 kcal mol⁻¹ for c5-a6) (Figure 5-6). E_{disp} has the largest contribution for E_{tot} of the stacking pair, which would be derived from the proximity of PCCp⁻ and ethyl substituents or π -plane of FB⁺. Therefore, E_{disp} decreased and E_{es} became the predominant contributor in the lateral pairs.

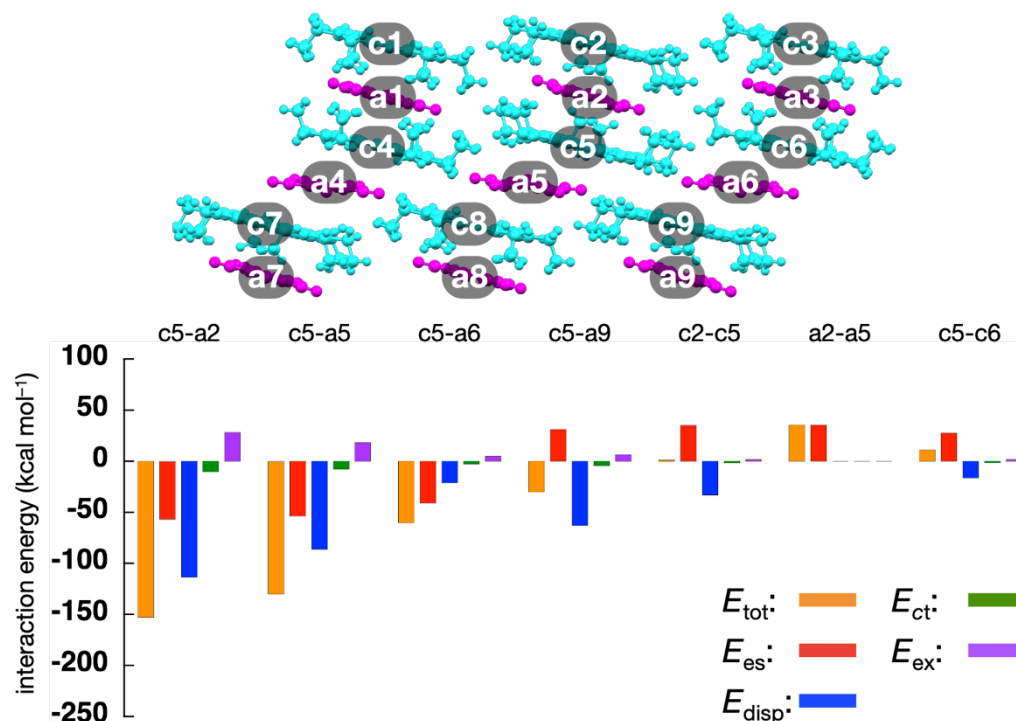


Figure 5-6. Decomposition of the total intermolecular interaction energy of **5-3FB**, derived from EDA based on the FMO2-MP2 method using the basis set NOSeC-V-DZP with MCP.

The EDA of **5-3Zn** exhibited the E_{tot} value was more stabilized than that of **5-3FB** (Figure 5-7). The E_{es} value and the E_{disp} value for c3-a1 were destabilized to $-61.03 \text{ kcal mol}^{-1}$ and $-138.32 \text{ kcal mol}^{-1}$, respectively. Compared with the electrostatic potential maps, the cationic charge of **5-3Zn** was delocalized on the zinc atom (Figure 5-8), suggesting the effect of coordination of cyano groups to zinc. The E_{es} and E_{disp} of the stacking ion pairs in **5-3FB** and **5-3Zn** were favored, suggesting a contribution from the $^i\pi\text{-}^i\pi$ interaction.

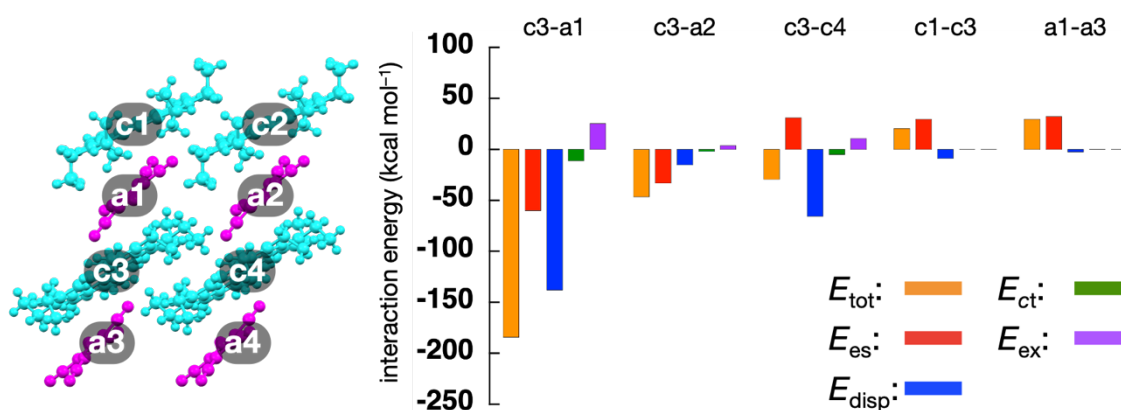


Figure 5-7. Decomposition of the total intermolecular interaction energy of **5-3Zn**, derived from EDA based on the FMO2-MP2 method using the mixed basis set including NOSeC-V-TZP with MCP for Zn and NOSeC-V-DZP with MCP for the other atoms.

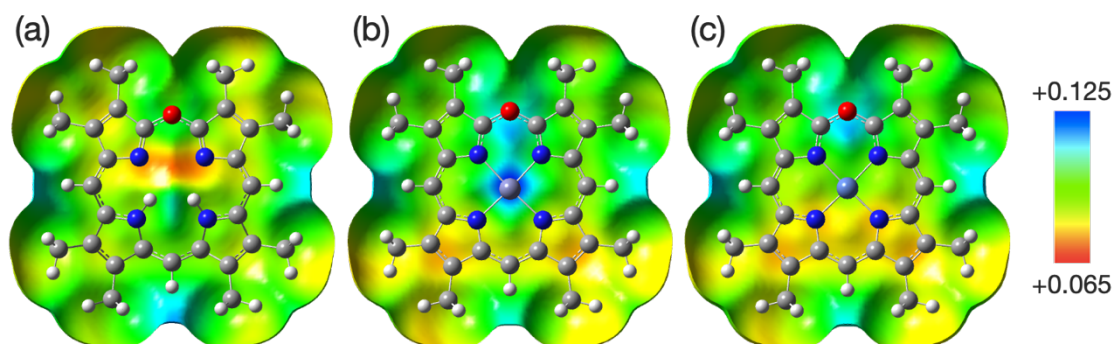


Figure 5-8. Electrostatic potential maps for cationic part of (a) **5-3FB**, (b) **5-3Zn**, and (c) **5-3Ni**. Ethyl substituents were replaced with methyl substituents to reduce the calculation cost.

The E_{tot} values of the two-by-two charge-by-charge assembly of nickel oxaporphyrinium cations c1-c2 and PCCp anions a1-a2 were -180.62 and -1.40 kcal mol $^{-1}$, respectively (Figure 5-9). The difference would be derived from the size of the contact area. The large overlapping of the cationic π -planes effectively stabilized the E_{disp} . The energetically favorable E_{disp} between the identically charged species (-230.44 and -59.97 kcal/mol for c1-c2 and a1-a2, respectively) exceeded the corresponding energetically unfavorable E_{es} (20.40 and 47.99 kcal/mol, respectively) and E_{ex} (51.15 and 15.68 kcal/mol, respectively), resulting in the formation of the unique packing structure.

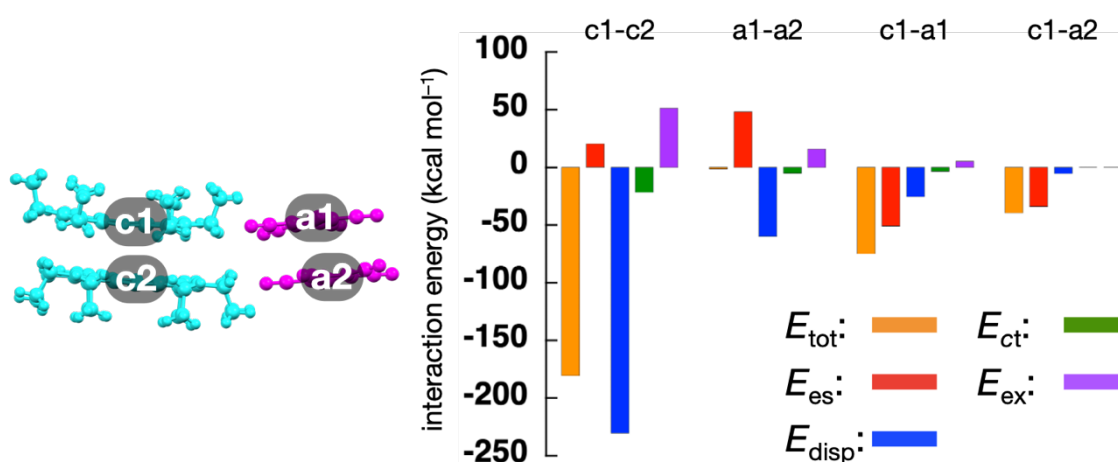


Figure 5-9. Decomposition of the total intermolecular interaction energy of **5-3Ni**, derived from EDA based on the FMO2-MP2 method using the mixed basis set including NOSeC-V-TZP with MCP for Ni and NOSeC-V-DZP with MCP for the other atoms.

5-4. Summary of Chapter 5

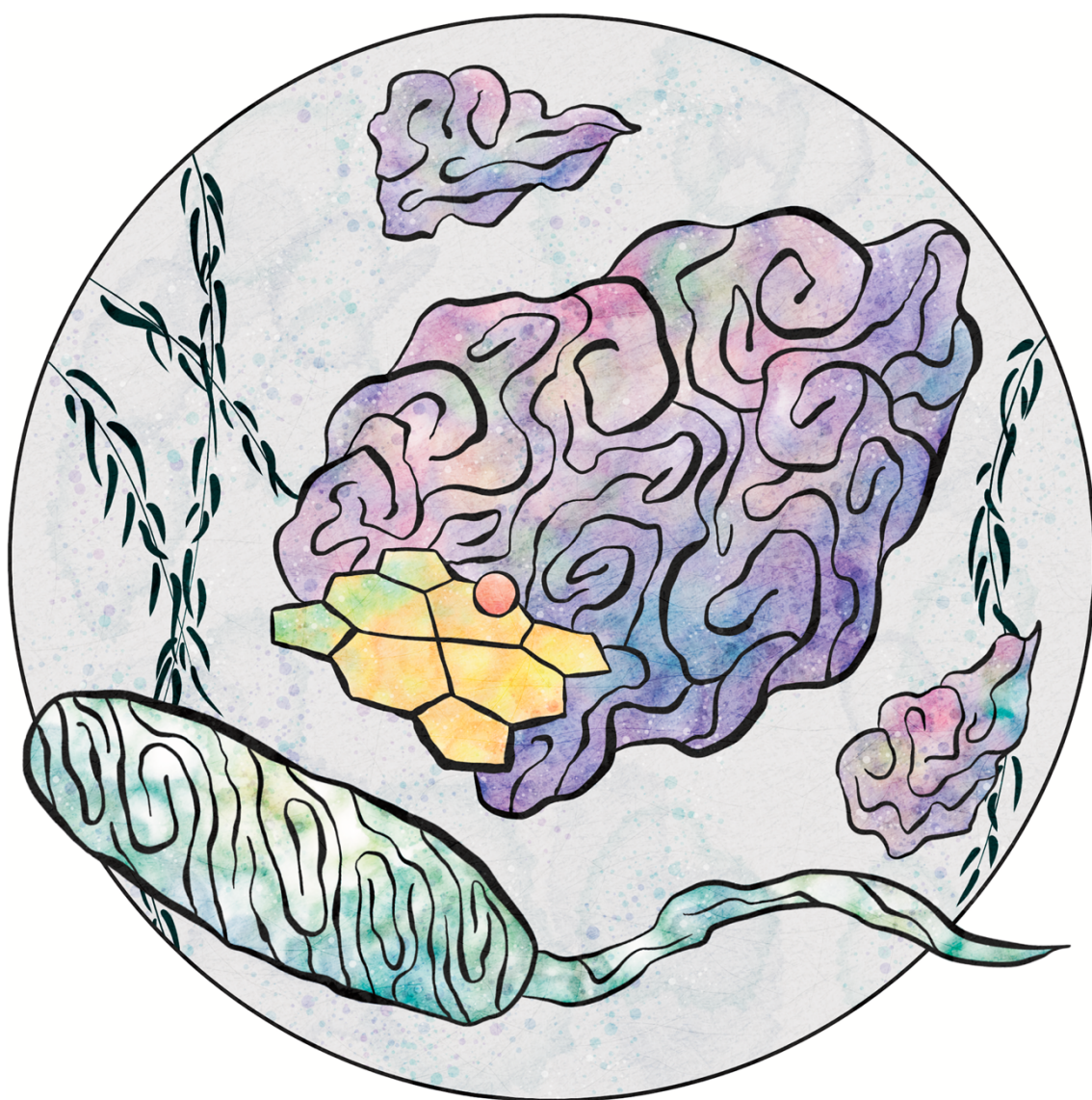
The author synthesized ion pairs of PCCp $^{-}$ and various metal oxaporphyrinium cations. They exhibited different packing structures, in which electrostatic and dispersion forces played a vital role in determining their packing mode, revealed by the EDA analysis. These findings are helpful for designing electronic materials.

5-5. References

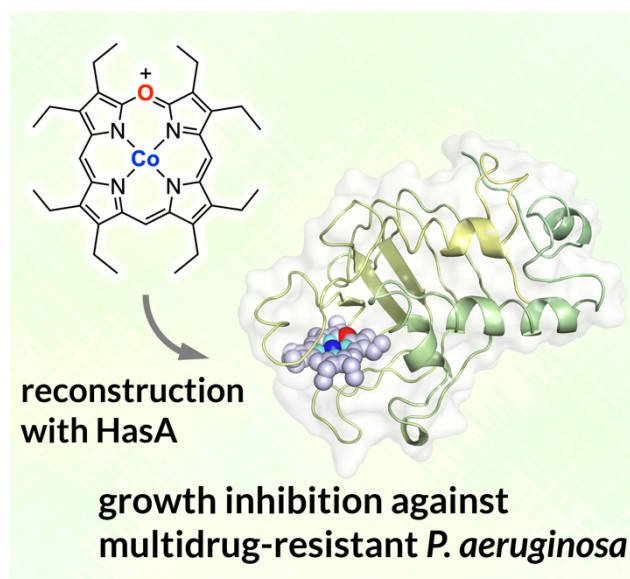
1. (a) Desiraju, G. R. *J. Am. Soc. Chem.* **2013**, *135*, 9952–9967. (b) Desiraju, G. R. *J. Chem. Sci.* **2010**, *122*, 667–675. (c) Nangia, A. K.; Desiraju, G. R. *Angew. Chem. Int. Ed.* **2019**, *58*, 4100–4107. (d) Yu, P.; Zhen, Y.; Dong, H.; Hu, W. *Chem* **2019**, *5*, 2814–2853.
2. (a) Sasano, Y.; Tanaka, H.; Haketa, Y.; Kobayashi, Y.; Ishibashi, Y.; Morimoto, T.; Sato, R.; Shigeta, Y.; Yasuda, N.; Asahi, T.; Maeda, H. *Chem. Sci.* **2021**, *12*, 9645–9657. (b) Yamasumi, K.; Maeda, H. *Bull. Chem. Soc. Jpn.* **2021**, *94*, 2252–2262.
3. (a) Richardson, C.; Reed, C. A. *Chem. Commun.* **2004**, 706–707. (b) Less, R. J.; McPartlin, M.; Rawson, J. M.; Wood, P. T.; Wright, D. S. *Chem. Eur. J.* **2010**, *16*, 13723–13728. (c) Bando, Y.; Haketa, Y.; Sakurai, T.; Matsuda, W.; Seki, S.; Takaya, H.; Maeda, H. *Chem. Eur. J.* **2016**, *22*, 7843–7850.
4. Sakai, T.; Seo, S.; Matsuoka, J.; Mori, Y. *J. Org. Chem.* **2013**, *78*, 10978–10985.
5. Phipps, M. J. S.; Fox, T.; Tautermann, C. S.; Skylaris, C.-K. *Chem. Soc. Rev.* **2015**, *44*, 3177–3211.
6. (a) Schmidt, M. W.; Baldrige, K. K.; Boatz, J. A.; Elbert, S. T.; Gordon, M. S.; Jensen, J. H.; Koseki, S.; Matsunaga, N.; Nguyen, K. A.; Su, S.; Windus, T. L.; Dupuis, M.; Montgomery, J. A. *J. Comput. Chem.* **1993**, *14*, 1347–1363. (b) Gordon, M. S.; Schmidt, M. W. In *Theory and Applications of Computational Chemistry: the first forty years*; Dykstra, C. E.; Frenking, G.; Kim, K. S.; Scuseria, G. E., Eds.; Elsevier Science: Amsterdam, 2005; pp 1167–1189.
7. Kitaura, K.; Ikeo, E.; Asada, T.; Nakano, T.; Uebayasi, M. *Chem. Phys. Lett.* **1999**, *313*, 701–706.
8. Fedorov, D. G.; Kitaura, K. *J. Comput. Chem.* **2006**, *28*, 222–237.

Chapter 6

A Heme-Acquisition Protein Reconstructed with a Cobalt 5-Oxaporphyrinium Cation



Selected as the Inside Back Cover.



Contents

6-1.	Introduction	67
6-2.	Synthesis of metal oxaporphyrinium cations and reconstruction into HasA	68
6-3.	Structure of reconstructed HasA	71
6-4.	Growth-inhibition activity toward <i>Pseudomonas aeruginosa</i>	73
6-5.	Summary of Chapter 6	75
6-6.	References	76

6-1. Introduction

Heme proteins fulfill essential roles in biological organisms, involving metabolism (cytochrome P450),¹ oxygen transport (myoglobin),² and heme degradation (heme oxygenase).³ These functions are essentially derived from iron protoporphyrin IX (heme) as a cofactor of heme proteins. Substitution of native heme with artificial hemes has attracted much attention with respect to improving the biological activity of heme proteins.⁴ In this area, research has mainly focused on two types of artificial hemes: Heme derivatives and core-modulated porphyrin analogues (Figure 6-1). The reconstruction of heme proteins with heme derivatives has been investigated given the ease of access to the latter through exchange of the central metals⁵ and modification of peripheral substituents.⁶ On the other hand, accommodation of core-modulated porphyrins such as heteroporphyrins⁷ and isomeric porphyrins⁸ should lead to enhanced functionality due to their substantial electronic perturbations. For example, myoglobin reconstructed by monoazaporphyrin exhibited an oxygen affinity that is 50 times higher than that of native myoglobin.⁷ However, incorporation of porphyrin analogues into heme proteins remains limited, because lengthy de novo synthesis is required to introduce heme-like peripheral substituents, which interact with heme proteins.

Recently, Shoji and co-workers have discovered that the heme-acquisition protein (HasA) accommodates artificial hemes without heme-like structures.⁹ The author thus anticipated that the use of HasA could potentially enable the inclusion of various types of heteroporphyrins to provide reconstructed heme proteins with superior functionality. In this chapter, the author clarified that HasA effectively accommodates a cobalt 5-oxaporphyrinium cation, which leads to strong growth-inhibition activity against *Pseudomonas aeruginosa* and multidrug-resistant *P. aeruginosa*.

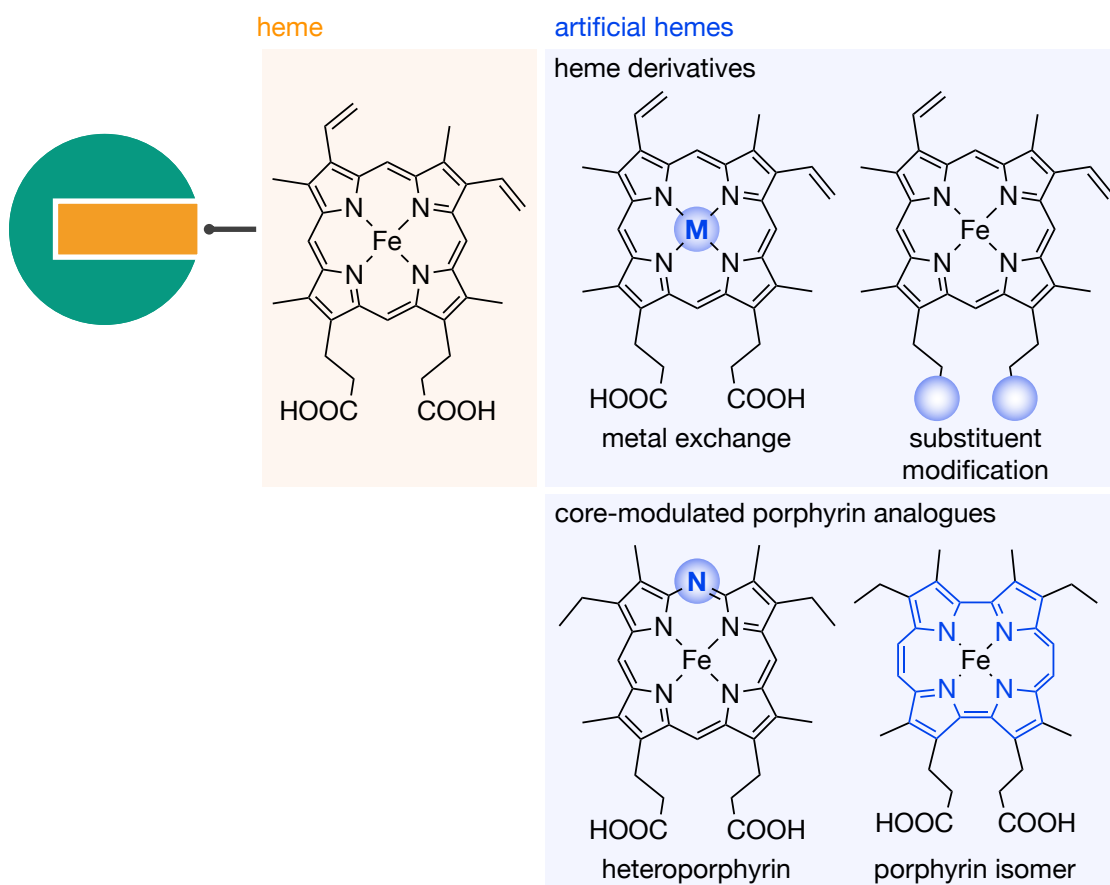
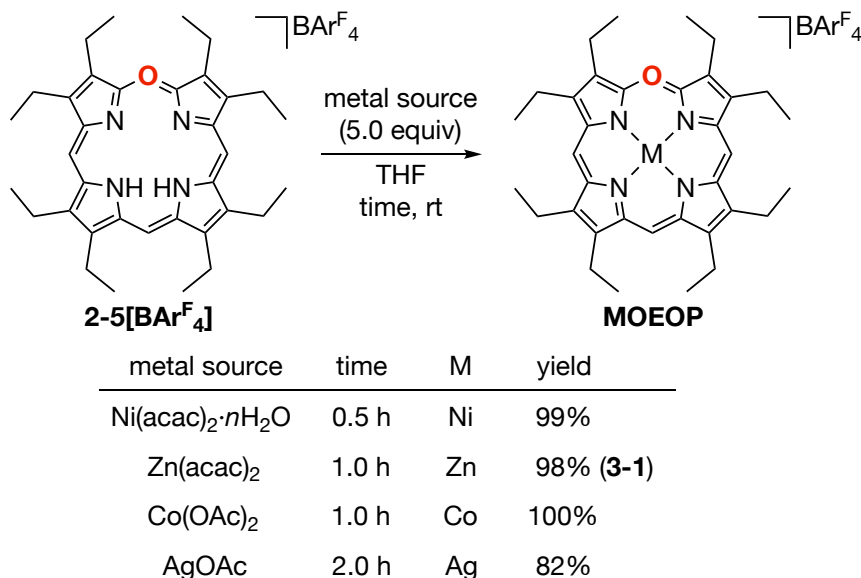


Figure 6-1. Reconstructed heme protein and artificial hemes.

6-2. Synthesis of metal oxaporphyrinium cations and reconstruction into HasA

Oxaporphyrin is observed as an intermediate in the heme degradation mediated by heme oxygenase.³ As described in Chapter 2, the author established the synthesis of a free-base 5-octaethyloxaporphyrinium cation (**2-5[Bar^F₄]**). Treatment of **2-5[Bar^F₄]** with nickel, zinc, cobalt, and silver salts afforded the corresponding metal 5-octaethyloxaporphyrinium cations (**MOEOPs**) in good yields (Scheme 6-1). Unfortunately, iron complexation was unsuccessful because the intrinsically reactive oxaporphyrin skeleton was not durable against the iron-complexation condition. The characterization of **MOEOPs** was accomplished by NMR and UV/Vis absorption spectroscopy, high-resolution mass spectrometry, single-crystal X-ray diffraction analysis, and cyclic voltammetry. Although several metal 5-oxaporphyrinium cations have already been reported, previously established synthetic methodologies remain limited to

autooxidation¹⁰ and the metalation of bilindione.¹¹ The present procedure via the metalation of **2-5[BAr^F₄]** offers direct and efficient access to a variety of metal 5-oxaporphyrinium cations.



Scheme 6-1. Synthesis of **MOEOPs**.

Next, the reconstruction of HasA with these metal oxaporphyrins was attempted. For that purpose, a solution of metal oxaporphyrin in DMSO was added to the heme-free open-form HasA (apo-HasA). After the removal of DMSO by dialysis, followed by purification via anion-exchange chromatography, the corresponding reconstructed HasAs were obtained. The complexation behavior differed depending on the central metal of the oxaporphyrins. For example, HasA did not accommodate **NiOEOP** and **AgOEOP**, and although **ZnOEOP** was slightly incorporated, purification of the reconstructed protein from apo-HasA failed. In contrast, the use of **CoOEOP** successfully afforded reconstructed HasA, which was separated from apo-HasA and purified. The difference in the incorporation behavior could be caused by the axial-coordination ability of the central metals. An ESI-TOF MS analysis of reconstructed HasA exhibited a peak at 19624.0 Da, which corresponds to the CoOEOP-HasA complex (Figure 6-2 (a)). The UV/Vis absorption spectrum of CoOEOP-HasA exhibited the characteristic change from that of CoOEOP after reconstruction (*vide infra*) (Figure 6-2 (b)). Additionally, HasA reconstituted with cobalt octaethylporphyrin (**CoOEP**) was also prepared in the same manner for comparison (Figure 6-2 (c)).

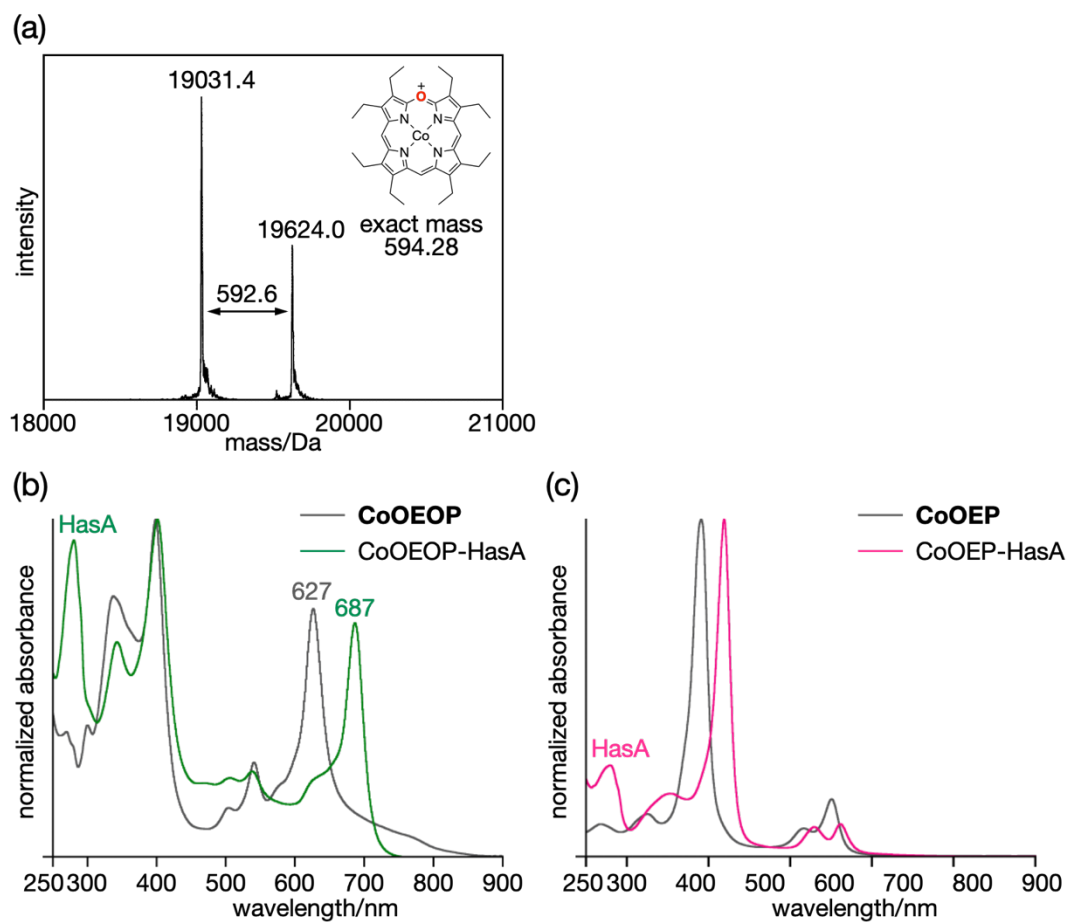


Figure 6-2. (a) ESI-TOF mass spectrum of CoOEOP-HasA. (b) UV/Vis absorption spectra of **CoOEOP** in dichloromethane (gray) and CoOEOP-HasA in phosphate-buffered saline (pH = 7.4; green). (c) UV/Vis absorption spectra of **CoOEP** in dichloromethane (gray) and CoOEP-HasA in phosphate-buffered saline (pH = 7.4; magenta).

6-3. Structure of reconstructed HasA

To acquire insight into reconstructed HasAs, the single-crystal X-ray diffraction structures of CoOEOP-HasA and CoOEP-HasA were both obtained at 1.35 Å resolutions. These structures are comparable to those of heme-bound HasA (holo-HasA) (Figure 6-3 (a), (b), and (c)). The root-mean-square deviations (RMSD) over 1–183 amino acid residues for $C\alpha$ atoms against holo-HasA (PDB 3ELL) were 0.648 and 0.616 respectively. The positions and angles of **CoOEOP** and **CoOEP** were almost identical with those of heme. The position of oxygen in **CoOEOP** was determined on the basis of the electron density (Figure 6-3 (c)). His32 and Tyr75 are ligated to the cobalt center of **CoOEOP** and **CoOEP**.

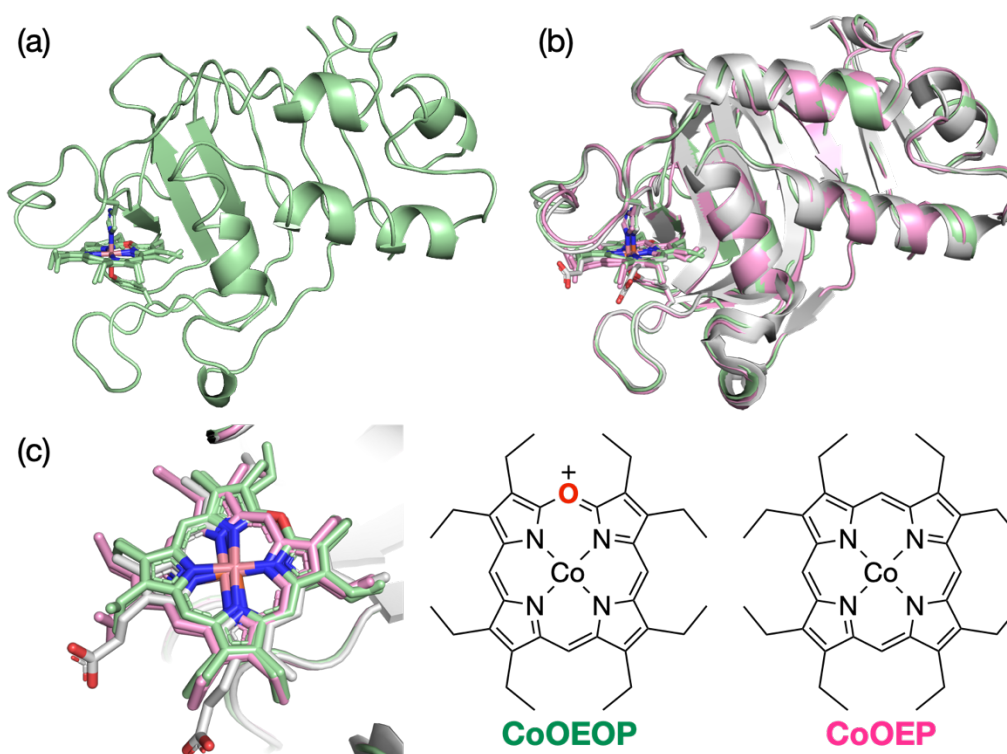


Figure 6-3. Single-crystal X-ray diffraction structures of CoOEOP-HasA (green, PDB 7VF8), CoOEP-HasA (magenta, PDB 7VF7), and holo-HasA (gray, PDB 3ELL). (a) Overall structures of CoOEOP-HasA. His32 and Tyr75 are shown as stick models. (b) Superimposed image of CoOEOP-HasA (green), CoOEP-HasA (magenta), and holo-HasA (gray). (c) Enlarged view of the complex-binding domain.

The UV/Vis absorption spectra of **CoOEOP** and CoOEOP-HasA differ substantially. In particular, the intense absorption band of **CoOEOP** at 627 nm was bathochromically shifted to 687 nm in CoOEOP-HasA (Figure 6-2 (b)). The absorption feature is similar to that of the Co(III) OEP complex.^{10c} To determine the valence of the cobalt center in HasA, ESR spectra of these cobalt complexes were measured. CoOEOP-HasA and CoOEP-HasA exhibited no ESR signals (Figure 6-4 (a) and (b)), supporting a +3 valence state of the cobalt center with a d^6 electron configuration in HasA, while **CoOEOP** and **CoOEP** were ESR active (Figure 6-4 (c) and (d)). Moreover, treatment of CoOEOP-HasA with dithionite resulted in hypsochromic shift in the absorption spectrum, suggesting the reduction of cobalt center. These results indicate that the Co(II) centers in **CoOEOP** and **CoOEP** are oxidized during the insertion into HasA. Probably, the axial coordination of the protein residues, especially that of axial tyrosinate ligands, stabilizes the high valence state of the cobalt center.

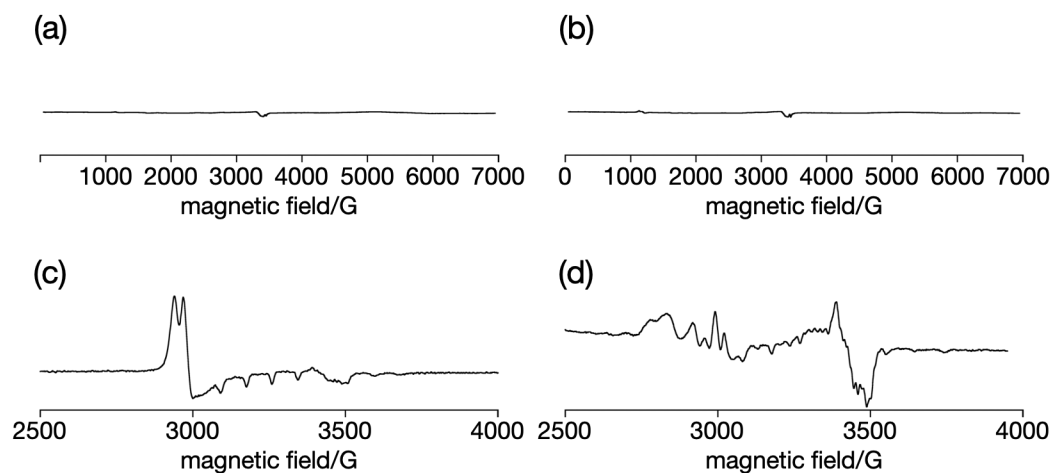


Figure 6-4. ESR spectra of (a) CoOEOP-HasA, (b) CoOEP-HasA, (c) **CoOEOP**, and (d) **CoOEP**. Measurement conditions of (a) and (b): 200 μ M, PBS solution, 4 K. Measurement conditions of (c) and (d): 200 μ M, 2-methyltetrahydrofuran, 77 K.

6-4. Growth-inhibition activity toward *Pseudomonas aeruginosa*

To investigate the potentially changed bioactivity of metal-5-oxaporphyrinium-cation-accommodating HasA, their growth-inhibition activities against *P. aeruginosa* were examined. Previously, Shoji and co-workers have reported that HasA coordinated with synthetic porphyrins inhibits the growth of *P. aeruginosa* even in the presence of holo-HasA as a heme source.⁹ In order to examine the growth inhibition ability of CoOEOP-HasA and CoOEP-HasA, *P. aeruginosa* was firstly cultured in M9-based medium containing EDTA as a free iron scavenger. Subsequent culturing was carried out in the presence of 1 μM of CoOEOP-HasA or CoOEP-HasA and 1 μM holo-HasA as the iron source. The growth of *P. aeruginosa* was monitored by checking the optical density at 600 nm (OD_{600}) of the bacterial cultures. Notably, CoOEOP-HasA inhibits the growth of *P. aeruginosa* more strongly than CoOEP-HasA (Figure 6-5). Half maximal inhibitory concentrations of CoOEOP-HasA and CoOEP-HasA were 0.090 μM and 0.52 μM , respectively. In addition, CoOEOP-HasA inhibited the growth even with an excess amount of holo-HasA. Reconstructed HasAs exhibited no toxicity against *P. aeruginosa* and HasA-free porphyrins (**CoOEOP** and **CoOEP**) did not affect the growth curve.

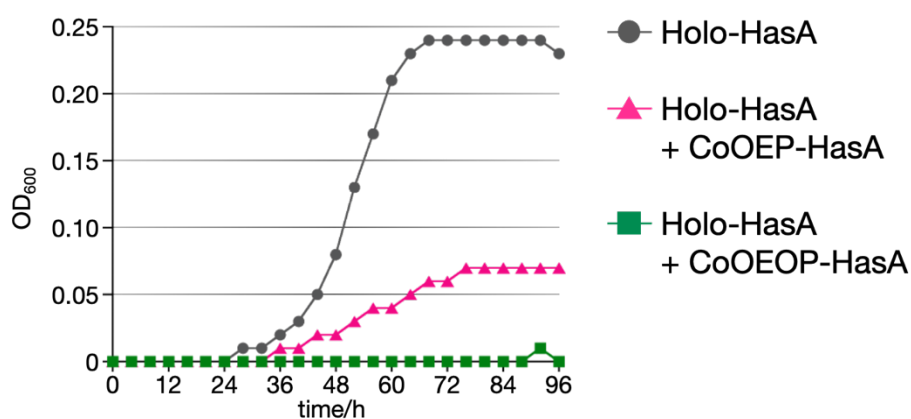


Figure 6-5. Growth curves of *P. aeruginosa*.

This inhibition is rationalized in terms of the tight binding of synthetic porphyrins to the HasA-specific outer-membrane receptor HasR, i.e., the receptor of heme delivered by HasA (Figure 6-6).⁹ HasR from *Serratia marcescens* forms a ternary complex of HasA-HasR-heme (PDB 3CSL), in which heme is bound by two histidine ligands of HasR.¹² Although the crystal structure of HasR from *P. aeruginosa* has not been obtained, the predicted structure by AlphaFold2¹³ exhibited the similar structure to that from *Serratia marcescens*. Consequently, HasR from *P. aeruginosa* probably forms the similar HasA-HasR-heme complex. The bound of synthetic porphyrins to HasR would prevent the subsequent acquisition of heme, thus inhibiting the growth of *P. aeruginosa*. The author speculates that the higher growth-inhibition activity of CoOEOP-HasA arises from the stronger binding of **CoOEOP** to the heme binding site of HasR with two histidine ligands (His221 and His624) than **CoOEP** on account of the enhanced ligand binding to the Co(III) center given the cationic charge of the OEOP ligand. The growth inhibition of multidrug-resistant *P. aeruginosa* was also examined. Importantly, CoOEOP-HasA effectively inhibited the growth of multidrug-resistant *P. aeruginosa* (MDRP0043)¹⁴ (Figure 6-7 (b)), which has been declared a hazardous bacterium by the WHO.¹⁵ Thus, the use of reconstructed proteins with heteroporphyrins shows promising potential to combat multidrug-resistant *P. aeruginosa*.

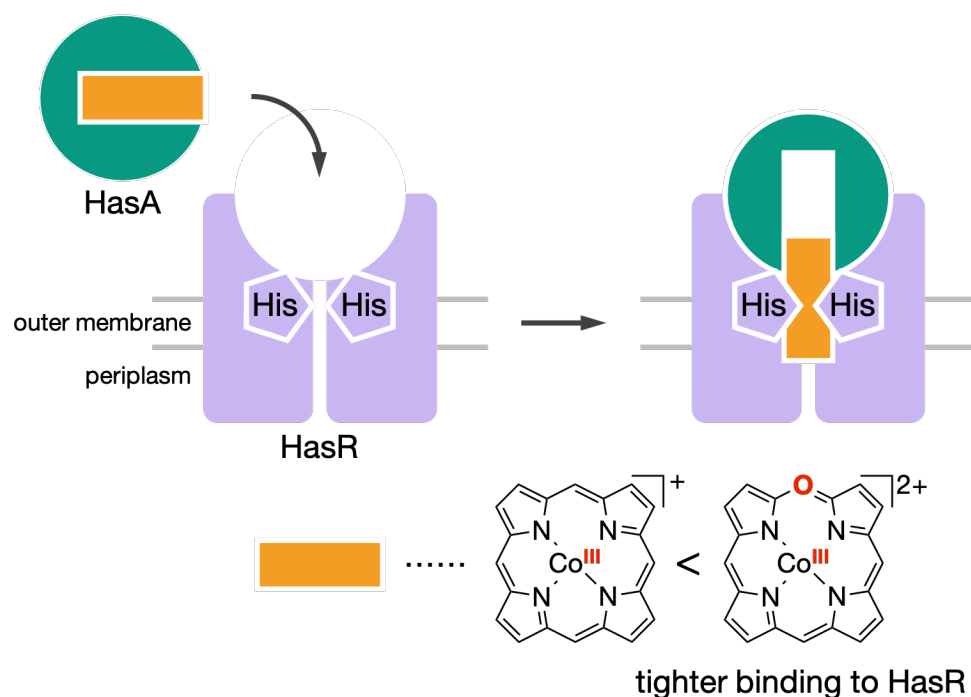


Figure 6-6. Proposed mechanism of growth inhibition of *P. aeruginosa* by reconstructed CoOEP-HasA and CoOEOP-HasA.

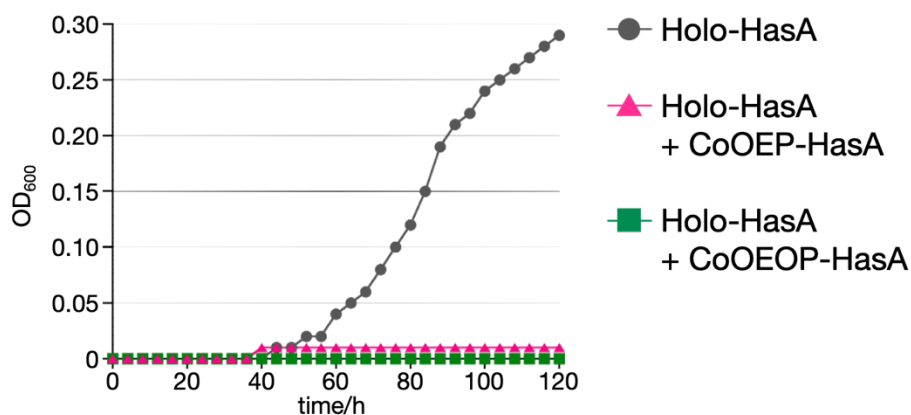


Figure 6-7. Growth curves of multidrug-resistant *P. aeruginosa*.

6-5. Summary of Chapter 6

In conclusion, a robust method for the synthesis of various metal oxaporphyrins has been established. Moreover, the author succeeded in the incorporation of **CoOEOP** into HasA. HasA accommodates artificial porphyrins that possess a cationic charge on the porphyrin core. Interestingly, CoOEOP-HasA exhibited a higher growth-inhibition ability against *P. aeruginosa* than CoOEP-HasA. The intense growth-inhibition activity of CoOEOP-HasA could be due to the enhanced ligand binding to the Co(III) center as a consequence of the cationic oxaporphyrin skeleton. The author thus proposes that the growth-inhibition ability is correlated to the porphyrin structure. The strong growth inhibition by CoOEOP-HasA was also effective for multidrug-resistant *P. aeruginosa*.

6-6. References

1. Ortiz de Montellano, P. R. In *Cytochrome P450: Structure, Mechanism, and Biochemistry*; 4th ed.; Plenum: New York, 2015.
2. Yuan, Y.; Tam, M. F.; Simplaceanu, V.; Ho, C. *Chem. Rev.* **2015**, *115*, 1702–1724.
3. (a) Ortiz de Montellano, P. R. *Curr. Opin. Chem. Biol.* **2000**, *4*, 221–227. (b) Matsui, T.; Unno, M.; Ikeda-Saito, M. *Acc. Chem. Res.* **2009**, *43*, 240–247.
4. (a) Fruk, L.; Kuo, C.-H.; Torres, E.; Niemeyer, C. M. *Angew. Chem. Int. Ed.* **2009**, *48*, 1550–1574. (b) Oohora, K.; Onoda, A.; Hayashi, T. *Acc. Chem. Res.* **2019**, *52*, 945–954.
5. (a) Lelyveld, V. S.; Brustad, E.; Arnold, F. H.; Jasanoff, A. *J. Am. Chem. Soc.* **2010**, *133*, 649–651. (b) Key, H. M.; Dydio, P.; Clark, D. S.; Hartwig, J. F. *Nature* **2016**, *534*, 534–537.
6. (a) Hayashi, T.; Hitomi, Y.; Ando, T.; Mizutani, T.; Hisaeda, Y.; Kitagawa, S.; Ogoshi, H. *J. Am. Chem. Soc.* **1999**, *121*, 7747–7750. (b) Kitagishi, H.; Oohora, K.; Yamaguchi, H.; Sato, H.; Matsuo, T.; Harada, A.; Hayashi, T. *J. Am. Chem. Soc.* **2007**, *129*, 10326–10327.
7. Neya, S.; Kaku, T.; Funasaki, N.; Shiro, Y.; Iizuka, T.; Imai, K.; Hori, H. *J. Biol. Chem.* **1995**, *270*, 13118–13123.
8. (a) Hayashi, T.; Dejima, H.; Matsuo, T.; Sato, H.; Murata, D.; Hisaeda, Y. *J. Am. Chem. Soc.* **2002**, *124*, 11226–11227. (b) Matsuo, T.; Hayashi, A.; Abe, M.; Matsuda, T.; Hisaeda, Y.; Hayashi, T. *J. Am. Chem. Soc.* **2009**, *131*, 15124–15125.
9. (a) Shirataki, C.; Shoji, O.; Terada, M.; Ozaki, S.; Sugimoto, H.; Shiro, Y.; Watanabe, Y. *Angew. Chem. Int. Ed.* **2014**, *53*, 2862–2866. (b) Uehara, H.; Shisaka, Y.; Nishimura, T.; Sugimoto, H.; Shiro, Y.; Miyake, Y.; Shinokubo, H.; Watanabe, Y.; Shoji, O. *Angew. Chem. Int. Ed.* **2017**, *56*, 15279–15283. (c) Shisaka, Y.; Iwai, Y.; Yamada, S.; Uehara, H.; Tosha, T.; Sugimoto, H.; Shiro, Y.; Stanfield, J. K.; Ogawa, K.; Watanabe, Y.; Shoji, O. *ACS Chem. Biol.* **2019**, *14*, 1637–1642. (d) Sakakibara, E.; Shisaka, Y.; Onoda, H.; Koga, D.; Xu, N.; Ono, T.; Hisaeda, Y.; Sugimoto, H.; Shiro, Y.; Watanabe, Y.; Shoji, O. *RSC Adv.* **2019**, *9*, 18697–18702.
10. (a) Saito, S.; Itano, H. A. *J. Chem. Soc. Perkin Trans. 1* **1987**, 1183–1188. (b) Balch, A. L.; Latos-Grażyński, L.; Noll, B. C.; Olmstead, M. M.; Safari, N. *J. Am. Chem. Soc.* **1993**, *115*, 9056–9061. (c) Balch, A. L.; Mazzanti, M.; St. Claire, T. N.; Olmstead, M. M. *Inorg. Chem.* **1995**, *34*, 2194–2200.
11. (a) Hempenius, M. A.; Koek, J. H.; Lugtenburg, J.; Fokkens, R. *Recl. Trav. Chim. Pays-Bas*

- 1987**, *106*, 105–112. (b) Lord, P. A.; Noll, B. C.; Olmstead, M. M.; Balch, A. L. *J. Am. Chem. Soc.* **2001**, *123*, 10554–10559. (c) Kakeya, K.; Nakagawa, A.; Mizutani, T.; Hitomi, Y.; Kodera, M. *J. Org. Chem.* **2012**, *77*, 6510–6519.
12. Krieg, S.; Huche, F.; Diederichs, K.; Izadi-Pruneyre, N.; Lecroisey, A.; Wandersman, C.; Delepelaire, P.; Welte, W. *Proc. Natl. Acad. Sci. USA* **2009**, *106*, 1045–1050.
13. Jumper, J.; Evans, R.; Pritzel, A.; Green, T.; Figurnov, M.; Ronneberger, O.; Tunyasuvunakool, K.; Bates, R.; Židek, A.; Potapenko, A.; Bridgland, A.; Meyer, C.; Kohl, S. A. A.; Ballard, A. J.; Cowie, A.; Romera-Paredes, B.; Nikolov, S.; Jain, R.; Adler, J.; Back, T.; Petersen, S.; Reiman, D.; Clancy, E.; Zielinski, M.; Steinegger, M.; Pacholska, M.; Berghammer, T.; Bodenstein, S.; Silver, D.; Vinyals, O.; Senior, A. W.; Kavukcuoglu, K.; Kohli, P.; Hassabis, D. *Nature*, **2021**, *596*, 583–589.
14. Kataoka, H.; Ida, T.; Ishii, Y.; Tateda, K.; Oguri, T.; Yoshida, A.; Okuzumi, K.; Oishi, T.; Tsukahara, M.; Mori, S.; Yoneyama, A.; Araoka, H.; Mitsuda, T.; Sumitomo, M.; Moriya, K.; Goto, M.; Nakamori, Y.; Shibayama, A.; Ohmagari, N.; Sato, T.; Yamaguchi, K. *J. Glob. Antimicrob. Resist.* **2013**, *1*, 91–96.
15. For the global priority list of antibiotic-resistant bacteria to guide research, discovery, and development of new antibiotics, see: World Health Organization, 2017. https://www.who.int/medicines/publications/WHO-PPL-Short_Summary_25Feb-ET_NM_WHO.pdf (accessed January 18, 2022).

Chapter 7

Summary of This Thesis

This thesis described the synthesis and functions of heteroporphyrinium cations. The author explored their functions by focusing on the effect of the cationic charge.

From Chapter 2 to Chapter 4, the author synthesized oxa-, thia-, and azaporphyrinium cations to reveal their properties. In Chapter 2, the synthesis of oxaporphyrinium cations was described. The author adopted bilindione as a key precursor and synthesized oxaporphyrinium cations via dehydration condensation by trifluoromethanesulfonic anhydride. The delocalized cationic charge stabilized the *cis*-form of inner-NH protons; meanwhile, regular porphyrins generally prefer *trans*-form to avoid the steric hindrance in the inner cavity. The oxaporphyrinium cation exhibited the dual-emission derived from *cis*- and *trans*-tautomers. Chapter 3 disclosed the synthesis of thiaporphyrinium cations and the excited state dynamics in comparison with oxaporphyrinium cations. Detailed photophysical measurements of the thiaporphyrinium cations elucidated their ultrafast nonradiative deactivation. The rate constant calculations disclosed the major decay pathway of thiaporphyrinium cations was the internal conversion, while that of oxaporphyrinium cations was the intersystem crossing to the T₂ state and the radiative deactivation. The insertion of sulfur caused out-of-plane vibrational motion, resulting in the short lifetime of the excited states. In Chapter 4, the synthesis and unique tautomerization of the azaporphyrinium cation was demonstrated. The azaporphyrinium cation was synthesized by cyclization of 1-oxo-19-(phenylamino)-bilin. Single-crystal X-ray analysis revealed the inner cavity of the azaporphyrinium cation was strained to a rectangle due to the steric repulsion between the *N*-phenyl substituent and β -ethyl substituents. The rectangular inner cavity lowered the activation barrier of proton migration in the short axis direction.

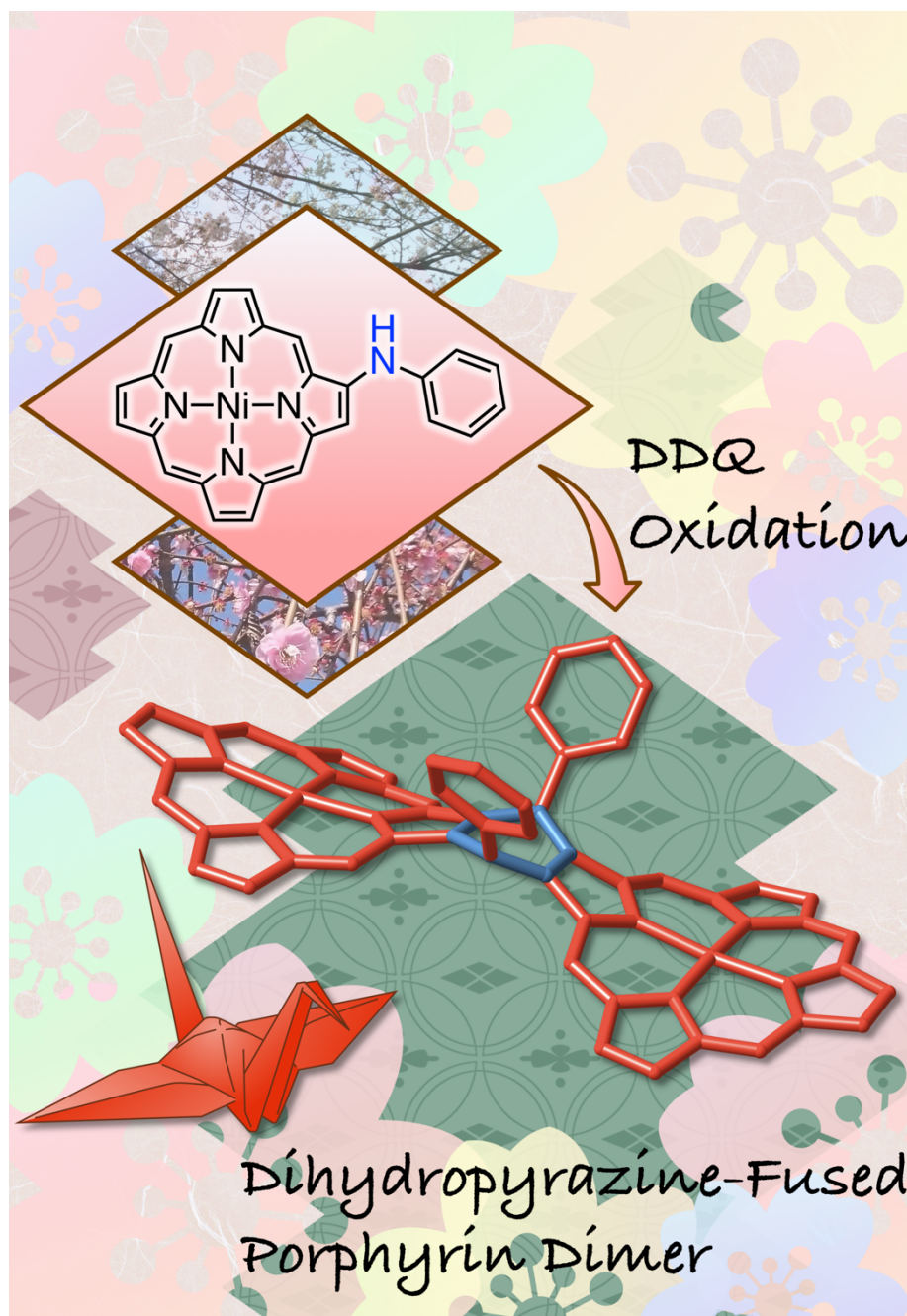
Chapters 5 and 6 focused on the utilization of the cationic charge of oxaporphyrinium cations. The introduction of the cationic charge into the porphyrinic skeleton induced charge delocalization and enhanced the electron acceptability. In Chapter 5, ion-pairing assembly of

various metal oxaporphyrinium cations with pentacyanocyclopentadienide was investigated. X-ray crystallography visualized various packing structures depending on the inner metals of the oxaporphyrinium cations. The energy decomposition analysis clarified that the different morphology originated from electrostatic and dispersion forces. The charge delocalization played an essential role in the interactions. Chapter 6 described the heme-acquisition protein HasA reconstructed with the cobalt oxaporphyrinium cation. The biological activity was investigated to demonstrate that the reconstructed HasA exhibited strong growth-inhibition ability against *P. aeruginosa* owing to the cationic charge incorporated into the porphyrin, which intensified the binding to the HasA-specific receptor HasR. The growth-inhibition activity was also valid for multidrug-resistant *P. aeruginosa*.

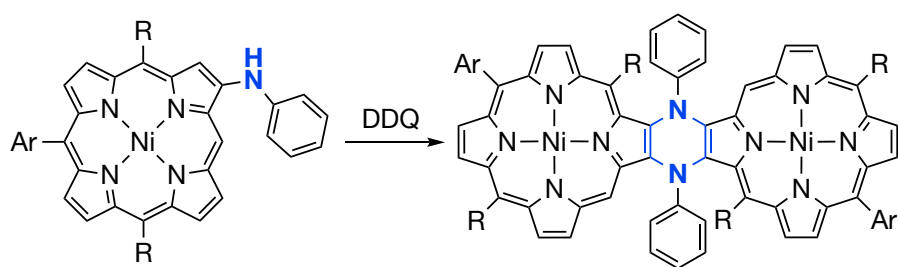
Through this thesis, the author shed light on the profound chemistry of heteroporphyrinium cations and elicited novel functions that stemmed from the cationic charge. These findings manifest the potentials of heteroatom-embedded charged porphyrins. Furthermore, the author expects the present results to promote the development of functional materials or bio-active molecules with electronic modulations induced by heteroatoms.

Appendix 1

Synthesis of Dihydropyrazine-Fused Porphyrin Dimers



Selected as the Inside Cover.



Contents

A1-1. Introduction	83
A1-2. Synthesis.....	84
A1-3. Structure analysis	85
A1-4. Electronic structure	86
A1-5. Summary of Appendix 1	87
A1-6. References	88

A1-1. Introduction

Dihydrophenazine is a reduced form of phenazine. The electron rich nature of dihydrophenazines has been applied to charge-transporting layers in solar-cells and semi-conducting materials.^{1,2} Recently, *N,N'*-diaryldihydrophenazines have regained the spotlight due to their intriguing stimuli-responsive properties.³ However, their limited synthesis has hampered further investigations of their fundamental characteristics.⁴ The conventional synthesis of dihydrophenazines often requires strongly basic conditions using organolithium reagents or high temperature process, both of which do not allow the incorporation of most of functional dye units.⁵ Shinokubo group has discovered that oxidation of *N*-aryl substituted aminoanthracenes produced *N,N'*-diaryl substituted dihydropyrazine-fused anthracene dimers **A1-1** in a one-step operation (Figure A1-1).⁶ In addition, their reversible conformational change upon electrochemical and chemical redox processes has been disclosed. Because this oxidative fusion reaction proceeds under neutral conditions at room temperature, the author expected that the methodology should be applied to the synthesis of π -extended dihydrophenazines containing functional dyes motifs. In this chapter, the author has succeeded in the synthesis of π -extended dihydrophenazines **A1-2** with two porphyrin units.

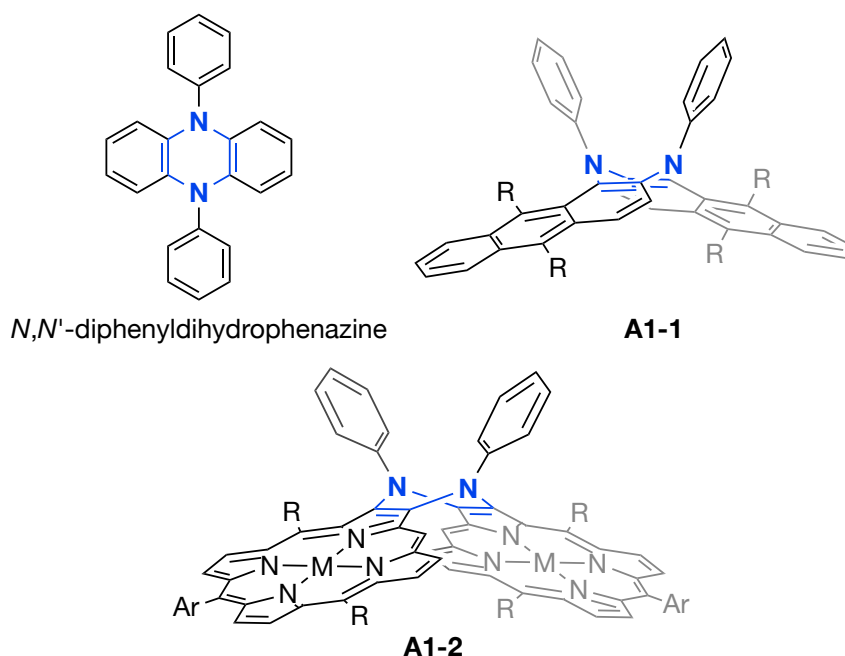
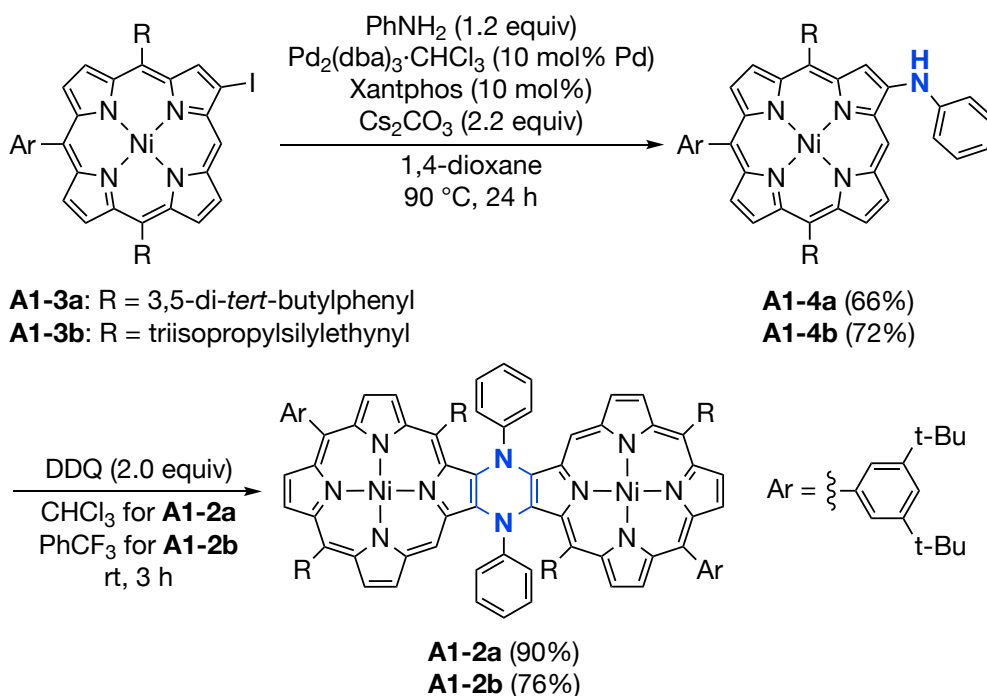


Figure A1-1. *N,N'*-Diphenyldihydrophenazines and π -extended dihydrophenazines.

A1-2. Synthesis

The synthesis started from preparation of amino-substituted porphyrin derivatives (Scheme A1-1). First, 2-(*N*-phenyl)amino-5,10,15-tris(3,5-di-*tert*-butylphenyl)porphyrin Ni(II) (**A1-4a**) was prepared as a precursor. Aminoporphyrin **A1-4a** was synthesized by palladium-catalyzed cross-coupling of **A1-3a** with aniline in 66% yield. Then, **A1-4a** was subjected to the oxidation reaction with DDQ (2.0 equiv), producing the corresponding dimer **A1-2a** in 90% yield. Its dimeric structure was confirmed by its high-resolution mass spectrum at $m/z = 2039.0440$. The ^1H NMR spectrum of **A1-2a** at room temperature contained several broadened peaks, which became sharp to be assignable as the temperature decreased. The spectrum appeared C_2 symmetrical feature, showing six kinds of β -protons and one *meso*-proton in the aromatic region. Disappearance of the singlet peak due to the β -proton adjacent to the amino group observed in **A1-4a** indicates the successful formations of intermolecular C–N bonds at these positions. The presence of more than three kinds of *ortho* protons due to *meso*-aryl groups suggests the non-planar structure of **A1-2a**. In addition, one of these signals shifted to the upper field (7.37 ppm) than others (7.84–8.38 ppm), indicating the presence of shielding effect from adjacent porphyrin unit.



Scheme A1-1. Synthesis of dihydropyrazine-fused porphyrin dimers **A1-2**.

The author also synthesized another diporphyrin **A1-2b** with triisopropylsilylethynyl substituents at *meso*-positions. In this case, the oxidative dimerization under the same conditions as **A1-2a** resulted in 44% yield. However, the use of α,α,α -trifluorotoluene as a solvent improved the yield of **A1-2b** to 76% yield.⁷

A1-3. Structure analysis

The structure of **A1-2a** was unambiguously elucidated by single crystal X-ray diffraction analysis. Figure A1-2 displays the crystal structure of **A1-2a**. As analyzed by the NMR spectroscopy, **A1-2a** exhibited a non-planar, saddle-shaped conformation in crystal.⁸ The dihedral angle consisted of two pyrrole units proximal to the dihydropyrazine unit was 145° . The smaller angle sum around the central nitrogen atoms ($344^\circ/350^\circ$) than 360° indicates sp^3 configuration of the nitrogen atoms of the dihydropyrazine ring. The central dihydropyrazine unit adopts a boat-like conformation. The average bond length of C–N bonds in the central dihydropyrazine unit was 1.42 Å, which is slightly shorter than the standard $C(sp^2)$ – $N(sp^3)$ bond. Each porphyrin unit forms a ruffle conformation as observed in common Ni(II) porphyrin complexes. The deviations from a mean plane consisted of carbon and nitrogen atoms of the main skeleton without aryl substituents were 0.311 and 0.336 Å.

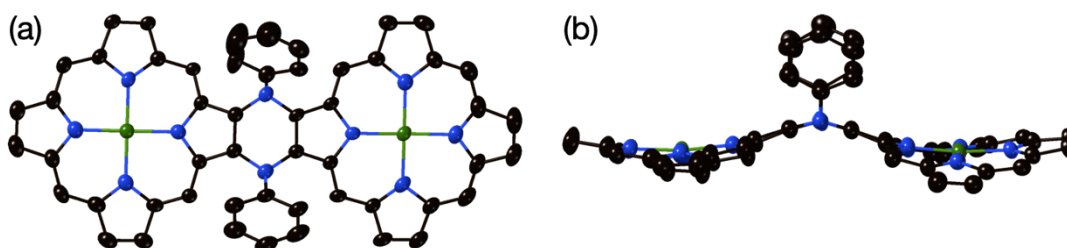


Figure A1-2. (a) Top and (b) side views of X-ray crystal structure of **A1-2a**. The thermal ellipsoids are scaled at 50% probability level. Hydrogen atoms and *meso*-aryl substituents are omitted for clarity.

A1-4. Electronic structure

Figure A1-3 shows UV/Vis absorption spectra of **A1-2a**, **A1-2b**, **A1-4a**, and **A1-4b** in dichloromethane. The Soret-band of **A1-2a** and **A1-2b** is split due to exciton coupling as often observed in closely arranged porphyrin dimers. Compared to **A1-4a**, the lowest energy band of **A1-2a** was slightly blue-shifted. The similar tendency was observed for **A1-2b** and **A1-4b**. To gain further insight on electronic structures of the dimers, electrochemical measurements were performed. The redox potentials were measured by CV and DPV. The results are summarized in Table A1-1. Both oxidation and reduction waves for the dimers were irreversible. The irreversibility suggests their dynamic motion under electrochemical conditions as anthracene-based dihydrophenazine reported previously.^{6b} The first oxidation potential of **A1-2b** was higher than that of **A1-2a**, reflecting the electron-withdrawing nature of ethynyl substituents. The gaps between the first oxidation and reduction potentials of the dimers were almost equal or smaller than those for the corresponding monomers. For **A1-2b**, the shift of the first reduction potential from **A1-4b** was relatively larger than that of the oxidation potentials, indicating the effect of electron-donating ability of the dihydrophenazine nitrogen atoms to the porphyrin units became weak upon dimerization.

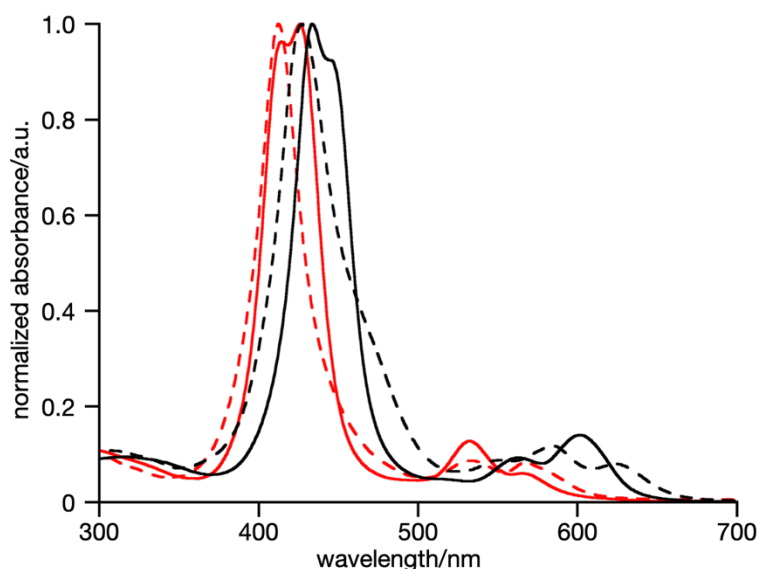


Figure A1-3. UV/Vis absorption spectra of **A1-4a** (red, dashed), **A1-4b** (black, dashed), **A1-2a** (red, solid), and **A1-2b** (black, solid). All spectra were recorded in dichloromethane.

Table A1-1. Summarized redox potentials of **A1-2a**, **A1-2b**, **A1-4a**, and **A1-4b**.

	E_{ox}^1	E_{red}^1	ΔE^b	ΔE_{opt}^c
A1-4a	0.247	−1.80	2.05	2.18
A1-4b	0.362	−1.56	1.92	1.98
A1-2a	0.257	−1.80	2.02	2.19
A1-2b	0.324	−1.47	1.79	2.06

^a Potentials versus ferrocene/ferrocenium cation couple. ^b $\Delta E = E_{\text{ox}}^1 - E_{\text{red}}^1$. ^c Calculated from electronic absorption spectral analysis.

Theoretical calculations by the DFT method were performed. The optimized geometry of **A1-2a** at the B3LYP/6-31G(d) level was almost identical to the experimental structure obtained by the X-ray analysis. LUMO of **A1-2a** was delocalized over the entire porphyrin units, while HOMO existed mainly on the central dihydropyrazine unit and the *N*-phenyl substituents. This result indicates the nitrogen atoms in **A1-2a** serve as an electron-acceptor due to their more electron negative nature than carbon atoms. This situation is in contrast with that of **A1-4a**, in which the nitrogen atom at the β -position works as an electron-donor due to its positive mesomeric effect. The simulated electronic absorption spectrum of **A1-2a** by the TD-DFT calculation revealed that the lowest energy transition is mainly contributed from HOMO–LUMO transition. This analysis is in good agreement with the experimental results: the lowest energy band of **A1-2a** or **A1-2b** appeared in the blue-shifted region compared to the corresponding monomers **A1-4a** or **A1-4b**.

A1-5. Summary of Appendix 1

In summary, the synthesis of dihydropyrazine-fused porphyrin dimers was achieved through oxidation of β -amino-substituted porphyrins. The saddle-like structure of the dimer was revealed by X-ray diffraction analysis. Optical measurements and theoretical calculations indicated the electronic effect of nitrogen atoms was switched from electron-donor to electron-withdrawer upon dimerization. The electrochemical study suggested that the dimers showed conformational change upon redox process. The present study demonstrated that the oxidative fusion reaction to construct π -extended dihydrophenazines is promising for the effective

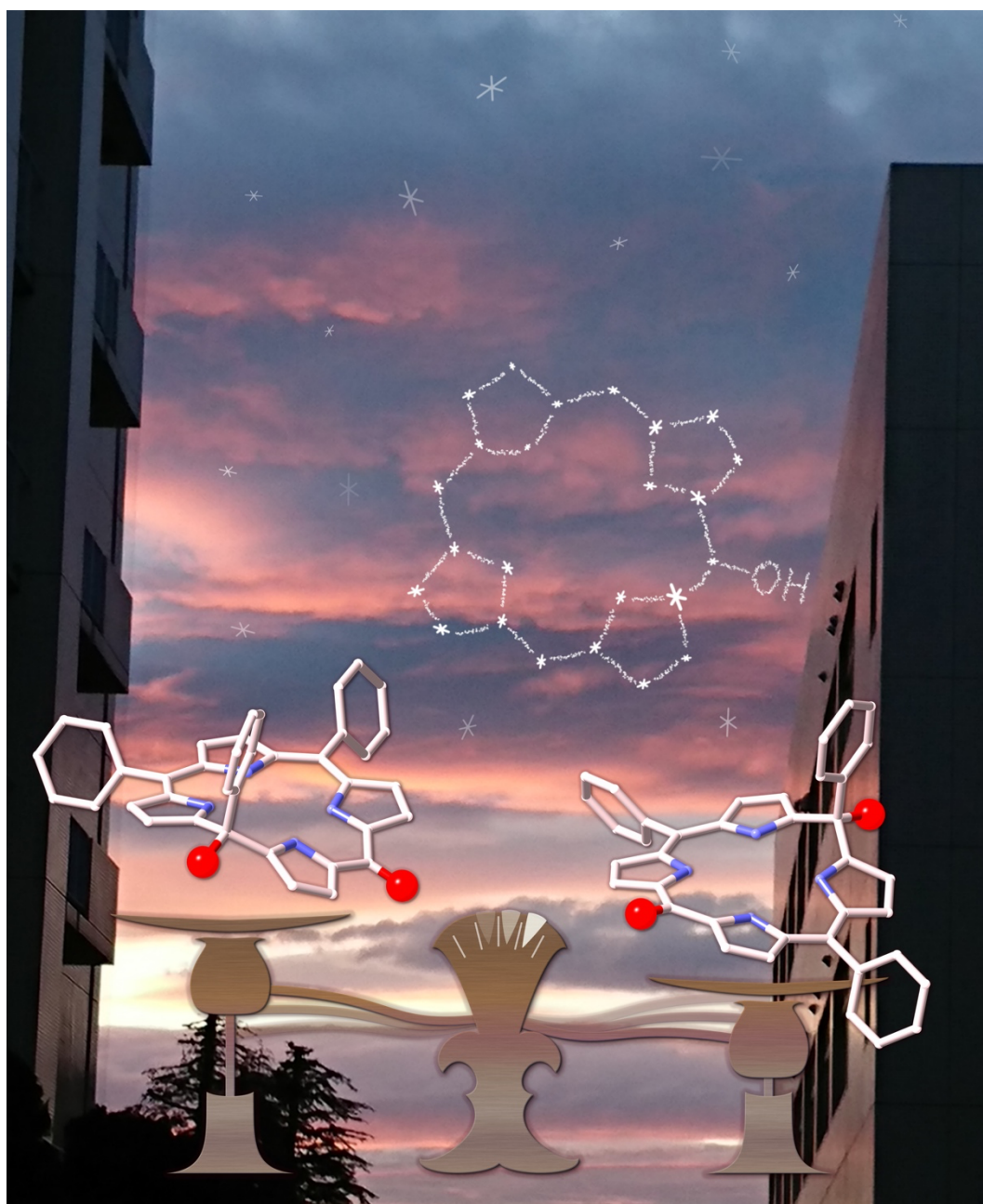
extension of other π -conjugated functional molecules.

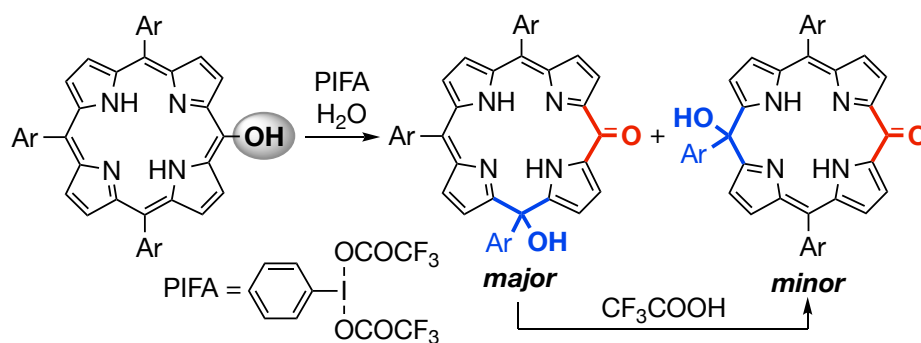
A1-6. References

1. Holzapfel, M.; Lambert, C.; Selinka, C.; Stalke, D. *J. Chem. Soc., Perkin Trans. 2* **2002**, 1553–1561.
2. (a) Lee, J.; Shizu, K.; Tanaka, H.; Nakanotani, H.; Yasuda, T.; Kaji, H.; Adachi, J. *Mater. Chem. C* **2015**, *3*, 2175–2181. (b) Huang, W.; Sun, L.; Zheng, Z.; Su, J.; Tian, H. *Chem. Commun.* **2015**, *51*, 4462–4464.
3. (a) Humeniuk, H. V.; Rosspeintner, A.; Licari, G.; Kilin, V.; Bonacina, L.; Vauthey, E.; Sakai, N.; Matile, S. *Angew. Chem. Int. Ed.* **2018**, *57*, 10559–10563. (b) Li, Y.; Shi, L.; Zhang, Y.; Sun, G.; Sun, L.; Su, J. *Dyes Pigm.* **2019**, *160*, 794–798.
4. (a) Bettinetti, G. F.; Maffei, S.; Pietra, S. *Synthesis* **1976**, 748–749. (b) Okamoto, T.; Terada, E.; Kozaki, M.; Uchida, M.; Kikukawa, S.; Okada, K. *Org. Lett.* **2003**, *5*, 373–376.
5. Wang, H.; Zhang, Z.; Zhou, H.; Wang, T.; Su, J.; Tong, X.; Tian, H. *Chem. Commun.* **2016**, *52*, 5459–5462.
6. (a) Hiroto, S. *Bull. Chem. Soc. Jpn.* **2018**, *91*, 829–838. (b) Nagasaki, J.; Hiroto, S.; Shinokubo, H. *Chem. Asian. J.* **2017**, *12*, 2311–2317.
7. Ito, S.; Hiroto, S.; Lee, S.; Son, M.; Hisaki, I.; Yoshida, T.; Kim, D.; Kobayashi, N.; Shinokubo, H. *J. Am. Chem. Soc.* **2015**, *137*, 142–145.
8. The similar conformation has been reported for gable-like porphyrins: (a) Uno, H.; Nakamoto, K.; Kuroki, K.; Fujimoto, A.; Ono, N. *Chem. Eur. J.* **2007**, *13*, 5773–5784. (b) Uoyama, H.; Kim, K. S.; Kuroki, K.; Shin, J.-Y.; Nagata, T.; Okujima, T.; Yamada, H.; Ono, N.; Kim, D.; Uno, H. *Chem. Eur. J.* **2010**, *16*, 4063–4074.

Appendix 2

Synthesis of Hydroxyisooxophlorins by Oxidative Degradation of *meso*-Hydroxyporphyrins





Contents

A2-1. Introduction	91
A2-2. Oxidation of <i>meso</i> -hydroxyporphyrins with PIFA.....	92
A2-3. Mechanistic study.....	93
A2-4. Metalation and physical properties	95
A2-5. Summary of Appendix 2	97
A2-6. References	98

A2-1. Introduction

Studies on oxidation of *meso*-hydroxyporphyrins have been encouraged by their biological importance because heme catabolism proceeds through *meso*-hydroxylation of its porphyrin skeleton.¹ Degradation of hemes in biological systems yields various oligopyrrolic endogenous pigments such as verdoheme, biliverdin, and bilirubin. The synthetic procedures to provide these pigments have been well-established.^{2,3} Furthermore, recent studies demonstrated that porphyrin *meso*-oxy radicals generated by hydrogen abstraction of *meso*-hydroxyporphyrins were remarkably stable under ambient conditions in spite of their open-shell character.^{3,4}

In 1997, Smith *et al.* examined the stability of *meso*-oxy radical **A2-1** in light of the steric effect at the 15-position (Figure A2-1).^{5b} They reported that the radical **A2-1** was fairly stable under ambient conditions but slowly underwent oxidative degradation after storage for 2 weeks in solution to form 15-hydroxy-15-iso-5-oxophlorin **A2-2**. Oxophlorin is a keto-form of hydroxyporphyrin and isooxophlorin is a tautomer of oxophlorin (Figure A2-2). Recently, Osuka and co-workers reported that 5-hydroxy-10,15,20-triarylporphyrins **A2-3** were oxidized with PbO₂ to generate the corresponding *meso*-oxy radicals **A2-4** as stable species.^{5d} They also conducted further oxidation of **A2-4** with tris(4-bromophenyl)aminium hexachloroantimonate to obtain the single-electron oxidized species, oxophlorin cations **A2-5**. However, the reactivity of oxophlorin cations **A2-5** has been scarcely examined. In this chapter, the author describes that oxidation of free-base *meso*-hydroxyporphyrin **A2-3a** with phenyliodine(III) bis(trifluoroacetate) (PIFA) in the presence of H₂O provided 15-hydroxy-15-iso-5-oxophlorin **A2-7a** and its regioisomer **A2-6a**. The mechanistic study suggested that oxophlorin cation **A2-10a** was a plausible intermediate. Furthermore, the metal complexation, acid-mediated isomerization of **A2-6a** to **A2-7a**, and physical properties of thus obtained hydroxyisooxophlorins were also examined.

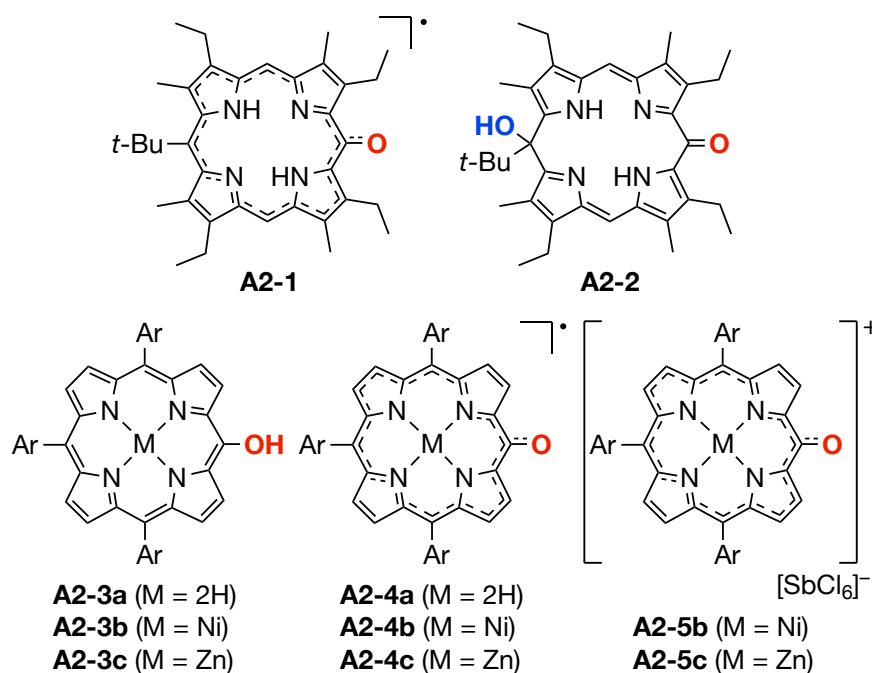


Figure A2-1. Structures of *meso*-hydroxyporphyrin and oxidized species **A2-1**–**A2-5**.

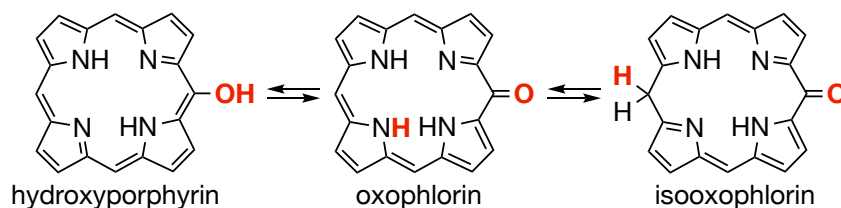


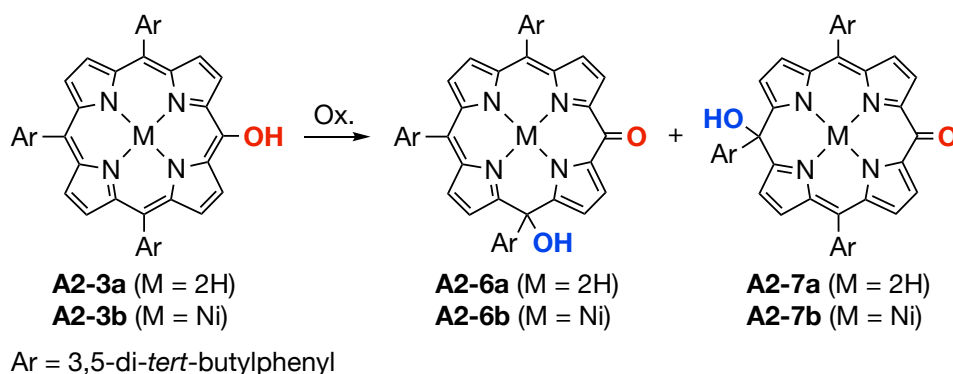
Figure A2-2. Tautomerization of *meso*-hydroxyporphyrin.

A2-2. Oxidation of *meso*-hydroxyporphyrins with PIFA

5-Hydroxy-10,15,20-triarylporphyrins **3**^{5d,6} were treated with PIFA (1.0 equiv) and an excess amount of H₂O in dichloromethane at room temperature (Table A2-1). In entry 1, the reaction of free-base porphyrin **A2-3a** for 30 min afforded 10-hydroxy-10-iso-5-oxophlorin **A2-6a** and 15-hydroxy-15-iso-5-oxophlorin **A2-7a** in 43% and 22% yields, respectively. Extension of the reaction time to 4 h increased the amount of **A2-7a** along with the decrease of **A2-6a** (entry 2). These results imply that **A2-6a** gradually isomerized to **A2-7a** during the reaction. The author realized that this isomerization was promoted by in situ generated TFA (vide infra). Then, the reactions in the presence of K₂CO₃ were conducted (entries 3 and 4). The isomerization was fully

suppressed to afford **A2-6a** and **A2-7a** in the ratio of ca. 2:1. The reaction of *meso*-hydroxyporphyrin nickel(II) complex **A2-3b** generated the corresponding nickel(II) complex **A2-7b** in a relatively low yield as a sole isolable product (entry 5).

Table A2-1. Oxidation of 5-hydroxyporphyrins **A2-3** with PIFA in the presence of H₂O.^a



entry	A2-3	K ₂ CO ₃ (equiv)	time (h)	yield (%)	
				A2-6	A2-7
1	A2-3a	–	0.5	43 (47)	22 (27)
2	A2-3a	–	4	36 (36)	29 (35)
3	A2-3a	5.0	0.5	55 (50)	27 (25)
4	A2-3a	5.0	4	48 (43)	26 (19)
5	A2-3b	5.0	0.5	–	16 (11)

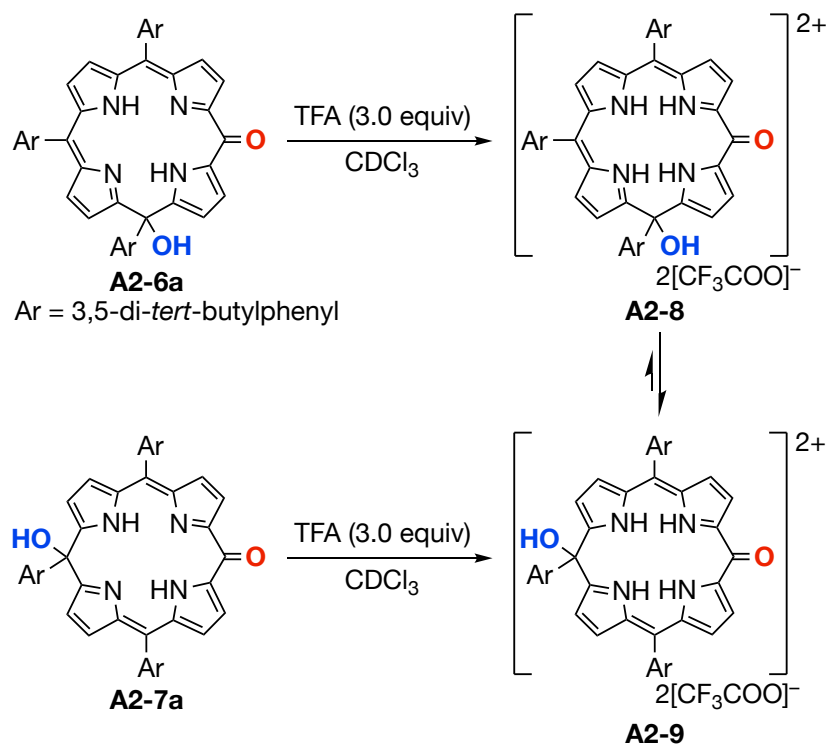
^a Conditions: 1) PIFA (1.0 equiv), K₂CO₃, H₂O (11 equiv), dichloromethane, rt; 2) sat. NaHCO₃ aq.

^b Isolated yields. Yields determined by ¹H NMR spectroscopy from the crude reaction mixture are shown in parentheses.

A2-3. Mechanistic study

The author examined the effect of TFA on the isomerization of 10-hydroxy-10-iso-5-oxophlorin **A2-6a** to 15-hydroxy-15-iso-5-oxophlorin **A2-7a** (Scheme A2-1). TFA was gradually added to a CDCl₃ solution of **A2-6a** with monitoring the ¹H NMR spectral change. Upon addition of 3.0 equiv of TFA, the spectral change was completed. The resulting ¹H NMR spectrum exhibited a low-symmetric spectral pattern with characteristic signals due to the inner NH protons in the range of 12–16 ppm.⁷ These downfield-shifted signals correspond to inner NH protons, indicating that protonation proceeded at the inner imine-type nitrogen atoms to produce

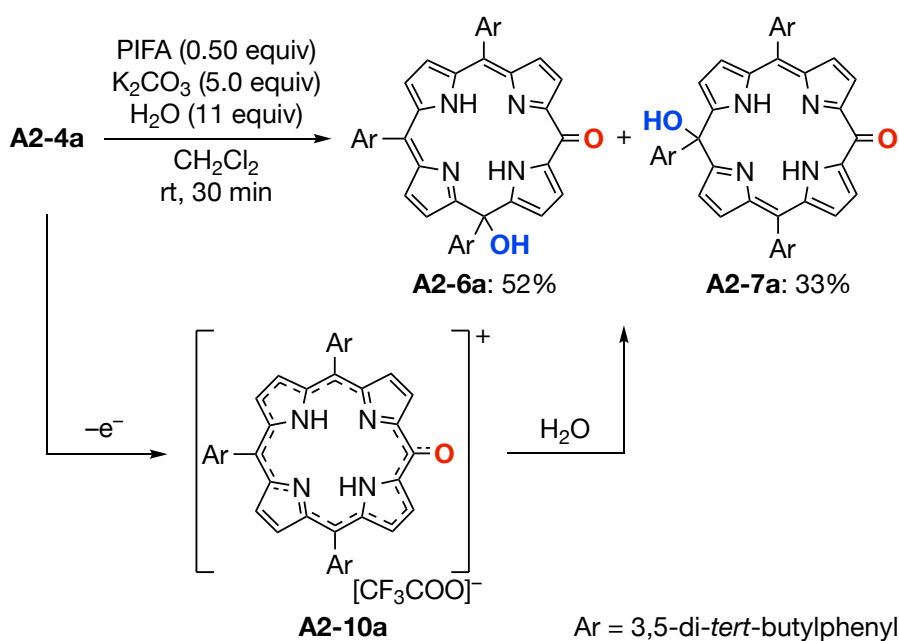
diprotonated species **A2-8**. Generation of an oxophlorin cation was not observed. The addition of TFA to a CDCl_3 solution of **A2-7a** also caused a similar spectral change, supporting the generation of diprotonated species **A2-9**. Importantly, the ^1H NMR spectrum of **A2-8** gradually changed to that of **A2-9** at room temperature. Such a spectral change was not observed in the absence of TFA. These results demonstrate that TFA induced the isomerization of kinetic product **A2-6a** to thermodynamically more stable product **A2-7a**. The total energies of diprotonated species **A2-8** and **A2-9** were calculated by the DFT method using the *Gaussian 09* software package at the CAM-B3LYP/6-31G(d,p) level. The calculations predict that **A2-9** is thermodynamically more stable than **A2-8** by 7.6 kcal/mol, which is in good agreement with the experimental results.



Scheme A2-1. Protonation of **A2-6a** and **A2-7a** with TFA.

To find a clue on the mechanism, *meso*-oxy radical **A2-4a** was subjected to the oxidation with PIFA (0.5 equiv) in the presence of H_2O and K_2CO_3 (Scheme A2-2). The reaction provided **A2-6a** and **A2-7a** in 52% and 33% yields, respectively, as is the case of oxidation of *meso*-hydroxyporphyrins **A2-3a**. This result implies that oxy radical **A2-4a** is a plausible intermediate. Accordingly, the author proposes the following mechanism. PIFA oxidizes **A2-3a** by one electron to produce its radical cation, which undergoes deprotonation to form *meso*-oxy radical **A2-4a**

along with TFA.⁸ The second single-electron oxidation of **A2-4a** produces the corresponding oxophlorin cation **A2-10a**, which is hydrated to afford **A2-6a** and **A2-7a**. The author also examined the oxidation of **A2-3a** with PIFA in the absence of H₂O. However, the reaction afforded a complex mixture of unidentifiable species probably because of the degradation of oxophlorin cation **A2-10a**. A similar result was reported by Osuka and co-workers on oxidation of **A2-3a** with tris(4-bromophenyl)aminium hexachloroantimonate.^{5d}

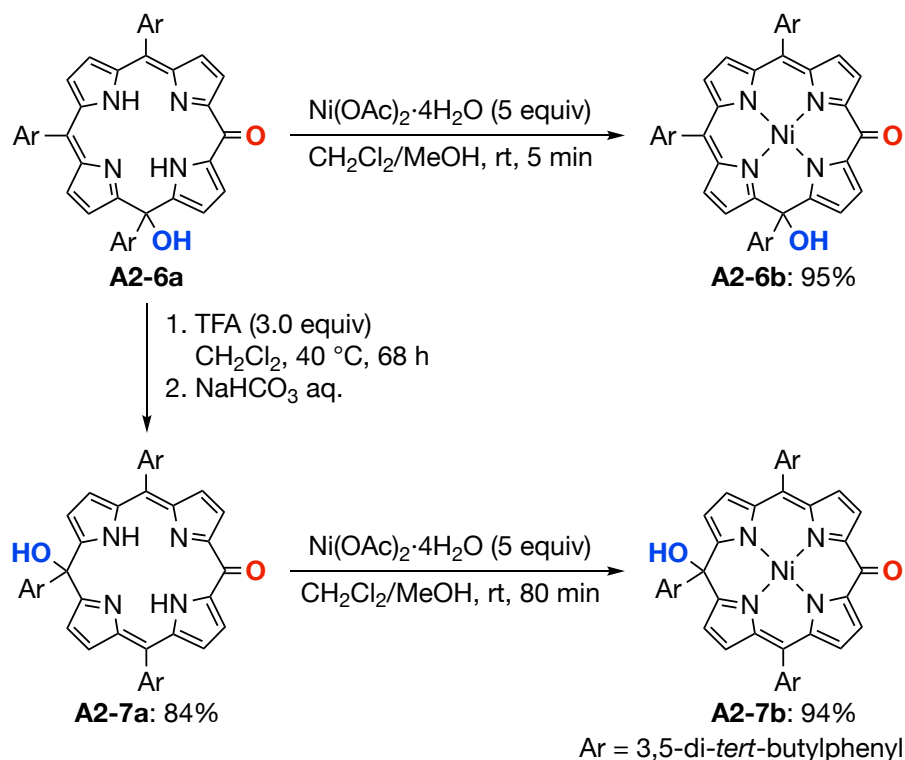


Scheme A2-2. Oxidation of free-base porphyrin *meso*-oxy radical **A2-4a** with PIFA in the presence of H₂O.

A2-4. Metalation and physical properties

With a synthetic protocol for **A2-6a** in hand (Table A2-1, entry 3), the conversions of **6a** were examined (Scheme A2-3). Treatment of **A2-6a** with Ni(OAc)₂·4H₂O provided the corresponding nickel(II) complex **A2-6b** in 95% yield. It is worth noting that **A2-6b** was not directly produced from *meso*-hydroxyporphyrin nickel(II) complex **A2-3b** (Table A2-1, entry 5). Furthermore, treatment of **A2-6a** with TFA followed by neutralization afforded **A2-7a** in 84% yield. The metal complexation of **A2-7a** with Ni(OAc)₂·4H₂O also furnished **A2-7b** in 94%. Nickel(II)-metalation of **A2-6a** and **A2-7a** was monitored by TLC analysis, respectively, indicating that the former proceeded more facile than the latter. DFT calculations suggested that

the structure of **A2-6a** is more distorted than that of **A2-7a**. The structural distortion would facilitate metalation of the central cavity of **A2-6a**. The stepwise route from **A2-6a** to **A2-7b** is more efficient than the direct oxidation of nickel(II) complex **A2-3b** to **A2-7b**. Although the complexation of **A2-7a** with $\text{Zn}(\text{OAc})_2 \cdot 2\text{H}_2\text{O}$ afforded the corresponding zinc(II) complex, the product underwent decomposition during the work-up processes.



Scheme A2-3. Conversions of free-base 10-hydroxy-10-iso-5-oxophlorin **A2-6a**.

The properties of 10-hydroxy-10-iso-5-oxophlorins **A2-6** and 15-hydroxy-15-iso-5-oxophlorins **A2-7** were examined by NMR and UV/Vis/NIR absorption spectroscopies as well as DFT calculations. The ^1H NMR spectra of free-bases **A2-6a** and **A2-7a** exhibited the signals due to the β -protons around 6–7 ppm, which are apparently downfield-shifted from those of porphyrin (8–9 ppm). In addition, the signals due to the inner NH protons were observed in the significantly upfield-shifted region (12–14 ppm). These results suggest the disruption of the aromatic macrocyclic conjugation circuit of the original porphyrin skeleton.⁹ Figure A2-3 shows the UV/Vis/NIR absorption spectra of **A2-6a**, **A2-6b**, **A2-7a**, and **A2-7b**. Free-base 10-hydroxy-10-iso-5-oxophlorin **A2-6a** displayed a relatively sharp absorption at 387 nm and broad absorption bands around 600 nm. This spectral feature resembles that of tripyrrin.¹⁰ Consequently, we

understand that the electronic structure of **A2-6a** is dominated by the tripyrrin unit. This assumption has been supported by the DFT calculation of **A2-6a**, in which the frontier orbitals are mainly delocalized on the tripyrrin unit. On the other hand, 15-hydroxy-15-iso-5-oxophlorin **A2-7a** exhibited intense absorption bands at 418 nm and weak absorption bands around 580 nm. The latter weak absorption bands were not observed for simple dipyrins.¹¹ The DFT calculation of **A2-7a** suggested that the two dipyrin units of **A2-7a** were electronically interacted with each other through the carbonyl linker, which explains the observed low-energy absorption. The UV/Vis/NIR absorption spectra of nickel(II) complexes **A2-6b** and **A2-7b** are significantly red-shifted from those of **A2-6a** and **A2-7a**. This feature shows their potential utility as functional dyes such as NIR-absorbing dyes and metal ion sensors.

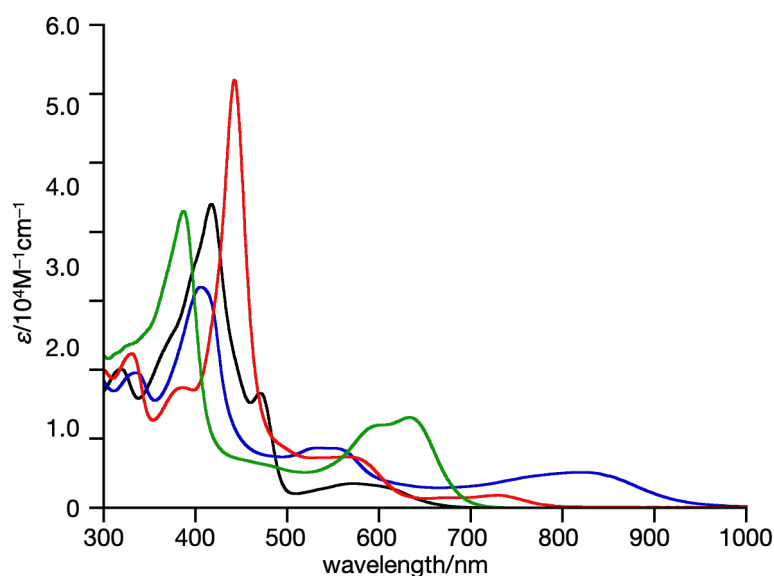


Figure A2-3. UV/Vis/NIR absorption spectra of **A2-6a** (green), **A2-6b** (blue), **A2-7a** (black), and **A2-7b** (red) in dichloromethane.

A2-5. Summary of Appendix 2

In summary, oxidation of free-base *meso*-hydroxyporphyrin **A2-3a** with PIFA in the presence of H₂O afforded 10-hydroxy-10-iso-5-oxophlorin **A2-6a** and 15-hydroxy-15-iso-5-oxophlorin **A2-7a** as major and minor products, respectively. The mechanistic studies suggested that PIFA serves as a single-electron oxidant toward **A2-3a** to afford oxophlorin cation **A2-10a**, which is hydrated to **A2-6a** and **A2-7a**. The author revealed acid-mediated isomerization of **A2-**

6a to **A2-7a** and metalation of **A2-6a** and **A2-7a** to their nickel(II) complexes. The properties of 10-hydroxy-10-iso-5-oxophlorins **A2-6** and 15-hydroxy-15-iso-5-oxophlorins **A2-7** were examined by NMR and UV/Vis/NIR absorption spectroscopies as well as DFT calculations. The electronic structures of **A2-6** were dominated by its tripyrrin unit, while the two dipyrin units of **A2-7** were conjugated with each other through the carbonyl linkage.

A2-6. References

1. (a) Ortiz de Montellano, P. R. *Acc. Chem. Res.* **1998**, *31*, 543–549. (b) Yoshida, T.; Migita, C. T. *J. Inorg. Biochem.* **2000**, *82*, 33–41. (c) Ortiz de Montellano, P. R.; Wilks, A. A. *Adv. Inorg. Chem.* **2000**, *51*, 359–407.
2. Reviews on oxidative degradation of *meso*-hydroxyporphyrins: (a) Balch, A. L. *Coord. Chem. Rev.* **2000**, *200–202*, 349–377. (b) Matano, Y. *Chem. Rev.* **2017**, *117*, 3138–3191.
3. (a) Jackson, A. H.; Kenner, G. W.; Smith, K. M. *J. Chem. Soc. C* **1968**, 302–310. (b) Fuhrhop, J.-H.; Besecke, S.; Subramanian, J.; Mengersen, C.; Riesner, D. *J. Am. Chem. Soc.* **1975**, *97*, 7141–7152. (c) Balch, A. L.; Noll, B. C.; Zovinka, E. P. *J. Am. Chem. Soc.* **1992**, *114*, 3380–3385. (d) Balch, A. L.; Noll, B. C.; Phillips, S. L.; Reid, S. M.; Zovinka, E. P. *Inorg. Chem.* **1993**, *32*, 4730–4736. (e) Balch, A. L.; Mazzanti, M.; Olmstead, M. M. *Inorg. Chem.* **1993**, *32*, 4737–4744. (f) Balch, A. L.; Latos-Grażyński, L.; Noll, B. C.; Olmstead, M. M.; Szterenber, L.; Safari, N. *J. Am. Chem. Soc.* **1993**, *115*, 1422–1429. (g) Balch, A. L.; Latos-Grażyński, L.; Noll, B. C.; Olmstead, M. M.; Safari, N. *J. Am. Chem. Soc.* **1993**, *115*, 9056–9061. (h) Khoury, R. G.; Jaquinod, L.; Nurco, D. J.; Smith, K. M. *Chem. Commun.* **1996**, 1143–1144. (i) Balch, A. L.; Koerner, R.; Latos-Grażyński, L.; Lewis, J. E.; St. Claire, T. N.; Zovinka, E. P. *Inorg. Chem.* **1997**, *36*, 3892–3897. (j) Yamashita, K.-i.; Hirano, D.; Asano, M. S.; Sugiura, K.-i. *Chem. Lett.* **2014**, *43*, 1049–1051.
4. Review on porphyrin-based stable organic radicals: Shimizu, D.; Osuka, A. *Chem. Sci.* **2018**, *9*, 1408–1423.
5. (a) Bonnett, R.; Dimsdale, M. J.; Sales, K. D. *Chem. Commun.* **1970**, 962–963. (b) Khoury, R. G.; Jaquinod, L.; Shachter, A. M.; Nelson, N. Y.; Smith, K. M. *Chem. Commun.* **1997**, 215–216. (c) Khoury, R. G.; Jaquinod, L.; Paolesse, R.; Smith, K. M. *Tetrahedron*, **1999**, *55*,

- 6713–6732. (d) Shimizu, D.; Oh, J.; Furukawa, K.; Kim, D.; Osuka, A. *J. Am. Chem. Soc.* **2015**, *137*, 15584–15594. (e) Esdaile, L. J.; Rintoul, L.; Goh, M. S.; Merahi, K.; Parizel, N.; Wellard, R. M.; Choua, S.; Arnold, D. P. *Chem. Eur. J.* **2016**, *22*, 3430–3446.
6. Esdaile, L. J.; Senge, M. O.; Arnold, D. P. *Chem. Commun.* **2006**, 4192–4194.
7. The chemical shifts of ^1H NMR signals due to the inner NH protons are comparable to those of protonated *meso*-aryl dipyrromethanes: Urieta, J.; Maroto, B. L.; Moreno, F.; Agarrabeitia, A. R.; Ortiz, M. J.; de la Moya, S. *RSC Adv.* **2015**, *5*, 68676–68680.
8. Kita and co-workers reported that PIFA worked as a single-electron oxidant: Kita, Y.; Tohma, H.; Hatanaka, K.; Takada, T.; Fujita, S.; Mitoh, S.; Sakurai, H.; Oka, S. *J. Am. Chem. Soc.* **1994**, *116*, 3684–3691.
9. (a) Johnson, A. W. *Pure Appl. Chem.* **1971**, *28*, 195–217. (b) Vogel, E. *Pure Appl. Chem.* **1993**, *65*, 143–152. (c) Vogel, E. *Pure Appl. Chem.* **1996**, *68*, 1355–1360. (d) Lash, T. D. *Chem. Rev.* **2017**, *117*, 2313–2446.
10. (a) Sessler, J. L.; Gebauer, A.; Král, V.; Lynch, V. *Inorg. Chem.* **1996**, *35*, 6636–6637. (b) Bröring, M.; Prikhodovski, S.; Brandt, C. D.; Tejero, E. C. *Chem. Eur. J.* **2007**, *13*, 396. (c) Bröring, M.; Prikhodovski, S.; Brandt, C. D.; Tejero, E. C.; Köhler, S. *Dalton Trans.* **2007**, 200–208. (d) Hung, C.-H.; Chang, G.-F.; Kumar, A.; Lin, G.-F.; Luo, L.-Y.; Ching, W.-M.; Diao, W.-G. *Chem. Commun.* **2008**, 978–980. (e) Gałęzowski, M.; Jaźwiński, J.; Lewtak, J. P.; Gryko, D. T. *J. Org. Chem.* **2009**, *74*, 5610–5613. (f) Wang, J.-F.; Yao, Y.; Ning, Y.; Meng, Y.-S.; Hou, C.-L.; Zhang, J.; Zhang, J.-L. *Org. Chem. Front.* **2018**, *5*, 1877–1885. (g) Umetani, M.; Tanaka, T.; Osuka, A. *Chem. Sci.* **2018**, *9*, 6853–6859.
11. (a) Stork, J. R.; Thoi, V. S.; Cohen, S. M. *Inorg. Chem.* **2007**, *46*, 11213–11223. (b) Shin, J.-Y.; Patrick, B. O.; Dolphin, D. *Org. Biomol. Chem.* **2009**, *7*, 2032–2035. (c) Yu, L.; Muthukumaran, K.; Sazanovich, I. V.; Kirmaier, C.; Hindin, E.; Diers, J. R.; Boyle, P. D.; Bocian, D. F.; Holten, D.; Lindsey, J. S. *Inorg. Chem.* **2003**, *42*, 6629–6647.

Experimental Section

Contents

E-1. Instruction and materials.....	100
E-2. Synthetic procedures and compounds data.....	101
E-3. Crystallographic data	118
E-4. References.....	125

E-1. Instruction and materials

^1H NMR (500 MHz), ^{13}C NMR (126 MHz), and ^{19}F NMR (471 MHz) spectra were recorded on a Bruker AVANCE III HD 500 spectrometer. Chemical shifts were reported as the delta scale in ppm relative to CHCl_3 ($\delta = 7.26$ ppm) for ^1H NMR, CDCl_3 ($\delta = 77.16$ ppm) for ^{13}C NMR, and benzotrifluoride ($\delta = -62.61$ ppm) and hexafluorobenzene ($\delta = -161.64$ ppm) for ^{19}F NMR. UV/Vis/NIR absorption spectra were recorded on a Shimadzu UV-2550 spectrometer, UV-2600 PC spectrophotometer (Shimadzu), and U-3310 spectrophotometer (Hitachi). Emission spectra were recorded on a JASCO FP-6500 spectrometer or JASCO FP-8500 spectrometer. Absolute fluorescence quantum yields were measured by the photon-counting method using an integration sphere. Absolute fluorescence quantum yields at 77 K were determined with a Hamamatsu Photonics C9920-03G calibrated integrating sphere system with A11238-01. Melting points were measured on a Stanford Research Systems OptiMelt MPA100. High-resolution atmospheric pressure chemical ionization time-of-flight (APCI-TOF) and electrospray ionization time-of-flight (ESI-TOF) mass spectra were taken on a Bruker microTOF instrument using a positive ionization mode and a negative ionization mode. The ESI-TOF mass spectrum of CoOEOP-HasA was recorded on a microTOF II (Bruker) using positive mode ESI-TOF method for protein solutions in 5 mM ammonium acetate buffer. X-ray data for oxaporphyrins were obtained using a Rigaku CCD diffractometer (Saturn 724 with MicroMax-007) with Varimax Mo optics and Bruker D8 QUEST X-ray diffractometer with an I μ S microfocus X-ray source and a PHOTON II detector. ESR spectra were recorded using an X-band (~ 9.6 GHz) spectrometer Bruker E500 spectrometer equipped with a gas-flow-type cryostat (Oxford-900) with 2.6 ϕ quartz sample tube. A TE₀₁₁ cylindrical cavity with a high quality factor was adopted for highly sensitive measurements. Cyclic voltammograms were recorded using an ALS electrochemical analyzer 612C. Measurements were performed in freshly distilled dichloromethane with tetrabutylammonium hexafluorophosphate (0.1 M) as the electrolyte. A three-electrode system

was used. The system consisted of a glassy carbon working electrode, a platinum wire, and Ag/AgClO₄ as the reference electrode. The scan rate was 100 mVs⁻¹. The measurement was performed under nitrogen atmosphere. All potentials are referenced to the potential of ferrocene/ferrocenium cation couple. All calculations except for the transition state structure at the excited state were carried out using the *Gaussian 09* software package.¹ Initial geometries for the calculations were obtained from the X-ray crystal structures. The ethyl substituents were replaced with hydrogen atoms or methyl substituents and the counter ion was not included to reduce the calculation cost. The calculations were performed using the density functional theory (DFT) method with restricted B3LYP² or CAM-B3LYP³ level, employing basis sets 6-31G(d), 6-31G(d,p), or 6-311+G(2d,p) for C, H, N, O, and S and SDD for Ni and Zn. The solvent effect (dichloromethane) was considered using the polarizable continuum model (PCM) method. The transition state structure at the ground states was obtained by the TS or QST2 method. For the calculation of the tautomerization process at the excited state, a rough transition state geometry was obtained using the *Reaction plus Pro* software package,³ based on the nudged elastic band (NEB) method.⁵ Then the transition state geometry was fully optimized using the *Gaussian 16* program.⁶ Zero-point energy and thermal energy corrections were conducted at the CAM-B3LYP/6-311+G(2d,p) level, and the sums of electronic and thermal free energies were obtained. The zero-point energies were not scaled, and the enthalpic corrections were made at 298.15 K. Preparative separations were performed by silica-gel column chromatography (Wakogel[®] C-300) and amino-functionalized silica-gel column chromatography (Fuji Silysia Chemical NH-DM1020). Dry dichloromethane was prepared by distillation from CaH₂. For reactions that require heating, the oil bath was used as the heat source. Unless otherwise noted, materials obtained from commercial suppliers were used without further purification.

E-2. Synthetic procedures and compounds data

Synthesis of 2,3,7,8,12,13,17,18-octaethyl-21*H*,23*H*,24*H*-bilin-1,19-dione 2-3

A round-bottomed flask containing **2-1**⁷ (1.3 g, 2.0 mmol), potassium cyanide (16 g, 0.24 mol), ascorbic acid (11 g, 60 mmol) was charged with methanol (1.0 L). The mixture was vigorously stirred at room temperature for 3 h. After evaporation, the resulting mixture was redissolved in dichloromethane, washed with water four times, and dried over anhydrous sodium sulfate. After removing dichloromethane in vacuo, ascorbic acid (0.70 g, 4.0 mmol), 1 M aqueous hydrochloric acid (80 mL), and acetone (400 mL) were added to the residue. The solution was stirred for 12 h at 50 °C. After removing acetone in vacuo, the resulting mixture was redissolved in dichloromethane, washed with water, sat. sodium hydrogen carbonate aq., and brine. The resulting solution was dried over anhydrous sodium sulfate and evaporated. The mixture was

purified by silica-gel column chromatography (dichloromethane/methanol = 100/3 as an eluent). The blue band was collected and further purified by silica-gel column chromatography (dichloromethane/acetonitrile = 10/1 as an eluent. After removal of the solvent in vacuo, recrystallization from dichloromethane/hexane afforded **2-3** (0.57 g, 1.0 mmol) in 51% yield as a blue solid. Compound data of **2-3** have been reported.⁸

Synthesis of free-base **2,3,7,8,12,13,17,18-octaethyl-5-oxaporphyrinium trifluoromethanesulfonate 2-5(OTf)**

A Schlenk tube containing **2-3** (55 mg, 0.10 mmol) was evacuated and then refilled with nitrogen gas. To the tube, dry and degassed dichloromethane (20 mL) and trifluoromethanesulfonic anhydride (98 μ L, 0.60 mmol) were added. The mixture was stirred at room temperature for 1.5 h. The reaction was quenched with 0.1 M aqueous hydrochloric acid, and the mixture was extracted with dichloromethane. The combined organic layers were washed with water and dried over anhydrous sodium sulfate. After removing the solvent, the mixture was purified by silica-gel column chromatography (dichloromethane/methanol = 25/2 as an eluent). The first blue band was **2-3**. The second blue band was collected. After removal of the solvent in vacuo, recrystallization from dichloromethane/hexane provided **2-5(OTf)** (38 mg, 55 μ mol) in 55% yield as a purple solid. M.p. 178 °C (decomposed); ¹H NMR (500 MHz, CDCl₃, 25 °C): δ = 9.44 (s, 1H, *meso*), 9.08 (s, 2H, *meso*), 3.71 (q, *J* = 7.7 Hz, 4H, ethyl), 3.61 (q, *J* = 7.8 Hz, 4H, ethyl), 3.52 (q, *J* = 7.7 Hz, 4H, ethyl), 3.45 (q, *J* = 7.7 Hz, 4H, ethyl), 3.13 (br-s, 2H, NH), 1.71–1.64 (m, 24H, ethyl) ppm; ¹³C NMR (126 MHz, CDCl₃, 25 °C): δ = 164.2, 151.2, 149.9, 148.4, 145.8, 140.3, 135.7, 135.6, 121.1 (q, *J* = 322 Hz, CF₃), 111.4, 109.2, 19.4, 19.1, 18.7, 18.6, 18.3, 17.8, 17.4, 15.6 ppm; ¹⁹F NMR (471 MHz, CDCl₃, 25 °C): δ = –78.0 (3F) ppm; UV/Vis (CH₂Cl₂): λ_{max} (ϵ [M^{–1} cm^{–1}]) = 367 (7.4×10^4), 565 (1.4×10^4), 607 (8.0×10^4), 667 (1.9×10^4) nm; HRMS (APCI-TOF, positive mode): [OEOP]⁺ Calcd for C₃₅H₄₅N₄O 537.3588; Found 537.3585.

Counter ion exchange of **2-5(OTf)** to free-base **2,3,7,8,12,13,17,18-octaethyl-5-oxaporphyrinium tetrakis[3,5-bis(trifluoromethyl)phenyl]borate 2-5[BAr^F₄]**

A round-bottomed flask containing **2-5(OTf)** (14 mg, 20 μ mol) and sodium tetrakis[3,5-bis(trifluoromethyl)phenyl]borate (18 mg, 20 μ mol) was charged with dichloromethane (5.0 mL). The mixture was stirred at room temperature for 5 min. The resulting mixture was washed with water three times, and dried over anhydrous sodium sulfate. After removing the solvent, the residue was purified by silica-gel column chromatography (dichloromethane/hexane = 1/1 as an eluent) to afford **2-5[BAr^F₄]** (22 mg, 16 μ mol) in 80% yield as a purple solid. M.p. 190 °C (decomposed); ¹H NMR (500 MHz, CDCl₃, 25 °C): δ = 9.41 (s, 1H, *meso*), 9.05 (s, 2H, *meso*), 7.69 (s, 8H, Ar-*o*), 7.47 (s, 4H, Ar-*p*), 3.65 (q, *J* = 7.7 Hz, 4H, ethyl), 3.57 (q, *J* = 7.7 Hz, 4H,

ethyl), 3.48 (q, $J = 7.8$ Hz, 4H, ethyl), 3.45 (q, $J = 7.7$ Hz, 4H, ethyl), 3.28 (br-s, 2H, NH), 1.71–1.62 (m, 24H, ethyl) ppm; ^{13}C NMR (126 MHz, CDCl_3 , 25 °C): $\delta = 164.4$, 161.8 (q, sep, $J_1 = 50$ Hz, $J_2 = 167$ Hz, Ar-*ipso*), 151.4, 149.7, 148.2, 145.9, 140.2, 136.0, 135.6, 134.9 (s, Ar-*o*), 129.0 (qq, $J_1 = 32$ Hz, $J_2 = 2.7$ Hz, Ar-*m*), 124.7 (q, $J = 273$ Hz, CF_3), 117.5 (t, $J = 3.8$ Hz, Ar-*p*), 111.0, 108.9, 19.3, 19.0, 18.7, 18.5, 18.1, 17.6, 17.2, 15.5 ppm; ^{19}F NMR (471 MHz, CDCl_3 , 25 °C): $\delta = -62.4$ (24F) ppm; UV/Vis (CH_2Cl_2): λ_{max} (ϵ [$\text{M}^{-1} \text{cm}^{-1}$]) = 367 (7.6×10^4), 565 (1.5×10^4), 607 (8.4×10^4), 667 (2.0×10^4) nm; HRMS (APCI-TOF, positive mode): $[\text{OEOP}]^+$ Calcd for $\text{C}_{35}\text{H}_{45}\text{N}_4\text{O}$ 537.3588; Found 537.3601; HRMS (APCI-TOF, negative mode): $[\text{BAr}^{\text{F}}_4]^-$ Calcd for $\text{C}_{32}\text{H}_{12}^{11}\text{BF}_{24}$ 863.0643; Found 863.0654.

Direct synthesis of 2-5[BAr^F₄]

A Schlenk tube containing **2-3** (0.17 g, 0.30 mmol) was evacuated and then refilled with nitrogen gas. To the tube, dry and degassed dichloromethane (60 mL) and trifluoromethanesulfonic anhydride (0.30 mL, 1.8 mmol) were added. The mixture was stirred at room temperature for 1.5 h. The reaction was quenched with 0.1 M aqueous hydrochloric acid, and the mixture was extracted with dichloromethane. The combined organic layers were washed with water and dried over anhydrous sodium sulfate. After removing the solvent, sodium tetrakis[3,5-bis(trifluoromethyl)phenyl]borate (0.32 g, 0.36 mmol) and dichloromethane (20 mL) were added to the residue. The mixture was stirred at room temperature for 5 min. The resulting mixture was washed with water three times and dried over anhydrous sodium sulfate. After removing the solvent, the residue was purified by silica-gel column chromatography (dichloromethane/hexane = 7/5 as an eluent) to afford **2-5[BAr^F₄]** (0.35 g, 0.25 mmol) in 82% yield as a purple solid.

Synthesis of zinc 2,3,7,8,12,13,17,18-octaethyl-5-oxaporphyrinium tetrakis[3,5-bis(trifluoromethyl)phenyl]borate **3-1**

A round-bottomed flask containing **2-5[BAr^F₄]** (0.14 g, 0.10 mmol) and bis(2,4-pentanedionato)zinc(II) (0.13 g, 0.50 mmol) was charged with tetrahydrofuran (20 mL). The mixture was stirred at room temperature for 1 h. After evaporation, the residue was purified by silica-gel column chromatography (dichloromethane as an eluent). After recrystallization from dichloromethane/hexane, **3-1** (0.14 g, 98 μmol , 98% yield) was obtained as purple crystals. M.p. 161 °C (decomposed); ^1H NMR (500 MHz, CDCl_3 , 25 °C): $\delta = 9.45$ (s, 1H, *meso*), 9.38 (s, 2H, *meso*), 7.62 (s, 8H, Ar-*o*), 7.43 (s, 4H, Ar-*p*), 3.65–3.54 (m, 16H, ethyl), 1.75–1.65 (m, 24H, ethyl) ppm; ^{13}C NMR (126 MHz, CDCl_3 , 25 °C): $\delta = 163.5$, 161.7 (q, $J = 50$ Hz, Ar-*ipso*), 151.4, 150.6, 147.8, 147.2, 143.5, 142.8, 134.9 (s, Ar-*o*), 131.7, 128.9 (q, $J = 31$ Hz, Ar-*m*), 124.6 (q, $J = 273$ Hz, CF_3), 117.5 (t, $J = 3.9$ Hz, Ar-*p*), 114.8, 112.8, 19.3, 19.2, 19.0, 18.4, 18.3, 18.1, 17.7, 15.7

ppm; ^{19}F NMR (471 MHz, CDCl_3 , 25 °C): $\delta = -62.4$ (24F) ppm; UV/Vis (CH_2Cl_2): λ_{max} (ϵ [$\text{M}^{-1} \text{cm}^{-1}$]) = 337 (3.3×10^4), 396 (5.5×10^4), 513 (6.7×10^3), 549 (1.0×10^4), 659 (6.6×10^4) nm; FL ($\lambda_{\text{ex}} = 590$ nm, CH_2Cl_2): λ_{max} (nm) = 670 (27%); HRMS (APCI-TOF, positive mode): $[\text{ZnOEOP}]^+$ Calcd for $\text{C}_{35}\text{H}_{43}\text{N}_4\text{OZn}$ 599.2723; Found 599.2702; HRMS (APCI-TOF, negative mode): $[\text{BAr}^{\text{F}}_4]^-$ Calcd for $\text{C}_{32}\text{H}_{12}^{11}\text{BF}_{24}$ 863.0649; Found 863.0653.

Synthesis of 2,3,7,8,12,13,17,18-octaethyl-21*H*,23*H*,24*H*-19-oxo-1-thioxo-bilin 3-2

A Schlenk tube of containing **3-1** (0.14 g, 98 μmol) and anhydrous sodium sulfide (23 mg, 0.30 mmol) was evacuated and then refilled with N_2 . To the tube, 20 mL of the dry tetrahydrofuran was added and stirred at room temperature for 0.5 h. After evaporation, the resulting mixture was redissolved in dichloromethane, washed with 1 M hydrochloric acid and water for two times. The combined organic layers were dried over anhydrous sodium sulfate. After evaporation, the residue was purified by amino-functionalized silica-gel column chromatography (dichloromethane as an eluent) and silica-gel column chromatography (dichloromethane as an eluent). After recrystallization from dichloromethane/hexane, **3-2** (55 mg, 96 μmol , 98% yield) was obtained as dark purple crystals. M.p. 196 °C (decomposed); ^1H NMR (500 MHz, CDCl_3 , 25 °C): $\delta = 9.09$ (br-s, 1H, NH), 7.62 (br-s, 2H, NH), 6.85 (s, 1H, *meso*), 6.22 (s, 1H, *meso*), 6.13 (s, 1H, *meso*), 2.70–2.49 (m, 14H, ethyl), 2.18 (q, $J = 7.6$ Hz, 2H, ethyl), 1.34 (t, $J = 7.7$ Hz, 3H, ethyl), 1.29 (t, $J = 7.7$ Hz, 3H, ethyl), 1.25–1.17 (m, 12 H, ethyl), 1.11 (t, $J = 7.6$ Hz, 3H, ethyl), 1.02 (t, $J = 7.6$ Hz, 3H, ethyl) ppm; ^{13}C NMR (126 MHz, CDCl_3 , 25 °C): $\delta = 191.8$, 172.1, 150.6, 148.7, 147.0, 144.2, 142.5, 142.4, 142.0, 141.9, 141.1, 140.5, 138.9, 135.6, 134.6, 133.0, 113.4, 97.8, 96.6, 18.4, 18.4, 18.1, 18.0, 17.9, 17.8, 17.2, 17.1, 17.0, 16.4, 16.1, 16.0, 15.8, 14.8, 13.4 ppm; UV/Vis (CH_2Cl_2): λ_{max} (ϵ [$\text{M}^{-1} \text{cm}^{-1}$]) = 320 (3.0×10^4), 410 (5.2×10^4), 708 (1.2×10^4) nm; HRMS (APCI-TOF, positive mode): $[\text{M}+\text{H}]^+$ Calcd for $\text{C}_{35}\text{H}_{46}\text{N}_4\text{OS}$ 571.3465; Found 571.3422.

Synthesis of free-base 2,3,7,8,12,13,17,18-octaethyl-5-thiaporphyrinium tetrakis[3,5-bis(trifluoromethyl)phenyl]borate 3-3

A Schlenk tube containing **3-2** (29 mg, 50 μmol) was evacuated and then refilled with nitrogen gas. To the tube, dry and degassed dichloromethane (10 mL) and trifluoromethanesulfonic anhydride (16 μL , 0.10 mmol) were added. The mixture was stirred at room temperature for 0.5 h. The mixture was washed with water and dried over anhydrous sodium sulfate. After removing the solvent, sodium tetrakis[3,5-bis(trifluoromethyl)phenyl]borate (54 mg, 61 μmol) and dichloromethane (10 mL) were added to the residue. The mixture was stirred at room temperature for 5 min. The resulting mixture was washed with water three times and dried over anhydrous sodium sulfate. After removing the solvent, the residue was purified by silica-gel column chromatography (dichloromethane/hexane = 1/1 as an eluent) to afford **3-3** (22 mg, ca.

15 μmol) along with ca. 1% of **2-5**[BAr^F₄] in 30% yield as a dark purple solid. After short column chromatography with amino-functionalized silica-gel (dichloromethane as an eluent), **2-5**[BAr^F₄] was completely removed from the residue and **3-3** was obtained in 21% yield (15 mg, 10 μmol). M.p. 186 °C (decomposed); ¹H NMR (500 MHz, CDCl₃, 25 °C): δ = 10.26 (s, 1H, *meso*), 10.24 (s, 2H, *meso*), 7.70 (s, 8H, Ar-*o*), 7.47 (s, 4H, Ar-*p*), 4.03–3.93 (m, 16H, ethyl), 1.90–1.84 (m, 24H, ethyl), –1.05 (s, 2H, NH) ppm; ¹³C NMR (126 MHz, CDCl₃, 25 °C): δ = 161.8 (q, *J* = 50 Hz, Ar-*ipso*), 149.6, 148.6, 148.4, 147.5, 147.4, 145.6, 144.3, 142.1, 134.9 (s, Ar-*o*), 129.0 (q, *J* = 32 Hz, Ar-*m*), 124.7 (q, *J* = 273 Hz, CF₃), 117.5 (t, *J* = 3.7 Hz, Ar-*p*), 111.4, 108.9, 19.9, 19.7, 19.5, 19.4, 18.5, 18.3, 18.2, 17.7 ppm; ¹⁹F NMR (471 MHz, CDCl₃, 25 °C): δ = –62.4 (24F) ppm; UV/Vis (CH₂Cl₂): λ_{max} (ϵ [M^{–1} cm^{–1}]) = 310 (3.0×10^4), 392 (1.1×10^5), 671 (5.6×10^4) nm; FL (λ_{ex} = 550 nm, CH₂Cl₂): λ_{max} (nm) = 686 (<1%); HRMS (APCI-TOF, positive mode): [thiaporphyrin]⁺ Calcd for C₃₅H₄₅N₄S 553.3359; Found 553.3354; HRMS (APCI-TOF, negative mode): [BAr^F₄][–] Calcd for C₃₂H₁₂¹¹BF₂₄ 863.0649; Found 863.0661.

Synthesis of zinc 2,3,7,8,12,13,17,18-octaethyl-5-thiaporphyrinium tetrakis[3,5-bis(trifluoromethyl)phenyl]borate **3-4**

A round-bottomed flask containing **3-3** (14 mg, 10 μmol) and bis(2,4-pentanedionato)zinc(II) (13 mg, 50 μmol) was charged with tetrahydrofuran (5 mL). The mixture was stirred at room temperature for 1 h. After evaporation, the residue was purified by silica-gel column chromatography (dichloromethane as an eluent). After recrystallization from dichloromethane/hexane, **3-4** (14 mg, 9.6 μmol , 96% yield) was obtained as dark purple crystals. M.p. 144 °C (decomposed); ¹H NMR (500 MHz, CDCl₃, 25 °C): δ = 10.19 (s, 1H, *meso*), 10.15 (s, 2H, *meso*), 7.62 (s, 8H, Ar-*o*), 7.43 (s, 4H, Ar-*p*), 4.00–3.90 (m, 16H, ethyl), 1.89–1.82 (m, 24H, ethyl) ppm; ¹³C NMR (126 MHz, CDCl₃, 25 °C): δ = 161.8 (q, *J* = 50 Hz, Ar-*ipso*), 153.9, 151.9, 150.2, 148.6, 148.1, 147.5, 145.7, 142.6, 134.9 (s, Ar-*o*), 128.9 (q, *J* = 32 Hz, Ar-*m*), 124.6 (q, *J* = 273 Hz, CF₃), 117.5 (t, *J* = 3.9 Hz, Ar-*p*), 111.3, 109.0, 19.8, 19.7, 19.5, 19.3, 18.6, 18.5, 18.3, 17.9 ppm; ¹⁹F NMR (471 MHz, CDCl₃, 25 °C): δ = –62.4 (24F) ppm; UV/Vis (CH₂Cl₂): λ_{max} (ϵ [M^{–1} cm^{–1}]) = 312 (3.2×10^4), 359 (3.5×10^4), 405 (9.9×10^4), 531 (5.2×10^3), 568 (5.9×10^3), 661 (4.5×10^4) nm; FL (λ_{ex} = 550 nm, CH₂Cl₂): λ_{max} (nm) = 675 (<1%); HRMS (APCI-TOF, positive mode): [thiaporphyrin]⁺ Calcd for C₃₅H₄₃N₄SZn 615.2494; Found 615.2495; HRMS (APCI-TOF, negative mode): [BAr^F₄][–] Calcd for C₃₂H₁₂¹¹BF₂₄ 863.0649; Found 863.0668.

Synthesis of 2,3,7,8,12,13,17,18-octaethyl-21*H*,23*H*-1-oxo-19-(phenylamino)-bilin **4-1**

A Schlenk tube of containing **2-5**[BAr^F₄] (42 mg, 30 μmol) was evacuated and then refilled with N₂. To the tube, 20 mL of the dry tetrahydrofuran and aniline (10 μL , 0.11 mmol) were added and stirred at room temperature for 0.5 h. After evaporation, the residue was purified by silica-

gel column chromatography (dichloromethane as an eluent) and amino-functionalized silica-gel column chromatography (dichloromethane as an eluent). After recrystallization from dichloromethane/hexane, **4-1** (14 mg, 22 μ mol, 72% yield) was obtained as dark green crystals. M.p. 231 °C (decomposed); ^1H NMR (500 MHz, CDCl_3 , 25 °C): δ = 13.81 (br-s, 1H, NH), 10.51 (br-s, 2H, NH), 7.98 (d, 2H, J = 7.8 Hz, Ph-*o*), 7.07 (t, 2H, J = 7.9 Hz, Ph-*m*), 6.78 (t, 1H, J = 7.3 Hz, Ph-*p*), 6.45 (s, 1H, *meso*), 6.09 (s, 1H, *meso*), 6.07 (br-s, 1H, NH), 5.07 (s, 1H, *meso*), 2.56–2.46 (m, 8H, ethyl), 2.31–2.23 (m, 4H, ethyl), 2.19 (q, 2H, J = 7.5 Hz, ethyl), 2.11 (q, 2H, J = 7.7 Hz, ethyl), 1.20–1.02 (m, 21 H, ethyl), 0.90 (t, 3H, J = 7.7 Hz, ethyl) ppm; ^{13}C NMR (126 MHz, CDCl_3 , 25 °C): δ = 171.7, 165.6, 164.8, 152.8, 151.1, 146.0, 145.1, 144.6, 142.5, 140.2, 137.4, 137.3, 135.0, 133.3, 132.1, 131.5, 130.6, 129.1, 122.1, 118.4, 115.0, 106.3, 97.5, 17.9, 17.7, 17.6, 17.4, 17.3, 17.3, 17.2, 17.1, 16.8, 16.8, 16.5, 15.1, 15.0, 14.2, 14.0 ppm; UV/Vis (CH_2Cl_2): λ_{max} = 314 (3.1×10^4), 407 (4.0×10^4), 709 (1.0×10^4) nm; HRMS (APCI-TOF, positive mode): $[\text{M}+\text{H}]^+$ Calcd for $\text{C}_{41}\text{H}_{51}\text{N}_5\text{O}$ 629.4088; Found 629.4100.

Synthesis of free-base *N*-phenyl-2,3,7,8,12,13,17,18-octaethyl-5-axaporphyrinium trifluoromethanesulfonate **4-2**

A Schlenk tube containing **4-1** (18 mg, 29 μ mol) and zinc(II) acetylacetonate (24 mg, 89 μ mol) were evacuated and then refilled with nitrogen gas. To the tube, dry and degassed dichloromethane (6.0 mL) and trifluoromethanesulfonic anhydride (50 μ L, 0.30 mmol) were added. The mixture was stirred at room temperature for 0.5 h. The mixture was extracted with dichloromethane. The combined organic layers were washed with water and dried over anhydrous sodium sulfate. After removing the solvent, the mixture was purified by silica-gel column chromatography (dichloromethane/methanol = 20/1 as an eluent). The second blue was collected. After removal of the solvent in vacuo, recrystallization from dichloromethane/hexane provided **4-2** (7.5 mg, 9.8 μ mol) in 34% yield as a purple solid. Due to the low solubility, decoupled peaks of CF_3 in ^{13}C NMR spectrum were detected as a doublet. M.p. 188 °C (decomposed); ^1H NMR (500 MHz, CDCl_3 , 25 °C): δ = 10.19 (s, 2H, *meso*), 10.06 (s, 1H, *meso*), 8.23 (d, J = 7.5 Hz, 2H, Ph-*o*), 8.14 (t, J = 7.7 Hz, 1H, Ph-*p*), 7.98 (t, J = 7.8 Hz, 2H, Ph-*m*), 3.96–3.88 (m, 12H, ethyl), 2.39 (q, J = 7.5 Hz, 4H, ethyl), 1.87–1.84 (m, 12H, ethyl), 1.81 (t, J = 7.7 Hz, 6H, ethyl), 1.09 (t, J = 7.5 Hz, 6H, ethyl), –0.59 (br-s, 1H, NH), –1.09 (br-s, 1H, NH) ppm; ^{13}C NMR (126 MHz, CDCl_3 , 25 °C): δ = 152.4, 148.5, 146.8, 146.7, 145.6, 144.3, 140.4, 140.2, 135.6, 133.1, 131.4, 129.8, 121.0 (d, J = 321 Hz, CF_3), 108.7, 107.3, 20.6, 20.0, 19.6, 19.6, 18.6, 18.5, 18.4, 17.6 ppm; ^{19}F NMR (471 MHz, CDCl_3 , 25 °C): δ = –78.2 (3F) ppm; UV/Vis (CH_2Cl_2): λ_{max} = 305 (2.2×10^4), 387 (1.1×10^5), 520 (6.6×10^3), 554 (7.8×10^3), 580 (9.4×10^3), 634 (6.8×10^4) nm; FL (λ_{ex} = 550 nm, CH_2Cl_2): λ_{max} (nm) = 644 (<1%); HRMS (APCI-TOF, positive mode): [azaporphyrin] $^+$ Calcd for $\text{C}_{41}\text{H}_{50}\text{N}_5$ 612.4061; Found 612.4069.

Synthesis of free-base *N*-phenyl-2,3,7,8,12,13,17,18-octaethyl-5-azaporphyrinium tetrakis[3,5-bis(trifluoromethyl)phenyl]borate **4-3**

A round-bottomed flask containing **4-2** (7.1 mg, 9.3 μ mol) and sodium tetrakis[3,5-bis(trifluoromethyl)phenyl]borate (9.9 mg, 11 μ mol) was charged with dichloromethane (5.0 mL). The mixture was stirred at room temperature for 5 min. The resulting mixture was washed with water three times, and dried over anhydrous sodium sulfate. After removing the solvent, the residue was purified by silica-gel column chromatography (dichloromethane/hexane = 2/1 as an eluent) to afford **4-3** (10 mg, 6.7 μ mol) in 73% yield as a purple solid. M.p. 184 °C (decomposed); ^1H NMR (500 MHz, CDCl_3 , 25 °C): δ = 10.21 (s, 2H, *meso*), 10.09 (s, 1H, *meso*), 8.14 (d, J = 7.2 Hz, 2H, Ph-*o*), 8.08 (t, J = 7.7 Hz, 1H, Ph-*p*), 7.90 (t, J = 7.9 Hz, 2H, Ph-*m*), 7.68 (s, 8H, Ar-*o*), 7.46 (s, 4H, Ar-*p*), 3.95–3.86 (m, 12H, ethyl), 2.36 (q, J = 7.5 Hz, 4H, ethyl), 1.86–1.82 (m, 12H, ethyl), 1.79 (t, J = 7.7 Hz, 6H, ethyl), 1.07 (t, J = 7.7 Hz, 6H, ethyl), –0.61 (br-s, 2H, NH), –1.12 (br-s, 2H, NH) ppm; ^{13}C NMR (126 MHz, CDCl_3 , 25 °C): δ = 161.8 (q, J = 50 Hz, Ar-*ipso*), 152.4, 148.3, 147.1, 146.8, 145.9, 144.5, 140.5, 140.1, 135.3, 134.9 (s, Ar-*o*), 133.1, 131.1, 129.6, 129.0 (q, J = 32 Hz, Ar-*m*), 124.7 (q, J = 273 Hz, CF_3), 117.5 (t, J = 3.6 Hz, Ar-*p*), 109.0, 107.3, 20.5, 20.0, 19.6, 19.5, 18.5, 18.4, 18.3, 17.6 ppm; ^{19}F NMR (471 MHz, CDCl_3 , 25 °C): δ = –62.4 (24F) ppm; UV/Vis (CH_2Cl_2): λ_{max} = 305 (2.2×10^4), 387 (1.1×10^5), 519 (6.5×10^3), 554 (7.7×10^3), 581 (9.3×10^3), 635 (6.8×10^4) nm; FL (λ_{ex} = 550 nm, CH_2Cl_2): λ_{max} (nm) = 644 (<1%); HRMS (APCI-TOF, positive mode): [azaporphyrin] $^+$ Calcd for $\text{C}_{41}\text{H}_{50}\text{N}_5$ 612.4061; Found 612.4045; HRMS (APCI-TOF, negative mode): [BAr^{F}_4] $^-$ Calcd for $\text{C}_{32}\text{H}_{12}^{11}\text{BF}_{24}$ 863.0643; Found 863.0668.

Synthesis of nickel 2,3,7,8,12,13,17,18-octaethyl-5-oxaporphyrinium trifluoromethanesulfonate **5-1**

A round-bottomed flask containing **2-5(OTf)** (27 mg, 40 μ mol) and nickel(II) acetylacetonate hydrate (51 mg, ca. 0.20 mmol) was charged with tetrahydrofuran (10 mL) and dichloromethane (5 mL). The mixture was stirred at room temperature for 4.5 h. After evaporation, the residue was purified by silica-gel column chromatography (dichloromethane/methanol = 25/2 as an eluent). After recrystallization from dichloromethane/hexane at 10 °C, **5-1** (23 mg, 30 μ mol, 76% yield) was obtained as dark purple crystals. Due to the low solubility, decoupled peaks of CF_3 in ^{13}C NMR spectrum were not detected. M.p. 291 °C (decomposed); ^1H NMR (500 MHz, CDCl_3 , 25 °C): δ = 9.46 (s, 2H, *meso*), 9.34 (s, 1H, *meso*), 3.70 (q, J = 7.7 Hz, 4H, ethyl), 3.66–3.57 (m, 12H ethyl), 1.74–1.63 (m, 24H, ethyl) ppm; ^{13}C NMR (126 MHz, CDCl_3 , 25 °C): δ = 156.0, 153.1, 149.1, 146.9, 145.7, 142.8, 136.8, 133.4, 112.3, 111.0, 19.7, 19.5, 19.2, 18.5, 18.4, 18.0, 17.8, 15.7 ppm; ^{19}F NMR (471 MHz, CDCl_3 , 25 °C): δ = –78.1 (3F) ppm; UV/Vis (CH_2Cl_2): λ_{max} (ϵ [$\text{M}^{-1}\text{cm}^{-1}$]) = 305 (2.0×10^4), 341 (3.3×10^4), 400 (4.5×10^4), 513 (8.3×10^3), 544 (1.4×10^4), 695 (2.2×10^4) nm; HRMS (APCI-TOF, positive mode): [NiOEOP] $^+$ Calcd for $\text{C}_{35}\text{H}_{43}\text{N}_4\text{NiO}$

593.2785; Found 593.2767.

Synthesis of zinc 2,3,7,8,12,13,17,18-octaethyl-5-oxaporphyrinium chloride 5-2

A round-bottomed flask containing **2-5(OTf)** (27 mg, 40 μ mol) and zinc(II) acetylacetonate (53 mg, 0.20 mmol) was charged with tetrahydrofuran (10 mL). The mixture was stirred at room temperature for 3 h. After evaporation, the residue was purified by silica-gel column chromatography (dichloromethane/methanol = 20/1 as an eluent). After removing the solvent, dichloromethane (10 mL) and 1 M hydrochloric acid (10 mL) was added to the residue. The mixture was stirred at room temperature for 15 min. The resulting mixture was washed with water three times and dried over anhydrous sodium sulfate. After removing the solvent, recrystallization from dichloromethane/hexane afforded **5-2** (23 mg, 36 μ mol, 90% yield) as dark purple crystals. M.p. 261 °C (decomposed); ^1H NMR (500 MHz, CDCl_3 , 25 °C): δ = 9.29 (s, 1H, *meso*), 9.20 (s, 2H, *meso*), 3.61–3.42 (m, 16H ethyl), 1.73–1.64 (m, 24H, ethyl) ppm; ^{13}C NMR (126 MHz, CDCl_3 , 25 °C): δ = 163.2, 151.3, 148.8, 147.7, 145.5, 142.8, 141.9, 130.7, 115.1, 112.8, 19.3, 19.2, 19.0, 18.4, 18.4, 18.1, 17.7, 15.8 ppm; UV/Vis (CH_2Cl_2): λ_{max} (ϵ [$\text{M}^{-1} \text{cm}^{-1}$]) = 274 (1.3×10^4), 304 (3.1×10^4), 335 (2.9×10^4), 393 (5.0×10^4), 514 (6.5×10^3), 549 (9.1×10^3), 659 (6.2×10^4) nm; FL (λ_{ex} = 550 nm, CH_2Cl_2): λ_{max} (nm) = 677 (5.6%); HRMS (APCI-TOF, positive mode): $[\text{ZnOEOP}]^+$ Calcd for $\text{C}_{35}\text{H}_{43}\text{N}_4\text{OZn}$ 599.2723; Found 599.2729.

Synthesis of free-base 2,3,7,8,12,13,17,18-octaethyl-5-oxaporphyrinium pentacyanocyclopentadienide 5-3FB

To a round-bottomed flask containing **2-5(OTf)** (14 mg, 20 μ mol) charged with acetonitrile (6 mL), acetonitrile solution (6 mL) of NaPCCp⁹ (13 mg, 60 μ mol) was added. The mixture was stirred at room temperature for 40 min. After evaporation, the residue was purified by silica-gel column chromatography (dichloromethane/acetonitrile = 100/3 as an eluent). After recrystallization from dichloromethane/hexane, **5-3FB** (7.8 mg, 11 μ mol, 54% yield) was obtained as dark purple crystals. M.p. 260 °C (decomposed); ^1H NMR (500 MHz, CDCl_3 , 25 °C): δ = 9.43 (s, 1H, *meso*), 9.08 (s, 2H, *meso*), 3.70 (q, J = 7.8 Hz, 4H, ethyl), 3.61 (q, J = 7.7 Hz, 4H, ethyl), 3.52 (q, J = 7.8 Hz, 4H, ethyl), 3.48 (q, J = 7.7 Hz, 4H, ethyl), 2.78 (br-s, 2H, NH), 1.76–1.68 (m, 24H, ethyl) ppm; ^{13}C NMR (126 MHz, CDCl_3 , 25 °C): δ = 164.2, 150.9, 149.5, 147.9, 146.0, 140.3, 135.9, 135.8, 112.0, 111.2, 109.1, 100.5, 19.5, 19.2, 18.9, 18.7, 18.1, 17.6, 17.2, 15.5 ppm; UV/Vis (CH_2Cl_2): λ_{max} (ϵ [$\text{M}^{-1} \text{cm}^{-1}$]) = 248 (5.9×10^4), 257 (9.6×10^4), 292 (3.6×10^4), 367 (7.3×10^4), 565 (1.4×10^4), 607 (8.0×10^4), 668 (2.0×10^4) nm; FL (λ_{ex} = 550 nm, CH_2Cl_2): λ_{max} (nm) = 677 (0.9%); HRMS (APCI-TOF, positive mode): $[\text{FBOEOP}]^+$ Calcd for $\text{C}_{35}\text{H}_{45}\text{N}_4\text{O}$ 537.3588; Found 537.3596.

Synthesis of nickel 2,3,7,8,12,13,17,18-octaethyl-5-oxaporphyrinium pentacyanocyclopentadienide **5-3Ni**

To a round-bottomed flask containing **5-1** (15 mg, 20 μmol) charged with acetonitrile (5 mL), acetonitrile solution (5 mL) of NaPCCp⁹ (13 mg, 60 μmol) was added. The mixture was stirred at room temperature for 1 h. After evaporation, the resulting mixture was washed with water three times and dried over anhydrous sodium sulfate. After removing the solvent, the residue was purified by silica-gel column chromatography (dichloromethane/methanol = 50/1 as an eluent). After recrystallization from dichloromethane/hexane, **5-3Ni** (13 mg, 17 μmol , 86% yield) was obtained as dark purple crystals. M.p. 306 °C (decomposed); ¹H NMR (500 MHz, CDCl₃, 25 °C): δ = 9.45 (s, 2H, *meso*), 9.46 (s, 1H, *meso*), 3.72–3.59 (m, 16H ethyl), 1.78–1.69 (m, 24H, ethyl) ppm; ¹³C NMR (126 MHz, CDCl₃, 25 °C): δ = 155.8, 152.0, 148.6, 146.2, 145.0, 142.5, 136.5, 132.9, 112.6, 111.7, 111.0, 100.5, 19.8, 19.5, 19.3, 18.5, 18.2, 17.8, 17.5, 15.6 ppm; UV/Vis (CH₂Cl₂): λ_{max} (ϵ [M⁻¹ cm⁻¹]) = 248 (2.0×10^4), 257 (8.5×10^4), 296 (2.3×10^4), 341 (3.2×10^4), 400 (4.4×10^4), 514 (8.1×10^3), 544 (1.4×10^4), 695 (2.2×10^4) nm; HRMS (APCI-TOF, positive mode): [NiOEOP]⁺ Calcd for C₃₅H₄₃N₄NiO 593.2785; Found 593.2799.

Synthesis of zinc 2,3,7,8,12,13,17,18-octaethyl-5-oxaporphyrinium pentacyanocyclopentadienide **5-3Zn**

To a round-bottomed flask containing **5-2** (9.6 mg, 15 μmol) charged with acetonitrile (5 mL), acetonitrile solution (5 mL) of NaPCCp⁹ (9.6 mg, 45 μmol) was added. The mixture was stirred at room temperature for 1 h. After evaporation, the resulting mixture was washed with water three times and dried over anhydrous sodium sulfate. After removing the solvent, the residue was purified by silica-gel column chromatography (dichloromethane/methanol = 20/1 as an eluent). After recrystallization from dichloromethane/hexane, **5-3Zn** (10 mg, 13 μmol , 87% yield) was obtained as dark purple crystals. M.p. 296 °C (decomposed); ¹H NMR (500 MHz, CDCl₃, 25 °C): δ = 9.45 (s, 1H, *meso*), 9.37 (s, 2H, *meso*), 3.65–3.57 (m, 16H ethyl), 1.79–1.68 (m, 24H, ethyl) ppm; ¹³C NMR (126 MHz, CDCl₃, 25 °C): δ = 163.3, 151.3, 150.2, 147.7, 146.9, 143.1, 142.6, 131.5, 115.2, 113.0, 111.9, 101.9 19.4, 19.3, 19.2, 18.4, 18.4, 18.1, 17.7, 15.8 ppm; UV/Vis (CH₂Cl₂): λ_{max} (ϵ [M⁻¹ cm⁻¹]) = 248 (5.4×10^4), 258 (8.2×10^4), 280 (2.3×10^4), 304 (3.5×10^4), 335 (3.4×10^4), 394 (5.7×10^4), 513 (7.0×10^3), 549 (1.0×10^4), 659 (7.0×10^4) nm; FL (λ_{ex} = 550 nm, CH₂Cl₂): λ_{max} (nm) = 670 (20%); HRMS (APCI-TOF, positive mode): [ZnOEOP]⁺ Calcd for C₃₅H₄₃N₄OZn 599.2723; Found 599.2716.

Synthesis of nickel 2,3,7,8,12,13,17,18-octaethyl-5-oxaporphyrinium tetrakis[3,5-bis(trifluoromethyl)phenyl]borate NiOEOP

A round-bottomed flask containing **2-5[BAR^F₄]** (56 mg, 40 μ mol) and bis(2,4-pentanedionato)nickel(II) hydrate (51 mg, ca. 0.20 mmol) was charged with tetrahydrofuran (10 mL). The mixture was stirred at room temperature for 30 min. After evaporation, the residue was purified by silica-gel column chromatography (dichloromethane/hexane = 1/1 as an eluent). After recrystallization from dichloromethane/hexane, **NiOEOP** (58 mg, 40 μ mol, 99% yield) was obtained as purple crystals. M.p. 201 °C (decomposed); ¹H NMR (500 MHz, CDCl₃, 25 °C): δ = 9.46 (s, 2H, *meso*), 9.42 (s, 1H, *meso*), 7.67 (s, 8H, Ar-*o*), 7.46 (s, 4H, Ar-*p*), 3.66–3.54 (m, 16H, ethyl), 1.72–1.62 (m, 24H, ethyl) ppm; ¹³C NMR (126 MHz, CDCl₃, 25 °C): δ = 161.5 (q, *J* = 50 Hz, Ar-*ipso*), 155.7, 152.5, 148.9, 146.3, 145.2, 142.7, 136.4, 134.9 (s, Ar-*o*), 133.1, 129.0 (q, *J* = 31 Hz, Ar-*m*), 123.6 (q, *J* = 273 Hz, CF₃), 117.5 (t, *J* = 3.8 Hz, Ar-*p*), 112.5, 110.9, 19.6, 19.4, 19.1, 18.4, 18.3, 17.9, 17.6, 15.6 ppm; ¹⁹F NMR (471 MHz, CDCl₃, 25 °C): δ = –62.4 (24F) ppm; UV/Vis (CH₂Cl₂): λ_{max} (ϵ [M^{–1} cm^{–1}]) = 341 (3.4×10^4), 400 (4.7×10^4), 511 (8.5×10^3), 544 (1.5×10^4), 695 (2.3×10^4) nm; HRMS (APCI-TOF, positive mode): [NiOEOP]⁺ Calcd for C₃₅H₄₃N₄NiO 593.2785; Found 593.2785; HRMS (APCI-TOF, negative mode): [BAR^F₄][–] Calcd for C₃₂H₁₂¹¹BF₂₄ 863.0649; Found 863.0665.

Synthesis of cobalt 2,3,7,8,12,13,17,18-octaethyl-5-oxaporphyrinium tetrakis[3,5-bis(trifluoromethyl)phenyl]borate CoOEOP

A round-bottomed flask containing **2-5[BAR^F₄]** (28 mg, 20 μ mol) and Co(II) acetate (25 mg, 0.10 mmol) was charged with tetrahydrofuran (10 mL). The mixture was stirred at room temperature for 1 h. After evaporation, the residue was purified by silica-gel column chromatography (dichloromethane/hexane = 1/1 as an eluent). After recrystallization from dichloromethane/hexane, **CoOEOP** (29 mg, 20 μ mol, 100% yield) was obtained as purple crystals. M.p. 172 °C (decomposed); ¹H NMR (500 MHz, CDCl₃, 25 °C): δ = 29.35 (br-s, 2H, *meso*), 18.37 (br-s, 1H, *meso*), 8.26 (br-s, 4H, ethyl), 7.43 (br-s, 8H + 4H, Ar-*o* and ethyl), 7.09 (br-s, 4H, Ar-*p*), 5.90 (br-s, 6H, ethyl), 5.77 (br-s, 6H, ethyl), 5.38 (br-s, 4H, ethyl), 4.84 (br-s, 4H, ethyl), 3.45 (br-s, 6H, ethyl), 3.68 (br-s, 6H, ethyl) ppm; ¹³C NMR (126 MHz, CDCl₃, 25 °C): δ = 161.5 (q, *J* = 50 Hz, Ar-*ipso*), 134.7 (s, Ar-*o*), 128.7 (q, *J* = 31 Hz, Ar-*m*), 124.4 (q, *J* = 273 Hz, CF₃), 117.3 (s, Ar-*p*), 31.7, 28.9, 28.3, 27.3, 20.2, 16.1, 15.2, 12.5 ppm; ¹⁹F NMR (471 MHz, CDCl₃, 25 °C): δ = –61.0 (24F) ppm; UV/Vis (CH₂Cl₂): λ_{max} (ϵ [M^{–1} cm^{–1}]) = 338 (3.4×10^4), 399 (4.4×10^4), 505 (6.4×10^3), 541 (1.2×10^4), 627 (3.2×10^4) nm; HRMS (APCI-TOF, positive mode): [CoOEOP]⁺ Calcd for C₃₅H₄₃CoN₄O 594.2763; Found 594.2745; HRMS (APCI-TOF, negative mode): [BAR^F₄][–] Calcd for C₃₂H₁₂¹¹BF₂₄ 863.0649; Found 863.0663.

Synthesis of silver 2,3,7,8,12,13,17,18-octaethyl-5-oxaporphyrinium tetrakis[3,5-bis(trifluoromethyl)phenyl]borate AgOEOP

A round-bottomed flask containing **2-5[BAr^F₄]** (84 mg, 60 μ mol) and silver(I) acetate (50 mg, 0.30 mmol) was charged with tetrahydrofuran (6.0 mL). The mixture was stirred at room temperature for 2 h. After evaporation, the residue was purified by silica-gel column chromatography (dichloromethane/hexane = 1/2 as an eluent). After recrystallization from dichloromethane/hexane, **AgOEOP** (74 mg, 49 μ mol, 82% yield) was obtained as purple crystals. M.p. 196 °C (decomposed); Some of NMR signals were not observed due to the paramagnetic nature of **AgOEOP**. ¹H NMR (500 MHz, CDCl₃, 25 °C): δ = 7.67 (s, 8H, Ar-*o*), 7.47 (s, 4H, Ar-*p*), 2.22 (br-s, 24H, ethyl) ppm; ¹³C NMR (126 MHz, CDCl₃, 25 °C): δ = 161.8 (q, *J* = 50 Hz, Ar-*ipso*), 134.9 (s, Ar-*o*), 129.0 (q, *J* = 30 Hz, Ar-*m*), 124.6 (q, *J* = 272 Hz, CF₃), 117.5 (s, Ar-*p*) ppm; ¹⁹F NMR (471 MHz, CDCl₃, 25 °C): δ = -62.4 (24F) ppm; UV/Vis (CH₂Cl₂): λ_{max} (ϵ [M⁻¹ cm⁻¹]) = 338 (2.5×10^4), 402 (5.1×10^4), 511 (7.8×10^3), 545 (8.7×10^3), 672 (5.0×10^4) nm; HRMS (ESI-TOF, positive mode): [AgOEOP]⁺ Calcd for C₃₅H₄₃AgN₄O 642.2482; Found 642.2512; HRMS (APCI-TOF, negative mode): [BAr^F₄]⁻ Calcd for C₃₂H₁₂¹¹BF₂₄ 863.0649; Found 863.0639.

Expression and purification of apo-HasA

Expression and purification of truncated HasA derived from *Pseudomonas aeruginosa* PAO1 were performed according to methods reported previously.¹⁰ The details of the purification of HasA are given below. The concentration of protein was determined by the BCA assay. *Escherichia coli* cells expressing HasA were suspended in an H buffer (20 mM sodium phosphate, 20 mM imidazole, 500 mM NaCl, pH 7.4) and broken using an ultrasonicator at 4 °C. After removing cell debris by centrifugation, the supernatant containing HasA was loaded on Ni-affinity column chromatography (cOmplete His-Tag Purification Resin; Roche). The weakly adsorbing proteins to Ni-affinity column were washed out using H buffer, and specific binding proteins including HasA were eluted with H buffer containing 200 mM imidazole. The resulting protein solution was treated with thrombin to remove His-tag on HasA and dialyzed against a phosphate-buffered saline (PBS; 140 mM NaCl, 2.7 mM KCl, 10 mM Na₂HPO₄, 1.8 mM KH₂PO₄, pH 7.4) solution overnight. This sample was further purified by the same Ni-affinity column chromatography equilibrated with PBS solution. The purified HasA solution was denatured by acetone including 0.2% (w/v) conc. HCl to remove heme. The precipitate of HasA was collected by centrifugation and dissolved in a solution of 7 M urea including 100 mM Tris-HCl (pH 7.5). The resulting solution was dialyzed against a PBS solution. After overnight dialysis, the solution was concentrated using Amicon Ultra (Merck Millipore, 3 kDa cutoff) and purified by a gel filtration column (HiPrep 16/60 Sephacryl S-200 HR; GE Healthcare) equilibrated with a PBS solution to remove unfolded HasA. The concentration of apo-HasA was determined by UV

absorption at 280 nm ($\epsilon_{280} = 28.6 \text{ mM}^{-1} \text{ cm}^{-1}$).¹¹ The purified apo-HasA solution was frozen by liquid nitrogen and stored at -80°C until use.

Preparation of CoOEOP-HasA and CoEOP-HasA

CoOEOP (2 equiv of apo-HasA) was dissolved in DMSO using a sonicator. This solution was added to the same volume of 150 μM apo-HasA solution. The mixture was dialyzed in PBS solution and filtrated to remove insoluble excess **CoOEOP**. To remove CoOEOP-free HasA, the filtrated solution was loaded on an anion exchange column (HiTrap capto DEAE; GE Healthcare) equilibrated with buffer A (20 mM Tris-HCl, pH 7.5) and washed by 1 column volume of the buffer A containing 10%(v/v) of buffer B (20 mM Tris-HCl, 1 M NaCl, pH 7.5). The binding proteins to the anion exchange column were then eluted with over 25 column volumes of a linear gradient from 10% to 80% as the ratio of buffer B, and sample fractions containing the complex of HasA with **CoOEOP** were collected. After buffer exchange to PBS solution using desalting column (PD-10; GE Healthcare), the CoOEOP-HasA solution was frozen by liquid nitrogen and stored at -80°C until use. The concentration of CoOEOP-HasA was determined by a bicinchoninic acid (BCA) method using apo-HasA as a standard. The molar extinction coefficient of CoOEOP-HasA at 687 nm was estimated to be $33.3 \text{ mM}^{-1} \text{ cm}^{-1}$. CoEOP-HasA was prepared using a similar procedure to CoOEOP-HasA. The molar extinction coefficient of CoEOP-HasA at 419 nm was estimated to be $193.3 \text{ mM}^{-1} \text{ cm}^{-1}$.

Crystallization of CoOEOP-HasA and CoEOP-HasA

The buffer of the purified HasA complexes was exchanged with 100 mM KPi (pH 7.0) using the desalting column (PD-10; GE Healthcare). After the concentration using an Amicon Ultra filter (Merck Millipore; 3 kDa cutoff), the concentration of each complex capturing HasA was determined by UV/Vis spectroscopy. Initial Screening was performed using Wizard Classic 1 and 2 (Rigaku). A 1.0 μL aliquot of the concentrated CoOEOP-HasA solution (42 mg/mL) was mixed with a 1.0 μL of the reservoir solution composed of 20% (w/v) PEG 1000, 100 mM sodium phosphate dibasic/citric acid (pH 4.2), and 200 mM lithium sulfate. The drop was equilibrated against 50 μL of the reservoir solution. CoOEOP-HasA was crystalized by a sitting-drop vapor-diffusion method at 20°C for 3 days. A 1.0 μL aliquot of the concentrated CoEOP-HasA solution (60 mg/mL) was mixed with a 1.0 μL of the reservoir solution composed of 30% (w/v) PEG 8000, 100 mM sodium acetate/acetic acid (pH 4.5) and 200 mM lithium sulfate. The drop was equilibrated against 50 μL of the reservoir solution. CoEOP-HasA was crystalized by a sitting-drop vapor-diffusion method at 20°C for 2 days.

Data collection and refinement

Crystals were flash-cooled by liquid nitrogen. X-ray diffraction data sets were collected at SPring-8 (Hyogo, Japan) on the BL45XU beamline equipped with a PILATUS3 6M detector at a wavelength of 1.000 Å at 100 K. Reflection data was automatically processed with XDS¹² implemented in KAMO software¹³ (<https://github.com/keitaroyam/yamtbx>). Initial phases were determined by the molecular replacement method using MOLREP.¹⁴ The structure of HasA with heme (PDB ID: 3ELL)¹⁵ was used as a search model. Model building and refinement were performed on Coot,¹⁶ Phenix,¹⁷ and REFMAC5.¹⁸ The models were generated by eLBOW.¹⁹ All protein figures were depicted by using PyMOL2.²⁰

Evaluating the inhibitory effect of reconstructed HasA on *P. aeruginosa* growth

Growth experiments were performed according to a previously reported procedure.²¹

Synthesis of 2-(*N*-phenyl)amino-5,10,15-tris(3,5-di-*tert*-butylphenyl)porphyrin Ni(II) **A1-4a**

A Schlenk tube containing 2-iodo-5,10,15-tris(3,5-di-*tert*-butylphenyl)porphyrin Ni(II)²² **A1-3a** (42.3 mg, 40.0 μmol), Pd₂(dba)₃·CHCl₃ (2.10 mg, 2.03 μmol), XantPhos (2.31 mg, 4.00 μmol), and Cs₂CO₃ (26.1 mg, 80.1 μmol) was evacuated and then refilled with N₂. To the tube, 3.5 mL of dry and deoxygenated 1,4-dioxane and aniline (4.3 μL, 47 μmol) were added. The mixture was stirred at 80 °C for 22 h. The resulting mixture was filtered over a pad of Celite (dichloromethane as an eluent) and the solvent was evaporated in vacuo. The residue was purified by silica-gel column chromatography (dichloromethane/hexane = 1/3 as an eluent) to afford **A1-4a** (27.1 mg, 26.5 μmol) in 66% yield as a red solid. ¹H NMR (500 MHz, CDCl₃, 25 °C): δ = 9.69 (s, 1H, *meso*), 9.05 (d, *J* = 4.7 Hz, 1H, β), 8.90 (d, *J* = 4.7 Hz, 1H, β), 8.81–8.76 (m, 4H, β), 8.40 (s, 1H, β), 7.91 (d, *J* = 1.8 Hz, 2H, Ar-*o*), 7.90 (d, *J* = 1.8 Hz, 2H, Ar-*o*), 7.87 (d, *J* = 1.8 Hz, 2H, Ar-*o*), 7.73 (t, *J* = 1.8 Hz, 1H, Ar-*p*), 7.70 (t, *J* = 1.8 Hz, 1H, Ar-*p*), 7.68 (t, *J* = 1.8 Hz, 1H, Ar-*p*), 7.60 (d, *J* = 7.6 Hz, 2H, Ph-*o*) 7.41 (s, 1H, NH), 7.42 (t, *J* = 7.5 Hz, 2H, Ph-*m*), 7.06 (t, *J* = 7.4 Hz, 1H, Ph-*p*), 1.49 (s, 18H, *t*Bu), 1.49 (s, 18H, *t*Bu), 1.46 (s, 18H, *t*Bu) ppm; ¹³C NMR (126 MHz, CDCl₃, 25 °C): δ = 149.2, 149.1, 149.0, 144.6, 143.8, 143.8, 143.6, 142.8, 142.7, 142.5, 142.3, 142.0, 140.4, 140.2, 137.0, 132.7, 132.7, 131.9, 131.9, 131.7, 130.8, 129.3, 129.2, 128.9, 128.8, 121.3, 121.2, 121.2, 121.0, 120.9, 118.2, 116.9, 112.4, 98.35, 35.17, 35.16, 35.13, 31.86, 31.83 ppm; UV/Vis (CH₂Cl₂): λ_{max} (ε [M⁻¹ cm⁻¹]) = 412 (1.4 × 10⁵), 532 (1.1 × 10⁴), 567 (1.1 × 10⁴) nm; HRMS (ESI-TOF, positive mode): [M]⁺ Calcd for C₆₈H₇₇N₅Ni⁺ = 1021.5527; Found 1021.5594.

Synthesis of *N,N'*-diphenyldihydropyrazine-fused 5,10,15-tris(3,5-di-*tert*-butylphenyl)porphyrin Ni(II) dimer **A1-2a**

A Schlenk tube containing **A1-4a** (10.2 mg, 10.0 μmol) was evacuated and then refilled with N_2 . To the tube, 1.8 mL of the dry chloroform (degassed by freeze-pump-thaw method) was added. After a solution of 2,3-dichloro-5,6-dicyano-1,4-benzoquinone (DDQ) (4.54 mg, 20.0 μmol) in the dry chloroform (1.8 mL) was added, the mixture was stirred at room temperature for 2 h. The reaction was quenched with aqueous $\text{Na}_2\text{S}_2\text{O}_3$, and the mixture was extracted with dichloromethane. The combined organic layers were washed with water and brine, and dried over anhydrous Na_2SO_4 . After removing the solvent, the mixture was purified by silica-gel column chromatography (dichloromethane/hexane=1/3 as an eluent) to afford **A1-2a** (9.16 mg, 4.49 μmol) in 90% yield as a red solid. ^1H NMR (500 MHz, CDCl_3 , -15°C): δ = 9.13 (s, 2H, *meso*), 9.07 (d, J = 4.7 Hz, 2H, β), 8.97 (d, J = 4.7 Hz, 2H, β), 8.85-8.82 (m, 6H, β), 8.75 (d, J = 4.8 Hz, 2H, β), 8.29 (s, 2H, Ar-*o*), 8.13 (s, 2H, Ar-*o*), 8.08 (s, 2H, Ar-*o*), 7.92 (t, 2H, J = 1.8 Hz, Ar-*p*), 7.86 (s, 2H, Ar-*o*), 7.83 (s, 2H, Ar-*o*), 7.76 (t, 2H, J = 1.8 Hz, Ar-*p*), 7.72 (t, 2H, J = 1.8 Hz, Ar-*p*), 7.25 (s, 2H, Ar-*o*), 7.00 (d, J = 8.7 Hz, 4H, Ph-*o*), 6.64 (t, J = 8.5 Hz, 4H, Ph-*m*), 6.59 (t, J = 7.0 Hz, 2H, Ph-*p*), 1.56 (s, 18H, *t*Bu), 1.53 (s, 18H, *t*Bu), 1.50 (s, 18H, *t*Bu), 1.50 (s, 18H, *t*Bu), 1.45 (s, 18H, *t*Bu), 0.44 (s, 18H, *t*Bu) ppm; ^{13}C NMR (126 MHz, CDCl_3 , 25°C): δ = 149.3, 149.2, 149.1, 149.0, 146.9, 144.8, 144.0, 143.8, 143.6, 143.4, 141.9, 140.2, 140.1, 139.6, 135.5, 135.2, 132.9, 132.2, 132.2, 129.1, 128.1, 121.5, 121.3, 121.3, 121.2, 120.4, 118.9, 116.1, 103.0, 35.24, 35.19, 31.91, 31.87 ppm; UV/Vis (CH_2Cl_2): λ_{max} (ϵ [$\text{M}^{-1}\text{cm}^{-1}$]) = 415 (2.5×10^5), 425 (2.6×10^5), 532 (3.1×10^4), 565 (1.5×10^4) nm; HRMS (ESI-TOF, positive mode): $[\text{M}]^+$ Calcd for $\text{C}_{136}\text{H}_{150}\text{N}_{10}\text{Ni}_2$ 2039.0746; Found 2039.0440.

Synthesis of 2-(*N*-phenyl)amino-5,15-bis(3,5-di-*tert*-butylphenyl)-10-triisopropylsilylethynylporphyrin Ni(II) **A1-4b**

A Schlenk tube containing **A1-3b** (37.5 mg, 36.0 μmol), $\text{Pd}_2(\text{dba})_3 \cdot \text{CHCl}_3$ (1.86 mg, 1.80 μmol), XantPhos (2.09 mg, 3.62 μmol), and Cs_2CO_3 (26.0 mg, 79.8 μmol) was evacuated and then refilled with N_2 . To the Schlenk tube, 3.2 mL of dry and deoxygenated 1,4-dioxane and aniline (4.0 μL , 44 μmol) were added. The mixture was stirred at 90°C for 24.5 h. The resulting mixture was filtered over a pad of Celite (dichloromethane as an eluent) and the solvent was evaporated in vacuo. The residue was purified by silica-gel column chromatography (dichloromethane/hexane = 1/5 as an eluent) to afford **A1-4b** (26.0 mg, 25.8 μmol) in 72% yield as a green solid. ^1H NMR (500 MHz, CDCl_3 , 25°C): δ = 9.57 (d, J = 4.6 Hz, 1H, β), 9.54 (s, 1H, *meso*), 9.50 (d, J = 4.8 Hz, 1H, β), 9.45 (d, J = 4.9 Hz, 1H, β), 9.07 (s, 1H, β), 8.99 (d, J = 4.7 Hz, 2H, β), 8.75 (d, J = 4.8 Hz, 1H, β), 8.73 (d, J = 4.8 Hz, 1H, β), 7.32 (d, J = 1.8 Hz, 2H, Ar-*o*), 7.72 (t, J = 1.8 Hz, 1H, Ar-*p*), 7.70 (d, J = 8.5 Hz, 2H, Ph-*o*), 7.56 (s, 1H, NH), 7.52 (t, J = 7.4 Hz, 2H,

Ph-*m*), 7.16 (t, $J = 7.4$ Hz, 2H, Ph-*p*), 1.49 (s, 18H, *t*Bu), 1.40 (s, 18H, *i*Pr), 1.39 (s, 3H, *i*Pr), 1.38 (s, 18H, *i*Pr), 1.37 (s, 3H, *i*Pr) ppm; ^{13}C NMR (126 MHz, CDCl_3 , 25 °C): $\delta = 149.1, 147.2, 146.0, 145.9, 144.4, 144.1, 143.2, 143.1, 142.7, 142.5, 139.7, 137.1, 133.7, 132.6, 131.9, 131.4, 131.0, 131.0, 129.9, 128.6, 122.6, 122.1, 121.5, 117.6, 109.3, 107.5, 107.1, 101.4, 99.50, 99.44, 98.76, 98.15, 35.14, 31.84, 19.20, 11.92, 11.89$ ppm; UV/Vis (CH_2Cl_2): λ_{max} (ϵ [$\text{M}^{-1} \text{cm}^{-1}$]) = 477 (1.4×10^5), 635 (1.6×10^4), 674 (1.1×10^4) nm; HRMS (ESI-TOF, positive mode): $[\text{M}]^+$ Calcd for $\text{C}_{68}\text{H}_{77}\text{N}_5\text{Ni}$ 1021.5527; Found 1021.5595.

Synthesis of *N,N'*-diphenyldihydropyrazine-fused 5,15-bis(triisopropylsilylethynyl)-10-(3,5-di-*tert*-butylphenyl)porphyrin Ni(II) dimer **A1-2b**

A Schlenk tube of containing **A1-4b** (10.5 mg, 10.4 μmol) was evacuated and then refilled with N_2 . To the Schlenk tube, 4.0 mL of the dry α,α,α -trifluorotoluene (degassed by freeze-pump-thaw method) was added. To the solution, a solution of DDQ (4.54 mg, 20.0 μmol) in dry trifluorotoluene (4.0 mL) was added. The mixture was stirred at room temperature for 3 h. The reaction was quenched with aqueous $\text{Na}_2\text{S}_2\text{O}_3$, and the mixture was extracted with dichloromethane. The combined organic layers were washed with water and brine, and dried over anhydrous Na_2SO_4 . After removing the solvent, the mixture was purified by silica-gel column chromatography (dichloromethane/hexane = 1/4 as an eluent) to afford **A1-2b** (7.94 mg, 3.95 μmol) in 76% yield as a green-purple solid. ^1H NMR (500 MHz, CDCl_3 , 25 °C): $\delta = 10.1$ (s, 2H, *meso*), 9.71 (d, $J = 4.9$ Hz, 2H, β), 9.59 (d, $J = 4.7$ Hz, 2H, β), 9.48 (d, $J = 4.9$ Hz, 2H, β), 9.03 (d, $J = 4.8$ Hz, 2H, β), 8.77 (d, $J = 4.9$ Hz, 2H, β), 8.76 (d, $J = 5.0$ Hz, 2H, β), 7.85 (br, 4H, Ar-*o*), 7.75 (t, $J = 1.8$ Hz, 2H, Ar-*p*), 7.54 (d, $J = 8.9$ Hz, 4H, Ph-*o*), 6.91 (t, $J = 7.25$ Hz, 4H, Ph-*m*), 6.76 (t, $J = 7.3$ Hz, 2H, Ph-*p*), 1.50 (s, 36H, *i*Pr), 1.41 (s, 18H + 3H, *i*Pr), 1.40 (s, 18H, *t*Bu), 1.29 (s, 18H + 3H, *i*Pr), 1.27 (s, 18H, *t*Bu) ppm; ^{13}C NMR (126 MHz, CDCl_3 , 25 °C): $\delta = 151.1, 150.1, 149.5, 149.3, 146.9, 145.5, 145.4, 143.0, 142.6, 142.4, 139.3, 136.4, 135.3, 133.5, 133.4, 133.1, 133.0, 132.6, 131.7, 128.6, 128.5, 123.0, 121.7, 121.6, 117.0, 106.9, 106.7, 106.4, 103.2, 100.3, 99.90, 99.04, 35.18, 31.85, 19.21, 12.44, 11.92$ ppm; UV/Vis (CH_2Cl_2): λ_{max} (ϵ [$\text{M}^{-1} \text{cm}^{-1}$]) = 484 (3.0×10^5), 612 (2.6×10^4), 651 (4.2×10^4) nm; HR-MS (ESI-TOF, positive mode): $[\text{M}]^+$ Calcd for $\text{C}_{124}\text{H}_{150}\text{N}_{10}\text{Ni}_2\text{Si}_2$ 2006.9823; Found 2006.9346.

Oxidation of **A2-3a** with PIFA in the presence of H_2O

To a round-bottomed flask, **A2-3a**²³ (44.5 mg, 49.9 μmol), dichloromethane (10 mL), and water (10 μL) were added. PIFA (21.6 mg, 50.2 μmol) was added to the mixture. The resulting mixture was stirred at room temperature for 30 min. The reaction was quenched with sat. NaHCO_3 aq., and the mixture was extracted with dichloromethane. The combined organic layers were washed with water and brine, and dried over anhydrous Na_2SO_4 . After removing the solvent, the

mixture was purified by silica-gel column chromatography (dichloromethane/hexane/triethylamine = 100/50/3 as an eluent). The first yellowish green band was collected. After removal of the solvent in vacuo, recrystallization from dichloromethane/acetonitrile afforded **A2-7a** (10.1 mg, 11.1 μ mol) in 22% yield as a green solid. The second blue-purple band was found to be a mixture of unidentifiable compounds. The third blue band was collected. After removal of the solvent in vacuo, recrystallization from acetonitrile provided **A2-6a** (19.4 mg, 21.4 μ mol) in 43% yield as a blue solid. **A2-7a**: ^1H NMR (500 MHz, CDCl_3 , 25 $^\circ\text{C}$): δ = 13.61 (br-s, 2H, NH), 7.74 (d, J = 1.8 Hz, 2H, Ar-*o*), 7.52 (t, J = 1.8 Hz, 2H, Ar-*p*), 7.39 (t, J = 1.7 Hz, 1H, Ar-*p*), 7.25 (d, J = 1.7 Hz, 4H, Ar-*o*), 7.14 (d, J = 4.4 Hz, 2H, β), 6.68 (d, J = 4.4 Hz, 2H, β), 6.61 (d, J = 4.4 Hz, 2H, β), 6.46 (d, J = 4.4 Hz, 2H, β), 3.30 (br-s, 1H, OH), 1.34 (s, 36H, *t*Bu), and 1.29 (s, 18H, *t*Bu) ppm; ^{13}C NMR (126 MHz, CDCl_3 , 25 $^\circ\text{C}$): δ = 177.46, 151.23, 150.11, 146.82, 142.23, 136.74, 131.54, 128.80, 125.95, 123.43, 122.37, 120.7, 118.09, 76.39, 35.23, 34.99, 31.56, and 31.52 ppm; UV/Vis (CH_2Cl_2): λ_{max} (ϵ [$\text{M}^{-1} \text{cm}^{-1}$]) = 418 (4.4×10^4), 471 (1.7×10^4), and 570 (3.5×10^3) nm; HRMS (APCI-TOF, positive mode): $[\text{M}]^+$ Calcd for $\text{C}_{62}\text{H}_{74}\text{N}_4\text{O}_2$ 906.5806; Found 906.5806. **A2-6a**: ^1H NMR (500 MHz, CDCl_3 , 25 $^\circ\text{C}$): δ = 13.66 (br-s, 1H, NH), 12.86 (br-s, 1H, NH), 7.51 (t, J = 1.8 Hz, 1H, Ar-*p*), 7.50–7.47 (m, 2H + 1H, Ar-*o* + Ar-*p*), 7.37 (t, J = 1.7 Hz, 1H, Ar-*p*), 7.27 (d, J = 1.7 Hz, 2H, Ar-*o*), 7.23–7.17 (m, 2H + 1H, Ar-*o* + β), 7.11 (d, J = 4.7 Hz, 1H, β), 6.96 (d, J = 4.7 Hz, 1H, β), 6.80–6.75 (m, 2H, β), 6.48 (dd, J_1 = 4.0 Hz, J_2 = 2.4 Hz, 1H, β), 6.24 (dd, J_1 = 4.3, J_2 = 2.3 Hz, 1H, β), 6.10 (dd, J_1 = 4.3, J_2 = 2.3 Hz, 1H, β), 3.11 (br-s, 1H, OH), 1.35 (s, 18H, *t*Bu), 1.33 (s, 18H, *t*Bu), 1.27 (s, 18H, *t*Bu) ppm; ^{13}C NMR (126 MHz, CDCl_3 , 25 $^\circ\text{C}$): δ = 181.69, 176.04, 168.29, 153.02, 152.77, 150.98, 150.23, 146.27, 144.13, 143.41, 141.83, 140.89, 139.35, 136.79, 136.69, 136.54, 132.67, 126.04, 125.83, 125.43, 125.38, 123.07, 123.04, 122.86, 122.28, 120.85, 116.77, 109.82, 76.51, 35.17, 35.03, 34.99, 31.57, 31.54, 31.53 ppm; UV/Vis (CH_2Cl_2): λ_{max} (ϵ [$\text{M}^{-1} \text{cm}^{-1}$]) = 387 (4.3×10^4), 589 (1.2×10^4), and 633 (1.3×10^4) nm; HRMS (APCI-TOF, positive mode): $[\text{M}+\text{H}]^+$ Calcd for $\text{C}_{62}\text{H}_{75}\text{N}_4\text{O}_2$ 907.5885; Found 907.5858.

Oxidation of **A2-3b** with PIFA in the presence of H_2O

To a round-bottomed flask, **A2-3b**²³ (47.4 mg, 50.0 μ mol), dichloromethane (10 mL), and water (10 μ L) were added. After sonicating the flask, PIFA (21.5 mg, 50.0 μ mol) was added to the mixture. The resulting mixture was stirred at room temperature for 30 min. The reaction was quenched with sat. NaHCO_3 aq., and the mixture was extracted with dichloromethane. The combined organic layers were washed with water and brine, and dried over anhydrous Na_2SO_4 . After removing the solvent, the mixture was purified by silica-gel column chromatography (dichloromethane/hexane/triethylamine = 100/50/3 as an eluent). After removal of the solvent in vacuo, recrystallization from dichloromethane/acetonitrile afforded **A2-7b** (6.69 mg, 6.94 μ mol)

in 14% yield as a red solid. ^1H NMR (500 MHz, CDCl_3 , 60 $^\circ\text{C}$): δ = 8.61 (d, J = 1.8 Hz, 2H, Ar-*o*), 7.56 (t, J = 1.8 Hz, 1H, Ar-*p*), 7.51 (t, J = 1.9 Hz, 2H, Ar-*p*), 7.23 (br-s, 4H, Ar-*o*), 6.78 (d, J = 4.4 Hz, 2H, β), 6.62 (d, J = 4.6 Hz, 2H, β), 6.60 (d, J = 4.7 Hz, 2H, β), 6.25 (d, J = 4.4 Hz, 2H, β), 2.67 (br-s, 1H, OH), 1.46 (s, 18H, *t*Bu), 1.35 (s, 36H, *t*Bu) ppm; ^{13}C NMR (126 MHz, CDCl_3 , 25 $^\circ\text{C}$): δ = 178.58, 167.744, 151.98, 150.22, 149.65, 148.90, 141.93, 139.89, 139.41, 135.88, 135.32, 129.95, 124.88, 123.21, 122.94, 120.79, 119.65, 118.91, 77.99, 35.50, 35.01, 31.72, 31.56 ppm; UV/Vis (CH_2Cl_2): λ_{max} (ϵ [$\text{M}^{-1} \text{cm}^{-1}$]) = 331 (2.2×10^4), 389 (1.7×10^4), 443 (6.2×10^4), 569 (7.0×10^3), and 728 (2.0×10^3) nm; HRMS (APCI-TOF, positive mode): $[\text{M}]^+$ Calcd for $\text{C}_{62}\text{H}_{72}\text{N}_4\text{O}_2\text{Ni}$ 962.5003; Found 962.4985.

Nickel(II) complexation of **A2-6a**

A round-bottomed flask containing **A2-6a** (13.6 mg, 15.0 μmol) and $\text{Ni}(\text{OAc})_2 \cdot 4\text{H}_2\text{O}$ (18.7 mg, 75.1 μmol) was charged with dichloromethane (5.0 mL) and methanol (2.0 mL). The mixture was stirred at room temperature for 5 min. After removing the solvent, the mixture was purified by silica-gel column chromatography (dichloromethane/ethyl acetate/triethylamine = 100/5/3 as an eluent) to afford **A2-6b** (13.7 mg, 14.2 μmol) in 95% yield as a purple solid. ^1H NMR (500 MHz, CDCl_3 , 25 $^\circ\text{C}$): δ = 8.69 (br-s, 2H, Ar-*o*), 7.55 (t, J = 1.8 Hz, 1H, Ar-*p*), 7.50 (t, J = 1.8 Hz, 1H, Ar-*p*), 7.46 (t, J = 1.8 Hz, 1H, Ar-*p*), 7.16 (br-s, 2H, Ar-*o*), 7.11 (br-s, 2H, Ar-*o*), 7.06 (d, J = 4.0 Hz, 1H, β), 6.86 (d, J = 4.8 Hz, 1H, β), 6.84 (d, J = 4.8 Hz, 1H, β), 6.67 (d, J = 4.9 Hz, 1H, β), 6.66 (d, J = 4.8 Hz, 1H, β), 6.32 (d, J = 4.0 Hz, 1H, β), 6.11 (d, J = 4.5 Hz, 1H, β), 5.94 (d, J = 4.6 Hz, 1H, β), 2.69 (br-s, 1H, OH), 1.47 (s, 18H, *t*Bu), 1.33 (s, 18H, *t*Bu), 1.30 (s, 18H, *t*Bu) ppm; ^{13}C NMR (126 MHz, CDCl_3 , 25 $^\circ\text{C}$): δ = 176.61, 174.10, 162.06, 151.51, 150.58, 150.55, 149.86, 149.29, 145.87, 145.80, 145.14, 144.07, 142.67, 142.14, 138.93, 136.47, 135.14, 135.04, 134.49, 129.89, 127.45, 124.69, 124.49, 123.81, 123.46, 123.33, 122.85, 122.54, 121.09, 120.55, 111.37, 77.78, 35.53, 35.04, 35.02, 31.79, 31.52 ppm; UV/Vis (CH_2Cl_2): λ_{max} (ϵ [$\text{M}^{-1} \text{cm}^{-1}$]) = 336 (1.9×10^4), 406 (3.2×10^4), 554 (9.0×10^3), and 819 (5.0×10^3) nm; HRMS (APCI-TOF, positive mode): $[\text{M}]^+$ Calcd for $\text{C}_{62}\text{H}_{72}\text{N}_4\text{O}_2\text{Ni}$ 962.5003; Found 962.4960.

Nickel(II) complexation of **A2-7a**

A round-bottomed flask containing **A2-7a** (13.6 mg, 15.0 μmol) and $\text{Ni}(\text{OAc})_2 \cdot 4\text{H}_2\text{O}$ (18.6 mg, 74.8 μmol) was charged with dichloromethane (5.0 mL) and methanol (2.0 mL). The mixture was stirred at room temperature for 80 min. The reaction was quenched with sat. NaHCO_3 aq., and the mixture was extracted with dichloromethane. The combined organic layers were washed with water and brine, and dried over anhydrous Na_2SO_4 . After removing the solvent, the mixture was purified by silica-gel column chromatography (dichloromethane/hexane/triethylamine = 100/50/3 as an eluent) to afford **A2-7b** (13.6 mg, 14.0 μmol) in 94% yield as a red solid.

E-3. Crystallographic data

Chapter 2

compound	2-5(OTf)^a	2-5[BAr^F₄]	3-1
formula	C ₃₅ H ₄₅ N ₄ O, CF ₃ O ₃ S [−] , 0.5(C ₆ H ₆)	C ₃₅ H ₄₃ N ₄ O ⁺ , C ₃₂ H ₁₂ BF ₂₄ [−] , 0.5(C ₆ H ₁₂)	C ₃₅ H ₄₅ N ₄ O ₂ Zn ⁺ , C ₃₂ H ₁₂ BF ₂₄ [−] , 0.5(C ₆ H ₁₂), H ₂ O
formula weight	725.87	1443.05	1584.51
crystal system	triclinic	triclinic	monoclinic
space group	<i>P</i> -1 (No. 2)	<i>P</i> -1 (No. 2)	<i>P</i> 2 ₁ / <i>c</i> (No. 14)
crystal color	purple	purple	purple
crystal description	block	plate	block
<i>a</i> [Å]	10.9921(2)	13.3760(3)	16.6389(5)
<i>b</i> [Å]	11.6438(2)	14.6712(3)	16.7946(5)
<i>c</i> [Å]	15.9803(3)	18.5644(4)	26.1992(8)
α [°]	108.458(2)	108.129(2)	90
β [°]	102.422(2)	99.319(2)	93.5900(10)
γ [°]	97.426(2)	99.318(2)	90
<i>V</i> [Å ³]	1851.18(6)	3327.87(13)	7306.8(4)
<i>Z</i>	2	2	4
<i>d</i> _{calcd} [g cm ^{−3}]	1.302	1.440	1.440
<i>R</i> ₁ (<i>I</i> > 2σ(<i>I</i>))	0.0637	0.0770	0.0494
<i>wR</i> ₂ (all data)	0.1637	0.2122	0.1318
goodness-of-fit	1.031	1.018	1.028
temperature [K]	93(2)	93(2)	93(2)
solvent	chloroform ^b benzene	chloroform ^b cyclohexane	dichloroethane cyclohexane

^a The crystal was prepared in a glovebox to avoid hydrolysis.

^b Chloroform stabilized with amylene was used to prevent ring-opening by ethanol added as a stabilizer.

Chapter 3

compound	3-2	3-3	3-4
formula	C ₃₅ H ₄₆ N ₄ OS	C ₃₅ H ₄₅ N ₄ S ⁺ , C ₃₂ H ₁₂ BF ₂₄ ⁻ , 0.5(C ₆ H ₁₂)	C ₃₅ H ₄₃ N ₄ SZn ⁺ , C ₃₂ H ₁₂ BF ₂₄ ⁻ , 1.5(C ₆ H ₆)
formula weight	570.82	1459.11	1597.55
crystal system	monoclinic	triclinic	triclinic
space group	<i>P</i> 2 ₁ / <i>n</i> (No. 14)	<i>P</i> -1 (No. 2)	<i>P</i> -1 (No. 2)
crystal color	purple	purple	purple
crystal description	block	block	block
<i>a</i> [Å]	11.9883(5)	13.4974(6)	15.2381(2)
<i>b</i> [Å]	21.0001(7)	14.6725(7)	15.9224(3)
<i>c</i> [Å]	12.8601(5)	18.5690(9)	16.4963(3)
α [°]	90	107.949(2)	80.9350(10)
β [°]	103.3000(10)	99.555(2)	63.946(2)
γ [°]	90	99.629(2)	89.9040(10)
<i>V</i> [Å ³]	3150.8(2)	3355.1(3)	3540.51(12)
<i>Z</i>	4	2	2
<i>d</i> _{calcd} [g cm ⁻³]	1.203	1.444	1.499
<i>R</i> ₁ (<i>I</i> > 2σ(<i>I</i>))	0.0655	0.0683	0.0473
<i>wR</i> ₂ (all data)	0.1270	0.1807	0.1289
goodness-of-fit	1.113	1.015	1.034
temperature [K]	93(2)	93(2)	93(2)
solvent	chloroform hexane	dichloroethane cyclohexane	chloroform benzene

Chapter 4

compound	4-1	4-2	4-3
formula	C ₄₁ H ₅₁ N ₅ O	C ₄₁ H ₅₀ N ₅ ⁺ , CF ₃ O ₃ S ⁻	C ₄₁ H ₅₀ N ₅ ⁺ , C ₃₂ H ₁₂ BF ₂₄ ⁻ C ₆ H ₁₂
formula weight	629.86	761.93	1560.24
crystal system	monoclinic	triclinic	triclinic
space group	<i>P</i> 2 ₁ / <i>c</i> (No. 14)	<i>P</i> -1 (No. 2)	<i>P</i> -1 (No. 2)
crystal color	green	purple	purple
crystal description	block	plate	plate
<i>a</i> [Å]	19.9080(5)	10.4627(2)	12.7175(2)
<i>b</i> [Å]	14.5343(4)	13.6823(2)	16.1660(3)
<i>c</i> [Å]	12.1651(3)	14.6582(2)	19.4702(3)
α [°]	90	80.1340(10)	72.649(2)
β [°]	97.937(2)	77.7650(10)	89.7130(10)
γ [°]	90	76.2820(10)	85.2950(10)
<i>V</i> [Å ³]	3486.24(16)	1975.95(6)	3807.08(12)
<i>Z</i>	4	2	2
<i>d</i> _{calcd} [g cm ⁻³]	1.200	1.281	1.361
<i>R</i> ₁ (<i>I</i> > 2σ(<i>I</i>))	0.0758	0.0414	0.0636
<i>wR</i> ₂ (all data)	0.1779	0.1077	0.1779
goodness-of-fit	1.035	1.018	1.032
temperature [K]	93(2)	93(2)	93(2)
solvent	chloroform cyclohexane	dichloroethane cyclohexane	dichloroethane cyclohexane

Chapter 5

compound	5-1	5-2	5-3FB
formula	$\text{C}_{35}\text{H}_{43}\text{N}_4\text{NiO}^+$, $\text{CF}_3\text{O}_3\text{S}^-$, $0.5(\text{C}_6\text{H}_6)$	$\text{C}_{35}\text{H}_{43}\text{ClN}_4\text{OZn}$, C_6H_{12}	$\text{C}_{35}\text{H}_{45}\text{N}_4\text{O}^+$, $\text{C}_{10}\text{N}_5^-$
formula weight	782.57	720.71	727.90
crystal system	triclinic	triclinic	triclinic
space group	<i>P</i> -1 (No. 2)	<i>P</i> -1 (No. 2)	<i>P</i> -1 (No. 2)
crystal color	purple	purple	purple
crystal description	block	plate	block
<i>a</i> [Å]	11.0202(2)	10.4223(5)	13.1662(4)
<i>b</i> [Å]	11.4897(2)	11.9901(7)	13.8960(3)
<i>c</i> [Å]	15.8377(3)	15.5674(9)	23.5817(4)
α [°]	107.966(2)	79.849(2)	82.864(2)
β [°]	102.793(2)	82.714(2)	82.483(2)
γ [°]	97.644(2)	79.855(2)	66.338(3)
<i>V</i> [Å ³]	1815.88(6)	1875.75(18)	3905.53(18)
<i>Z</i>	2	2	4
<i>d</i> _{calcd} [g cm ⁻³]	1.431	1.276	1.238
<i>R</i> ₁ (<i>I</i> > 2σ(<i>I</i>))	0.0526	0.0439	0.1208
<i>wR</i> ₂ (all data)	0.1455	0.0860	0.3805
goodness-of-fit	1.038	1.130	1.362
temperature [K]	93(2)	93(2)	93(2)
solvent	dichloromethane benzene	dichloroethane cyclohexane	dichloroethane benzene

Chapter 5 & 6

compound	5-3Zn	5-3Ni	NiOEOP
formula	$\text{C}_{35}\text{H}_{43}\text{N}_4\text{OZn}^+$, $\text{C}_{10}\text{N}_5^-$	$\text{C}_{35}\text{H}_{43}\text{N}_4\text{NiO}^+$, $\text{C}_{10}\text{N}_5^-$	$\text{C}_{35}\text{H}_{43}\text{N}_4\text{NiO}^+$, $\text{C}_{32}\text{H}_{12}\text{BF}_{24}^-$, $0.5(\text{C}_6\text{H}_{12})$
formula weight	791.25	784.59	1499.74
crystal system	monoclinic	orthorhombic	triclinic
space group	$C2/c$ (No. 15)	$Cmca$ (No. 64)	$P-1$ (No. 2)
crystal color	purple	purple	purple
crystal description	block	block	block
a [Å]	11.8316(2)	31.7189(9)	13.5008(4)
b [Å]	15.0381(2)	29.1124(8)	14.5592(4)
c [Å]	21.3062(4)	16.8723(4)	18.5114(6)
α [°]	90	90	108.0490(10)
β [°]	91.680(2)	90	99.8160(10)
γ [°]	90	90	99.8440(10)
V [Å ³]	3789.27(11)	15580.1(7)	3310.24(17)
Z	4	16	2
d_{calcd} [g cm ⁻³]	1.387	1.338	1.505
R_1 ($I > 2\sigma(I)$)	0.0318	0.0629	0.0571
wR_2 (all data)	0.0807	0.1654	0.1397
goodness-of-fit	1.089	1.133	1.036
temperature [K]	93(2)	93(2)	93(2)
solvent	dichloroethane cyclohexane	chloroform benzene	dichloroethane cyclohexane

Chapter 6 & Appendix 1

compound	CoOEOP	AgOEOP	A1-2a
formula	$\text{C}_{35}\text{H}_{43}\text{N}_4\text{NiO}^+$, $\text{C}_{32}\text{H}_{12}\text{BF}_{24}^-$, $1.5(\text{C}_6\text{H}_6)$, $0.5(\text{C}_2\text{H}_4\text{Cl}_2)$	$\text{C}_{35}\text{H}_{43}\text{AgN}_4\text{O}^+$, $\text{C}_{32}\text{H}_{12}\text{BF}_{24}^-$, $0.5(\text{C}_6\text{H}_{12})$	$\text{C}_{136}\text{H}_{150}\text{N}_{10}\text{Ni}_2$, $\text{CHCl}_{3.33}$, $1.853(\text{CHCl}_3)$
formula weight	1624.52	1548.90	2394.32
crystal system	triclinic	triclinic	triclinic
space group	<i>P</i> -1 (No. 2)	<i>P</i> -1 (No. 2)	<i>P</i> -1 (No. 2)
crystal color	purple	purple	red
crystal description	block	plate	prism
<i>a</i> [Å]	15.5622(5)	13.3465(5)	16.1831(4)
<i>b</i> [Å]	15.6847(5)	14.7153(5)	17.5405(4)
<i>c</i> [Å]	16.3766(4)	18.5674(7)	24.2054(6)
α [°]	64.8190(10)	108.1800(10)	103.795(2)
β [°]	87.9970(10)	99.2110(10)	98.948(2)
γ [°]	85.0580(10)	99.4610(10)	102.536(2)
<i>V</i> [Å ³]	3604.01(19)	3329.4(2)	6356.0(3)
<i>Z</i>	2	2	2
<i>d</i> _{calcd} [g cm ⁻³]	1.497	1.545	1.251
<i>R</i> ₁ (<i>I</i> > 2σ(<i>I</i>))	0.0402	0.0491	0.0998
<i>wR</i> ₂ (all data)	0.1005	0.1372	0.3206
goodness-of-fit	1.014	1.194	1.011
temperature [K]	93(2)	93(2)	93(2)
solvent	dichloroethane benzene	dichloroethane cyclohexane	chloroform methanol

Chapter 6

	CoOEOP-HasA	CoOEP-HasA
PDB ID	7VF8	7VF7
Data collection		
Beamline (Spring-8)	BL45XU	BL45XU
Wavelength (Å)	1.0000	1.0000
Space group	$P6_1$	$P2_12_12_1$
Cell dimensions		
a, b, c (Å)	153.84, 153.84, 37.75	46.28, 76.12, 168.62
α, β, γ (°)	90, 90, 120	90, 90, 90
Resolution (Å)	44.45–1.35	45.26–1.35
	(1.43–1.35) ^c	(1.39–1.35) ^c
Total No. of reflections	2228601	3781691
No. of unique reflections	111120	131672
R_{merge} (%)	12.2 (167.7)	11.1 (453.4)
Completeness (%)	98.5 (97.0)	100.0 (100.0)
$\langle I/\sigma(I) \rangle$	21.25 (1.91)	15.59 (1.25)
$CC_{1/2}$ (%)	99.9 (74.5)	99.9 (50.4)
Multiplicity	20.1 (20.2)	28.7 (27.3)
Wilson B factor (Å ²)	16.4	20.0
Refinement statistics		
Resolution (Å)	44.45–1.35	46.28–1.35
No. of monomers per asymmetric unit	2	3
$R_{\text{work}}/R_{\text{free}}$ (%)	12.8/14.4	13.8/16.2
RMSD bond lengths (Å)	0.007	0.008
RMSD bond angles (°)	1.42	1.42
No. of non-hydrogen atoms	3632	5083
Average B -factor (Å ²)	19.0	26.0

RMSD, root-mean-square deviations.

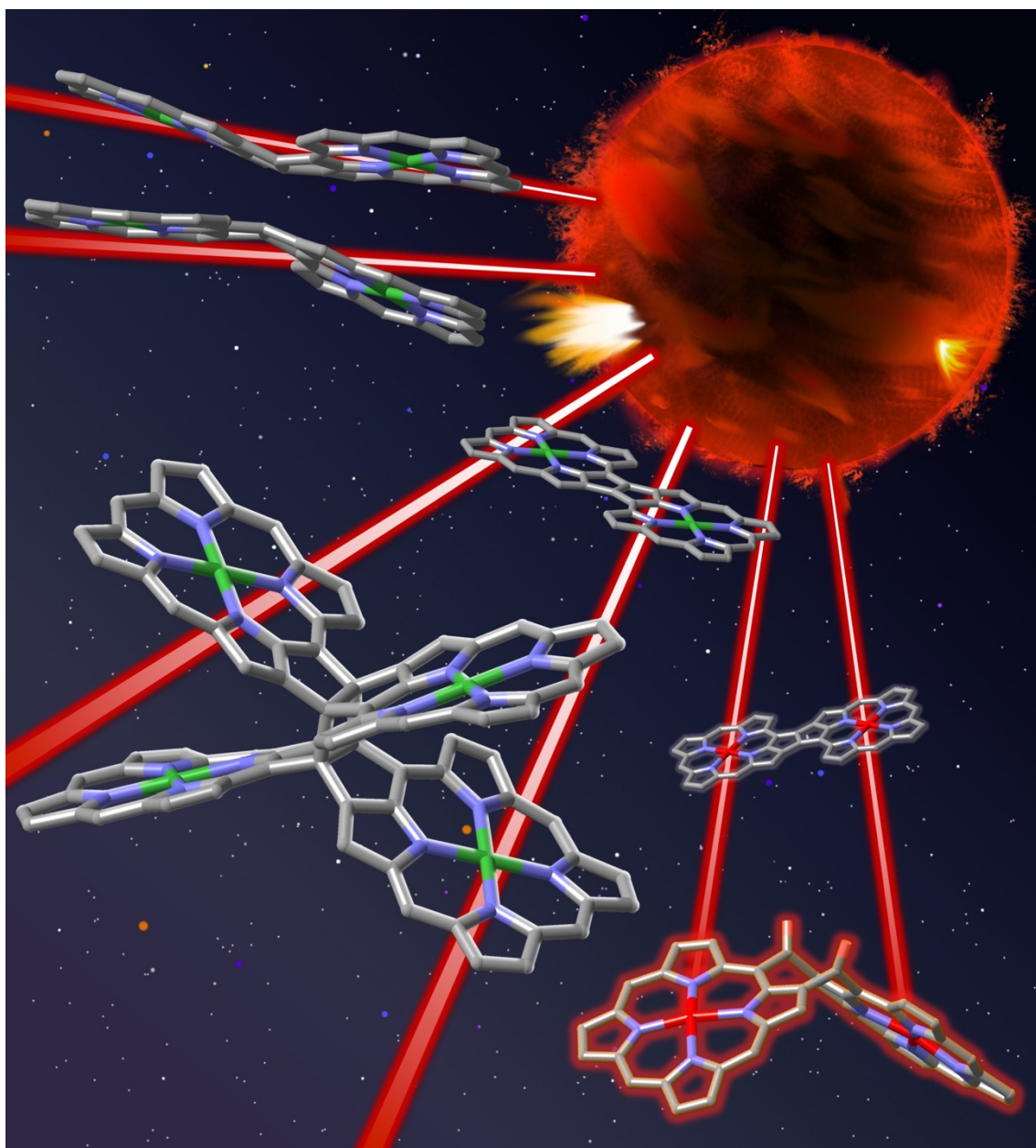
^c Values in parentheses are for the highest-resolution shell.

E-4. References

1. Frisch, M. J.; Trucks, G. W.; Schlegel, H. B.; Scuseria, G. E.; Robb, M. A.; Cheeseman, J. R.; Scalmani, G.; Barone, V.; Mennucci, B.; Petersson, G. A.; Nakatsuji, H.; Caricato, M.; Li, X.; Hratchian, H. P.; Izmaylov, A. F.; Bloino, J.; Zheng, G.; Sonnenberg, J. L.; Hada, M.; Ehara, M.; Toyota, K.; Fukuda, R.; Hasegawa, J.; Ishida, M.; Nakajima, T.; Honda, Y.; Kitao, O.; Nakai, H.; Vreven, T.; Montgomery, J. A., Jr.; Peralta, J. E.; Ogliaro, F.; Bearpark, M.; Heyd, J. J.; Brothers, E.; Kudin, K. N.; Staroverov, V. N.; Kobayashi, R.; Normand, J.; Raghavachari, K.; Rendell, A.; Burant, J. C.; Iyengar, S. S.; Tomasi, J.; Cossi, M.; Rega, N.; Millam, J. M.; Klene, M.; Knox, J. E.; Cross, J. B.; Bakken, V.; Adamo, C.; Jaramillo, J.; Gomperts, R.; Stratmann, R. E.; Yazyev, O.; Austin, A. J.; Cammi, R.; Pomelli, C.; Ochterski, J. W.; Martin, R. L.; Morokuma, K.; Zakrzewski, V. G.; Voth, G. A.; Salvador, P.; Dannenberg, J. J.; Dapprich, S.; Daniels, A. D.; Farkas, O.; Foresman, J. B.; Ortiz, J. V.; Cioslowski, J.; Fox, D. J. *Gaussian 09*, revision E.01; Gaussian, Inc.: Wallingford, CT, 2009.
2. Becke, A. D. *J. Chem. Phys.* **1993**, *98*, 5648–5652.
3. Yanai, T.; Tew, D. P.; Handy, N. C. *Chem. Phys. Lett.* **2004**, *393*, 51–57.
4. Software to optimize reaction paths along the user's expected ones, HPC Systems Inc., <http://www.hpc.co.jp/chem/react1.html>.
5. (a) Jónsson, H.; Mills, G.; Jacobsen, K. W. In *Classical and Quantum Dynamics in Condensed Phase Simulations*; Berne, B. J.; Ciccotti, G.; Coker, D. F., Eds.; World Scientific Publishing: Singapore, 1998; pp 385–404. (b) G. Henkelman, H. Jónsson, *J. Chem. Phys.* **2000**, *113*, 9978–9985.
6. Frisch, M. J.; Trucks, G. W.; Schlegel, H. B.; Scuseria, G. E.; Robb, M. A.; Cheeseman, J. R.; Scalmani, G.; Barone, V.; Petersson, G. A.; Nakatsuji, H.; Li, X.; Caricato, M.; Marenich, A. V.; Bloino, J.; Janesko, B. G.; Gomperts, R.; Mennucci, B.; Hratchian, H. P.; Ortiz, J. V.; Izmaylov, A. F.; Sonnenberg, J. L.; Williams-Young, D.; Ding, F.; Lipparini, F.; Egidi, F.; Goings, J.; Peng, B.; Petrone, A.; Henderson, T.; Ranasinghe, D.; Zakrzewski, V. G.; Gao, J.; Rega, N.; Zheng, G.; Liang, W.; Hada, M.; Ehara, M.; Toyota, K.; Fukuda, R.; Hasegawa, J.; Ishida, M.; Nakajima, T.; Honda, Y.; Kitao, O.; Nakai, H.; Vreven, T.; Throssell, K.; Montgomery, J. A., Jr.; Peralta, J. E.; Ogliaro, F.; Bearpark, M. J.; Heyd, J. J.; Brothers, E. N.; Kudin, K. N.; Staroverov, V. N.; Keith, T. A.; Kobayashi, R.; Normand, J.; Raghavachari, K.; Rendell, A. P.; Burant, J. C.; Iyengar, S. S.; Tomasi, J.; Cossi, M.; Millam, J. M.; Klene, M.; Adamo, C.; Cammi, R.; Ochterski, J. W.; Martin, R. L.; Morokuma, K.; Farkas, O.; Foresman, J. B.; Fox, D. J. *Gaussian 16*, rev. B.01; Gaussian, Inc.: Wallingford, CT, 2016.
7. (a) Milgram, B. C.; Eskildsen, K.; Richter, S. M.; Scheidt, W. R.; Scheidt, K. A. *J. Org. Chem.* **2007**, *72*, 3941–3944. (b) Baldwin, J. E.; Bottaro, J. C. *J. Chem. Soc., Chem. Commun.* **1982**, 624–625. Synthesis of **2-1** (c) Jiao, J.; Schmidt, I.; Taniguchi, M.; Lindsey, J. S.; Bocian, D.

- F. *Langmuir* **2008**, *24*, 12047–12053.
8. Bonnett, R.; Buckley, D. G.; Hamzesh, D. *J. Chem. Soc., Perkin Trans. 1* **1981**, 322–325.
 9. Sakai, T.; Seo, S.; Matsuoka, J.; Mori, Y. *J. Org. Chem.* **2013**, *78*, 10978–10985.
 10. Shirataki, C.; Shoji, O.; Terada, M.; Ozaki, S.; Sugimoto, H.; Shiro, Y.; Watanabe, Y. *Angew. Chem. Int. Ed.* **2014**, *53*, 2862–2866.
 11. Yukl, E. T.; Jepakorir, G.; Alontaga, A. Y.; Pautsch, L.; Rodriguez, J. C.; Rivera, M.; Moënnelocoz, P. *Biochemistry* **2010**, *49*, 6646–6654.
 12. Kabsch, W. *Acta Crystallogr., Sect. D: Biol. Crystallogr.* **2010**, *66*, 125–132.
 13. Yamashita, K.; Hirata, K.; Yamamoto, M. *Acta Crystallogr. D Struct. Biol.* **2018**, *74*, 441–449.
 14. Vagin, A.; Teplyakov, A. *J. Appl. Crystallogr.* **1997**, *30*, 1022–1025.
 15. Alontaga, A. Y.; Rodriguez, J. C.; Schönbrunn, E.; Becker, A.; Funke, T.; Yukl, E. T.; Hayashi, T.; Stobaugh, J.; Moënnelocoz, P.; Rivera, M. *Biochemistry* **2008**, *48*, 96–109.
 16. Emsley, P.; Cowtan, K. *Acta Crystallogr., Sect. D: Biol. Crystallogr.* **2004**, *60*, 2126–2132.
 17. Adams, P. D.; Afonine, P. V.; Bunkóczi, G.; Chen, V. B.; Davis, I. W.; Echols, N.; Headd, J. J.; Hung, L.-W.; Kapral, G. J.; Grosse-Kunstleve, R. W.; McCoy, A. J.; Moriarty, N. W.; Oeffner, R.; Read, R. J.; Richardson, D. C.; Richardson, J. S.; Terwilliger, T. C.; Zwart, P. H. *Acta Crystallogr., Sect. D: Biol. Crystallogr.* **2010**, *66*, 213–221.
 18. Murshudov, G. N.; Skubák, P.; Lebedev, A. A.; Pannu, N. S.; Steiner, R. A.; Nicholls, R. A.; Winn, M. D.; Long, F.; Vagin, A. A. *Acta Crystallogr., Sect. D: Biol. Crystallogr.* **2011**, *67*, 355–367.
 19. Moriarty, N. W.; Grosse-Kunstleve, R. W.; Adams, P. D. *Acta Crystallogr., Sect. D: Biol. Crystallogr.* **2009**, *65*, 1074–1080.
 20. DeLano, W. L. *Pymol Mol. Graph. Syst.* **2002**, <http://www.pymol.org>.
 21. Uehara, H.; Shisaka, Y.; Nishimura, T.; Sugimoto, H.; Shiro, Y.; Miyake, Y.; Shinokubo, H.; Watanabe, Y.; Shoji, O. *Angew. Chem. Int. Ed.* **2017**, *56*, 15279–15283.
 22. K. Fujimoto, H. Yorimitsu, A. Osuka, *Org. Lett.* **2014**, *16*, 972–975.
 23. Shimizu, D.; Oh, J.; Furukawa, K.; Dongho, K.; Osuka, A. *J. Am. Chem. Soc.* **2015**, *137*, 15584–15594.

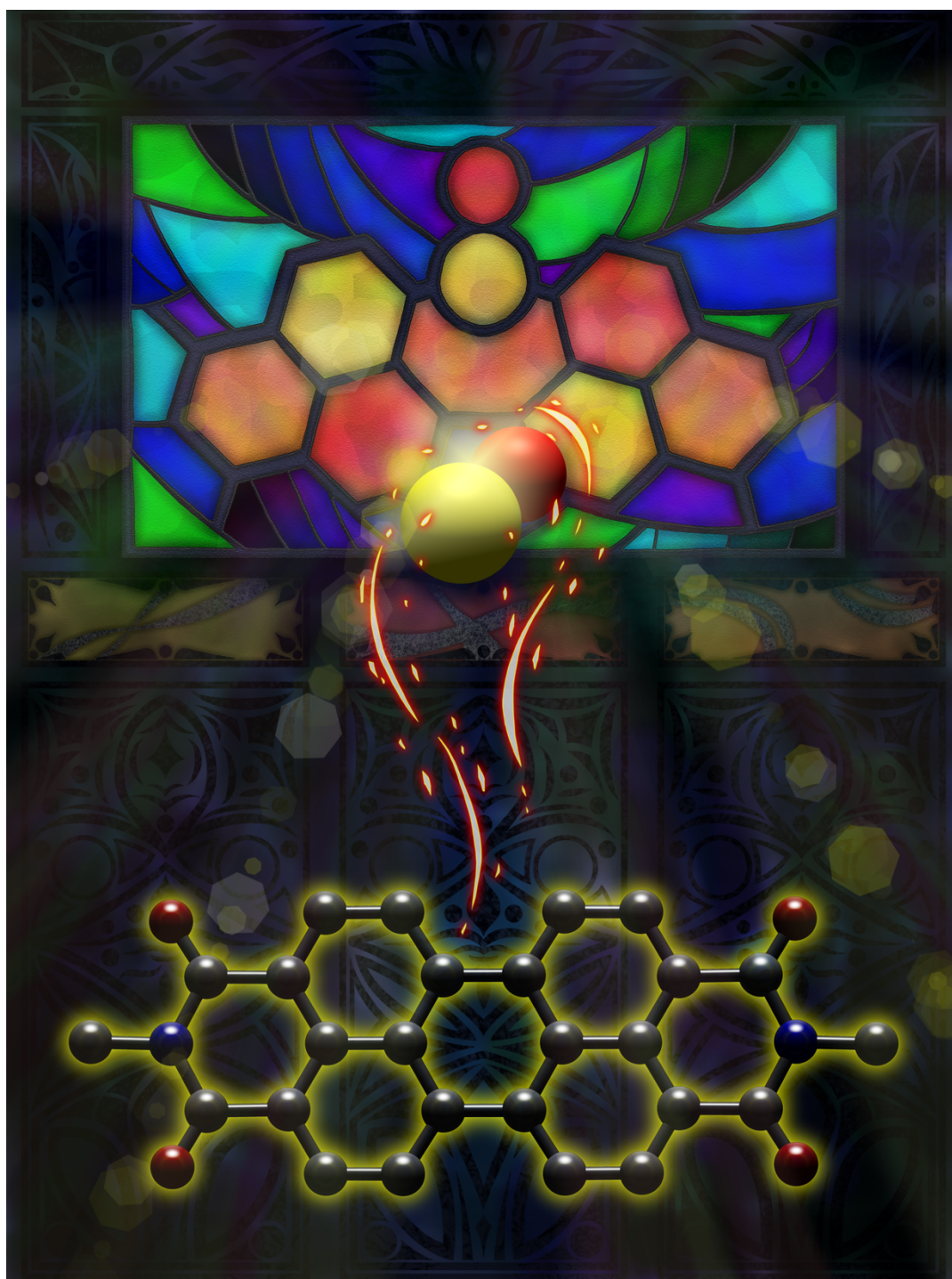
Cover Art Gallery



X-Shaped Cyclobutane-Linked Tetraporphyrins through a Thermal [2+2] Cycloaddition of Etheno-Fused Diporphyrins

Nagai, T.; Takiguchi, A.; Ueda, M.; Oda, K.; Hiroto, S.; Shinokubo, H.

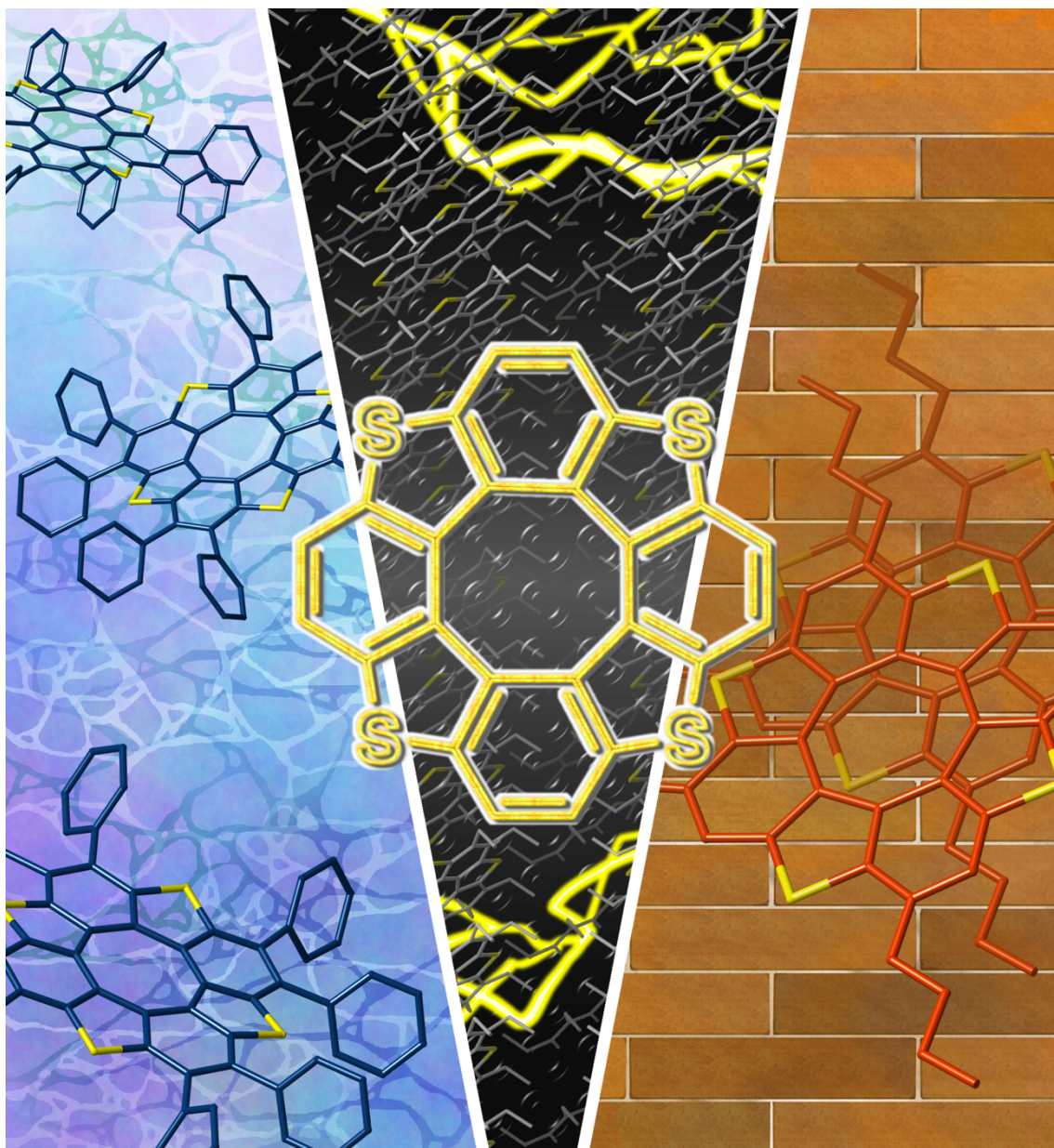
J. Am. Chem. Soc. **2019**, *141*, 19807–19816.



Inserting Nitrogen: An Effective Concept to Create Nonplanar and Stimuli-Responsive Perylene Bisimide Analogues

Hayakawa, S.; Kawasaki, A.; Hong, Y.; Uraguchi, D.; Ooi, T.; Kim, D.; Akutagawa, T.; Fukui, N.; Shinokubo, H.

J. Am. Chem. Soc. **2019**, *141*, 19807–19816.

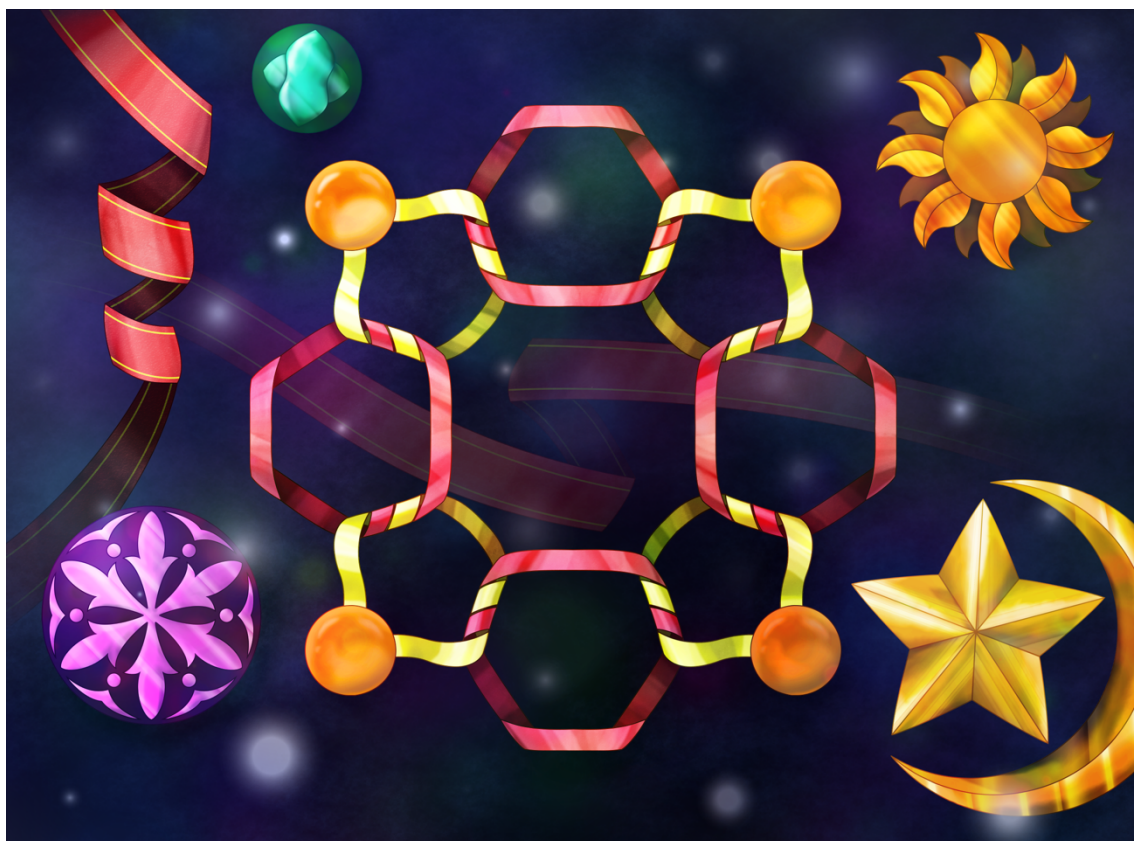


Systematic Synthesis of Tetrathia[8]circulenes: The Influence of Peripheral Substituents on the Structures and Properties in Solution and Solid States

Kato, S.; Akahori, S.; Serizawa, Y.; Lin, X.; Yamauchi, M.; Yagai, S.; Sakurai, T.; Matsuda, W.; Seki, S.; Shinokubo, H.; Miyake, Y.

J. Org. Chem. **2020**, *85*, 62–69.

Selected as the Supplementary Cover.

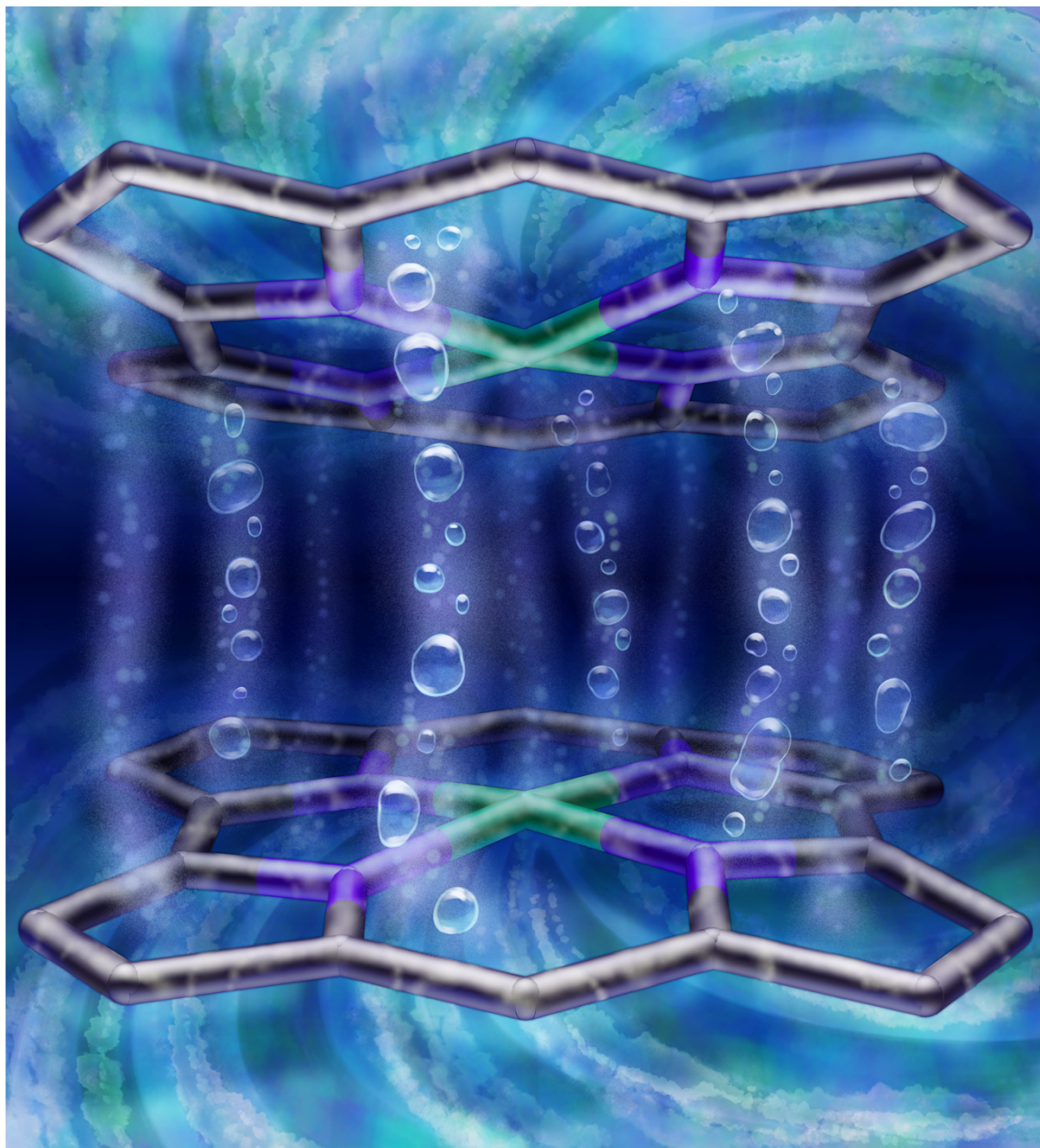


Hetero[8]circulenes: synthetic progress and intrinsic properties

Miyake, Y.; Shinokubo, H.

Chem. Commun. **2020**, *56*, 15605–15614.

Selected as the Front Cover.



Determinant Factors of Three-Dimensional Aromaticity in Antiaromatic Cyclophanes

Kawashima, H.; Ukai, S.; Nozawa, R.; Fukui, N.; Fitzsimmons, G.; Kowalczyk, T.; Fliegl, H.; Shinokubo, H.

J. Am. Chem. Soc. **2021**, *143*, 10676–10685.

Selected as the Supplementary Cover.

List of Publications

1. Synthesis of Dihydropyrazine-fused Porphyrin Dimers
Takiguchi, A.; Wakita, M.; Hiroto, S.; Shinokubo, H.
Chem. Lett. **2019**, *48*, 371–373.
2. Synthesis of Hydroxyisooxophlorins by Oxidative Degradation of *meso*-Hydroxyporphyrins
Takiguchi, A.; Fukui, N.; Shinokubo, H.
Org. Lett. **2019**, *21*, 3950–3953.
3. Dual Emission of a Free-Base 5-Oxaporphyrinium Cation from its *cis*- and *trans*-NH Tautomers
Takiguchi, A.; Kang, S.; Fukui, N.; Kim, D.; Shinokubo, H.
Angew. Chem. Int. Ed. **2021**, *60*, 2915–2919.
4. A Heme-Acquisition Protein Reconstructed with a Cobalt 5-Oxaporphyrinium Cation and Its Growth-Inhibition Activity Toward Multidrug-Resistant *Pseudomonas aeruginosa*
Takiguchi, A.; Sakakibara, E.; Sugimoto, H.; Shoji, O.; Shinokubo, H.
Angew. Chem. Int. Ed. **2022**, *61*, e202112456.
5. 5-Thiaporphyrinium Cation: Effect of Sulphur Incorporation into Porphyrin Skeleton
Takiguchi, A.; Inai, N.; Kang, S.; Hagai, M.; Lee, S.; Yanai, T.; Kim, D.; Shinokubo, H.
submitted
6. Diverse Crystal Structures of Ion Pairs Consisting of Oxaporphyrinium Cations and Pentacyanocyclopentadienide
Takiguchi, A.; Tanaka, H.; Maeda, H.; Shinokubo, H.
submitted

7. Synthesis and Tautomerization of 5-Azaporphyrinium Cations

Takiguchi, A.; Shinokubo, H.

manuscript in preparation

The following paper is not included in this thesis.

8. X-Shaped Cyclobutane-Linked Tetraporphyrins through a Thermal [2+2] Cycloaddition of Etheno-Fused Diporphyrins

Nagai, T.; Takiguchi, A.; Ueda, M.; Oda, K.; Hiroto, S.; Shinokubo, H.

J. Am. Chem. Soc. **2018**, *140*, 8392–8395.

Acknowledgment

First of all, the author would like to express her deepest gratitude to Prof. Dr. Hiroshi Shinokubo at Graduate School of Engineering, Nagoya University, for invaluable guidance and heartwarming encouragement throughout this thesis. The author is deeply grateful to Prof. Dr. Yoshihiro Miyake, Prof. Dr. Satoru Hiroto, Prof. Dr. Norihito Fukui, and Prof. Dr. Ji-Young Shin for their kind and helpful discussions and suggestions of this study. The author was always inspired by the insightful advice from Prof. Shinokubo and the professors in the Shinokubo Group.

The author wishes to express profound gratitude to Prof. Dr. Hiroyuki Furuta at Graduate School of Engineering, Kyushu University and Prof. Dr. Takashi Ooi at Graduate School of Engineering, Nagoya University, for their precious suggestions and discussions on her dissertation committee. The author feels honored to have had this thesis reviewed by two leading researchers.

The author would like to show her tremendous appreciation to Prof. Dr. Osami Shoji and Ms. Erika Sakakibara at Graduate School of Science, Nagoya University, for their worthful discussions and complaisant guidance to accomplish the research on the reconstructed heme protein. The fruitful collaboration with them became her irreplaceable experience.

The author appreciates Prof. Dr. Hiromitsu Maeda, Prof. Dr. Yohei Haketa, Mr. Hiroki Tanaka, and Mr. Shinya Sugiura at College of Life Sciences, Ritsumeikan University for their valuable suggestions and support regarding the study of ion-pairing assembly.

The author gratefully acknowledges Prof. Dr. Dongho Kim, Mr. Seongsoo Kang, and Mr. Seokwon Lee at Department of Chemistry, Yonsei University, to measure excited states dynamics of oxa- and thiaporphyrinium cations.

The author is obliged to Prof. Dr. Tsuyoshi Yanai, Mr. Naoto Inai, and Mr. Masaya Hagai at Graduate School of Science, Nagoya University, for the theoretical analysis regarding thiaporphyrinium cations.

The author expresses her sincere gratitude to everyone as follows to fulfill her studies; Prof. Dr. Shigehiro Yamaguchi, Prof. Dr. Aiko Fukazawa, Dr. Chenguang Wang, Dr. Masato Ito, Mr. Keiji Kajiwarra, Ms. Nao Kimura, and Ms. Mika Sakai at Graduate School of Science, Nagoya University, for the various optical measurements; Prof. Dr. Taishi Takenobu and Prof. Dr. Hisaaki Tanaka at Graduate School of Engineering, Nagoya University, for the ESR measurements; Senior Research Scientist Dr. Hiroshi Sugimoto at RIKEN SPring-8 Center for the X-ray crystallography of reconstructed heme proteins; Prof. Dr. Kazuhiro Tateda and Prof. Dr. Tetsuo Yamaguchi at Graduate School of Medicine, Toho University, for the gift of the multidrug-resistant strains of *P. aeruginosa*; Prof. Dr. Takahiro Sasamori at Faculty of Pure and Applied Sciences, University of Tsukuba, for the X-ray crystallography; Ms. Mana Wakita at Graduate School of Human and Environmental Studies, Kyoto University, for the measurements concerning Appendix 1; Ms. Mie Torii at Graduate School of Engineering, Nagoya University, for the NMR measurements; Prof. Dr. Takashi Ooi and Prof. Dr. Yoshitaka Aramaki at Graduate School of Engineering, Nagoya University, for the transient absorption measurements; Prof. Dr. Shu Seki and Prof. Dr. Yusuke Tsutsui at Graduate School of Engineering, Kyoto University, for the measurements of time-resolved microwave conductivity.

The author is deeply grateful to Prof. Dr. Kunio Miki, Prof. Dr. Kazuki Takeda, Prof. Dr. Masahiro Fujihashi, Dr. Yuichi Nishitani, and Dr. Satomi Niwa, as well as all members of the Miki group at Graduate School of Science, Kyoto University, for their helpful guidance and generous encouragement to her former study from April 2016 to March 2017. What the author learned at the Biological Structural Chemistry Group was applicable for this thesis.

The author also acknowledges the Japan Society for Promotion of Science (JSPS) Research Fellowships for Young Scientists, the Graduate Program of Transformative Chem-Bio Research (GTR), and the Hoshizaki Scholarship for financial support.

The author wishes to express her deep appreciation to the following members of the Shinokubo Group. The author was able to spend a meaningful time thanks to them.

Dr. Hiroki Yokoi	Dr. Hiroto Omori	Dr. Ryo Nozawa
Dr. Takuya Yoshida	Dr. Shuhei Akahori	Ms. Shiori Itabuchi
Mr. Tatsuya Ochiai	Mr. Motoki Takeda	Dr. Tsubasa Nishimura
Mr. Tomohiro Nagai	Dr. Takumi Nakazato	Mr. Yuma Shiratani
Mr. Yasutaka Nakamura	Ms. Sakiho Hayakawa	Mr. Daisuke Yamashita
Mr. Shuto Yokoyama	Mr. Nathan Hikaru Faialaga	Ms. Siham Asyiqin Shafie
Ms. Haruka Takekoshi	Mr. Yuki Tanaka	Mr. Hiroyasu Murase
Mr. Tomoya Yokota	Ms. Wen Xi Chia	Ms. Si-Yu Liu
Dr. Jean-François Longevial	Ms. Mayu Nishijo	Mr. Hiroyuki Kawashima
Mr. Takahiro Sakurai	Mr. Keita Tajima	Mr. Kazuya Miyagawa
Ms. Shiho Mori	Mr. Shusaku Ukai	Mr. Atsumi Yagi
Ms. Mai Odajima	Mr. Masahiro Odawara	Mr. Masaki Kato
Mr. Ryohei Noge	Mr. Kensuke Hanida	Ms. Mao Komura
Mr. Shota Kino	Mr. Yoshihiro Takeo	Mr. Yuki Tanaka
Mr. Shigetatsu Tsugimoto	Mr. Takumi Hayashi	Ms. Kyoka Kusano
Mr. Yusei Takahashi	Mr. Ren Takayanagi	Mr. Ryoya Tomida
Ms. Ayako Kimata		

The author would like to express thankfulness to all members of the Kyoto University Symphony Orchestra and the Nagoya Citizens' Orchestra for their passion for music.

Last but not least, the author desire to express profound gratefulness to her father, Mr. Takumi Takiguchi, her mother, Ms. Yukimi Takiguchi, her brother, Mr. Daichi Takiguchi, her grandfathers, Mr. Akira Takiguchi and Mr. Sueno Sato, and her grandmothers, Ms. Tomoko Takiguchi and Ms. Yoko Sato. This thesis would not have appeared in the present form without their hearty encouragements and devoted supports.

Asahi Takiguchi

瀧口 あさひ

March 2022